Integrated (theoretical, experimental and petrological) study of the stability of zircon and its isotopic systems at dry high-T and hydrothermal medium- to low-T conditions

Irene Morales López

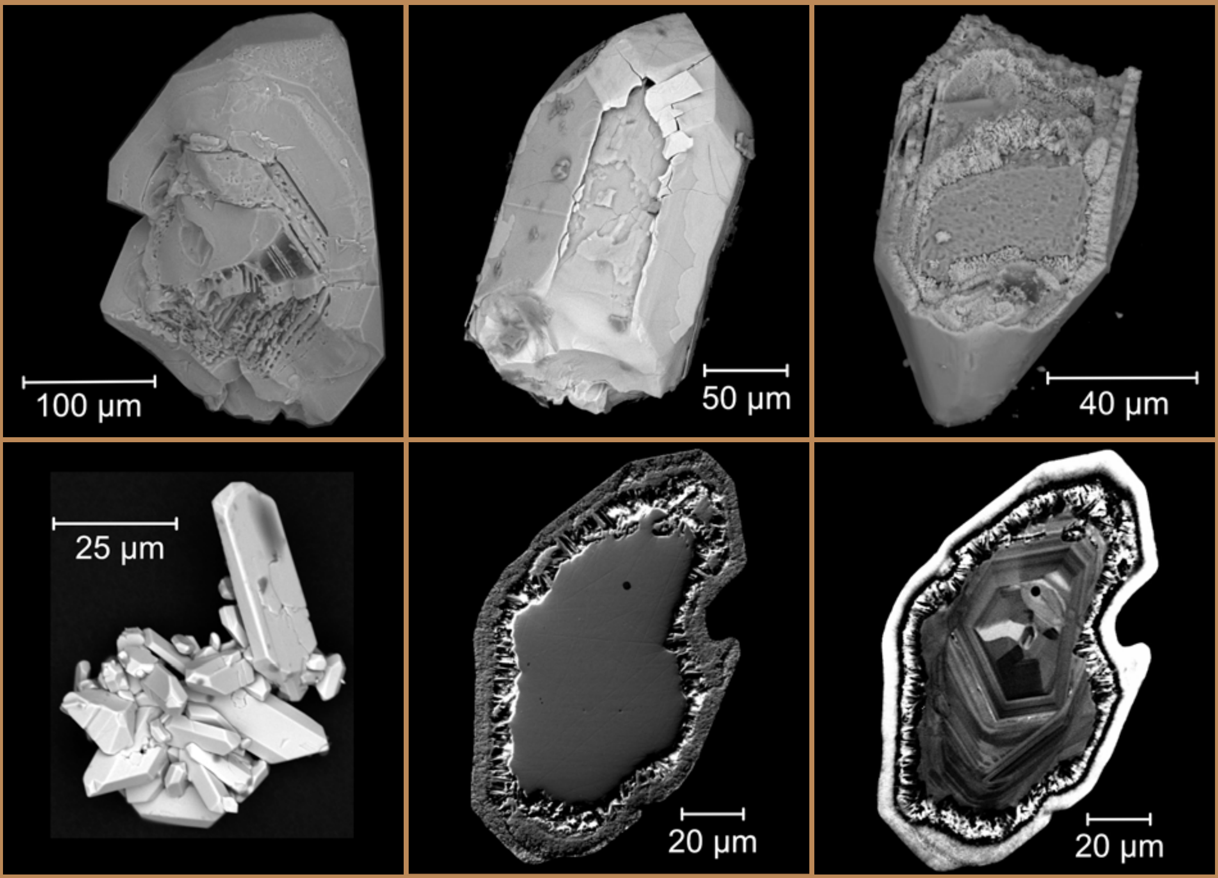

Directores

José Francisco Molina Palma y Mª del Pilar González Montero

Tutor: Fernando Bea Barredo

Tesis Doctoral

2022

UNIVERSIDAD
DE GRANADA

Programa Doctorado
Ciencias de la Tierra

University of Granada

Department of Mineralogy and Petrlogy

Integrated (theoretical, experimental and petrological) study of the stability of zircon and its isotopic systems at dry high-T and hydrothermal medium- to low-T conditions

Irene Morales López

Doctoral thesis
University of Granada
2022

Editor: Universidad de Granada. Tesis Doctorales
Autor: Irene Morales López
ISBN: 978-84-1117-626-2
URI: https://hdl.handle.net/10481/79148

Esta Tesis Doctoral ha sido financiada por el proyecto CGL2017-84469 del Ministerio de Economía y Competitividad, el Grupo de Investigación RNM302 de la Junta de Andalucía, así como por la beca disfrutada por la doctoranda del programa de Formación de Personal Investigador (FPI) por el Ministerio de Ciencia e Innovación. El trabajo de investigación se ha llevado a cabo en el Departamento de Mineralogía y Petrología de la Universidad de Granada (UGR) y en el Centro de Instrumentación Científica (CIC) ambos sitos en Granada.

Agradecimientos

Me gustaría expresar mi más sincera gratitud a todos aquellos que han contribuido en el desarrollo de este trabajo, y sin los cuales no hubiera sido posible.

En primer lugar, quiero agradecer a mi tutor Fernando Bea por la confianza depositada en mí e integrarme en el grupo de investigación y por toda la ayuda y apoyo en estos años. También por poner a mi disposición todos los medios necesarios para la realización de esta tesis, todos los equipos, los circones utilizados en los experimentos así como el software utilizado en los modelos numéricos. Muchas gracias también por todo lo que me has enseñado.

En segundo lugar, a mis directores José Francisco Molina y Pilar Montero. Muchas gracias por darme la oportunidad de formar parte de este grupo de investigación y por guiarme durante este periodo. Muchas gracias Pepe, por la dedicación que has invertido en esta tesis, por buscar un hueco siempre que ha sido necesario para que esta tesis se haya podido terminar. Gracias por todo lo que he aprendido en todos estos años y por la confianza que has demostrado en todo momento. Muchas gracias Pilar, por la dedicación invertida en la tesis, por buscar siempre tiempo, aunque no lo hubiera, para ayudarme y por confiar en mí.

A Aitor Cambeses por la ayuda que me ha prestado siempre que la he necesitado, por tu apoyo y consejo y por ayudarme no solo a realizar la estancia sino por estar ahí conmigo ayudandome las primeras semanas. También gracias por todo lo que me has enseñado, que han sido muchas cosas, sobre todo a tener todo despejado cuando se esta trabajando en un laboratorio.

Agradecer también al apoyo institucional del Departamento de Mineralogía y Petrología de la Universidad de Granada y también a todo el personal del Centro de Instrumentación Científica que he conocido durante este periodo, en especial a Delia Ortega, Olga Cazalla e Isabel Nieto.

Un especial agradecimiento a Sumit Chakraborty por su acogida en Bochum, por todo lo que me ha enseñado durante la estancia sobre termodinámica y petrología experimental en esas charlas hasta tarde.

Un gran agradecimiento va también a mis compañeros de doctorado, especialmente a todos mis compañeros diarios del despacho 5: Fabian, Jesús, Maria, Poliana, Dámaris, Julia, Natalia, Nuria, Paula, Haoyu por todos los buenos momentos, que han sido muchos. También a Sarah del despacho de al lado, que no te me olvidas. Un especial agradecimiento a Ana Cassano (que coincidimos en ese bus antes de conocernos, jajaja), decirte que fue muy bonito conocerte y que te agradezco todas esas salidas por Granada y por darme tanto ánimo durante todo este tiempo.

También me gustaría agradecer a gente ajena al ambito profesional pero que me han ayudado sin duda con sus ánimos y charlas. Me gustaría acordarme en primer lugar de Ile que tantos buenos momentos hemos pasado y seguiremos pasando, muchas gracias amiga por estar siempre. También acordarme de Guio por apoyarme tanto en este camino y por todos esos grandes momentos de campo. A Magda y Nico por todas esas noches de risas que tanto han ayudado a desconectar un poco.

Y por último, pero no menos importante, me gustaría agradecer a mi familia por el apoyo y la confianza que han puesto en mí y todos los ánimos. Gracias.

Esta Tesis Doctoral ha sido financiada por el proyecto CGL2017-84469 del Ministerio de Economía y Competitividad, el Grupo de Investigación RNM302 de la Junta de Andalucía, así como por la beca disfrutada por la doctoranda del programa de Formación de Personal Investigador (FPI) por el Ministerio de Ciencia e Innovación.

Table of contents

PART I. INTRODUCTION

PART II. EXPERIMENTAL STUDY

PART III. NUMERICAL MODELING

PART IV. CONCLUSIONS

ABSTRACT

Resumen

Abstract

Zircon is one of the most studied minerals by Earth Scientists because of its widespread occurrence in a large diversity of rocks and its key role in the distribution of crucial incompatible trace elements, such as U, Th, Y, Hf and rare earth elements (REE), its generalized application in U-Th-Pb geochronometry and the determination of magma sources throughout the signature of its oxygen and hafnium isotopes. Its remarkable mechanical and chemical resilience makes it possible to carry out all these studies. However, the stability of zircon and its geochemical behavior in environmental conditions very different from its formation are still not well understood. On the other hand, for a better understanding of the geochronological and geochemical information recorded in zircon, it is necessary to know the mechanisms that allow the inheritance of zircon in granites and the formation of zircon in hot mafic magmas that are generally undersaturated in it.

This PhD thesis aims to deepen our understanding of zircon stability and its geochemical behavior at extremely high-T conditions, such as those occurring during assimilation processes in basic magmas that can lead to zircon xenocryst entrapment in cumulus mafic minerals and in hydrothermal environments, where it can be a source of trace elements for ore genesis. These purposes have been accomplished by performing annealing experiments using a tubular furnace on the one side, and hydrothermal experiments with Teflon bombs and autoclave reactor, on the other. In addition, the parameters that control zircon inheritance in granitic magmas and the mechanisms of zircon crystallization in low-Zr mafic magmas are modeled numerically.

Three samples of zircon separates, chosen based on their morphology and degree of metamictization, were used for the experiments. The samples are

The Cambrian-Ordovician orthogneiss SAB50, because it contains numerous pristine zircons that often have inherited cores of Ediacaran or older age.

The Variscan tonalite SAB51, because it contains zircons with a very uniform isotopic composition and occasional metamict bands.

The Early Paleoproterozoic to Neoarchaean syenite REG20 because it contains highly metamict zircons that are very rich in inclusions and show high ^{204}Pb and radiogenic Pb loss.

For the dry high-T experiments, zircon grains embedded in pure cristobalite were placed in open crucibles and heated in a horizontal tubular furnace under an N_2 atmosphere at 1300°C for 1, 3 and 6 months.

Ultra-pure H_2O and 2M NaCl, 2M $CaCl_2$ and 1M NaF solutions were used for the hydrothermal experiments. Zircon + granite powder + solution and granite powder + solution were placed into the teflon bombs and heated at 170 ºC at ca. 10 bar for 43 days. In the autoclave experiments, zircon + solution and zircon + quartz + solution were heated at 550 ºC, at ca. 2 kbar for 3 and 8 days.

For determining the most important parameters that control zircon inheritance, we calculated the melt fraction as a function of the temperature in three selected protoliths: a peraluminous greywacke, a metaluminous granodiorite, and a gabbrodiorite. The calculations were done from 650°C to their liquidus temperatures at 3, 6 and 9 kbar and 2, 4, 6, 8 and 10 wt% of H_2O using rhyolite-MELTS. Melt production rates were determined using COMSOL^{TM}. For understanding the mechanisms that enable zircon crystallization from low-Zr mafic magmas, diffusion kinetics of Zr rejected by growing minerals in pore-confined MORB melts was determined using moving mesh 2D finite element models computed with COMSOL^{TM}.

The annealing experiments show recrystallization of metamict domains, melting of polymineralic inclusions, formation of nanopores and microcracking propagated by thermo-elastic stress accumulated at the interface between domains with different lattice orientations. The zircon-to-baddeleyite transformation occurred by (i) incongruent zircon dissolution in molten mineral inclusions with a high CaO/SiO_2 ratio and (ii) recrystallization of metamict domains mediated by silica releasing from the reaction site. Highly metamict zircon was successfully dated after annealing at 1300 ºC because all their common Pb but little radiogenic Pb were lost due to the generation of a melt. Ti concentration increased in the zircon lattice of annealed zircon grains with minute inclusions of rutile or other Ti-bearing minerals. Tungsten could achieve high abundances in zircons from regions with W deposits. An overall increase in W concentration occurred upon annealing because of the dissolution of minute W impurities into the zircon lattice. However, given the limited solubility of W in zircon, a fraction of the released W was consumed in forming W-rich minerals. The oxygen isotope composition of annealed zircon grains embedded in cristobalite drifted quickly to that of this latter. This leads to the conclusion that crustal-derived zircon xenocrysts with high $\partial^{18}O$ from mantle rocks could not have resided in the mantle for a long time.

The hydrothermal experiments show that in all low-T, silica-saturated fluids, congruent zircon dissolution took place in the presence of H_2O and saline fluids, leading to an increase of zircon permeability along microcracks. In the high-T, silica-saturated experiments, zircon dissolution was congruent for H_2O, $CaCl_2$ and NaCl fluids and incongruent for NaF fluids with precipitation of Na-Zr silicate. In all the high-T, silica-undersaturated experiments, zircon was transformed to baddeleyite by coupled dissolution-precipitation mechanisms enhanced by microcracks and pores and permeability creation associated with the lower molar volume of baddeleyite and the silica releasing from the reaction site. The total zircon-to-baddeleyite transformation occurred in the NaCl and NaF fluids, indicating that solutions with Na^+ are more reactive than those with Ca^{2+}. Leachates extracted from both high- and low-T hydrothermal experiments presented a remarkable decoupling of Y from HREE, with the former being significantly more partitioned into the fluid. Pb was also partitioned into the leachates with respect to U in all experiments, whereas a significant Th-U fractionation was only present in $CaCl_2$ and NaCl fluids at low-T conditions, with Th being more partitioned into the fluid.

The numerical models predicted that the capacity of granitic magmas to inherit zircons from their source was a consequence of the interplay between zircon saturation in the melt and magma mobility, being water content of magmas as the key parameter for controlling the abundance of inherited zircon in granitic rocks. In most cases, the rate of zircon dissolution was significantly faster than this of melt generation. It is estimated that a much more intense heat flux than the one supplied by radioactive decay or asthenospheric upwelling is required for generating melts fast enough to prevent equilibrium with zircon. This requirement is fulfilled only by hot mafic magma underplating, where most of the heat released to the crust comes from its latent heat of crystallization. Zircon inheritance may be substantial in S-type water-rich granite magmas generated at 4.5–6 kbar. In contrast, water-poor granite magmas have moderate or no inheritance because they need higher temperatures to produce a similar melt fraction.

The numerical models also predicted that local Zr enrichment at growing interfaces of major minerals could only occur when magma reached a crystallinity high enough to confine residual melts into pores; otherwise, erosion of Zr-rich melt created in the diffusion boundary layers could occur. This process can explain the appearance of Mid-Atlantic syn-magmatic zircons being limited chiefly to cumulate rocks. The calculations showed that local saturation next to growing mineral interfaces seems to be the only possible mechanism for explaining zircon growth before attaining zircon saturation in the bulk mafic magma. On the other hand, the proposed mechanism will be hampered, or even totally inhibited, by the crystallization of major minerals that can partition Zr. Thus, the model predicts that the growth of minerals with Zr mineral/melt partition coefficient > 0.2, such as clinopyroxene and amphibole, will not produce a zircon-saturated diffusion boundary layer. This implies that the crystallization of these minerals in mafic systems will never reach zircon saturation unless they are much richer in Zr than the MORB considered in the model. These relationships explain the appearance of zircon primocrysts only in the earliest cumulates from the Mid-Atlantic rocks.

Resumen

El zircón es uno de los minerales más estudiados en Ciencias de la Tierra debido a su presencia en una gran diversidad de rocas, su papel clave en la distribución de elementos traza incompatibles muy importantes, como U, Th, Y, Hf y las tierras raras (REE), su aplicación generalizada en geocronología de U-Th-Pb y en la determinación de fuentes magmáticas a través de la firma de sus isótopos de oxígeno y hafnio. Su notable resistencia mecánica y química permite realizar todos estos estudios. Sin embargo, la estabilidad del zircón y su comportamiento geoquímico en condiciones ambientales muy diferentes a las de su formación aún no se conocen bien. Por otro lado, para una mejor comprensión de la información geocronológica y geoquímica registrada en el zircón, es necesario conocer los mecanismos que permiten la herencia de zircón en granitos y la formación de zircón en magmas máficos calientes que generalmente están subsaturados en esta fase mineral.

Esta Tesis Doctoral pretende profundizar en el conocimiento de la estabilidad del zircón y su comportamiento geoquímico en condiciones de T extremadamente alta, como las que se producen durante los procesos de asimilación en magmas básicos que pueden dar lugar a la inclusión de xenocristales de zircón en minerales máficos acumulados, y en ambientes hidrotermales, donde puede ser una fuente de elementos traza para la génesis de yacimientos minerales. Estos objetivos se han logrado realizando experimentos de annealing con un horno tubular, por una parte, e hidrotermales con bombas de teflón y, una autoclave, por otra. Además, se modelan numéricamente los parámetros que controlan la herencia del zircón en magmas graníticos y los mecanismos de cristalización de zircón en magmas máficos con bajo contenido en Zr.

Para los experimentos se han utilizado tres muestras de concentrados de zircón, elegidos en base a su morfología y grado de metamictización. Las muestras son: (i) el ortogneis cambro-ordovícico SAB50 con zircones escasamente metamícticos con una herencia abundante, (ii) la tonalita varisca SAB51 con zircones que presentan bandas metamícticas localizadas y homogeneidad isotópica, y (iii) la sienita REG20 del Paleoproterozoico temprano al Neoarcaico con zircones muy metamícticos, con inclusiones abundantes y presencia de Pb común y pérdida de Pb radiogénico.

Para los experimentos de alta T en seco, se colocaron granos de zircón embebidos en cristobalita pura en crisoles abiertos y se calentaron en un horno tubular horizontal bajo una atmósfera de N_2 a 1300°C durante 1, 3 y 6 meses.

Para los experimentos hidrotermales se utilizó agua ultrapura y soluciones de NaCl 2M, $CaCl_2$ 2M y NaF 1M. Mezclas de zircón + polvo de granito + solución y polvo de granito + solución se colocaron en las bombas de teflón y se calentaron a 170 ºC a aprox. 10 bar durante 43 días. En los experimentos en autoclave, mezclas de zircón + solución y zircón + cuarzo + solución se calentaron a 550 ºC, a unos 2 kbar durante 3 y 8 días.

Para determinar los parámetros más importantes que controlan la herencia del zircón, se calcularon con rhyolite-MELTS las fracciones de fundido para tres protolitos seleccionados con composiciones de grauvaca peraluminosa, granodiorita metaluminosa y gabrodiorita, para unos rangos de temperatura que variaban desde 650 ºC hasta la temperatura liquidus de cada composición. Los cálculos se realizaron a presiones de 3, 6 y 9 kbar y contenidos en agua del 2, 4, 6, 8 y 10 wt%. Las tasas de producción de fundido se determinaron con COMSOL^{TM}. Por otra parte, para entender los mecanismos que permiten la cristalización del zircón a partir de magmas máficos pobres en Zr, se determinó la cinética de difusión del Zr rechazado por los minerales de la interfase de crecimiento en fundidos MORB confinados en poros, utilizando modelos de

elementos finitos 2D con malla móvil calculados con COMSOL™.

Los experimentos de annealing muestran recristalización de dominios metamícticos, fusión de inclusiones poliminerales, formación de nanoporos y microfracturación propagada por la tensión termoelástica acumulada en la interfase entre dominios con diferente orientación cristalográfica. La transformación de zircón a baddeleyita tuvo lugar por dos mecanismos diferentes: (i) disolución incongruente de zircón en inclusiones minerales fundidas con una relación CaO/SiO_2 elevada, y (ii) recristalización de dominios metamíticos mediada por la liberación de sílice del sitio de reacción. Los zircones extremadamente metamíticos se pudieron datar con éxito tras annealing a 1300 ºC debido a que todo su Pb común, pero poco Pb radiogénico, se perdió del zircón como consecuencia de la formación de un fundido. Se observó un aumento de la concentración de Ti en los granos de zircón con inclusiones diminutas de rutilo u otros minerales portadores de Ti. El wolframio pudo alcanzar una abundancia relativamente elevada en los zircones de regiones con depósitos de W. Se produjo un aumento generalizado de la concentración de W tras el annealing debido a la disolución de impurezas diminutas de W en la red del zircón. Sin embargo, dada la limitada solubilidad del W en el zircón, una fracción del W liberado se consumió en la formación de minerales ricos en W. La composición isotópica de oxígeno de los granos de zircón embebidos en cristobalita se desvió rápidamente hacia los valores de esta última. Esta evidencia permite concluir que los xenocristales de zircón de origen cortical con valores de $\partial^{18}O$ altos encontrados en rocas del manto no podrían haber residido en éste durante mucho tiempo.

Los experimentos hidrotermales mostraron que en todos los fluidos saturados en sílice de baja T, el zircón se disolvió congruentemente en presencia de H_2O y fluidos salinos, lo que llevó a un aumento de su permeabilidad a lo largo de microfracturas. En los experimentos saturados en sílice a alta T, la disolución de zircón fue congruente en presencia de fluidos con H_2O, $CaCl_2$ y NaCl, e incongruente en fluidos con NaF donde precipitaron silicatos de Na-Zr. En todos los experimentos subsaturados en sílice a alta T, el zircón se transformó en baddeleyita por mecanismos acoplados de disolución-precipitación potenciados por la presencia de microfracturas y poros y por la creación de permeabilidad asociada al volumen molar más pequeño de la baddeleyita y a la liberación de sílice de la zona de reacción. Una transformación total de zircón a baddeleyita se produjo en fluidos con NaCl y NaF, lo que indica que las soluciones con Na^+ son más reactivas que las de Ca^{2+}. Los lixiviados extraídos de los experimentos hidrotermales de alta y baja T presentaron un notable fraccionamiento de Y con respecto a HREE, presentando el primero una mayor concentración en el fluido. El Pb también se concentró preferentemente en los lixiviados con respecto al U en todos los experimentos, mientras que un fraccionamiento significativo de Th con respecto a U sólo se produjo en los fluidos con $CaCl_2$ y NaCl en condiciones de baja T, presentando el Th una mayor concentración en el fluido.

Los modelos numéricos predijeron que la capacidad de los magmas graníticos para heredar zircones de su fuente era una consecuencia de la interacción entre la saturación de zircón en el fundido y la movilidad del magma, siendo el contenido en agua del magma el parámetro clave que controlaba la abundancia de zircón heredado en las rocas graníticas. En la mayoría de los casos, la tasa de disolución de zircón fue significativamente más grande que la de generación de fundido. Se estima que se requiere un flujo de calor mucho más intenso que el suministrado por desintegración radioactiva o ascenso del manto astenosférico para generar fundidos con la suficiente rapidez como para evitar el equilibrio con el zircón. Este requisito sólo lo cumple el magmatismo máfico de la base de la corteza que está caracterizado por la generación de una gran cantidad de calor latente de cristalización que es transferido a la corteza. La supervivencia del zircón es más probable en rocas metasedimentarias peraluminosas fértiles que en félsicas a máficas metaluminosas que dominan la fuente. La herencia de zircón es más importante en los magmas graníticos de tipo S ricos en agua generados a 4.5-6 kbar. Por el contrario, los magmas graníticos pobres en agua se caracterizan por una herencia moderada o nula porque necesitan temperaturas más altas para producir una fracción de fundido similar.

Los modelos numéricos también predijeron que el enriquecimiento local de Zr en las interfase de crecimiento de minerales esenciales sólo podría ocurrir cuando el magma alcanzaba una cristalinidad lo suficientemente elevada como para confinar los fundidos residuales en los poros de la roca; de lo contrario, podría producirse la dispersión de los fundidos ricos en Zr creados en las capas límite de difusión. Este proceso puede explicar que la aparición de zircones sin-magmáticos del Atlántico Medio se limite principalmente a las rocas acumuladas. Los cálculos mostraron que la saturación local en las proximidades de la interfase de crecimiento mineral parece ser el único mecanismo posible que es capaz de explicar el crecimiento de zircón mucho antes de que el fundido alcance la saturación en esta fase mineral a escala global. Por otra parte, el mecanismo propuesto puede ser inhibido parcial o totalmente por la cristalización de minerales con un coeficiente de partición mineral/fusión para Zr>0.2, como clinopiroxeno y anfíbol. Ello implica que debido a la cristalización de estas fases minerales en sistemas máficos, nunca se alcanzará la saturación de zircón salvo que la composición del magma sea mucho más rica en Zr que el MORB considerado en el modelo. Estas relaciones explican porqué en el Atlántico Medio solo aparecen primocristales de zircón en los acumulados más precoces.

PART I. INTRODUCTION

I.1 Introduction

I.2 Objectives

I.3 Previous research

I.1 Introduction

I.1.1 Introduction

Zircon is currently the most studied mineral by Earth Scientists because of several reasons:

- Its widespread occurrence as an accessory mineral in a large diversity of rocks.
- Its key role in the distribution of geochemically essential trace elements, such as U, Th, Y, Hf and rare earth elements (REE)
- It is the favorite mineral used for the U-Th-Pb geochronometry because its U and Th concentrations are much higher than in host rocks, and it hardly uptakes the daughter element Pb during crystallization.
- Its oxygen and hafnium isotope signature provide essential clues about its origin and the nature of its crystallization environment.
- Its remarkable mechanical and chemical resilience. It is robust enough to retain its original chemical and isotopic signatures during the sedimentary cycle; it also can stand high-temperature processes and remain as inherited grains in magmatic rocks.
- Its solubility in silicate melts has been thoroughly studied experimentally; being the leading Zr carrier in most igneous rocks, their concentration can be straightforwardly related to the magma crystallization temperature.

These features are described in the following sections, evidencing that most aspects of zircon behavior in natural rocks have been thoroughly studied over the years. However, many points still remain obscure, especially those related to high-T and hydrothermal processes, which are the objective of this work, as described in **section I.2**.

I.1.2 Zircon occurrence

I.1.2.1 Igneous rocks

Zircon is likely the most abundant accessory phase in igneous rocks. Its modal fraction in a given rock hardly goes over 0.1 %, but most rocks contain zircon (be this pristine or inherited), even those which were classically supposed to be exempt from this mineral, such as MORB mafic and ultramafic (e.g., Pilot et al., 1998; Grimes et al., 2007; Aranovich et al., 2017; Bortnikov et al., 2022 and references therein) orogenic peridotites (e.g. Bea et al., 2001; Sánchez-Rodríguez & Gebauer, 2000; Zanetti et al., 2016, and references therein), kimberlites (Kresten et al., 1975; Belousova et al., 1998; Hoskin, 1998; Konzett et al., 1998), or carbonatites (e.g., Savva et al., 2009; Montero et al., 2016; Borisova et al., 2020, and references therein).

I.1.2.2. Detrital rocks

Zircon is a common component of detrital rocks' heavy mineral fraction. The oldest material on Earth has been found as detrital zircons in the Jack Hills - Mount Narryer sandstones (Froude et al., 1983; Compston & Pidgeon, 1986; Kinny et al., 1988, etc.). Detrital zircon studies to identify sedimentary rocks provenance have been prevalent since the LA-MC-ICPMS technique has become widely available (e.g., Fedo et al., 2003; Avigad et al., 2003; Dhuime et al., 2011; Gehrels, 2012; Talavera et al., 2012; Rojas-Agramonte et al., 2011; Kemp, 2018, and references therein).

I.1.2.3 Metamorphic rocks

Zircon from metamorphic rocks can be divided into inherited and newly grown during the metamorphism. The former appear in all types of metamorphic rocks; their external morphology is either fragmental or rounded, rarely euhedral; they may show metamorphic overgrowths or signs of resorption and preserve the original internal zoning. The latter appear either as rims over older cores or as new crystals typically with rounded or ovoidal (Hoskin & Black, 2000; Wayne & Sinha, 1988; Hanchar & Miller, 1993; Degeling et al., 2001), even "football-shaped" zircons (Vavra et al., 1996; Schaltegger et al., 1999). Their internal textures are varied because they can grow under various P-T-x stress conditions. The most common are metamorphic growth zones and recrystallized domains, often with preserved igneous cores (Hanchar & Rudnick, 1995; Rubatto & Gebauer, 2000; Kempe et al., 2000; Corfu et al., 2003); fine-scale alternating zoning is characteristically absent.

I.1.2.4 Hydrothermal zircon

Hydrothermal zircon is mostly found in quartz veins or metasomatic rocks related to economic deposits of Au and other metals at relatively low to medium temperatures and low pressure (Claoué-Long et al., 1990; Kerrich & King, 1993; Li et al., 1997; Yeats et al., 1996; Mueller et al., 1996; Flowers, 2000; Ramezani et al., 2000). A characteristic spongy texture (Hoskin et al., 1998) and high abundances of common Pb (Watson et al., 1997), F, LREE, Nb, Ta and other incompatible elements (Rubin et al., 1989; Hoskin et al., 1998) helps to identifies it.

I.1.3 Zircon as a trace-element reservoir

Despite its low modal fraction, in most rocks, zircon controls a significant part of trace elements such as Zr, the heat-producing Th and U, the HREE, Y and other HFS elements (Bea, 1996b).

Belousova et al. (2002) studied trace element signatures in zircon, finding that these can be correlated with the nature and origin of the host rock. This fact can be helpful in situations where the origin of the zircon grain is not evident from its geological context, for example, inherited cores, xenocrysts, and detrital zircons. Grimes et al. (2007, 2009, and 2015) expanded these types of work for the zircons found in the oceanic lithosphere, which resulted in an invaluable tool for deciphering the provenance of zircon xenocrysts found in the Mid-Atlantic Ridge gabbros and ultramafic rocks (e.g. Bortnikov et al., 2008, Bea et al., 2020, and references therein).

Rubatto & Hermann (2007) studied the trace element partitioning between zircon and melt on the one side, and between zircon and garnet, on the other side, using different experiments with variable temperatures. They showed that the trace element partitioning in zircon increases with temperature, proposing that the trace element partitioning of zircon/melt tends to increase with decreasing temperature. They found that zircon contains more HREE than coexisting garnet, whereas the MREE are similar. They concluded that the trace element partitioning data would be a basis for correlating zircon ages with garnet growth, helping to construct detailed pressure-temperature-time trajectories in high-grade metamorphic rocks.

Of particular interest is the existence of two well-proven and experimentally calibrated geothermometers based on zircon. The first geothermometer introduced was based on the absolute abundance of Ti (Watson & Harrison, 2005; Watson et al., 2006; Ferry & Watson, 2006); it has revealed extraordinary utility in studying the crystallization temperature of igneous rocks (e.g. Bea et al., 2006a; Harrison et al., 2007; Bea et al., 2007). The second is based on the Zr/Hf ratio (Aranovich & Bortnikov, 2018); although it has not yet been extensively applied, it seems promising.

I.1.4 Zircon geochronology

U-Pb dating in zircon started in the early sixties (Silver & Deutsch, 1963). It was performed by melting zircon grains with Na-tetraborate, dissolution of the resulting glass, and subsequent separation of Pb as a dithizonate. The isotope composition of the concentrate was then measured in a thermal ionization mass spectrometer (TIMS) similar to the ones developed by Alfred Nier during the thirties-early forties impulsed by the Manhattan project. This method produced enormous blanks caused by Pb contamination in the reagents, thus hindering the obtention of reliable U-Pb ages. The introduction of hydrothermal decomposition and ion-exchange separation (Krogh, 1973) greatly reduced the blanks; this and the further introduction of abrasion techniques (Krogh, 1982a) and refined magnetic separation (Krogh, 1982b) improved the blanks and made of zircon U-Pb TIMS dating a mature and widely employed technique. Combined with isotope dilution, it is still the most precise way of dating zircons, provided these come from a single-age population.

This requirement, however, cannot be taken for granted because many rocks contain a mixture of pristine and inherited components, even in the same grain. The Ollo de Sapo Formation of Central Iberia case is worth mentioning because most of its zircons consist of Cambrian-Ordovician rims around Ediacaran or older cores (Montero et al., 2007). In this situation, the only way to get precise U-Pb ages is to use single-grain techniques such as the Kober evaporation method (Kober, 1986 and 1987), also done in an unmodified TIMS spectrometer, or more spatially-resolved techniques such as secondary ions mass spectrometry (SIMS) or laser-ablation ICP-MS techniques, massively employed in the last years. SIMS and LA-Mc-ICPMS also permit the determination of ^{232}Th in the same run, so these analyses normally include three geochronometers, ^{206}Pb/^{238}U, ^{207}Pb/^{235}U, and ^{208}Pb/^{232}Th, with a very high spatial resolution and lower blanks, especially SIMS, than any other technique.

I.1.5 Oxygen and Hafnium isotopes

I.1.5.1 Oxygen isotopes

Microanalytical techniques are increasingly helpful for oxygen isotope analysis of refractory minerals such as zircon. Both laser fluorination and SIMS offer significant advantages over conventional techniques for zircon analysis. The laser fluorination optimizes the analysis of ∂^{18}O in zircon by using a CO_2 laser (λ = 10.6 µm). For homogeneous samples of approximately 2 mg, an accuracy and precision of ±0.05 to ±0.1‰ is achieved (Valley et al., 1994; Valley et al., 1995). For a normal range of igneous zircon grain sizes, 2 mg would represent the order of ten to several hundred grains, so grain separation and sorting can affect data quality. However, the ion microprobe has significantly improved spatial resolution for oxygen isotope analyses obtained in situ from single zircon crystals (Eiler et al., 1997; Valley et al., 1998a; Peck et al., 2001). Analytical precision for ∂^{18}O of 0.5‰ can be obtained from samples of approximately 3 ng (10 to 20 µm diameter spot).

Many studies have shown that non-metamict zircons retain their ∂^{18}O value from the time of crystallization e.g. (Valley et al., 1994; Watson & Cherniak, 1997; Cherniak et al., 1997a; Valley et al., 1998b), hence oxygen isotopes can be correlated with U-Pb age or trace element composition. The ∂^{18}O record of zircon is generally preserved despite other minerals having been reset by high-grade metamorphism (Lackey et al., 2002) or intense hydrothermal alteration (King et al., 1997). Therefore, zircon analysis can provide evidence for magmatic crystallization in a closed system versus assimilation in an open system, contamination or post-magmatic alteration. For example, if zircon crystallizes during a period of time when the magmatic composition changes, then the core to rim growth zoning will record this change (King & Valley, 2001; Wilde et al., 2001; Valley, 2003).

On the other hand, metamict zircons that have suffered more radiation damage and are therefore more U-rich, may develop microfractures due to hydration and swelling of the damaged U-rich domains, with this radiation damage enhancing oxygen diffusion and exchange by creating fast exchange pathways, which may hinder slower volumetric diffusion (Valley, 2003). Oxygen diffusion in zircon is discussed in **section I.1.6.2.3**.

I.1.5.2 Hf isotopes

The worldwide use of the LA-MC-ICPMS technique (e.g. Thirlwall & Walder, 1995; Griffin et al., 2002; Woodhead et al., 2004) has made Hf isotope analysis of individual zircon grains increasingly popular for studying the crustal formation and petrogenesis of igneous rocks, because 1) zircon is a ubiquitous accessory mineral in igneous and high-grade metamorphic rocks, 2) it can record initial Hf isotope composition at the time of crystallization owing to its low Lu/Hf and resistance to secondary Hf isotope disturbance, 3) its crystallization age can be precisely determined by U-Pb dating, and 4) it offers an archive of crustal formation from 4.4 Ga to the present (Jonathan Patchett et al., 1982; Stevenson & Patchet, 1990; Corfu & Noble, 1992; Vervoort & Patchett, 1996; Scharer et al., 1997; Amelin et al., 2000; Wilde et al., 2001).

The Hf isotope composition changes with time because of the ß decay of ^{176}Lu: ^{176}Lu <—> ^{176}Hf + ß. This change is nearly imperceptible because the ^{176}Lu abundance is low (0.0256 of total Lu) against ^{176}Hf (0.0526 of total Hf), and zircon has Lu/Hf ≈ 0.06-0.08 (Bea et al., 2018a). Therefore, the ^{176}Hf/^{177}Hf ratio of zircon can be considered as the initial value when it crystallizes. As mentioned above, zircon also has a high resistance to subsequent thermal events.

This effect does not detract from the fact that when studying hafnium isotopes, four sources of uncertainty can lead to an error in interpretation: 1) the choice of the decay constant, 2) the choice of the mantle curve, 3) the estimation of the age of crystallization of U-Pb zircon, and 4) the choice of the Lu/Hf of the crustal source. For more information on the points see (e.g., Vervoort & Patchett, 1996; Blichert-Toft & Albarede, 1997; Patchett et al., 2004; Kemp et al., 2007; Blichert-Toft & Albarède, 2008; Dhuime et al., 2011; Vervoort & Kemp, 2016; Iizuka et al., 2017 and Bea et al., 2018a).

I.1.6 Zircon mechanical and chemical resilience

I.1.6.1 Mechanical

Zircon is a hard mineral, ranking 7.5 on the Mohs scale. It is brittle, with conchoidal to uneven fracture, with poor to indistinct {110} and {111} cleavage. For these reasons, it does not break easily under impact during sedimentary transport, being preserved in detrital rocks, although with rounded shapes.

I.1.6.2 Chemical

Zircon is chemically inert at low temperatures, insoluble in most acids, and even hydrofluoric at T< 100 ºC. For this reason, it is not affected by chemical weathering.

Zircon is also remarkably resilient to high-temperature processes such as diffusive re-equilibration and dissolution into high-T melts and fluids. This last aspect will be discussed in **section I.1.7**, here focusing on the diffusive re-equilibration of interesting ions.

I.1.6.2.1 Th-U-Pb diffusion

Given the importance of zircon as a geochronometer, diffusion measurements (especially of Pb) have been attempted over the years (see Cherniak & Watson (2003), and references therein).

One problem in zircon diffusion measurements is that the diffusion of most atomic species is extremely slow, making low spatial resolution techniques such as EMPA of limited use, as demonstrated by Sommerauer

(1976). Advances in techniques that allow depth profiling, such as SIMS, Rutherford Backscattering Spectrometry (RBS) and Nuclear Reaction Analysis (NRA), have rendered it possible to measure diffusivities of many elements in zircon.

As expected, the diffusivity decreases with increasing valence and, for the same charge, decreases with increasing ionic ratio (Cherniak et al., 1997b; Cherniak & Watson, 2003). The Arrhenius equations to express diffusion coefficients of Pb, U, and Th (Cherniak, 2010) are:

$D_{Pb} = 0.0776 \exp(5 \pm 25 \text{ kJ mol}^{-1}/RT) \text{ m}^2\text{s}^{-1}$ (1)

$D_U = 1.63 \exp(-726 \pm 83 \text{ kJ mol}^{-1}/RT) \text{ m}^2\text{s}^{-1}$ (2)

$D_{Th} = 86.3 \text{ e}(-792 \pm 54 \text{ kJ mol}^{-1}/RT) \text{ m}^2\text{s}^{-1}$ (3)

These equations indicate that at temperatures of 1000 ºC, Pb^{2+} diffuses about four orders of magnitude faster than U^{4+} and seven orders faster than Th^{4+}. Accordingly, Th and U seem virtually immobile in zircon, but Pb can suffer diffusive redistribution over geologically reasonable times and temperatures (Bea & Montero, 2013).

It has been argued that radiogenic Pb in zircon would be tetravalent because it comes from the decay of a tetravalent ion (Kramers et al., 2009). However, there are compelling reasons to assume that it is mainly generated as Pb^{2+} during radioactive decay (Watson et al., 1997) or, if some are generated as Pb^{4+}, it is quickly reduced to divalent due to the strong reducing environment of the zircon (Kogawa et al., 2012). Accordingly, the above Arrhenius equation for Pb diffusion in zircon holds.

Pb diffusion in zircon is especially important if zircon crystals experience a high-T event. In the absence of fluids, for example, in high-T metamorphism (Kooijman et al., 2011), zircon may remain stable until thermal decomposition to silica + baddeleyite (occurring at T > 1400 ºC, see discussion in **section I.3.1**). In the presence of melts, the elevated solubility of zircon (see **section I.3.2**) causes it to dissolve before Pb diffusion is perceptible. However, if zircon is shielded, for example, included in a major mineral in a crystallizing magma, it may as well stay stable indefinitely. In these cases, if zircon is surrounded by minerals such as olivine, pyroxene or garnet, which have a very low Pb^{2+} partitioning, these will seal the zircon, thus preventing lead loss outside (Bea & Montero, 2013) and limiting the diffusion to the internal crystal domain. Therefore, the effects of the U-Th-Pb system will be controlled by the heterogeneity of the U and Th distributions, being inexistent if the crystal is chemically homogeneous.

I.1.6.2.2 Hf diffusion

Other critical issues with zircon stability are whether the Hf and Oxygen preserve their isotopic signatures if zircon crystals experience a post-crystallization high-T event. According to Cherniak (2010), the Hf^{4+} diffusion in zircon can be represented by the following Arrhenius equation:

$D_{Hf} = 1600 \exp(-812 \pm 54 \text{ kJ mol}^{-1}/RT) \text{ m}^2\text{s}^{-1}$ (4)

Equation 4 yields similar diffusivity to U and Th (equations 2 and 3). Accordingly, Hf in zircon can be considered immobile under any reasonable geological conditions.

I.1.6.2.3 Oxygen diffusion

The diffusion of Oxygen in zircon is rather puzzling because experimentalists found this element to diffuse differently depending on whether the experiments were conducted in “dry” or “wet” conditions (Watson & Cherniak, 1997). For dry experimental conditions at 1100-1500 degrees C, these authors calculated the following Arrhenius expression for “dry” and “wet” conditions;

$D_{O\text{-}dry} = 1.33 \times 10^{-4} \exp(-53920/T)\ m^2s^{-1}$(5)

$D_{O\text{-}wet} = 5.5 \times 10^{-12} \exp(-25280/T)\ m^2s^{-1}$ (6)

These equations imply that at 900 ºC the oxygen diffuses five orders of magnitude faster in wet than in dry conditions. The question, therefore, for applying these values to geologic problems is to know whether the system of interest is ‘wet’ or ‘dry’. Under dry conditions, zircons are extremely retentive of their oxygen isotopic signatures if T keeps lower than 900 ºC. Under wet conditions, in contrast, $\partial^{18}O$ of zircons can be quickly and deeply modified in a relatively short time.

Watson & Cherniak (1997) estimated that the crust is likely to be in “wet” rather than “dry” conditions, so $\partial^{18}O$ would normally be affected by partial melting or high-grade metamorphism. However, Peck et al. (2003) and our preliminary work on migmatitic zircons revealed that this is a rare case. Oxygen diffusion will be extensively studied in this work.

I.1.7 Zircon solubility in magmas and the zircon saturation temperature

The solubility of zircon in silicate melts depends on the temperature and melt composition, as revealed by numerous experimental studies (Dickinson & Hess, 1982; Watson & Harrison, 1983; Boehnke et al., 2013; Gervasoni et al., 2016; Borisov & Aranovich, 2019; Shao et al., 2019). These works also reveal that zircon solubility does not depend (or very little) on the pressure, so it is possible to use the experimental models to calculate the temperature at which a given rock should have reached zircon saturation from its Zr and major element concentrations. The resulting number is called the Zircon Saturation Temperature (Hanchar & Watson, 2003) and has proved to be very helpful for studying igneous rocks (e.g. Miller et al., 2003).

One of the hottest points in zircon studies is that all above-mentioned experimental models unanimously signal that zircon solubility in silicate melts increases exponentially with decreasing silica; accordingly, crystallizing mafic magmas would only precipitate zircon from the last drops of residual melts, likely of granophyric composition. However, this view is inconsistent with the abundance of syn-magmatic zircons in many mafic rocks, in which zircon often occupies textural positions compatible with early crystallization.

To explain this paradox, we have recently proposed that zircon precipitation from mafic magmas must involve the formation of small zircon-saturated transient zones (Bea et al., 2022), this being a part of the research summarized in this dissertation.

I.2 Objectives of this dissertation

Because of the characteristics exposed before, zircon studies are one of the most actively developed branches of modern Earth Sciences.

In igneous rocks, zircon geochronology is used to determine the rock's crystallization age and to identify the nature of the magmatic source if inherited zircons are present, a phenomenon more frequent than previously believed. In sedimentary rocks, zircon geochronology is used to determine the provenance of sediments and establish potential correlations.

However, several aspects of zircon behavior are not still adequately studied. These include

1. The diffusive stability and the distribution of oxygen isotopes, U, Th Pb and REE when the environmental conditions of zircon change dramatically compared to its crystallization;
2. The precipitation of zircon in $ZrSiO_4$-undersaturated magmas;
3. The subsolidus stability of zircon in $ZrSiO_4$-undersaturated rocks;
4. The zircon to reidite transformation.

This memory is focused on the first three problems, especially on the behavior of elements and isotopes in high-temperature processes and under hydrothermal conditions. Understanding the former is essential for interpreting the isotopic features of inherited zircons. Understanding the latter is additionally required for the interpretation of detrital zircons.

To fulfill these objectives, we have used two different but complementary approaches, experimental and numeric. We carried out:

1. High-temperature experiments to study the diffusivity of Pb and O isotopes
2. Hydrothermal experiments to study trace elements mobilization to the leachate and zircon-baddeleyite stability
3. Numerical modeling of the survival of inherited zircons in granitoids
4. Numerical models of the crystallization of MORB melts confined in pores in order to calculate how there is zircon precipitation in Zr-low mafic magmas.

I.3 Previous research and their influence on planning our experimental work

I.3.1 The thermal decomposition of zircon and high-temperature experiments

Many authors have extensively studied the thermal decomposition of zircon at high temperatures to produce silica + baddeleyite. The early results were inconsistent, ranging from congruent melting at 2550ºC (Washburn & Libman, 1920) or 2430 ºC (Zhirnowa, 1934) to incongruent melting at 1775 ºC or 1720 ºC (Geller & Lang, 1949) (Cocco & Schromek, 1958), and solid-state decomposition (Curtis & Sowman, 1953). The uncertainty associated with these results was later cleared by Butterman (1967) who incorporated the results of Butterman (1965) and Beard et al. (1965) into a new phase diagram that showed that the decomposition of pure, unaltered zircon into SiO_2 + ZrO_2 occurs at a temperature of 1676 ± 7 °C.

This value is within errors of the temperatures given later by Kamaev et al. (2005) (1674 ± 7 °C) and Kaiser et al. (2008) (1673 ± 10 °C). However, it should be considered that this value only holds for pure $ZrSiO_4$. The presence of impurities or radiation damage causes zircon to decompose at temperatures much below 1673 °C (e.g., 1380−1480 ºC (Kober, 1986); 1477 ºC (Mursic et al., 1992); 1285 ºC (Pavlik et al., 2001); 1400 ºC (Wang et al., 2006); 1400 °C (Váczi et al., 2009); and 1300 ºC (Morales et al., 2022); see also Kamaev et al., 2005 and Pena & de Aza, 1984). This fact hinders and even prevents the experimental study of diffusion with natural zircon at high temperatures, which is necessary to get geologically significant results in a reasonably short time. It must be considered that diffusion is ruled for an Arrhenius-type equation: $D = D_0\exp(E/RT)$ so that different combinations of time and temperature may cause the same diffusive effects, as shown in Fig. 1.

This figure represents an example that for different degrees of diffusion (lines) 10^5 years would be needed for temperatures of 942, 1004, 1068 and 1122 ºC (points A_1, A_2, A_3 and A_4), whereas the same amount of diffusion could be reached in less time, 10^1 years, if the temperature of the experiment is increased to 1193, 1273, 1371 and 1489 ºC respectively (points B_1, B_2, B_3 and B_4).

It follows that to get the same effects as a thermal event at 900ºC lasting 1 million years, we need to heat at 1450 ºC for 1 month or 1330 ºC for 3 months. Therefore, simulating diffusion in geologic processes with reasonably-timed experiments requires temperatures above 1300ºC, i.e. within the range at which impure zircons decompose (see Váczi et al. (2009) for example). For this reason, we had to devise a way to keep the zircons stable at temperatures > 1300ºC during the experiments (Bea et al., 2018b). This method, described in detail in **section II.1.2.1**, consists of embedding the zircons in pure microcrystalline cristobalite to displace the reaction $ZrSiO_4 = SiO_2 +$ to the left ZrO_2 because of the excess SiO_2.

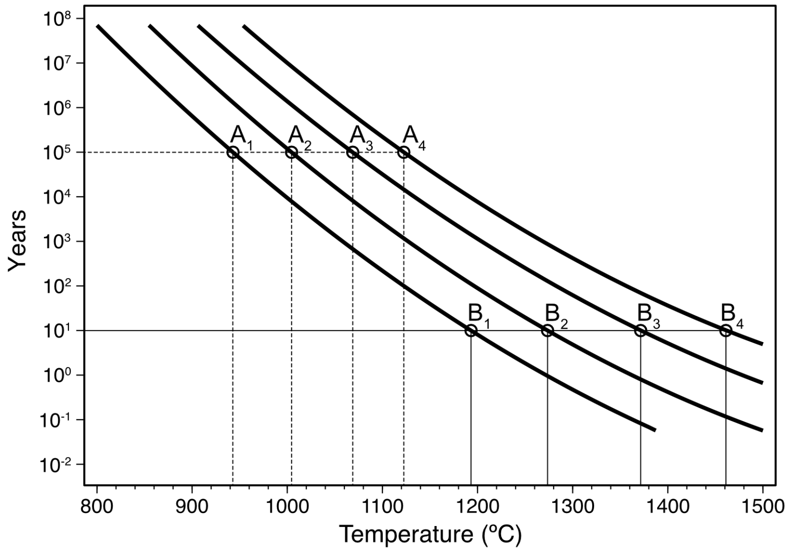

Figure 1. Representation of different diffusion curves as a function of time and temperature. The calculations have been performed with COMSOL modeling program using a two-domain diffusion model that simulates a zircon with two domains of different Pb concentration.

I.3.2 The diffusion of Pb and O in zircon at high temperatures

The diffusivity of U, Th, Pb and O in zircon has been extensively experimentally studied by different authors (see a summary in Cherniak, 2010). Concerning the U-Th-Pb isotope system, of outstanding importance in geochronology, this author proposed the Arrhenius equations (1, 2, and 3 reported in **section I.1.6.2.1**), which reveal that between 800 ºC and 1200 ºC Pb^{2+} diffuses much faster than U^{4+} and Th^{4+}, and the two actinide cations are virtually immobile below T ≈ 1200 ºC. Based on these data and the fact that zircon crystals often contain domains with different concentrations of U and Th (Bea & Montero, 2013) modeled how the thermal shock undergone by inherited zircon crystals affects their U/Pb and Th/Pb ages.

These authors showed that pre-magmatic zircons found in magma could only be perturbed perceptibly by diffusion at 800-830 °C, but this requires more than 10^6 years. Higher temperatures increase the Pb^{2+} diffusivity and, at a higher rate, the solubility of zircon in the melt, which leads zircon to dissolve before diffusion is effective.

On the other hand, if the zircon is protected from the liquid because it is included in a major mineral, it can withstand much higher temperatures. The so-shielded zircons cannot lose Pb outside, which gets homogenized all over the crystal. This fact causes discordias with the upper extreme placed above the concordia line (see Fig. 7 in Bea & Montero, 2013), i.e. “reverse discordias” (Williams et al., 1984).

However, if zircon grains have fusible inclusions and these inclusions melt, the so-formed liquids can react with the host zircon and act as sinks for the Pb^{2+} diffusing throughout the crystal (Bea et al., 2018b; Morales et al., 2022). Accordingly, we have studied here the nature of inclusions in a variety of natural zircons from different environments, how they fuse and whether the so-produced melt can migrate through the crystals lixiviating Pb^{2+} and other incompatible elements.

I.3.3 The decomposition of zircon under hydrothermal conditions

Hydrothermal zircons typically occur in low- to medium-temperature hydrothermal deposits associated with F-rich or alkaline fluids (Hoskin & Schaltegger, 2003; Schaltegger, 2007). These fluids can dissolve/

precipitate zircon resetting its isotopic clocks and changing its composition and internal zonation (Pidgeon, 1992; Pidgeon et al., 1998). Laboratory studies have also demonstrated that Zr is soluble in aqueous fluids under certain conditions. Zircon mobility occurs during the alteration of granite rocks (Alderton et al., 1980; Rubin et al., 1993) and the metasomatism caused by alkaline fluids and melts (Aja et al., 1996; Gieré, 1990; Kebede et al., 2007; Taylor et al., 1981). Zr-rich hydrothermal assemblages are often found in veins and replacement deposits genetically related to igneous intrusions (Claoué-Long et al., 1990; Gieré, 1990; Rubin et al., 1989; Rubin et al., 1993). Zircon can also grow over a wide range of metamorphic conditions, from greenschist (Rasmussen, 2005) to eclogite facies conditions (Rubatto & Hermann, 2003).

Numerous hydrothermal experiments have been carried out at temperatures between 100 ºC and 800 °C with durations between a few hours to a hundred days and under pressures from < 0.05 to 6 kbar using aqueous solutions of $CaCl_2$, $CaCl_2$ + HCl, $Ca(OH)_2$ NaCl, NaCl + HCl, NaOH, HF, HF + $HClO_4$, H_2O, Na_2CO_3, $AlCl_3$, HNO_3, multi-cation (Na^+, K^+, Mg^{2+}, Ca^{2+}, Ba^{2+}, Al^{3+} and Cl^-), $NaHCO_3$ and HCl. These are summarized in Figs. 2-8 and Table 1.

I.3.3.1 Experiments with 1m $CaCl_2$, 0.5m $CaCl_2$+HCl and $Ca(OH)_2$ aqueous solutions

Geisler et al. (2001) carried out experiments at 450 ºC for 31 days at 1.3 kbar using 10-15 mg zircon powder and a 1m $CaCl_2$ solution (5: cream triangle in Fig. 2). They found that reaction rims form on zircon grains gaining Ca and H_2O and losing Pb, Zr and Si. In addition, the more metamict samples also show a loss of Th.

Geisler et al. (2002) carried out experiments at 175 ºC for 1340 hours at < 0.05 kbar. They used 20 grains of heavily metamict zircon together with a 0.5m $CaCl_2$ + HCl solution (6: pale pink 270º-triangle in Fig. 2) and found reaction rims formed around zircon grains that were enriched in Ca and H_2O and depleted in Si, Th, U, and REE.

Geisler et al. (2003a) carried out experiments at 554 ºC, 600 ºC, 617 ºC and 650 ºC for 3 days at 1 kbar (8: Blue 90º-triangle in Fig. 2). In each experiment, they used 20 grains of metamict zircon and a 1m $CaCl_2$ solution producing reaction rims with the same gains and losses as those with 0.5m $CaCl_2$ + HCl solutions.

Lewerentz et al. (2019) carried out experiments at 600 ºC for 166 hours over 10 to 50 days at pressures of 3.7, 4.2 and 4.4 kbar (14: dark-green hollow-trapezoid in Fig. 2). They used 4-9 mg of natural and unaltered zircon grains in 2.06 to 9.12 mg of $Ca(OH)_2$ and $CaCl_2$ solutions adding variable amounts of silica. They found that zircon partially decomposes to baddeleyite in the experiments with Ca/Si < 0.6. Baddeleyite occurs as a fine-grained intergrowth with a Ca-silicate completely replacing zircon within the reaction rim. In experiments with Ca/Si ≈ 0.6 - 2.09, baddeleyite only forms on the zircon grain surface, primarily as intergrowths within the altered zircon.

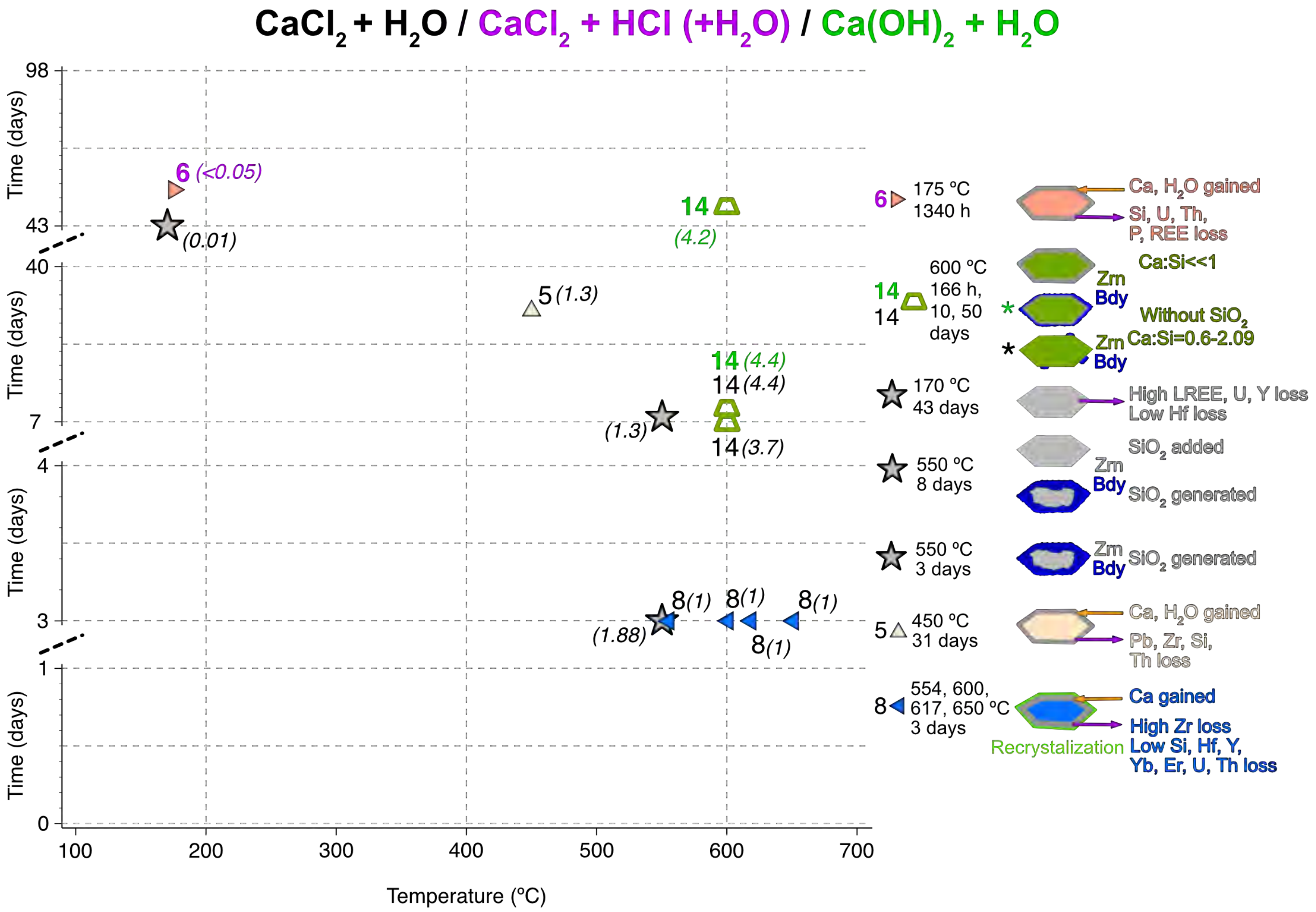

Fig. 2. Summary of bibliography experiments and experiments carried out in this thesis under hydrothermal conditions below 800 ºC for $CaCl_2$ and $CaCl_2$ + HCl aqueous solutions. The different symbols together with a number represent experiments taken from the bibliography. The numbers in italics are the pressures at which the experiments were conducted in kbar. The star-shaped symbols without a number are the hydrothermal experiments carried out in this thesis. The colors of the numbers represent different composition of the solution used: black ($CaCl_2$ aqueous solution), purple ($CaCl_2$ + HCl aqueous solution) and green ($Ca(OH)_2$ + H_2O solution). The orange arrows represent gain, and the purple arrows represent loss of elements. The grey rim means that there is an alteration rim, and the light green rim means that there is zircon recrystallization. The dark blue masses in the zircons represent baddeleyite. Bibliography (see text and Table 1 for more detail): 5) Geisler et al. (2001); 6) Geisler et al. (2002); 8) Geisler et al. (2003a); 14) Lewerentz et al. (2019). For experiments carried out in this thesis see Table 8. Mineral abbreviations after Whitney & Evans (2010).

I.3.3.2 Experiments with 1m and 2m NaCl and 1m NaCl + 0.5m HCl aqueous solutions

Pidgeon et al. (1966) carried out experiments at a temperature of 500 °C with durations of one, 11, 79 and 312 hours at 1 kbar pressure (2: brown circles in Fig. 3). They used metamict zircon grains in each experiment together with a 2m NaCl solution, concluding that zircon lost about 50 % Pb but retained almost all U in the first 24 hours.

Sinha et al. (1992) conducted a series of experiments on two, 20 and 30 mg metamict and non-metamict zircons with a 1m NaCl solution at a temperature of 600 °C with durations of 170 and 720 hours at the pressures of 4 to 6 kbar (3: green squares in Fig. 3). They concluded that the higher Pb loss occurred within the first 24 hours.

Rizvanova et al. (2007) carried out experiments at 200 ºC, 300 ºC, 400 ºC, 500 ºC and 600 ºC under the pressures of 0.01 and 1 kbar during 3, 7 and 14 days (9: yellow 45º-triangle in Fig. 3). They used in each experiment metamict zircon grains together with 1m and 2m NaCl and 1m NaCl + 0.5m HCl solutions and concluded, for a given pressure and temperature condition, Pb loss was higher in experiments with HCl. In addition, Pb losses are high for temperatures below 300 and above 500 °C, while U losses are high only for temperatures below 300 °C.

I.3.3.3 Experiments with NaOH aqueous solutions

Maurice (1949) carried out experiments at 400 ºC and 0.7 kbar over 70 hours using variable proportions of ZrO_2 and SiO_2 and solutions with variable NaOH concentrations (1: purple hollow-squares in Fig. 4). They concluded that in alkaline and near-neutral solutions with $ZrO_2/SiO_2 \approx 1$ the stable phases are baddeleyite + zircon-silicate and zircon + baddeleyite, respectively. With increasing SiO_2 content ($ZrO_2/SiO_2 < 1$), baddeleyite would no longer form, but zircon + quartz, zircon + zircon-silicate, quartz + zircon-silicate or zircon-silicate, depending on the silica and Na content available in the solution.

Rizvanova et al. (2007) experimented at 400 ºC and 1 kbar over 7 days with zircon metamict grains and 0.5m NaOH solution (9: yellow 45º-triangle in Fig. 4), founding that zircon grain lost very little Pb.

Ayers et al. (2012) experimented at 450 ºC, 600 ºC, and 750 ºC at 2 kbar over several days using zircon and zircon + silica and 0 m, 0.05 m and 0.5 m NaOH solutions (12: red diamond in Fig. 4). They found that the stable phases in the silica-absent experiment are zircon and baddeleyite for all temperatures and that Na-Zr-silicates are also formed at 450 ºC. In silica-present experiments, the stable phases are zircon and quartz, and Na-Zr-silicates are formed again at 450 ºC. The solubility of zircon increases with the NaOH molality, and Zr forms $Zr(OH)^{5-}$ anions.

Mysen (2015) carried out experiments between 575 ºC and 800 ºC at pressures between 0.59 and 6.8 kbar for 1 hour (13: orange hollow-triangle in Fig. 4) using crystalline ZrO_2 alone and mixed with silica in NaOH dissolutions of diverse molarity, concluding that the concentration of Zr^{4+} in the aqueous fluid increases by about an order of magnitude when the concentration of NaOH increases from 0 to 0.5m, reflecting the formation of zirconate complexes.

I.3.3.4 Experiments with varying concentrations of HF and HF+$HClO_4$

Kovalenko & Ryzhenko (2009) conducted experiments with a gem-quality zircon with an HF solution at 500 ºC and 1 kbar for 14, 24, 30 and 90 days, using zircon and silica as solid phases (10: pink hollow-circles in Fig. 4). They concluded that baddeleyite forms in experiments without quartz and that increasing slightly the Zr concentration requires a significant increase in the HF concentration.

Migdisov et al. (2011) carried out experiments at 100-250 ºC at atmospheric pressure (11: bluish-grey hollow rectangles in Fig. 4), and at 400 ºC at 0.7 kbar using baddeleyite as starting material and HF and HF + $HClO_4$ solutions of different concentrations (10: bluish-grey hollow squares in Fig. 4). They concluded that the concentration of Zr in the solution increases with increasing HF concentration, and Zr is present predominantly as a hydroxyl-fluoride species ($ZrF(OH)_3$ and $ZrF_2(OH)_2$).

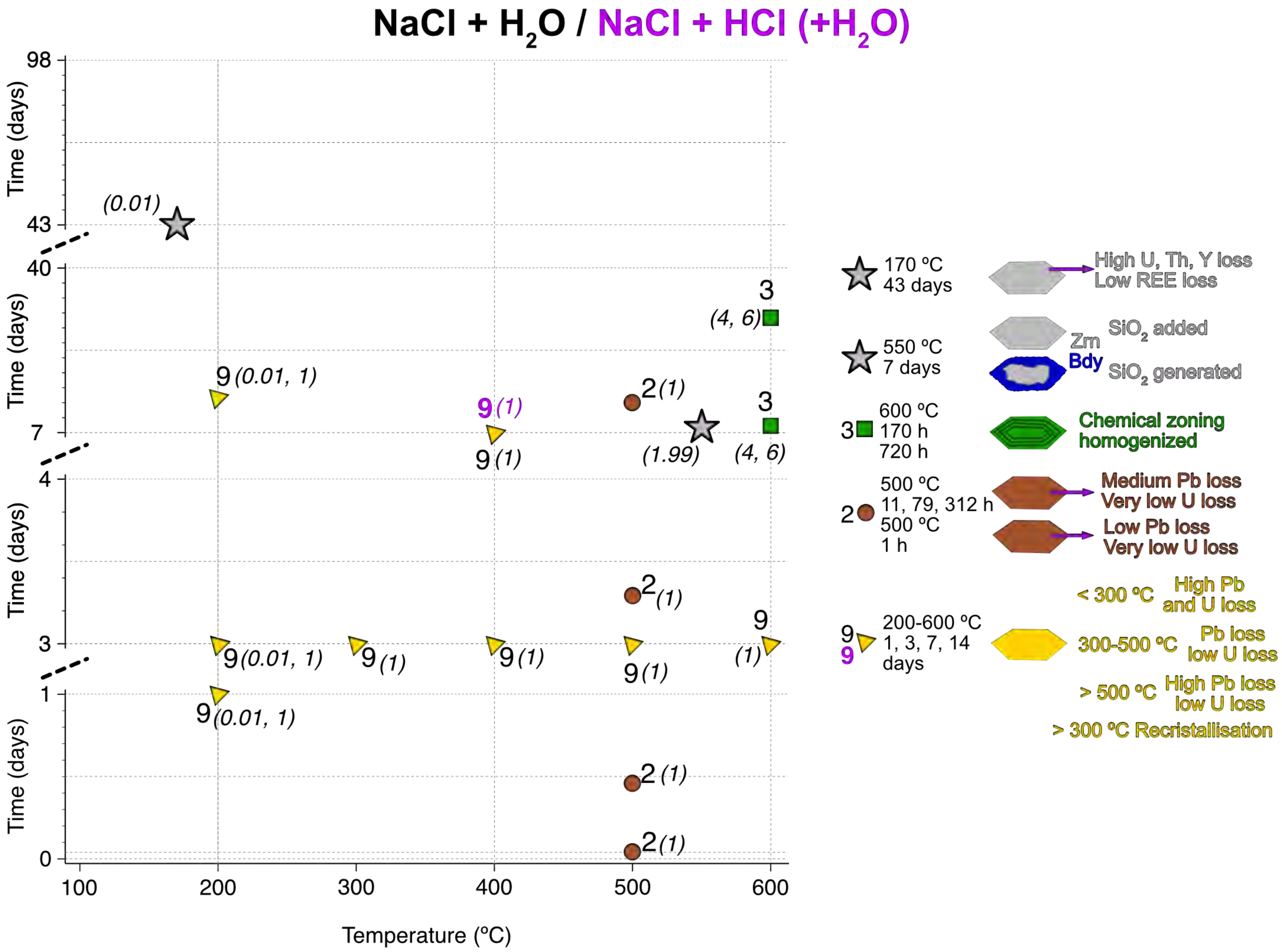

Fig. 3. Summary of bibliography experiments and experiments carried out in this thesis under hydrothermal conditions below 800 ºC for NaCl and NaCl + HCl aqueous solutions. The different symbols together with a number represent experiments taken from the bibliography. The numbers in italics are the pressures at which the experiments were conducted in kbar. The star-shaped symbols without a number are the hydrothermal experiments carried out in this thesis. The colors of the numbers represent different composition of the solution used: black (NaCl aqueous solution) and purple (NaCl + HCl aqueous solution). The purple arrows represent loss of elements. The dark blue masses in the zircons represent baddeleyite. Bibliography (see text and Table 1 for more detail): 2) Pidgeon et al. (1966); 3) Sinha et al. (1992); 9) Rizvanova et al. (2007). For experiments carried out in this thesis see Table 8. Mineral abbreviations after Whitney & Evans (2010).

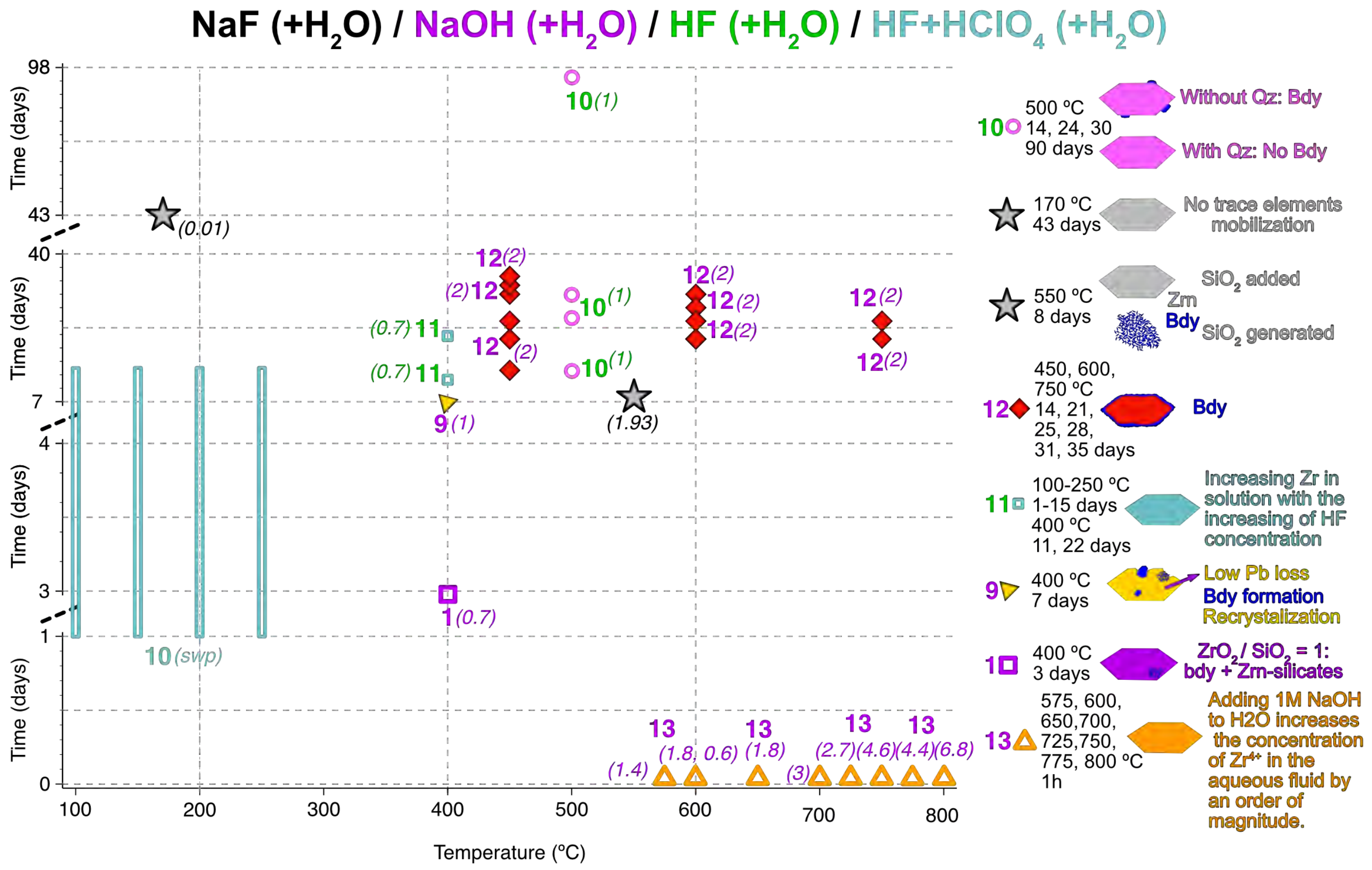

Fig. 4. Summary of bibliography experiments and experiments carried out in this thesis under hydrothermal conditions below 800 ºC for NaF, NaOH, HF, and HF+$HClO_4$ aqueous solutions. The different symbols together with a number represent experiments taken from the bibliography. The numbers in italics are the pressures at which the experiments were conducted in kbar. The star-shaped symbols without a number are the hydrothermal experiments carried out in this thesis. The colors of the numbers represent different composition of the solution used: black (NaF aqueous solution), purple (NaOH aqueous solution), green (HF aqueous solution) and light blue (HF + $HClO_4$ aqueous solution). The purple arrows represent loss of elements. The dark blue masses in the zircons represent baddeleyite. swp: saturated water pressure. Bibliography (see text and Table 1 for more detail): 1) Maurice (1949); 9) Rizvanova et al. (2007); 10) Kovalenko & Ryzhenko (2009); 11) Migdisov et al. (2011); 12) Ayers et al. (2012); 13) Mysen (2015). For experiments carried out in this thesis see Table 8. Mineral abbreviations after Whitney & Evans (2010).

I.3.3.5 Experiments with H_2O

Maurice (1949) carried out experiments at 400 ºC and 0.7 kbar for 70 hours using variable proportions of ZrO_2 and SiO_2 together with H_2O (1: purple hollow-squares in Fig. 5). They concluded that for neutral solutions, the stable phases are zircon + baddeleyite if $ZrO_2/SiO_2 \approx 1$.

Geisler et al. (2003b) experimented at 200 ºC and 1 kbar for 195 hours using a single zircon crystal heavily metamict and H_2O (7: maroon hollow-diamond in Fig. 5). They show that the recrystallization of zircon started at 200 ºC.

Geisler et al. (2003a) experimented at 600 ºC and 1 kbar for 170 hours with 20 grains of metamict zircon and H_2O (8: Blue 90º-triangle in Fig. 5). They showed profound recrystallization of zircon grains.

Rizvanova et al. (2007) experimented at 200 ºC, 400 ºC and 600 ºC at 0.01 and 1 kbar during 1, 3, 7 and 14 days using metamict zircon and H_2O (9: yellow 45º-triangle in Fig. 5). They concluded that the Pb loss is higher at 600 ºC than at 400 ºC, the reverse being true for U.

Kovalenko & Ryzhenko (2009) conducted experiments with gem-quality zircon and H_2O at 500 ºC and 1 kbar for 14, 24, 30 and 90 days, using zircon oxide, zircon and silica (10: pink hollow-circles in Fig. 5). They found that ZrO_2 and $ZrSiO_4$+ZrO_2 are practically insoluble in H_2O, and baddeleyite formed in the experiments without silica.

Mysen (2015) carried out experiments at 550 ºC, 575 ºC, 625 ºC, 650 ºC, 700 ºC, 725 ºC, 775 ºC and 800 ºC for 1 hour under the pressure of 2.99, 5.44, 4.31, 7.01, 6.37, 7.83, 8.42 and 10.13 kbar. He uses ZrO_2 and ZrO_2 + SiO_2 together with H_2O (13: orange hollow triangles in Fig. 5). The conclusion is that the Zr^{4+} concentration varies from ≤10 to ~70 ppm with increasing temperature and pressure. The addition of SiO_2 does not appreciably affect these values.

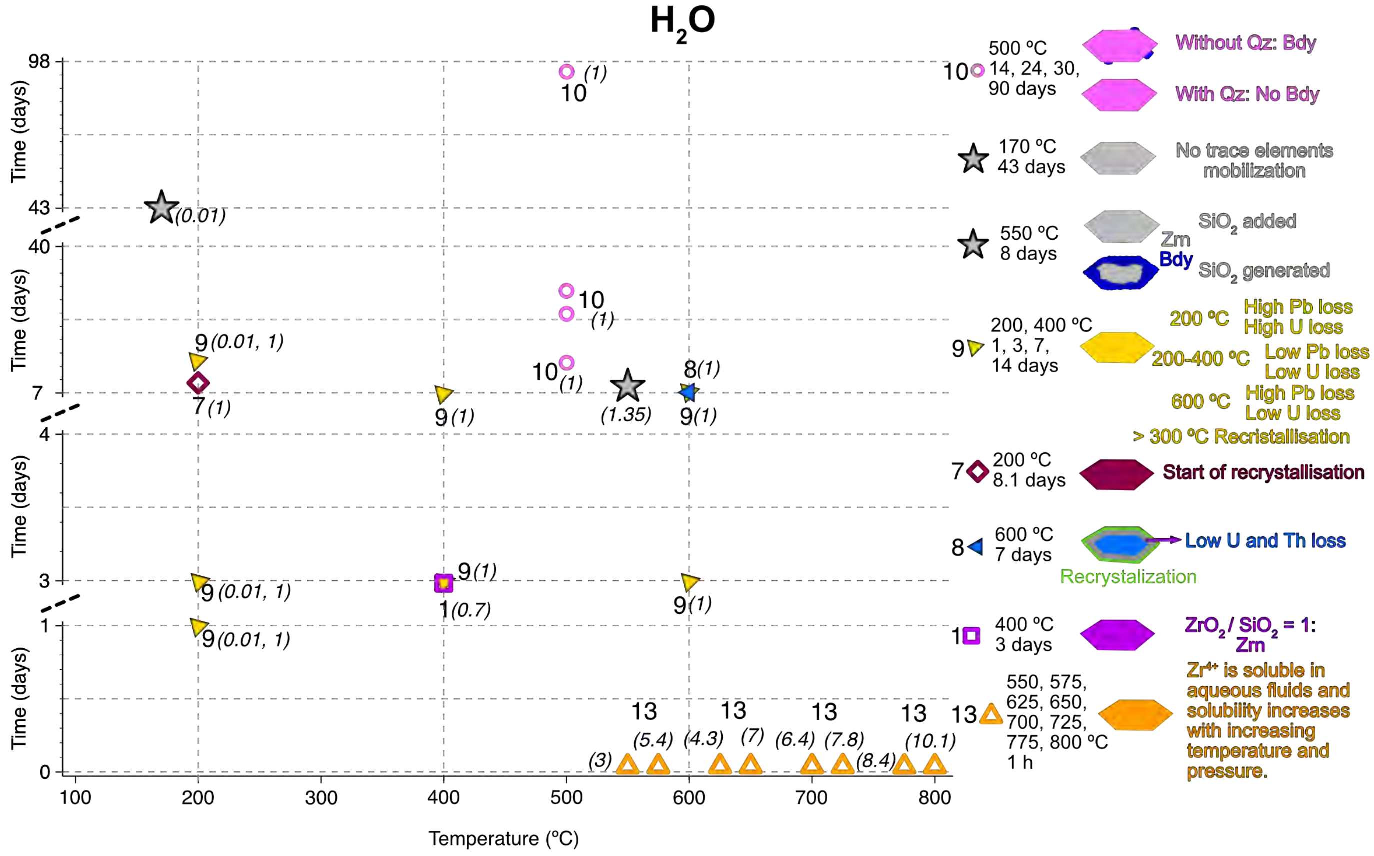

Fig. 5. Summary of bibliography experiments and experiments carried out in this thesis under hydrothermal conditions below 800 ºC for H_2O. The different symbols together with a number represent experiments taken from the bibliography. The numbers in italics are the pressures at which the experiments were conducted in kbar. The star-shaped symbols without a number are the hydrothermal experiments carried out in this thesis. The purple arrows represent loss of elements. The grey rim means that there is an alteration rim, and the light green rim means that there is zircon recrystallization. The dark blue masses in the zircons represent baddeleyite. Bibliography (see text and Table 1 for more detail): 1) Maurice (1949); 7) Geisler et al. (2003b); 8) Geisler et al. (2003a); 9) Rizvanova et al. (2007); 10) Kovalenko & Ryzhenko (2009); 13) Mysen (2015). For experiments carried out in this thesis see Table 8. Mineral abbreviations after Whitney & Evans (2010).

I.3.3.6 Experiments with 2m and 0.9m Na_2CO_3 aqueous solutions

Rizvanova et al. (2000) carried out experiments at 200 ºC, 300 ºC, 400 ºC, 500 ºC, 600 ºC, 700 ºC and 800 ºC under the pressures of 1 and 5 kbar during 3, 7 and 14 days (4: orange reverse triangle in Fig. 6). They used 10-15 mg of metamict zircon grains and 0.9 m Na_2CO_3 x 10 H_2O solutions. They found that baddeleyite and zircon-silicate form if the temperature was higher than 400 ºC and that the dissolution of metamict zircon was faster than recrystallization using a carbonate solution.

Rizvanova et al. (2007) carried out experiments at 200 ºC, 300 ºC, 400 ºC, 500 ºC, 600 ºC and 800 ºC at 0.01, 1 and 5 kbar during 1, 3 and 14 days (9: yellow 45º-triangle in Fig. 6). They used metamict zircon grains and 2 m Na_2CO_3 solution and showed that at 300 ºC, zircons lose more U than Pb, but at 400 ºC, the situation is reversed.

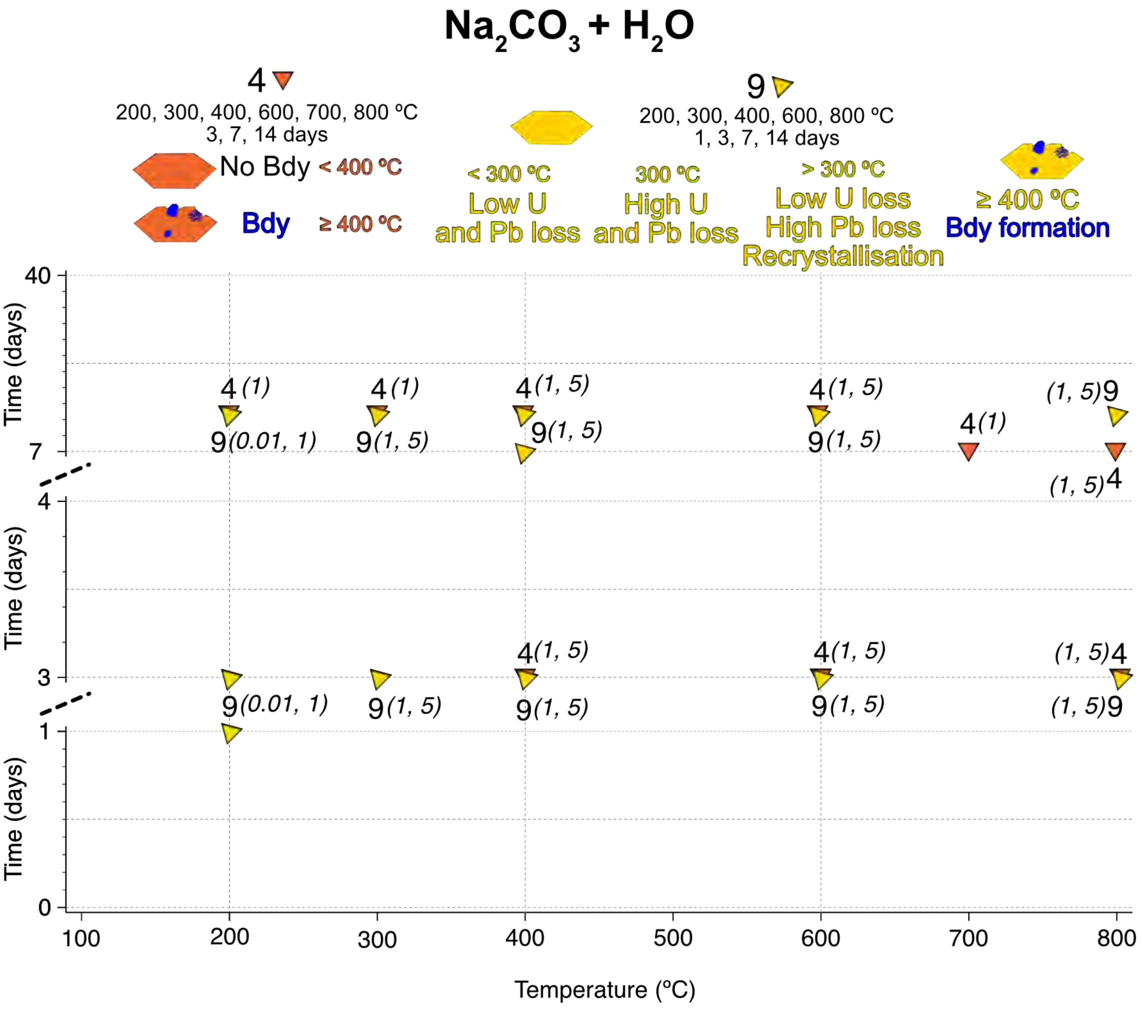

Fig. 6. Summary of bibliography experiments and experiments carried out in this thesis under hydrothermal conditions below 800 ºC for Na_2CO_3 aqueous solutions. The different symbols together with a number represent experiments taken from the bibliography. The numbers in italics are the pressures at which the experiments were conducted in kbar. The dark blue masses in the zircons represent baddeleyite. Bibliography (see text and Table 1 for more detail): 4) Rizvanova et al. (2000); 9) Rizvanova et al. (2007). Mineral abbreviations after Whitney & Evans (2010).

I.3.3.7 Experiments with 1m $AlCl_3$ and multi-cation aqueous solutions

Geisler et al. (2002) carried out experiments at 175 ºC < 0.05 kbar for 1340 hours. They used 20 grains of heavily metamict zircon and a 1m $AlCl_3$ solution (6: pale pink 270º-triangle in Fig. 7), finding that the so-formed reaction rim gains Al and H_2O but loses Si, Th, U and REE.

Geisler et al. (2003a) experimented at 350 ºC and 0.25 kbar for 504, 1124, 1770 and 2300 hours (8: Blue 90º-triangle in Fig. 7) with 20 grains of metamict zircon and a 1m $AlCl_3$ solution. Additionally, they experimented with 585 ºC and 1 kbar for 3 days with 20 grains of heavily metamict zircon together with a

Multi-cation (Na^+, K^+, Mg^{2+}, Ca^{2+}, Ba^{2+}, Al^{3+} and Cl^-) solution. These authors found reaction rims that gained Na^+, K^+, Mg^{2+}, Ca^{2+}, Ba^{2+}, Al^{3+}, P and H_2O and lost Zr, Si, Hf, Th, U, P, REE and radiogenic Pb.

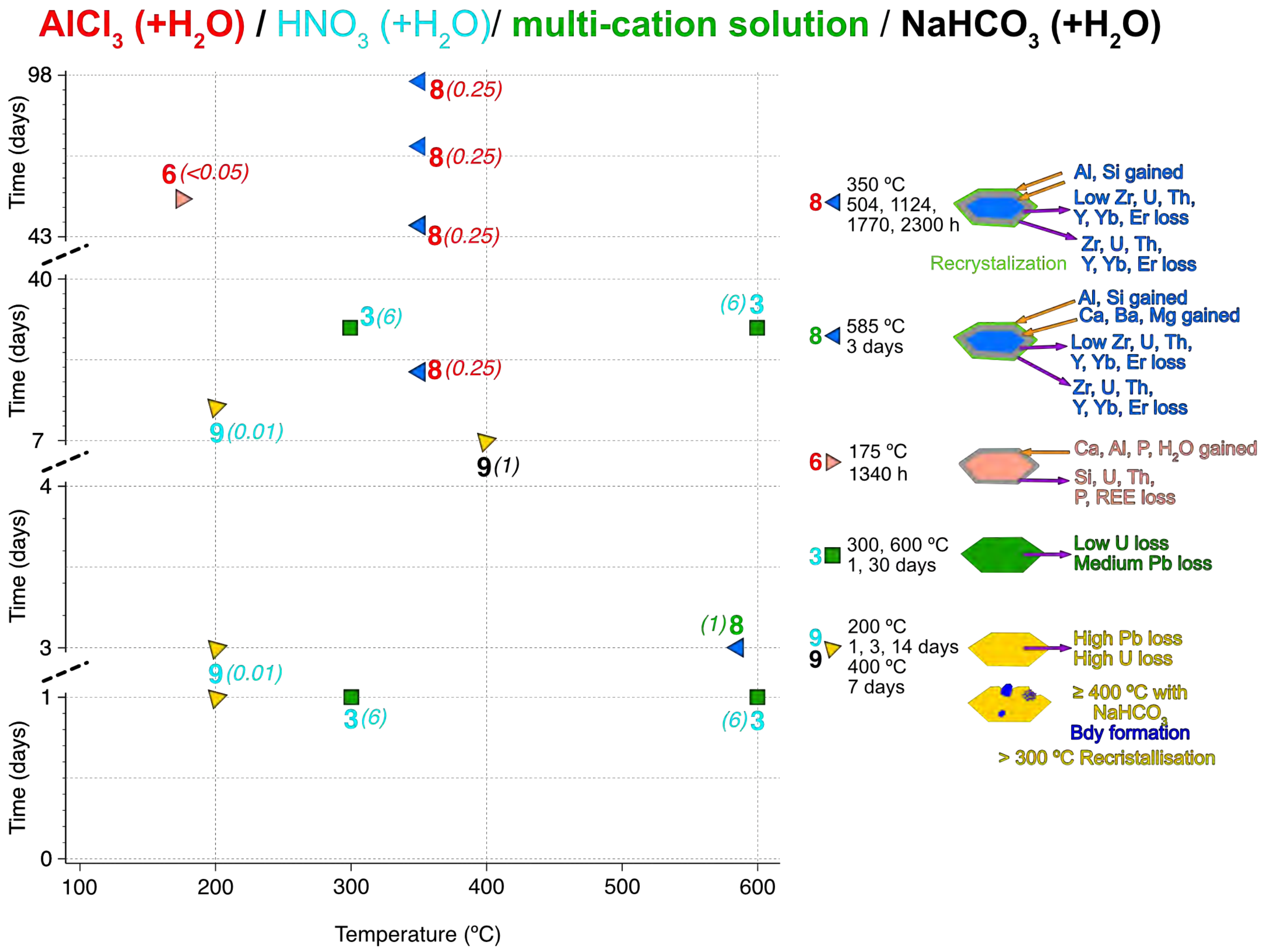

Fig. 7. Summary of bibliography experiments and experiments carried out in this thesis under hydrothermal conditions below 800 ºC for $AlCl_3$, HNO_3, Multi-cation and $NaHCO_3$ aqueous solutions. The different symbols together with a number represent experiments taken from the bibliography. The numbers in italics are the pressures at which the experiments were conducted in kbar. The colors of the numbers represent different composition of the solution used: red ($AlCl_3$ aqueous solution), blue (HNO_3 aqueous solution), green (multi-cation solution) and black ($NaHCO_3$ aqueous solution). The orange arrows represent gain, and the purple arrows represent loss of elements. The grey rim means that there is an alteration rim, and the light green rim means that there is zircon recrystallization. The dark blue masses in the zircons represent baddeleyite. Bibliography (see text and Table 1 for more detail): 3) Sinha et al. (1992); 6) Geisler et al. (2002); 8) Geisler et al. (2003a); 9) Rizvanova et al. (2007). Mineral abbreviations after Whitney & Evans (2010).

I.3.3.8 Experiments with HNO_3 and $NaHCO_3$ aqueous solutions

Sinha et al. (1992) performed a series of experiments on 2, 20 and 30 mg metamict and non-metamict zircons using 0.3m HNO_3 at 300 and 600 °C and 6 kbar with durations of 1 and 30 days (3: green squares in Fig. 7) finding that the heaviest Pb loss occurred in the first 24 hours.

Similar results were reached by Rizvanova et al. (2007) at 200 ºC and 0.01 kbar for 1 day using metamict zircon grains and 0.5m HNO_3 (9: yellow 45º-triangle in Fig. 7).

Rizvanova et al. (2007), also carried out experiments at 400 °C under a pressure of 1 kbar for 7 days (9: yellow 45º-triangle in Fig. 7). They used metamict zircons with a 1m $NaHCO_3$ solution, concluding that baddeleyite formation occurs for the conditions used in the experiment.

I.3.3.9 Experiments with HCl and KOH solutions

Maurice (1949) experimented at 400 ºC and 0.7 kbar for 70 hours using variable proportions of ZrO_2 and SiO_2 and HCl + H_2O solution (1: purple hollow-squares in Fig. 8). He showed that in acid solutions, the stable phase is zircon if $ZrO_2/SiO_2 = 1$.

Geisler et al. (2003b) experimented at 100-650 ºC and 1 kbar for 195 hours using a single heavily metamict zircon crystal and 0.07 m HCl, 2.2 m HCl, 0.02 m KOH and 0.7 m KOH (7: maroon hollow-diamond, and maroon line in Fig. 8). They showed that recrystallization of zircon started at 200 ºC and increased with temperature so that at 400 ºC, only 51 hours is enough to reach the maximum possible recrystallization.

Kovalenko & Ryzhenko (2009) experimented with a gem-quality zircon and HCl+H_2O solution at 500 ºC and 1 kbar for 14, 24, 30 and 90 days, using zircon and silica (10: pink hollow-circles in Fig. 8). They concluded that ZrO_2 and $ZrSiO_4$+ ZrO_2 are practically insoluble in HCl.

I.3.3.10 High-T hydrothermal experiments

Mysen (2015) and Lewerentz et al. (2019) also performed experiments at temperatures above 800°C with conclusions similar to those of the lower temperature experiments. Ayers & Watson (1991) experimented at 1000-1100 ºC and 1-2 kbar, concluding that the solubility of zircon is higher in H_2O and HCl than in silica-saturated fluids and that zircon solubility is much higher in silica-free solutions relative to silica-saturated fluids. Bernini et al. (2013) performed experiments at 680-1025 ºC and 6.2 to 20 kbar for 120 and 220 minutes using mixtures of zircon, baddeleyite and thorite with silica in H_2O, H_2O+15 wt% NaCl and H_2O+4.5 wt% albite. They concluded that the solubility of zircon is very low in aqueous fluids (1-3.3 ppm) but adding 4.5 wt.% albite or 15 wt.% NaCl to quartz-saturated fluids increased the solubility of zircon by a factor of five and three respectively. Wilke et al. (2012) carried out experiments at 300-800 ºC and 0.6 to 16.8 kbar using zircon + glass + an aqueous solution, concluding that solubility of zircon is enhanced in aqueous fluids containing $Na_2Si_3O_7$ or $Na_2Si_2O_5$ components, but the addition of alumina decreases the concentration of Zr in the fluid. Finally, Louvel et al. (2013) investigate Zr complexation in subduction-related fluids up to 800 °C and 2. 4 kbar. They revealed the formation of Zr-O-Si/Na polymeric species in alkali-(alumino) silicate fluids. They found no evidence of extensive Zr-Cl complexation in dilute fluid up to 420 °C and proved that adding dissolved Na and Si species to the fluids favours the formation of alkali-zirconosilicate Zr-O-Si/Na clusters similar to those found in the mineral vlasovite. Accordingly, they proposed that the alkali-zirconosilicate clusters can explain the enhanced solubility of zircon $ZrSiO_4$ (and other HFSE-bearing minerals) in alkali-aluminosilicate-bearing aqueous fluids produced by dehydration and melting of the slab, so providing with a favorable mechanism for the mobilization of HFSE in subduction zones.

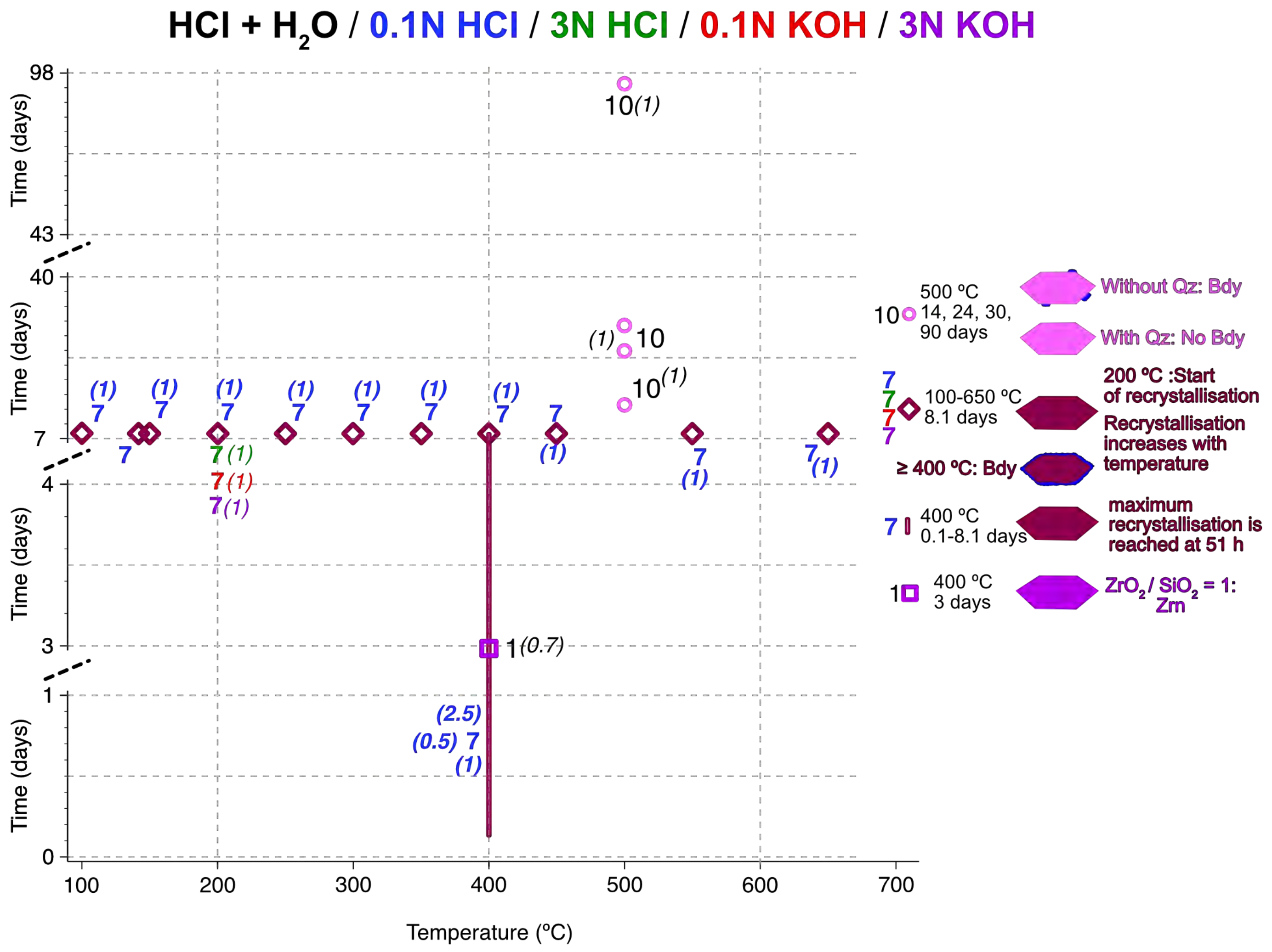

Fig. 8. Summary of bibliography experiments and experiments carried out in this thesis under hydrothermal conditions below 800 ºC for HCl and KOH aqueous solutions. The different symbols together with a number represent experiments taken from the bibliography. The numbers in italics are the pressures at which the experiments were conducted in kbar. The colors of the numbers represent different composition of the solution used: black (HCl aqueous solution), blue (0.1N HCl solution), green (3N HCl solution), red (0.1N KOH solution), and purple (3N KOH solution). The dark blue masses in the zircons represent baddeleyite. Bibliography (see text and Table 1 for more detail): 1) Maurice (1949); 7) Geisler et al. (2003b); 10) Kovalenko & Ryzhenko (2009). Mineral abbreviations after Whitney & Evans (2010).*

I.3.3.11 Planned experimental work

With this information in mind, we carried out experiments using fresh zircons with H_2O, 2M NaCl, 2M $CaCl_2$ and 1M NaF solutions. We did not consider pressure as it does not affect the exchange of elements between zircon and fluid. We experimented with rock + solution, rock + zircon + solution, zircon + solution and zircon + quartz + solution at different temperatures and solution compositions, keeping the fluid/zircon ratio high, which is necessary to simulate what occurs in nature when fluid infiltrates a rock. The choice of NaF solutions was because despite the importance of F for the mobilization of U, Zr and REE (McGloin et al., 2015), we found no experiments performed with alkaline fluoride solutions, only experiments with HF (see Kovalenko & Ryzhenko, 2009, and Migdisov et al., 2011).

The rock + solution and rock + zircon + solution experiments were done to determine what proportions of U, Pb, Th, Y, Hf and REE are leached from the rock and what proportions would come from the added zircon. The experiments zircon + solution and zircon + quartz + solution are performed to study the zircon-baddeleyite relationship for the different solutions and the differences in the leachates when quartz is added or not. For more details of the experimental conditions, see the "methods" section in Part II: Experimental Study (sections **II.1.2.2** and **II.1.2.3**).

I.3.4 Zircon inheritance in magmatic rocks.

Inherited zircons can be found in magmatic rocks because a variable fraction of zircons entrained in magmas either from the source or from xenoliths can survive contact with the melt. These inherited zircons, older than the host, appear as individual grains or old cores rimmed by newly formed magmatic zircon. Zircon inheritance is not only frequent in granitoids (Miller et al., 2003) but also in mafic rocks (Bea et al., 2020) and even in carbonatites (Montero et al., 2016). Since zircon solubility increases exponentially with temperature and the melt basicity (Watson, 1979), zircons inherited in mafic rocks usually do not come from the magmatic source but from entrained xenoliths or mixed felsic magma, which would provide information on the emplacement dynamics and the nature of the pierced crust (Bea et al., 2020). However, inherited zircons in granitic rocks mostly come from the magmatic source, thus providing information on the melt extraction mechanisms, the materials that melted and their melting conditions. Following the work of Watson (1979), some authors (Hanchar & Watson, 2003) have studied the solubility of zircon in melts, using it to determine zircon saturation temperatures (T_{Zr}). Miller et al. (2003) based on this parameter and using total rock Zr contents, divided granitic rocks into two: 1) "hot" (T_{Zr} > 800 °C), with little or no inherited zircon, and 2) "cold" (T_{Zr} < 800 °C) with abundant inherited zircon.

Since coeval and neighboring granites with T_{Zr}< 750 ºC, derived from similar sources, have been found to show radically different zircon inheritance (Bea et al., 2021), a numerical study will be carried out to study this aspect and to know the conditions at which these differences in zircon inheritance would be possible to occur. More information on the methodology used can be found in the section Starting Materials and Methods in part **III.1**.

Table 1. Sum up of hydrothermal experiments from bibliography

N	Paper	RD (days)	T (ºC)	P (kbar)	SM	Solution	Comments
1	Maurice, 1949	2,92	400	0,7	25 % ZrO_2+SiO_2 ZrO_2/ SiO_2	75% NaOH+H_2O HCl+H_2O	ZrO_2/SiO_2=1 In near-neutral solution: Zrn+Bdy. In alkaline solutions: Bdy+Zrn-silicates In acid solution: Zrn
2	Pidgeon et al., 1966	0.04 0.46 3.29/13	500	1	Metamict Zrn	2m NaCl	24 hours Zrn lost about 50% Pb, but retain almost all U
3	Sinha et al., 1992	8.33/ 30	600	4/ 6	2/ 20/ 30 mg Metamict and non-metamict Zrn	60 ml 2M NaCl	Higher Pb loss in the first 24 hours
		1/ 30	300, 600	6		60 ml 2% HNO_3	
4	Rizvanova et al., 2000	14	200	1	10-15 mg Metamict Zrn	50-100 mg 2M Na_2CO_3 x 10 H_2O	Zrn + Bdy + Silicate phase of Zr and Na Dissolution is faster than recrystallisation in carbonate solutions
		14	300	1			
		3/ 14	400	1/ 5			
		3/ 14	600	1/ 5			
		7	700	1			
		3/ 7	800	1/ 5			
5	Geisler et al., 2001	31	450	1,3	10-20 mg Zrn powder	2M $CaCl_2$	Reaction rims gain Ca and H_2O, lose Pb, Zr and Ti. Th loss detected in most metamict sample
6	Geisler et al., 2002	55,83	175	< 0.05	20 grains heavily metamict Zrn	4 ml 1M $CaCl_2$+HCl 2M $AlCl_3$	Reaction rims gain Ca, Al, P and H_2O and lose Si Th, U, P and REE
7	Geisler et al., 2003	8,1	100-650	1	Heavely metamict Zrn	0.1N HCl	200 ºC: start recrystallisation. Recrystallisation increases with temperature. 51h is enough to reach maximum recrystallisation at 400 ºC
		8,1	200	1		H_2O/ 3N HCl/ 0.1N KOH/ 3N KOH	
		0.1-8.1	400	1 0.5 2.5		0.1N HCl	

N: Number; RD: run durations; SM: starting material. Mineral abbreviations after Whitney and Evans. Other abbreviations: swp (saturated water pressure)

Table 1. Continued

N	Paper	RD (days)	T (°C)	P (kbar)	SM	Solution	Comments
8	Geisler et al., 2003	3	554/ 600/ 617/ 650	1	20 grains metamict Zrn	2M $CaCl_2$	Altered areas gain Na^+, K^+, Ca^{2+}, Mg^{2+}, Ba^{2+} and Al^{3+} and lose Zr, Si, Hf, REE, U, Th and radiogenic Pb Recrystallisation of zircon grains
		3	585	1		Multi-cation (0.1mol/l Na^+, K^+, Ca^{2+}, Mg^{2+}, Ba^{2+}, Al^{3+}, 1.1mol/l Cl^-)	
		7,08	600	1		H_2O	
		21 46.83 73.75 95.83	350	0,25		0.5 ml 2M $AlCl_3$	
9	Rizvanova et al., 2007	1/ 3/ 14	200	0.01/ 1	Metamict Zrn	H_2O	400 °C: low Pb, U loss. 600 °C: High Pb, low U loss
		3/ 7	400/ 600	1			
		7	400	1		1m NaCl+ 0.5m HCl	High Pb loss
		3/ 7	400	1		1m NaCl	Pb loss, low U loss
		1/ 3/ 14	200	0.01/ 1		2m NaCl	200-500 °C: Pb, low U loss. 600 °C: High Pb, low U loss
		3	300-600	1			
		7	400	1		1m $NaHCO_3$	High Pb, low U loss
		7	400	1		0.1m Na_2CO_3	
		7	400	1		1m Na_2CO_3	
		1/ 3/ 14	200	0.01/ 1		2m Na_2CO_3	300 °C: high U and Pb loss. 400 °C, 14 days, 5 bar: low U, high Pb loss. 400 °C, 3 days, 1 bar: high U and Pb loss. 600 °C: low U, high Pb loss. 800 °C, 1 bar: no U loss. 800 °C, 5 bar: low U loss
		3/ 14	300/ 400/ 600/ 800	1/ 5			
		7	400	1		1m NaOH	Low Pb loss
		1	200	0,01		3% HNO_3	High Pb loss

N: Number; RD: run durations; SM: starting material. Mineral abbreviations after Whitney and Evans. Other abbreviations: swp (saturated water pressure)

Table 1. Continued

N	Paper	RD (days)	T (ºC)	P (kbar)	SM	Solution	Comments
10	Kovalenko & Ryzhenko, 2009	14/ 24/ 30/ 90	500	1	Zrn+Qz+S Zrn+S Qz+Zr(aq)+S	H_2O/ HF/ HCl	ZrO_2 and $ZrSiO_4$+ZrO_2 practically insoluble in H_2O+HCl. Slight increase in the Zr concentration in the solution at a very significant increase in the HF concentration. Qz was significant dissolved. In experiments without Qz there is Bdy formation
11	Migdisov et al., 2011	1-15	100-250	swp	Synthetic crystalline Bdy	HF/ HF+$HClO_4$	The concentration of Zr in solution increases with increasing HF concentration. For similar HF concentrations, the concentration of Zr in solution is independent of pH. Zr is present in solution predominantly as hydroxyl-fluoride species
		11/ 22	400	0,7		0.048 mol/kg HF	
12	Ayers et al., 2012	14	450	2	0.04-0.06 g Zrn	0.2 ml 1m NaOH	Qz-undersatured experiments: Zrn+Bdy (all temperatures) and at 450 °C Zrn+Bdy+Na-Zr-silicates. Qz-satured experiments: Zrn+Qz (600 and 750 °C) and at 450 °C Zrn+Qz+Na-Zr-silicates. Aqueous solubility of Zrn increase with increasing molality of NaOH (pH). Low silica activities: Zr in alkaline fluids form Zr(OH)5-. In alkaline fluids Zr complexation with silica increases Zrn solubility.
		21	450		0.04-0.06 g Zrn+Qz/ Zrn	0.2 ml 1m NaOH	
		31	450		0.04-0.06 g Zrn+Qz/ Zrn	0.2 ml 1m NaOH	
		35	450		0.04-0.06 g Zrn	0.2 ml 1m NaOH	
		21	600		0.04-0.06 g Zrn	0.2 ml 1m NaOH 0.1m NaOH	
		25	600		0.04-0.06 g Zrn+Qz/ Zrn	0.2 ml 1m NaOH 0.1m NaOH 0m NaOH	
		28	600		0.04-0.06 g Zrn	0.2 ml 0.1m NaOH	
		31	600		0.04-0.06 g Zrn	0.2 ml 1m NaOH	
		21	750		0.04-0.06 g Zrn	0.2 ml 0m NaOH	
		25	750		0.04-0.06 g Zrn	0.2 ml 1m NaOH 0.1m NaOH	

N: Number; RD: run durations; SM: starting material. Mineral abbreviations after Whitney and Evans. Other abbreviations: swp (saturated water pressure)

Table 1. Continued

N	Paper	RD (days)	T (°C)	P (kbar)	SM	Solution	Comments
13	Mysen 2015	0,04	550	2,99	ZrO_2 ZrO_2+Qz	H_2O	Zr^{4+} concentration varies from ≤10 to ~70 ppm with increasing temperature and pressure. The addition of SiO_2 does not appreciably affect these values.
			575	5,44			
			625	4,31			
			650	7,01			
			700	6,37			
			725	7,83			
			775	8,42			
			800	10,13			
			575	1,38		1M NaOH + H_2O	Zr^{4+} concentration in the aqueous fluid increases by about an order of magnitude when 1 M NaOH is added to H_2O, reflecting the formation of zirconate complexes. Addition of SiO_2 increases Zr^{4+} by a factor of 5 and alkali zircon silicates are formed.
			600	0.59 / 1.83			
			650	1,83			
			700	3,04			
			725	2,66			
			750	4,57			
			775	4,35			
			800	6,8			
14	Lewerentz et al., 2019	6,92	600	3,7	Zrn+Qz	$CaCl_2$ + H_2O	Ca:Si<<1 no baddeleyite. Ca:Si=0.6-2.09 baddeleyite forms. Experiments without Qz: baddeleyite forms.
		10		4,4	Zrn+Qz Zrn	$CaCl_2$ + H_2O $Ca(OH)_2$ + H_2O	
		50		4,2		$Ca(OH)_2$ + H_2O	

N: Number; RD: run durations; SM: starting material. Mineral abbreviations after Whitney and Evans. Other abbreviations: swp (saturated water pressure)

I.3.5 Zircon crystallization from mafic magmas.

Early experimental studies on lunar basalts revealed that zircon could not form until 99.96-99.92% of the liquid had already crystallized (Hess et al., 1980; Dickinson & Hess, 1982), an idea confirmed by later experiments on terrestrial low-silica melts (e.g., Borisov & Aranovich, 2019; Shao et al., 2019) (Fig. 9).

Nonetheless, and against what is foreseen by the experimental data, syn-magmatic zircon crystals abound in many mafic and ultramafic rocks (e.g. Claeson, 1999; Williams & Hergt, 2000; Bea et al., 2006a; Grimes et al., 2011; Yang et al., 2018; etc.), even as inclusions in early-formed major minerals (Fig. 10), thus indicating that zircon can precipitate before the bulk mafic melt became zircon-saturated. A remarkable case is the occurrence of zircon in the troctolites and gabbros from the Mid-Atlantic Core Complexes (Bortnikov et al., 2005; Bortnikov et al., 2008; Grimes et al., 2009; Silantyev et al., 2010; Skolotnev et al., 2010), where most zircon-bearing rocks are early-stage cumulates formed from zircon-undersaturated incompatible-element depleted MORB magmas. Additionally, and to further increase the incongruence with bulk-rock composition, these zircons have abundant inclusions rich in incompatible elements (see **section III.2**).

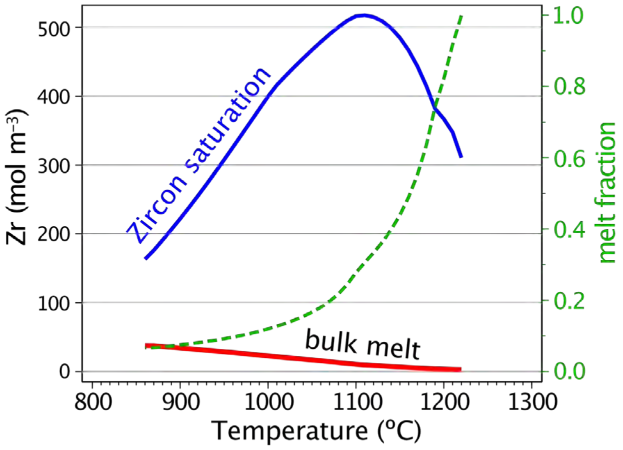

Fig. 9. Plot of the Zr concentration required for zircon saturation calculated from Borisov & Aranovich (2019), the concentration of Zr in the residual melt assuming that no Zr is incorporated in the crystallizing minerals and the initial magma had 2.86 mol m^{-3} (≈100 ppm) of Zr, the melt fraction calculated with rMELTS. The residual melt remains deeply zircon-undersaturated when the crystallinity is approx. 0.9; rough extrapolation beyond the rMELTS lowest temperature output suggest that the residual melt would reach saturation only after the crystallinity is approx. 0.99.

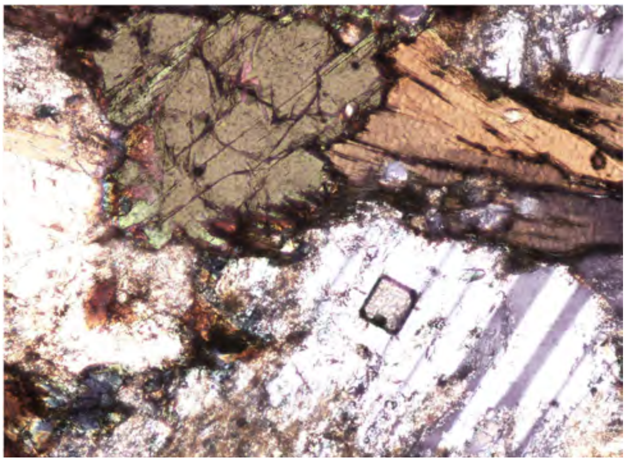

Fig. 10. Euhedral zircon grain included in a labradorite (An$_{54}$) crystal from an appinitic gabbro (48 wt% SiO$_2$, Bea et al., 2006a) with 355 ppm (≈ 10.15 mol m^{-3}) Zr. The zircon is syn-magmatic and was formed when the melt required more than 1100 ppm (≈ 31.45 mol m^{-3}) Zr for zircon saturation, according to the temperature and composition calculated for the formation of An$_{54}$ plagioclase (1020 ºC).

The notable coincidence of the experimental models signaling the elevated solubility of zircon in mafic magmas indicates that this is a genuine feature unaffected by factors other than the melt composition and temperature. Therefore, to explain why zircon precipitates from zircon-undersaturated magmas, we must consider other factors different from increasing the Zr bulk concentration in the melt because of volume reduction as the crystallization progresses. To this end, we did a 2D finite element study of how the Zr^{4+} ions rejected by growing major minerals diffuse into the melt. The study was based on Smith et al. (1955) mathematical analysis of solute redistribution during solidification. It was constrained to simulate the evolution of inter-cumulus melt in the Mid-Atlantic zircon-bearing gabbroic cumulates because these contain abundant syn-magmatic zircon. Our results reveal that the formation of transient locally-saturated zones at the crystals-melt interfaces during confined crystallization can explain the discrepancy between experiments and observations.

PART II. EXPERIMENTAL STUDY

II.1 Materials and methods

II.2 Results of the high-temperature experiments: annealing

II.3 Results of hydrothermal experiments

II.1 Materials and methods

This section is divided into starting materials, experiments carried out and analytical methods.

II.1.1 Starting materials for the experiments

Natural zircon grains from the three samples are used in this work, representing a broad spectrum of situations (Figs. 11, 12 and 13). The samples are:

1) one Cambrian-Ordovician orthogneiss (SAB50) from the Ollo de Sapo Formation in the Central Iberian Zone (described in detail by Bea et al., 2018b)
2) one Variscan tonalite (SAB51) from Sanabria appinites (described in detail by Bea et al., 2018b)
3) one Early Paleoproterozoic to Neoarchaean syenite (REG20) from the Awsard Kalsilite-nepheline syenitic complex, in the Reguibat Shield of the Western African Craton (described in Bea et al., 2014).

Apart from zircon grains, powder from a leucogranite GREB-354 will be used in some hydrothermal experiments. This powder has been chosen because it corresponds to a peraluminous granite whose composition is well known and which can be used either as a buffer or to saturate the medium in granite components. The choice to use granite powder is to facilitate the leaching of the elements.

These three particular samples have been chosen because of their morphology, internal structure, and degree of metamictization. Zircon grains from the orthogneiss are not metamict; they have inherited Ediacaran cores with crystallographic orientations different from the surrounding Cambrian-Ordocivian rims: they, however, are interesting because their core-rim configuration seems ideal for studying the effects of thermal decompaction (Zaraisky & Balashov, 1994) and the melt accumulation at the interfaces.

Zircon grains from the Variscan tonalite are euhedral with a marked sector zoning and remarkably uniform isotope homogeneity despite occasionally showing small metamict areas. They are thus suitable for studying the migration of radiogenic lead from low-U to high-U domains during post-crystallization heating.

Zircon grains from the heavily metasomatized syenite are U- and Th- rich, highly metamict and have plenty of inclusions, with elevated common-Pb and a marked radiogenic Pb-loss. These grains were thought to be ideal for studying common-lead rejection from zircon crystals upon heating (Mattinson, 2005).

Fig. 11. Macro-photographs of untreated zircon grains from orthogneiss SAB50, tonalite SAB51, and syenite REG20. Untreated SAB50 zircons are transparent and colorless or slightly pinkish, mostly euhedral short stubby prisms terminated by long pyramids. Untreated SAB51 zircons are euhedral transparent and colorless to slightly pinkish, most of them forming long narrow prisms terminated by short pyramids. Highly metamict REG20 zircons are euhedral to subhedral, translucent to opaque with different colors (from yellow to purple and brown), forming short stubby prisms terminated by short pyramids. Images obtained by optical microscopy using a focus stacking technique and non-polarized visible light (see ***Section II.1.3****. for details).*

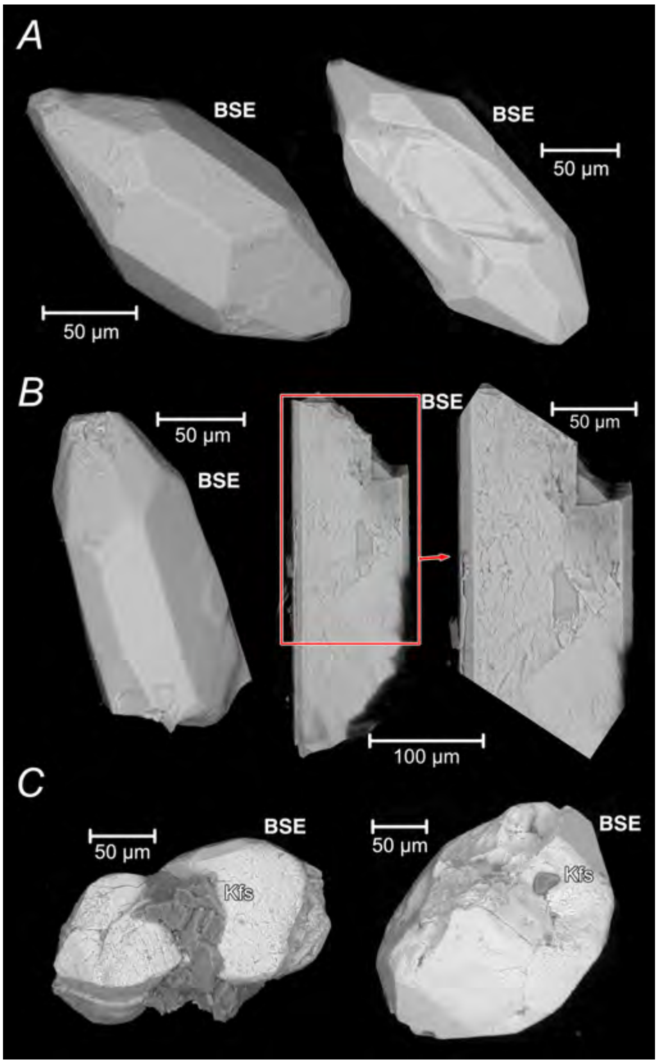

Fig. 12. BSE images of untreated zircons from orthogneiss SAB50 (A), tonalite SAB51 (B), and syenite REG20 (C). A: Euhedral short stubby prism terminated by long pyramids with smooth and slightly rough faces; Subhedral short stubby prism terminated by long pyramids with a partially broken face exposing the inner core. B: Subhedral narrow prism terminated by short pyramid with smooth faces; Split zircon grain with microporous bands exposed at a fracture surface perpendicular to the prismatic faces. C: Subhedral short stubby prisms terminated by short pyramids with abundant cracks and porosity, both grains joined by inclusion of K-feldspar; Euhedral short stubby prism terminated by short pyramids with abundant porosity and a tiny K-feldspar inclusion.

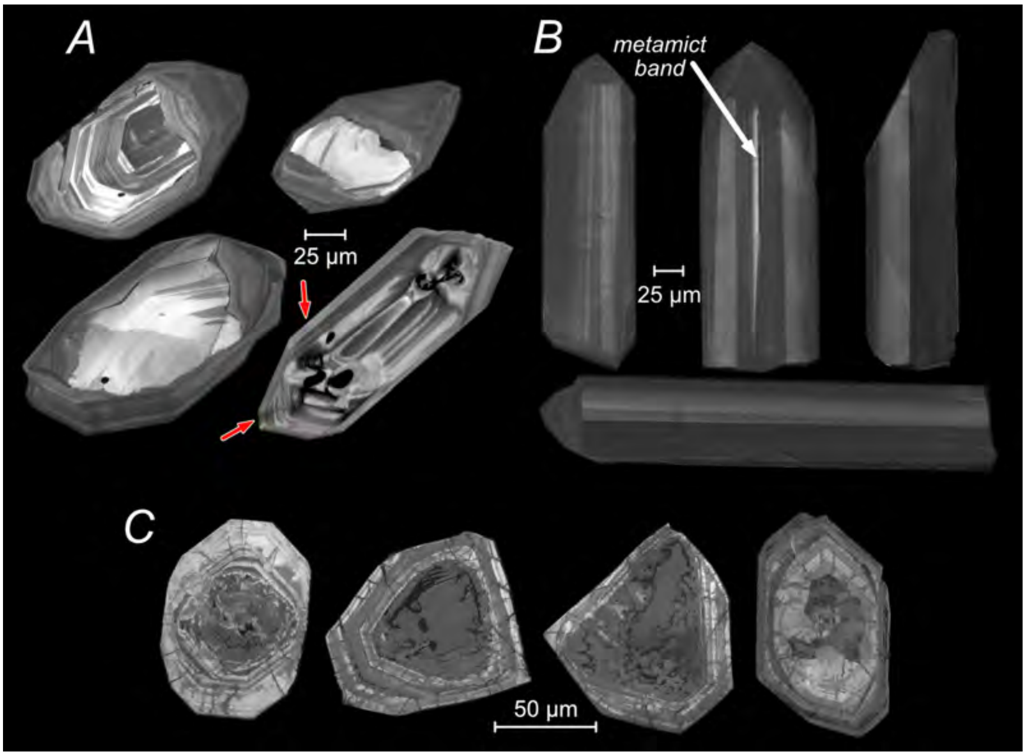

Fig. 13. CL images of untreated zircon grains from orthogneiss SAB50, tonalite SAB51, and syenite REG20. (A) SAB50 zircons show oscillatory zoning and an Ediacaran euhedral inherited core overgrown by a Cambro−Ordovician rim, which generally truncates the core zoning. Red arrows show radial fractures. (B) SAB51 zircons appear zoned with alternating light-gray and dark-gray bands parallel to the longest axis. (C) Highly metamict REG20 zircons show a marked oscillatory zoning, locally partially obliterated, and abundant inclusions, and cracks, in most cases with a radial disposition.

II.1.1.1 Orthogneiss SAB50

The gneiss belongs to the Ollo de Sapo Formation in the NW boundary of the Central Iberian Zone (Diez Montes et al., 2004). It was derived from a mildly deformed porphyritic peraluminous granite detailedly studied by Montero et al. (2007). The rock has a marked augen structure, with large crystals of K-feldspar —often rapakivi— between a coarse-grained and foliated groundmass composed of quartz, oligoclase, muscovite and biotite as major minerals, and abundant apatite, monazite and zircons as accessories, During the Variscan orogeny, the gneiss was markedly deformed and slightly metamorphosed, albeit far below the anatexis isograde. This fact indicates that the abundant zircon grains in the gneiss are pristine and untouched by the Variscan metamorphism.

Zircon grains are abundant. They are transparent, colorless, or slightly pinkish, mostly euhedral short stubby prism terminated by long pyramids (Figs. 11). The grain surface can be smooth or slightly rough. The outermost shell is broken in some grains, exposing the inner grain core (Fig. 12A). Most of them comprise a Cambrian-Ordovician rim (480-485 Ma) and an Ediacaran core (600-610 Ma), which in most cases have a different crystallographic orientation as revealed by a different angle of extinction (Fig. 14). Radial microcracks, probably produced by the volume increase of the grain core during metamictization, are widespread (see Fig. 13).

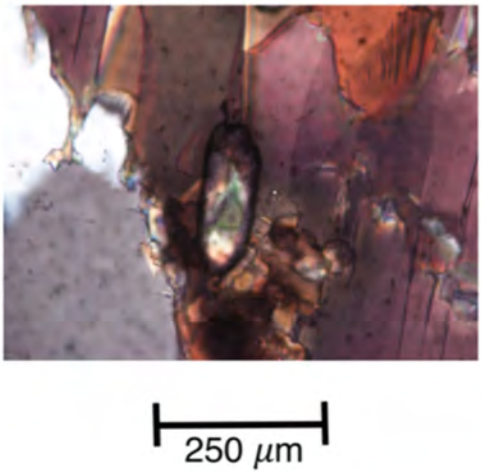

Fig. 14. Microphotograph of zoned zircon grain from orthogneiss SAB50 under crossed polarized light showing a heterogeneous extinction what suggests that core and rims have a different lattice orientation.

Zircons are plenty of mineral inclusions, more abundant in the inherited Ediacaran cores than in Cambrian-Ordovician rims (see Table 2). The inclusions can be monomineralic, i.e. single crystals of quartz, K-feldspar, chlorite, apatite and fluor-apatite, rutile, or hercynite, or polymineralic, mainly tear drop-shaped globules of quartz + alkali feldspar, quartz + K-feldspar + ilmenite, plagioclase + biotite + ilmenite, and quartz + monazite + fluor-apatite (Fig. 15A, B). Fluorine-rich inclusions, either mono- or polymineralic, are common, consisting either of fluorite (Fig. 15A), a fluoro-silicate with a composition close to that of fluorite-illite (Fig.15C; Table 3) or a complex Mg-Fe-Ca-Na alumino-fluoride mineral, probably hydro-kenoralstonite (Fig. 15D; Table 3). The zircon cores also contain up to 50 µm in diameter nano-pores, which likely represent gas bubbles (Fig. 15B) that suggest fluid presence during zircon growth.

Laser Ablation Inductively Coupled Plasma-Mass Spectrometry (LA-ICP-MS) analyses (Table 4) show that the cores are slightly depleted in P, Ti, Y and Hf with respect to the rims. U, Pb and Th values are similar at rims and cores. In addition, cores and rims show similar REE abundances with a marked negative Eu anomaly (Fig. 16). The main difference between cores and rims is in the oxygen isotopes. Fig. 17 shows two populations, one from the Ediacaran inherited cores at six of ∂^{18}O and one from the Cambro-Ordovician rims at nine ∂^{18}O.

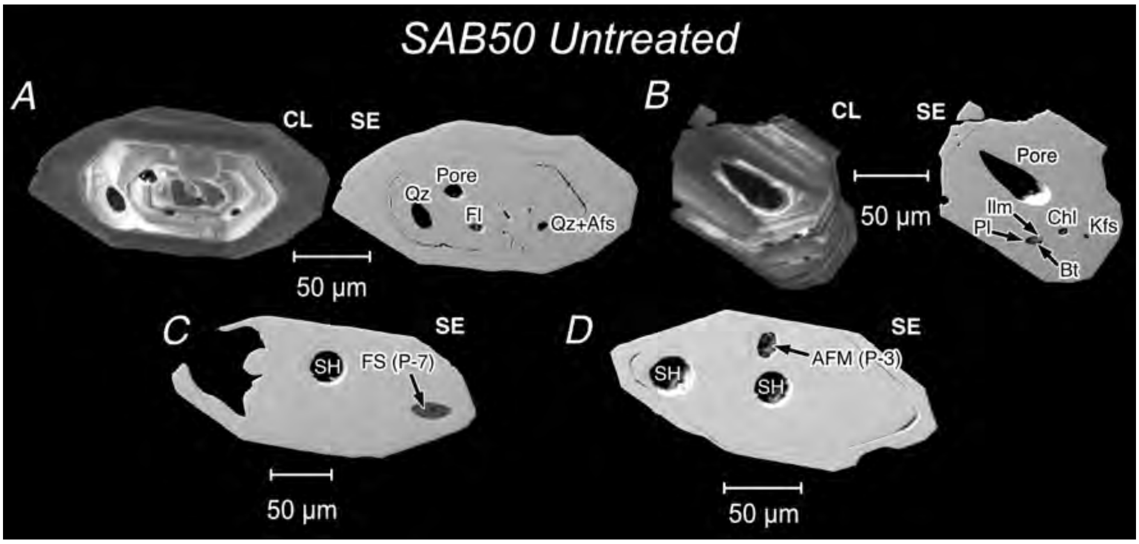

Fig. 15. CL and SE images of untreated zircons from orthogneiss SAB50. The zircons show oscillatory zoning and an Ediacaran inherited core overgrown by a Cambro−Ordovician rim, with a core−rim interface outlined in many cases by a tiny cleft on the polished surface. Mineral inclusions in the zircons are restricted to the cores. (A) Zircon with oscillatory zoning hosting monomineralic inclusions of quartz and fluorite and a tear drop-shaped polymineralic inclusion of quartz + alkali feldspar. Note the variable orientation of the oscillatory zoning in the inner core. (B) Zircon with oscillatory zoning hosting a coarse pore, which may represent a gas bubble, a polymineralic inclusion of plagioclase + biotite + ilmenite, and monomineralic inclusions of chlorite and K-feldspar. Note that the oscillatory zoning of the core is not truncated by that of the rim. (C) Monomineralic inclusion of fluorosilicate with a composition close to that of fluor-illite (see analysis in Table 3). (D) Monomineralic inclusion of a complex Mg−Fe−Ca−Na aluminofluoride mineral (probably hydro-kenoralstonite; see analysis in Table 3;(Atencio et al., 2017). Mineral abbreviations after Whitney & Evans (2010). Other abbreviations: AFM = aluminofluoride mineral; FS = fluorosilicate; and SH = SHRIMP analysis spot.

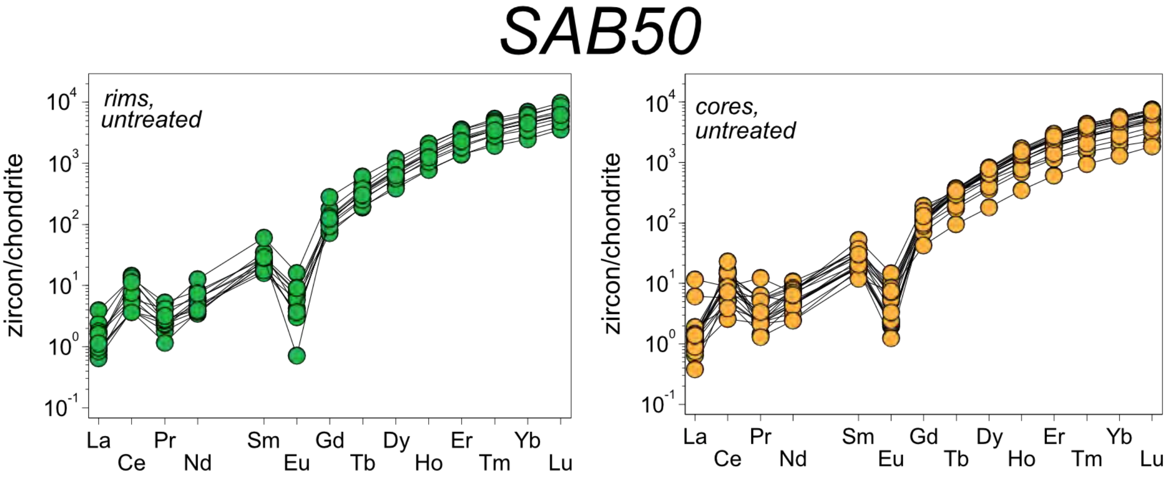

Fig. 16. Chondrite-normalized REE patterns from untreated zircon grains from orthogneiss SAB50. The REE compositions of the rims and cores are clearly close to each other.*

Table 2. Summary of mineral assemblages and textures in untreated zircon grains

Sample	Rock type	Grain number	Mineral inclusions	Main textural features
SAB50	Orthogneiss	212	Qz (9) Kfs (6) Chl (2) Ap and F-Ap (20) Rt (1) Hc (1) Fl (5) FS (1) AFM (1)	Tear drop and anhedral shapes
			Qz + Afs (1) Qz + Kfs + Ilm (1) Pl + Bt + Ilm (1) Qz + Mnz + F-Ap (1)	Tear drop shaped globules
SAB51	Tonalite	194	Qz (1) Kfs (4) Fl (1)	Tear drop shapes
			Qz + Ab + Kfs (2)	Tear drop globules
			FS (1)	Partially filled coarse gas bubbles
			AFM (1)	Euhedral shapes
REG20	Syenite	133	F-Ap (6) Thr/Hut (4) Che-Hut (4) Bt + Ab + Kfs (1) Ab + Mag + Ep + Aln (1) Kfs + Mag (1)	Anhedral shapes
			Secondary phyllosilicates and Ep (5)	Tiny grains infilling microcracks

Mineral abbreviations after Whitney & Evans (2010). Other abbreviations: AFM = aluminofluoride mineral (probably hydrokenoralstonite); Che-Hut = cheralite-huttonite solid solution; FS = fluorosilicate; Thr/Hut = thorite/huttonite. Number of grains with the reported inclusions indicated in parentheses.

Table 3. Selected EDX analyses of mineral inclusions (atoms per formula unit)

Sample	**SAB50**				**SAB51**				**REG20**				
Rock type	**Orthogneiss**				**Tonalite**				**Syenite**				
Type[a]	**U**	**U**	**U**	**A**	**U**	**U**	**A**	**A**	**U**	**U**	**U**	**U**	**U**
Mineral[b]	**AFM**	**F-Ap**	**FS**	**Sri**	**AFM**	**MB Zrn**	**Sch**	**Bdy**	**F-Ap**	**Thr/Hut**	**Kfs**	**Pl**	**Che-Hut**
Point	3	82	7	125	4	133	32	199	57	6	5	26	40
Nº of atoms	2.5 Cat	12.5 O	11 O	3 Cat	2.5 Cat	4 O	4 O	1 Cat	12.5 O	4 O	5 Cat	5 Cat	4 Cat
Si	-	-	3.49	-	-	1.556	-	-	-	0.944	2.952	2.867	1.194
Ti	-	-	-	2.559	-	-	-	-	-	-	-	-	-
Al	1.007	-	2.17	0.034	0.914	-	-	-	-	-	1.015	0.99	-
Fe	0.108	0.075	0.16	-	0.142	-	-	-	-	-	-	0.171	-
Mn	0.014	-	-	-	-	-	-	-	-	-	-	-	-
Mg	0.868	-	0.25	-	0.896	0.066	-	-	-	-	-	-	-
Ca	0.111	4.898	-	-	0.547	0.181	0.91	-	5.01	0.119	-	0.107	0.633
Na	0.392	-	-	-	-	-	-	-	-	-	0.039	0.865	-
K	-	-	0.72	-	-	0.045	-	-	-	-	0.993	-	-
F	5.62	1.097	2.59	-	5.645	4.986	-	-	1.235	0.525	-	-	-
Cl	0.024	-	-	-	0.034	-	-	-	-	-	-	-	-
P	-	3.102	-	-	-	-	-	-	2.99	-	-	-	0.611
W	-	-	-	-	-	-	1.03	-	-	-	-	-	-
Zr	-	-	-	0.407	-	2.152	-	0.986	-	-	-	-	-
Hf	-	-	-	-	-	-	-	0.014	-	-	-	-	-
Th	-	-	-	-	-	-	-	-	-	0.937	-	-	1.562
Total	8.144	9.172	9.37	3	8.18	8.986	1.94	1	9.235	2.525	5	5	4

[a] A = annealed; U = untreated.

[b] Mineral abbreviations after Whitney & Evans (2010). Other abbreviations: AFM = aluminofluoride mineral (probably hydrokenoralstonite); Che-Hut = cheralite-huttonite solid solution; FS = fluorosilicate; Thr/Hut = thorite/huttonite; MB = metamict band; Sri = srilankite.

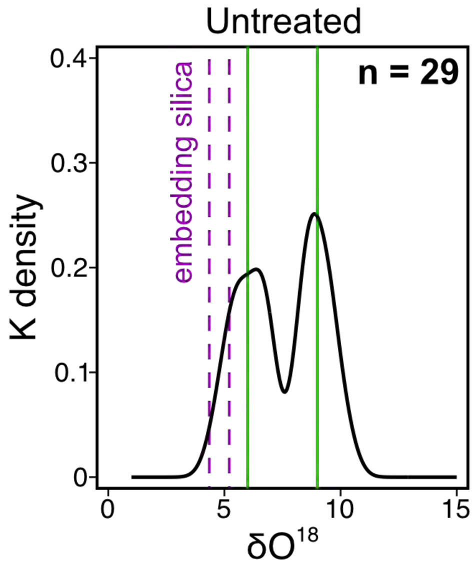

Fig. 17. ∂^{18}O distributions of untreated zircon grains from samples SAB50. There are two populations, one from the Ediacaran inherited cores at 6 of ∂^{18}O and one from the Cambro-Ordovician rims at 9 ∂^{18}O.

Table 4. LA-ICP-MS analyses of trace elements in SAB50 zircon grains (data in ppm)

Sample	**SAB50, Orthogneiss**														
Type	**Untreated**														
Point	**71**	**72**	**73**	**77**	**78**	**79**	**80**	**81**	**83**	**86**	**87**	**19**	**20**	**23**	**16**
Texture[a]	**R**	**R**	**R**	**R**	**R**	**R**	**R**	**R**	**R**	**R**	**R**	**C**	**C**	**C**	**C**
P	1460	989	860	724	514	505	1498	908	670	1291	869	877	888	712	620
Ti	43.4	12	25	46.5	32.3	25.8	17.8	17.5	25.2	18.0	26.1	8.38	11.5	11.1	10.7
Y	3163	2403	2196	1703	1192	1179	3303	2213	1632	2918	1954	2044	2214	1566	2016
La	0.18	0.15	0.22	0.94	0.56	0.29	0.42	0.38	0.38	0.23	0.27	0.25	0.32	0.32	0.42
Ce	3.84	2.39	2.3	8.05	8.87	8.29	3.72	3.26	4.74	2.26	7.06	3.15	7.21	10.1	8.86
Pr	0.19	0.17	0.11	0.49	0.38	0.23	0.39	0.22	0.25	0.26	0.30	0.2	0.54	0.23	0.51
Nd	2.63	1.58	1.72	3.75	2.89	2.09	5.79	2.86	2.19	1.83	3.42	2.07	4.94	3.63	4.08
Sm	5.16	3.91	3.24	4.03	3.09	2.39	8.98	3.47	2.65	4.23	4.3	2.76	4.63	4.39	5.55
Eu	0.24	0.43	0.18	0.45	0.39	0.33	0.91	0.17	0.21	0.04	0.52	0.11	0.42	0.6	0.35
Gd	35.6	26.4	22.6	21.5	16.1	14.5	55.9	23.3	19.1	27.0	25.1	20.8	24.4	23.2	31.7
Tb	16.4	12.8	12.1	9.61	6.89	7.13	22.0	11.8	9.19	13.9	11.0	11.1	12.1	10.1	13.7
Dy	247	188	184	136	107	96	294	171	141	222	160	169	183	136	183
Ho	112	83.3	77.9	63.2	43.4	42.7	116	78.1	59.1	97.4	68.8	76.7	79.6	57.4	75.6
Er	571	434	395	318	221	223	567	406	296	521	376	416	417	288	369
Tm	132	96.9	85.7	71.8	52.7	48.0	122	92.7	70.4	114	86.8	93.1	98.6	67.7	82.5
Yb	1118	848	723	655	456	396	1018	829	569	970	735	768	873	596	689
Lu	239	177	148	135	98.3	88.2	150	153	184	55.5	155	153	174	125	133
Hf	9256	9123	9375	9180	9333	8777	9290	9467	9046	7059	9391	8815	9281	8805	8805
Pb	25.5	20.7	15.5	20.1	17.5	13.3	18.3	22.5	20.5	10.7	22.3	21	25.9	21.9	19.9
Th	44.4	29.6	19.3	41.8	38.8	33.3	19.7	17.5	23.0	47.2	43.5	19.2	48.1	46	45.1
U	294	219	162	195	155	124	182	233	215	81.2	224	212	260	185	188
Sc	449	379	460	253	195	225	407	366	378	238	386	290	388	438	336
Nb	0.73	0.43	0.39	0.39	0.38	0.41	0.43	0.50	0.42	0.76	0.75	0.28	0.71	1.08	1.56
Ta	bdl	bdl	bdl	bdl	bdl	bdl	bdl	bdl	bdl	bdl	bdl	bdl	bdl	bdl	bdl

[a] R = rim; C = core; bdl = below detection limit.

Table 4. Continued (data in ppm)

Sample	**SAB50, Orthogneiss**															
Type	**Untreated**															
Point	**17**	**24**	**25**	**26**	**27**	**29**	**35**	**37**	**38**	**39**	**40**	**41**	**42**	**43**	**44**	**45**
Texture[a]	**C**	**C**	**C**	**C**	**C**	**C**	**C**	**C**	**C**	**C**	**C**	**C**	**C**	**C**	**C**	**C**
P	696	959	559	918	870	607	877	922	1025	168	490	521	432	195	817	949
Ti	10.5	19.5	14.5	12.3	8.34	10.8	13.7	6.65	9.41	13.5	9.44	12.8	9.61	6.62	9.5	14.7
Y	1646	2537	1814	2175	2258	1729	2106	2183	2468	1109	1036	1640	1262	530	2065	2324
La	0.25	0.36	0.32	1.46	0.29	0.36	0.15	0.18	0.45	0.09	0.30	0.31	0.35	0.21	2.74	0.33
Ce	6.61	8.88	5.88	3.52	3.30	5.32	3.08	1.58	2.42	4.61	6.75	5.84	9.44	14.2	5.39	4.45
Pr	0.21	0.49	0.32	0.59	0.21	0.48	0.13	0.20	0.24	0.20	0.24	0.28	0.20	0.12	1.14	0.32
Nd	1.47	3.84	3.48	2.19	2.22	3.46	2.03	1.13	2.09	3.39	2.43	3.57	1.97	1.11	3.25	2.97
Sm	2.27	3.92	5.72	2.85	2.96	4.51	2.75	2.47	2.85	7.78	2.61	5.52	3.61	1.78	3.11	4.51
Eu	0.13	0.29	0.42	0.12	0.12	0.35	0.13	0.07	0.13	0.83	0.31	0.48	0.41	0.42	0.14	0.19
Gd	17.9	26.0	30.2	22.1	21.7	24.4	21.3	22.7	24.5	38.2	14.0	31.7	18.2	8.53	19.8	26.0
Tb	8.93	13.2	12.4	11.2	11.3	11.1	11.5	11.5	13.5	11.9	6.29	11.7	7.02	3.44	10.8	12.5
Dy	127	200	165	183	180	156	166	178	202	127	88.6	157	99.7	44.8	164	197
Ho	56.4	90.5	64.1	79.9	82.2	63.1	73.4	77.7	94.0	45.1	37.4	65.1	43.6	19.1	74.7	85.4
Er	299	467	326	405	408	334	380	398	482	191	185	311	229	98.1	395	441
Tm	66.7	107	68.5	101	100	71.3	84.1	92.4	108	37.4	43.8	64.8	51.9	23.5	91.1	100
Yb	572	898	584	776	855	646	723	769	921	301	378	572	448	209	771	852
Lu	124	186	119	159	158	127	150	153	184	55.5	78.5	107	95.0	45.7	158	178
Hf	8197	8989	8090	8798	9247	8670	9290	9467	9046	7059	8530	7911	8714	9154	9237	8699
Pb	41.6	21.2	16.6	19.7	19.9	15.8	18.3	22.5	20.5	10.7	11.5	14.8	16.6	14.3	17.2	19.9
Th	42.1	38.6	39.1	19.6	19.7	28.0	19.7	17.5	23.0	47.2	23.0	39.6	46.2	50.3	19.4	37.3
U	152	201	152	198	211	142	182	233	215	81.2	115	142	154	116	177	199
Sc	327	375	121	256	268	212	407	366	378	238	337	211	286	230	391	466
Nb	bdl	0.88	0.11	0.29	0.29	0.39	0.43	0.50	0.42	0.76	0.37	0.62	0.55	0.78	0.37	2.76
Ta	bdl	bdl	bdl	bdl	bdl	bdl	bdl	bdl	bdl	bdl	bdl	bdl	bdl	bdl	bdl	bdl

[a] R = rim; C = core; bdl = below detection limit.

II.1.1.2 Tonalite SAB51

This rock is an undeformed Variscan amphibole-biotite tonalite; it has abundant zircon grains with a SHRIMP U-Pb concordant age of 318 ± 2 Ma and a very constant oxygen isotope composition around $\partial^{18}O = 6.9$ (Bea et al., 2018b). The grains are euhedral, transparent, colorless to slightly pinkish. Most form long, narrow prisms terminated by short pyramids (Fig. 11). The microporous metamict bands can emerge on the grain surface because the thin outermost shell of this may occasionally be broken, leading to the development of rough surfaces. The microporous bands are also exposed on the fracture surfaces of grains broken perpendicularly to the prismatic faces (Fig. 12B). Under cathodoluminescence, most grains appear zoned with alternating white and dark bands parallel to the longest axis (Fig. 13B). In some cases, they also present partially metamict and microporous bands parallel to —or developed over— the darkest compositional bands.

LA-ICP-MS analyses showed that the lighter bands are more depleted in U, Th, Y, and HREE than darker bands (Fig. 18; Table 5). Some dark bands that contain detectable F and K are partially metamict and microporous (Fig. 19D; Table 3). Electron Microprobe (EMPA) analyses of zircon grains also show systematic variations in W abundances (Table 6) that are higher in the darker bands (av. 138 ppm; range:

109−179 ppm) than in the light ones [av. 99 ppm; range: from <dl (detection limit = 78 ppm) to 116 ppm], whereas in the metamict bands, they are higher with an average concentration of ca. 280 ppm (range: 185−363 ppm). The ∂^{18}O distribution in this sample is pretty uniform and unimodal, clustering at around 6.8 ∂^{18}O (Fig. 20*).

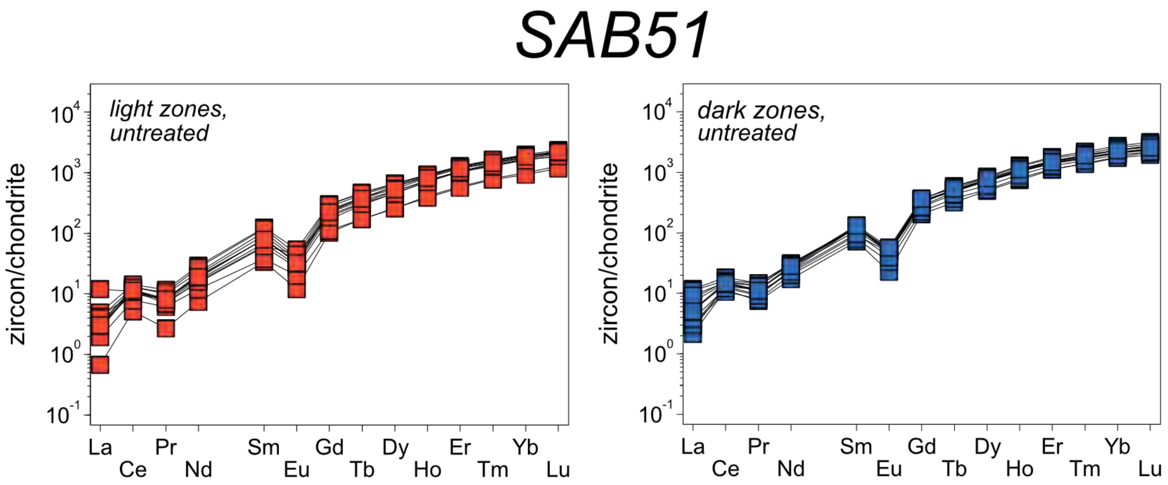

Fig. 18. Chondrite-normalized REE patterns from untreated zircon grains from tonalite SAB51. The darker bands are richer in HREE than the lighter ones.

SAB-51 zircons also contain abundant monomineralic and polymineralic inclusions (Fig. 19; Table 2). The monomineralic inclusions comprise quartz, K-feldspar, fluorite, and a complex euhedral Mg−Fe−Ca−Al fluoride mineral (ca. 20−35 μm long), most probably hydro-kenoralstonite (Fig. 19C). The polymineralic inclusions consist of teardrop-shaped globules of quartz + albite + K-feldspar (Fig. 19A) that can be associated with relatively coarse gas bubbles (ca. 40 μm long) partially filled with fluoride + silicate mineral phases (Fig. 19B).

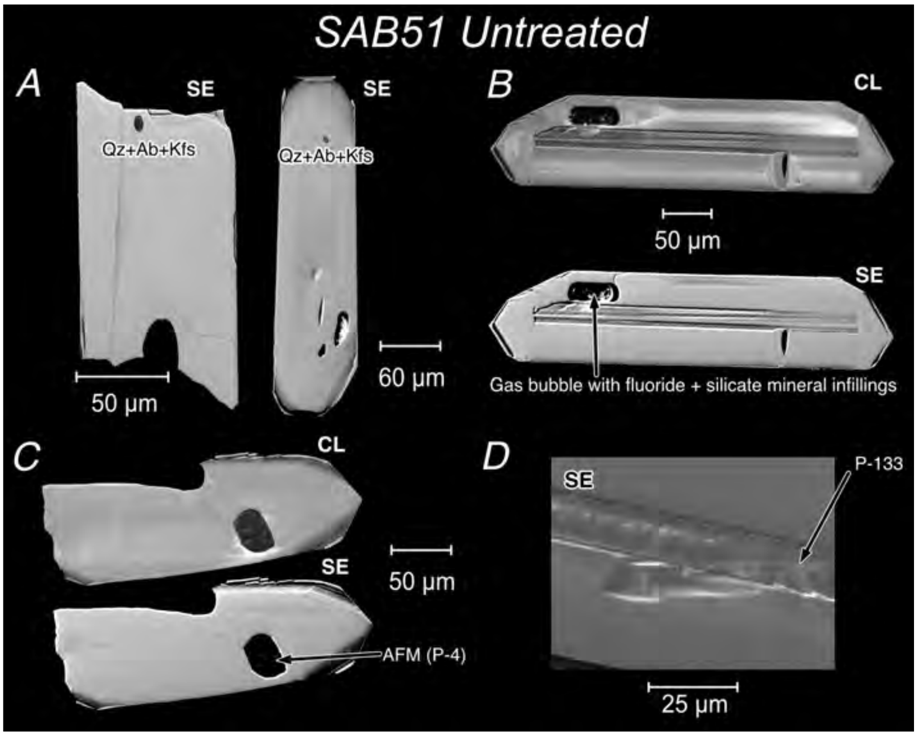

Fig. 19. CL and SE images of untreated zircons from tonalite SAB51. The zircons present a slightly oscillatory zoning and non- luminescent metamict porous bands parallel to pyramidal and/or prismatic faces. (A) Zircons with metamict porous bands and polymineralic tear drop-shaped inclusions of quartz + albite + K- feldspar. (B) Zircon with non-luminescent metamict porous bands and a coarse gas bubble filled with fluoride + silicate minerals. (C) Zircon with non-luminescent metamict porous bands and euhedral inclusion of a complex Mg−Fe−Ca−Na aluminofluoride mineral (probably hydro-kenoralstonite; see analysis in Table 3;(Atencio et al., 2017). (D) SE image of zircon with metamict porous bands containing impurities of Mg, Ca, K, and F (see analysis in Table 3). Mineral abbreviations after Whitney & Evans (2010). Other abbreviations: AFM = aluminofluoride mineral.

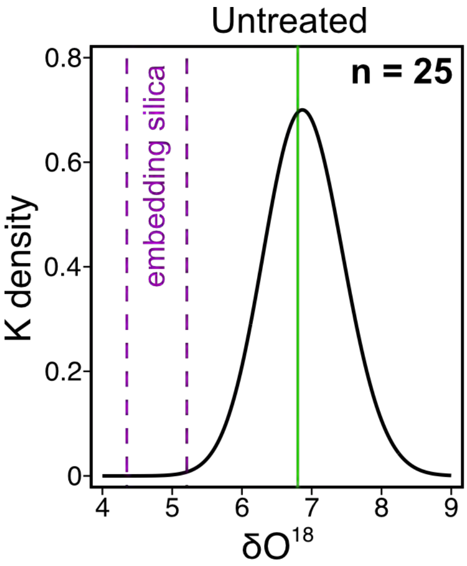

Fig. 20. ∂^{18}O distributions of untreated zircon grains from samples SAB51. There are one population at 6.8 of ∂^{18}O.

Table 5. LA-ICP-MS analyses of trace elements in untreated SAB51 zircon grains (data in ppm)

Sample	**SAB51 (Tonalite)**											
Type	**Untreated**											
Point	**1**	**2**	**3**	**5**	**12**	**9**	**6**	**8**	**11**	**14**	**7**	**13**
Texture[a]	**LB**	**LB**	**LB**	**LB**	**LB**	**LB**	**LB**	**LB**	**LB**	**LB**	**LB**	**LB**
P	638	659	408	321	387	148	254	299	542	298	142	804
Ti	10,3	8,11	16	13,6	8,2	8,0	11,0	10,0	10,0	11,6	8,8	9,92
Y	1015	974	1164	1033	1233	552	1212	1167	1188	1104	575	939
La	0,67	0,7	0,63	0,8	0,95	0,46	1,17	1,00	0,74	0,72	0,16	2,83
Ce	6,87	6,41	7,09	7,29	7,94	4,83	8,72	6,09	7,85	7,02	3,16	6,76
Pr	0,73	0,76	0,77	0,69	0,97	0,57	1,08	0,76	0,93	0,76	0,25	0,65
Nd	7,73	9,19	8,42	7,01	12,3	5,46	13,4	9,73	10,4	8,8	3,36	7,29
Sm	10,1	11,7	12,1	8,86	17,7	5,64	18,4	13,6	15,6	11,8	4,98	9,14
Eu	1,67	1,91	1,88	1,52	2,52	1,12	3,05	2,05	2,2	1,83	0,67	2,55
Gd	39,8	43,6	47,1	33,6	59,1	22,3	59,9	49,0	54,7	44,9	20,3	37,2
Tb	11,6	12,7	13,5	10,6	16,8	6,2	16,9	13,9	15,8	13,6	6,2	11,3
Dy	122	123	145	114	161	64	164	146	155	134	63,0	112
Ho	40,1	41,1	47,7	38,3	50,9	21,3	51,0	46,4	49,3	45,4	22,3	39,0
Er	169	171	198	170	207	90	206	189	198	191	94	164
Tm	33,8	32,5	39,8	35,0	40,7	19,0	39,0	36,4	37,6	36	20,0	31,6
Yb	272	263	319	289	308	150	310	281	307	303	161	262
Lu	50,4	45,6	58	57	52	29	52	52	55	54,6	32	47,1
Hf	8477	7973	9106	8610	8261	7833	7794	7409	8099	8150	8129	8213
Pb	23	23,6	28,7	25,2	26,1	13,8	27,2	20,6	27,9	27,1	18,3	25,2
Th	213	225	251	191	299	197	311	231	295	250	213	212
U	377	349	440	404	423	221	392	318	415	403	262	366
Sc	240	255	252	256	268	224	266	246	274	267	237	253
Nb	0,48	0,52	0,54	0,56	0,60	0,37	0,62	0,49	0,65	0,59	0,5	0,59
Ta	0,38	0,37	0,43	0,33	0,38	0,31	0,37	0,34	0,42	0,38	0,39	0,42

[a] LB = light band

Table 5. Continued

Sample	**SAB51 (Tonalite)**												
Type	**Untreated**												
Point	**50**	**56**	**57**	**65**	**69**	**47**	**49**	**60**	**70**	**68**	**61**	**62**	**58**
Texture[a]	**DB**	**DB**	**DB**	**DB**	**DB**	**DB**	**DB**	**DB**	**DB**	**DB**	**DB**	**DB**	**DB**
P	299	663	392	614	491	389	459	518	403	460	514	543	478
Ti	8,02	7,69	9,98	7,84	8,13	9,60	9,86	9,80	10,1	10,1	9,80	10,3	10,6
Y	1385	1664	1487	1037	1197	1396	1457	1069	1450	1339	1450	1592	1335
La	0,70	2,80	0,60	0,72	0,89	1,29	1,25	0,51	1,21	2,22	1,70	1,93	2,64
Ce	7,93	11,2	8,04	6,56	7,46	8,36	9,44	7,04	9,05	9,3	9,33	9,66	10,0
Pr	0,89	1,36	1,07	0,75	0,86	1,08	0,97	0,70	1,04	1,23	1,07	1,24	1,37
Nd	11	13,8	12,4	9,31	10,8	12,8	10,0	7,92	13,1	14,0	12,2	13,8	14,4
Sm	18,3	17,9	18,3	11,8	14,3	18,1	13,6	10,6	19,8	18,0	16,0	19,0	18,3
Eu	2,61	2,94	3,08	1,88	2,26	2,75	2,71	1,29	3,24	2,80	2,70	2,99	2,68
Gd	65,9	70,7	65,7	45,2	53,3	66,7	56,2	40,6	73,4	67,3	62,3	71,5	67,2
Tb	17,8	21,3	18,7	13,4	15,8	18,7	17,1	11,6	19,9	18,6	18,8	20,9	18,4
Dy	181	211	190	128	150	180	179	123	199	178	183	205	175
Ho	57,1	71,6	61	43,7	50,2	59,0	58,2	40,7	62,3	57,5	61,4	68,5	56,5
Er	224	289	240	182	207	234	238	177	243	228	250	273	223
Tm	43,9	54,1	47	34,3	39	43,7	47	35	48,7	43,1	47,0	51	41,9
Yb	333	442	374	281	314	348	378	288	379	344	381	414	333
Lu	60,6	78,1	67	48	54	61	69	54	65	58	66	73	57,2
Hf	7647	7786	7977	7934	7991	7397	8269	8789	7617	7202	7894	7625	7211
Pb	33,5	31,8	28,2	24,4	26,4	30,9	29,4	23,2	26,8	25,3	29,8	31,5	28,0
Th	352	428	385	242	287	374	327	223	398	361	358	426	362
U	481	522	464	370	412	463	486	413	440	417	474	498	453
Sc	283	266	256	258	263	274	245	241	268	259	264	273	262
Nb	0,8	0,71	0,73	0,53	0,57	0,78	0,58	0,47	0,75	0,7	0,63	0,77	0,75
Ta	0,43	0,44	0,46	0,37	0,38	0,45	0,42	0,37	0,42	0,44	0,41	0,45	0,47

[a] DB = dark band

Table 6. EMP analyses of Mg, Ca, Fe and W in untreated zircon grains (data in ppm)

Sample	**SAB50, Orthogneiss**														
Type	**Untreated**														
Point	**1**	**2**	**3**	**4**	**5**	**6**	**7**	**8**	**9**	**10**	**11**	**12**	**13**	**14**	**15**
Texture[a]	R	C	R	C	R	R	R	R	C	C	C	C	R	R	R
Mg	38	33	34	38	39	38	36	36	38	42	38	36	114	38	58
Ca	-	-	-	399	-	-	-	-	-	2102	28	57	750	-	168
Fe	-	-	-	189	-	-	29	-	104	65	-	25	93	-	-
W	437	199	256	-	99	654	477	554	218	186	-	126	1028	633	726
Sample	**SAB51, Tonalite**														
Type	**Untreated**														
Point	**1**	**2**	**3**	**4**	**5**	**6**	**7**	**8**	**9**	**10**	**11**	**12**	**13**	**14**	**15**
Texture[a]	MB	MB	H LB	H DB	MB	H LB	MB	H DB	H LB	H DB	H LB	H LB	H DB	MB	H DB
Mg	351	271	37	127	103	36	64	47	40	35	36	38	144	428	45
Ca	3945	3464	-	1000	1128	-	933	42	-	-	-	-	416	1791	19
Fe	41	43	-	25	-	-	58	-	-	-	-	-	45	100	-
W	332	363	-	179	243	-	275	149	116	165	78	100	109	185	113

[a] H = host; LB = light band; DB = dark band; MB = metamict band; RB= recrystallised band; R = rim; C = core.

II.1.1.3 Syenite REG20

This rock consists of a silica-saturated syenite from the outer envelope of the 2.45 Ga Awsard kalsilite-syenite intrusion of the west Reguibat Shield (Bea et al., 2014). Zircon grains are abundant, forming translucent to opaque and euhedral to subhedral crystals (Fig. 11). The most abundant shape consists of short stubby prism forms terminated by short pyramids with different colors, from yellow to purple and brown. (Figs. 11 and 12C) These zircon grains are highly metamict, especially in cores (Fig. 13C), with a pristine oscillatory zoning partially obliterated and abundant inclusions and cracks, in most cases with a radial disposition. This appearance is typical in zircons that have suffered intense high-T hydrothermalism or fenitization because of the expansion caused by metamictization.

Previous studies have revealed that these zircons are extremely rich in U, Th and —despite heavy lead losses— radiogenic Pb, with a notable common-lead abundance; this is why they are customarily used at the IBERSIMS SHRIMP laboratory for a mass calibration routine that includes ^{204}Pb.

REG-20 zircons contain abundant inclusions (Table 2). These are euhedral to subhedral single crystals of fluor-apatite, cheralite-huttonite, and thorite/huttonite solid solution or diverse associations of albite + magnetite + epidote + allanite, biotite + albite + K-feldspar, and K-feldspar + magnetite (Fig. 21). Secondary phyllosilicates and epidote appear either as tiny grains or as veins-infilling microcracks (Fig. 21). The high density of inclusions prevented us from obtaining LA-ICP-MS clean analyses, so the trace element composition of the REG20 zircons is not yet adequately known.

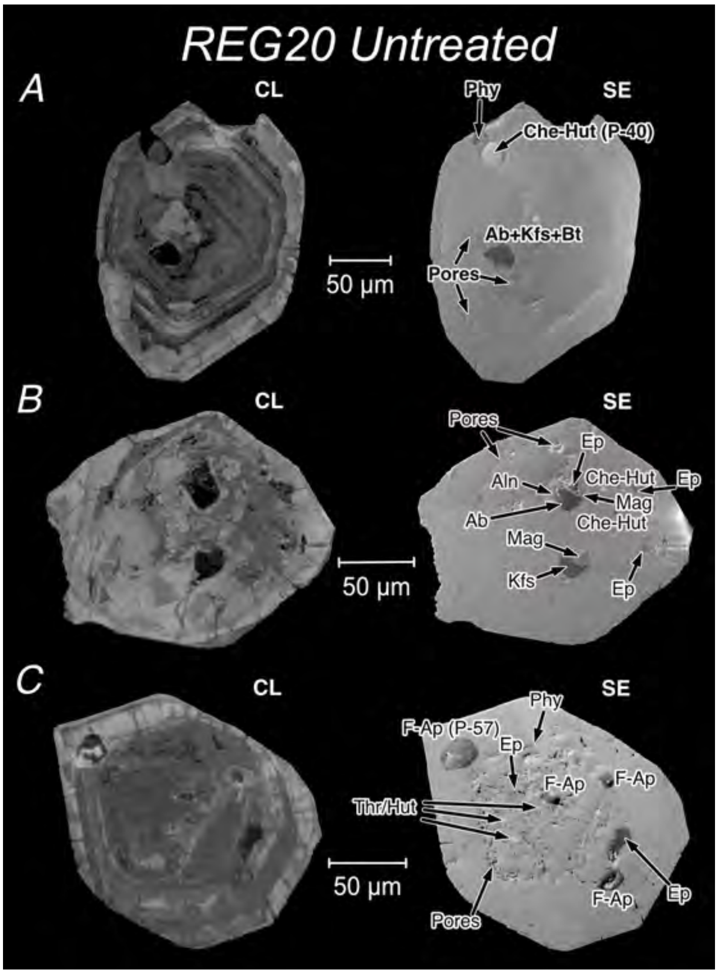

Fig. 21. CL and SE images of untreated zircons from syenite REG20. The zircons are metamict, having oscillatory or patchy zoning with porous metamict zones in the core and in bands parallel to the zoning. (A) Zircon with oscillatory zoning and an inclusion of relatively coarse cheralite−huttonite solid solution (see analysis in Table 3) surrounded by a tiny aggregate of secondary phyllosilicates and polymineralic inclusions of biotite + albite + K-feldspar. (B) Zircon with patchy zoning and polymineralic inclusions of albite + magnetite + epidote + allanite and K-feldspar + magnetite and tiny inclusions of epidote, which appears to fill in microcracks, and cheralite−huttonite solid solution. (C) Zircon with oscillatory zoning and inclusions of F-bearing apatite (see analysis in Table 3), thorite/ huttonite, and secondary phyllosilicates and epidote. Note the presence in the three grains of non-luminescent radial microcracks crosscutting the oscillatory zoning. Mineral abbreviations after Whitney & Evans (2010). Other abbreviations: Che−Hut = cheralite− huttonite solid solution; Phy = phyllosilicates; and Thr/Hut = thorite/huttonite.

II.1.1.4 Leucogranite GREB-354

This rock is a leucogranite from the Avila batholith, located in the Gredos sector (Fig. 1 from Bea et al., 1999). It is markedly peraluminous (ASI = 1.67); it may contain any combination of biotite, muscovite, cordierite, almandine garnet, sillimanite and andalusite (see Bea et al., 1999). Its composition (Table 7) reveals that the leucogranite has 71.37 wt % SiO_2, high alumina content (14.85 wt %), low Na_2O and CaO contents (2.87 and 0.91 wt %, respectively), and high Rb and low Sc contents (317.32 and 5.513 ppm respectively), indicating that it is an S-type granite. The trace contents are between 200 and 10 normalized to chondrite with lower amounts of HREE than LREE with a negative Eu anomaly (see Bea et al., 1999, Fig. 11). The choice of this granite is due, as mentioned above, to the fact that it is a typical S-type granite of known composition. We used it as a powder rather than a fragment to saturate the hydrothermal medium in granite components and simulate the elements' leaching from zircon in natural hydrothermal systems.

Table 7. Composition of granite GREB-354 used in hydrothermal experiments.

Mayor elements (wt %)		**Trace elements (ppm)**	
SiO_2	71,4	**Y**	18,7
TiO_2	0,43	**Nb**	18,1
Al_2O_3	14,9	**Ta**	2,91
FeO tot	2,61	**Zr**	199
MgO	0,46	**Hf**	6,00
MnO	0,05	**Mo**	3,53
CaO	0,91	**Sn**	12,1
Na_2O	2,87	**Tl**	1,70
K_2O	5,10	**Pb**	24,9
P_2O_5	0,28	**U**	4,67
Trace elements (ppm)		**Th**	25,8
Li	104	**La**	33,9
Rb	317	**Ce**	79,9
Cs	13,9	**Pr**	9,46
Be	4,63	**Nd**	36,1
Sr	81,2	**Sm**	7,05
Ba	366	**Eu**	0,58
Sc	5,51	**Gd**	4,94
V	28,0	**Tb**	0,72
Cr	197	**Dy**	3,46
Co	3,76	**Ho**	0,64
Ni	13,3	**Er**	1,58
Cu	0,88	**Tm**	0,24
Zn	57,6	**Yb**	1,49
Ga	23,4	**Lu**	0,23

II.1.2 Types of experiments

The separation of zircon grains was carried out in the grinding and hydrodynamics separation laboratories of the Department of Mineralogy and Petrology at the University of Granada. Grinding was carried out in a tungsten ring mill, followed by sieving to select the sample between 50 µm and 300 µm. Afterwards, zircon grains were separated by panning, first in water and then in ethanol. Once the dry concentrate was cleaned from magnetic minerals with a neodymium magnet, zircon grains were hand-picked to remove all the other minerals.

Using the so-separated zircons, we conducted two types of experiments: high-temperature experiments in a horizontal tubular furnace and hydrothermal experiments in Teflon bombs and a high-pressure autoclave.

II.1.2.1 Horizontal tubular furnace experiments (High-T experiments)

Annealing experiments were done in open crucibles within an N_2 atmosphere. The furnace was a Hobersal model ST166060 which can reach a temperature of up to 1600 °C. The experiments were done at 1300 °C over 6 months using the zircon grains SAB50, SAB51 and REG20 (see **section II.1.1** for samples description). Additional experiments with samples SAB50 and SAB51 at 1300 ºC over 1 and 3 months were done to obtain a complete perspective of the behavior of oxygen isotopes at mantle temperatures; sample REG20 was excluded because of the abundance of other minerals inclusions hinders the oxygen diffusion within zircon’s lattice. At the experiment temperatures, Váczi et al. (2009) have shown that natural and synthetic zircons heater in either alumina, platinum, or zirconia crucibles decomposes rapidly to baddeleyite plus silica. However, in previous experimental work (Bea et al., 2018b), we have found that embedding zircon in silica stops the decomposition and temperatures of 1300-1450 °C can be sustained for several months. The procedure we used is therefore based on this work and is as follows (Fig. 22): we filled with a 5 mm layer of fine-powdered cristobalite cylindrical alumina crucibles with a diameter of 12 mm and height of 14 mm; then, we transferred with a needle about 100 zircon grains on top of the cristobalite layer; lastly, we covered the zircon grains with another 5 mm layer of cristobalite, pressing the whole load with a steel piston. The crucibles were placed in an alumina boat and transferred to the centre of the tube furnace. The furnace alumina tube was closed on each side with a water-cooled steel gauge that permitted maintain an inert atmosphere (N_2 in this case) inside the tube for the whole duration of the experiments.

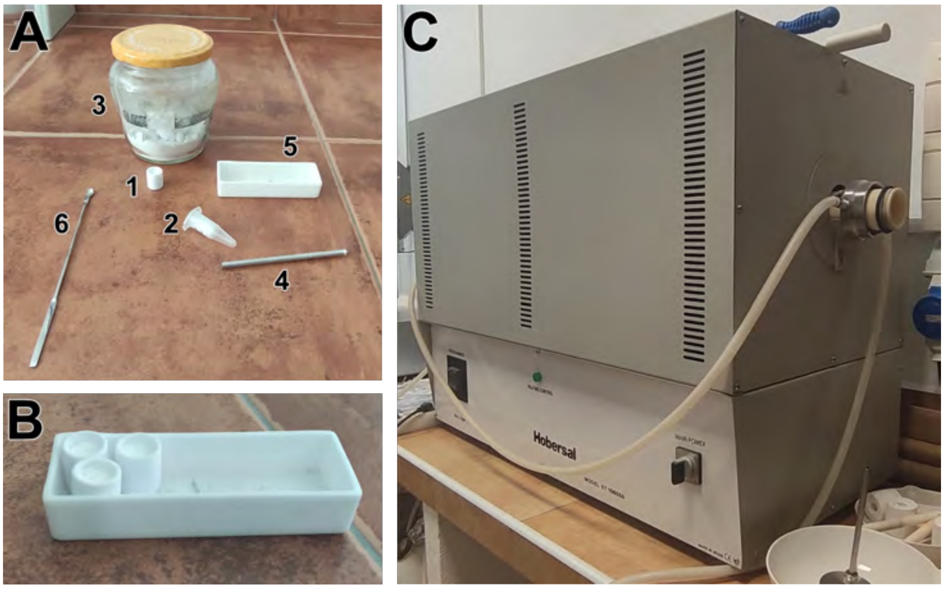

Fig. 22. Step by step procedure for the preparation of high-temperature experiments in a horizontal tubular furnace. A) Material used in experiments. 1: alumina crucible; 2: zircon grains; 3: Cristobalite; 4: steel piston; 5: alumina boat; 6: Spatula to put the cristobalite into the crucibles. B) Alumina boat with the crucibles of the experiments. C) Horizontal tubular furnace.

Once finished the experiments, the crucibles were slowly cooled to room temperature, and the zircon grains were removed from the cristobalite shell by dissolving the shell with warm HF, decanting the fluid, and washing the zircon grains with a saturated solution of H_3BO_3 first, and then with ultrapure water to remove all traces of acid.

II.1.2.2 Teflon bomb experiments (Low-T hydrothermal experiments)

The hydrothermal leaching experiments at low-T were carried out in Teflon bombs that can reach a maximum of 250 °C and 150 bar. These bombs are placed in a Hobersal furnace model HD-230 which can reach a temperature of up to 1200 °C.

All experiments (Fig. 23) were done with 0.5 g of granite powder (sample GREB-354, see **section II.1.1** for sample information), about 200 zircon grains of either SAB50 or SAB51 samples and 5 ml of solution.

These were made with ultrapure water and consisted of 2 M calcium chloride, 2 M sodium chloride and 1 M sodium fluoride. The experiments were carried out at temperatures of 170 °C and pressure of saturated water vapor (~ 10 bar) for 43 days (see Table 8). The fluid/zircon ratio chosen for the experiments is high (Fl/Zrn: 0.98, by weight; see table 8) because this is what is expected if a fluid infiltrates a rock.

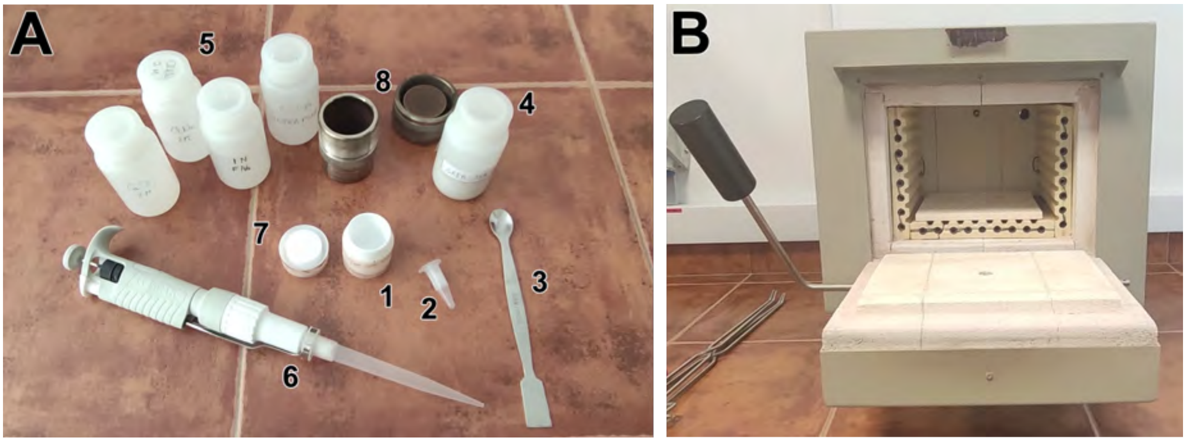

Fig. 23. Step by step procedure for the preparation of hydrothermal experiments in Teflon bombs. A) Material used in experiments. 1: Teflon container; 2: zircon grains; 3: spatula to put the granite powder; 4: Granite powder (GREB-354); 5: Ultrapure water, 2M $CaCl_2$, 2M NaCl and 1N NaF solutions; 6: Pipette to measure and introduce the liquid into the experiment; 7: Teflon stopper; 8: Steel container. B) Furnace.

Once experiments are finished, the Teflon containers are slowly cooled to room temperature and opened. One milliliter of ultrapure water is added to dissolve as many salts as possible that may have formed during quenching. Migdisov et al. (2009) use a similar procedure, only they form REE(III) precipitates and require sulfuric acid to dissolve them. After this, an aliquot of the solution is extracted for subsequent analysis of trace and major elements by ICP-MS and ICP-OES, respectively. The sample is left to dry so the zircons can be separated by handpicking from the granite powder.

II.1.2.3 Autoclave experiments (High-T hydrothermal experiments)

The hydrothermal leaching experiments at high-T were carried out in a Top Industries model 3167-0000 autoclave, using 3.5 cm Ag capsules with a diameter of 5 mm. The experiments have been divided into two: silica-undersaturated and silica-saturated. The formers were done with 70-100 zircon grains and 1 ml of solution. The latter were done in the same way but adding SiO_2 powder. The solutions used are the same as those used in the lower temperature hydrothermal experiments (ultrapure water, 2 M $CaCl_2$, 2 M NaCl and 1 M NaF), and zircon grains are from sample SAB50 (see **section II.1.1**). The procedure (Fig. 24) consists of heating the capsule with a blowtorch for a few minutes to make it malleable, then welding the lower part of the capsule. The zircon grains are added, silica is added if necessary, the solution is added, and the upper part of the capsule is welded. The capsule is weighed every time something is put in it and after welding. The welding was carried out with a Lampert PUK 5 arc welder. The capsule is then placed in the autoclave with 17 ml of water to reach the necessary pressure when heating the autoclave and balance the pressure inside the capsule. An accurate record of the whole experiment is kept, as the autoclave has a thermocouple (TKA 15x18 HMP) and a pressure sensor (WIKA HP-2-S) that are linked to a recording and visualization program (LabVIEW 3167). The experiments were carried out at temperatures of 550 °C and pressures between 850-2000 bar for 8 and 3 days (see Table 8). The fluid/zircon ratio chosen for the experiments is high for both silica-saturated and silica-undersaturated experiments(Fl/Zrn: 0.97 and 0.99, by weight, respectively; see table 8).

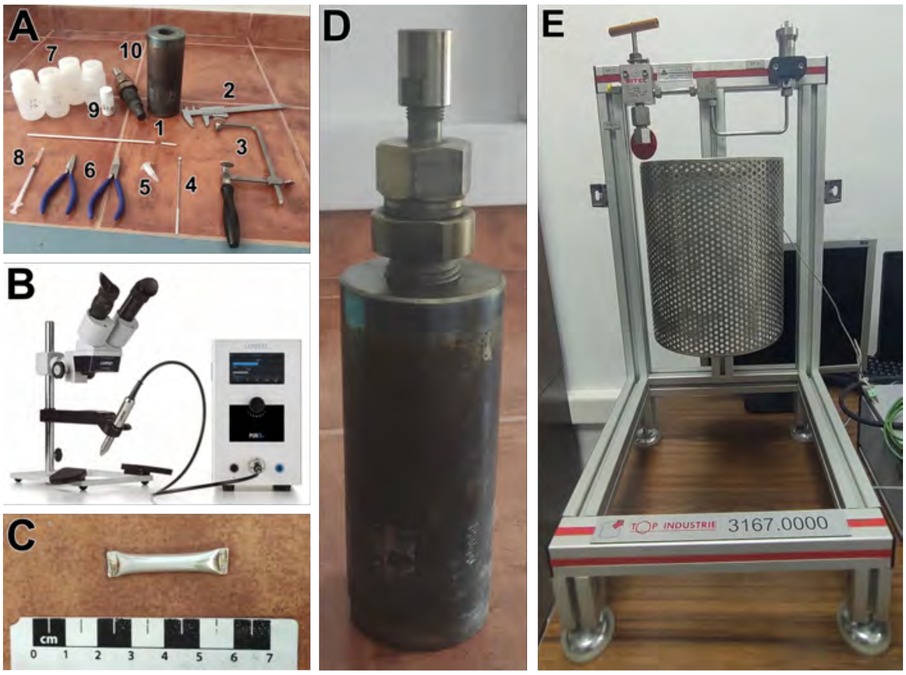

Fig. 24. Step by step procedure for the preparation of hydrothermal experiments in the autoclave. A) Material used for experiments. 1: Ag tube; 2: Calliper; 3: Saw; 4: Spatula for introducing the quartz into the capsule; 5: Zircon grains; 6) Pliers to close the capsule; 7) Ultrapure water, 2M $CaCl_2$, 2M NaCl and 1N NaF solutions; 8) Syringe to introduce the liquid into the capsule; 9) Quartz powder; 10) Autoclave vessel. B) Lampert PUK 5 arc welder. C) Welded capsule ready for the experiment. D) Autoclave vessel. E) Support for autoclave vessel with a furnace.

Once experiments are finished, the autoclave is slowly cooled to room temperature; the capsule is removed and opened with pliers from the top enough to collect most of the solution with a syringe. Then, the capsule is fully opened and carefully washed with 1 ml of ultrapure water to dissolve any salts that may have formed during quenching (as was done in the previous section). The solutions are mixed and analyzed by ICP-MS, whereas zircon grains are dried and handpicked.

Separated zircon grains for both the high-temperature and hydrothermal experiments are placed in a conductive carbon layer to study their morphology, first using a focus stacking technique under an optical microscope and then using a variable-pressure scanning electron microscope (ESEM). Afterwards, the studied zircon grains are recovered and mounted in epoxy resin to produce 35 mm diameter mounts to be analyzed with the SHRIMP. The large mounts are required to minimize the oxygen isotope fractionation during the extraction of secondary ions (Ickert et al., 2008).

Table 8. Hydrothermal experiments**.** Experimental conditions, starting materials and products of teflon bomb and autoclave experiments.

Teflon bomb hydrothermal experiments

Runs	**Experimental conditions**			**Sample**	**Zircon grains**	**Solution type**	**Solution (ml)**	**GREB-354 (g)**	**Recovered zircon grains (%)**	**Products**	**Fl/Zrn**
	Temperature (°C)	**Pressure (bar)**	**time (days)**								
G-1	170	10	43	-	-	H_2O	5	0,5	-	-	
Z-2	170	10	43	SAB51	200	H_2O	5	0,499	96	Zrn	0,98
Z-3	170	10	43	SAB50	200	H_2O	5	0,499	97	Zrn	0,98
G-2	170	10	43	-	-	NaCl	5	0,5	-	-	
Z-4	170	10	43	SAB51	200	NaCl	5	0,501	95	Zrn	0,98
Z-5	170	10	43	SAB50	200	NaCl	5	0,501	98	Zrn	0,98
G-3	170	10	43	-	-	$CaCl_2$	5	0,5	-	-	
Z-6	170	10	43	SAB51	200	$CaCl_2$	5	0,517	96	Zrn	0,98
Z-7	170	10	43	SAB50	200	$CaCl_2$	5	0,502	97	Zrn	0,98
G-4	170	10	43	-	-	NaF	5	0,5	-	-	
Z-8	170	10	43	SAB51	200	NaF	5	0,501	95	Zrn	0,98
Z-9	170	10	43	SAB50	200	NaF	5	0,502	95	Zrn	0,98

Autoclave hydrothermal experiments

Runs	**Experimental conditions**			**Sample**	**Zircon grains**	**Solution type**	**Solution (ml)**	**Cristobalite (g)**	**Recovered zircon grains (%)**	**Products**	**Fl/Zrn**
	Temperature (°C)	**Pressure (bar)**	**time (days)**								
HT-14	550	1328	8	SAB50	70	$CaCl_2$	0,31	-	71	Bdy + Ca-Cl silicate	0,99
HT-19	550	1884	3	SAB50	70	$CaCl_2$	0,44	-	81	Bdy + Ca-Cl silicate	0,99
HT-15	550	858	8	SAB50	70	$CaCl_2$	0,31	0,033	90	Zrn + Qtz + Ca-Cl silicate	0,97
HT-20	550	1993	8	SAB50	70	NaCl	0,424	-	33	Bdy	0,99
HT-22	550	1110	8	SAB50	70	NaCl	0,421	0,033	44	Zrn + Qtz	0,97
HT-17	550	1807	8	SAB50	70	NaF	0,42	-	0	Bdy + Qtz	0,99
HT-21	550	1926	8	SAB50	70	NaF	0,433	-	0	Bdy + Qtz	0,99
HT-24	550	1304	8	SAB50	70	NaF	0,448	0,033	31	Zrn + Na-Zr silicate	0,97
HT-31	550	1346	8	SAB50	100	H_2O	0,42	-	73	Bdy	0,99
HT-30	550	1346	8	SAB50	100	H_2O	0,37	0,033	94	Zrn + Qtz	0,97

Minerals abbreviation after Whitney & Evans (2010). Fl/Zrn: fluid/zircon ratio

II.1.3 Analytical methods

All analytical determinations have been done out in the Scientific Facilities Center of the University of Granada (CIC-UGR).

II.1.3.1 Morphology and surface studies

The zircon grains' morphology and composition surface composition have been studied with optical and variable-pressure scanning electron microscopy that does not require conductive coating. To this end, the hand-picked grains were arranged in a sticky carbon tape from which they can be easily recovered for further studies.

The focus stacking technique on an optical microscope consists of assembling different photograms of the same object varying the focus to enlarge the field depth. In this way, it is possible to obtain high-definition photographs of single zircon grains. We have used this technique to take pictures of the surface of zircon grains before polishing or coating. The equipment used was a Sony A7RII Evil camera with Mitutoyo M PLAN APO microscope objectives (Fig. 25).

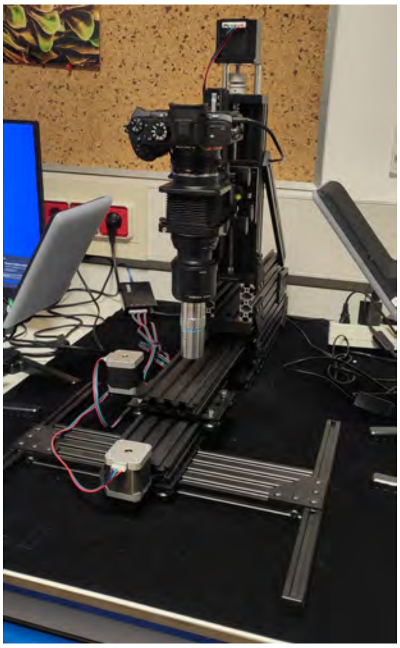

Fig. 25. Sony A7RII Evil camera with Mitutoyo M PLAN APO microscope objectives used for the focus stacking technique at the CIC-UGR.

The SEM surface studies was done with a variable pressure scanning electron microscope model Quanta 400 equipped with Secondary Electron (SE) and Back-Scattered Electron (BSE) detectors and X-ray energy dispersive system (EDS) operated at 20 kV with an analytical spot fixed at 5 µm (Fig. 26). This system permits high-magnification pictures and qualitative and semiquantitative analyses of the zircon grains' surface.

Fig. 26. Environmental Scanning Electron Microscope (ESEM) with SE, BSE detectors and EDS system at the CIC-UGR.

II.1.3.2 Internal morphology and included minerals studies

Zircon grains recovered from the carbon tape were cleaned and embedded in epoxy resin to produce 35 mm diameter mounts suitable for further studies. The mounts were polished until the zircon grains are cut more or less in half and then coated with 10 nm thick gold layer.

The internal structures of zircon grains and the nature of their inclusions were studied with a high-vacuum scanning electron microscope ZEISS EVO-10 (Fig. 27) equipped with secondary electron (SE), back-scattered electrons (BSE), cathodoluminescence (CL), and EDAX detectors.

Identifying mineral and glass inclusions hosted in zircon grains and determining their major-element composition were done using energy-dispersive X-ray (EDX) analysis with pure Ti as an internal standard. The conditions for microanalysis were 15 kV and I probe of 1.0-7.0 nA.

The internal morphology of zircon grains was studied using SE, BSE and CL imaging. The conditions for SE were 10 kV and 300 pA. The conditions for BSE were 10 kV and 670 pA. The conditions for CL were 10kV and 1 nA.

Fig. 27. Scanning Electron Microscope (SEM) with BSE, SE, CL and EDAX detectors at the CIC-UGR.

II.1.3.3 Chemical analyses

Electron microprobe analyses (EMP)

Besides SEM-EDAX, we used an electron microprobe CAMECA SX-100 (Fig. 28) for analyzing W, Fe, Ca, and Mg in the zircon grains that underwent high-temperature experiments because in these, we found tungsten minerals which were not present in the untreated zircon grains.

The electron microprobe was used to determine W instead of the laser ablation system because the abundant erbium oxides ($^{16}O^{166}Er^+$, $^{16}O^{167}Er^+$, $^{16}O^{168}Er^+$, and $^{16}O^{170}Er^+$) generated during the ablation of zircon cause isobaric interferences on the four tungsten isotopes, ^{182}W, ^{183}W, ^{184}W, and ^{186}W.

The conditions for microprobe analyses were 25 kV and 300 nA. W was analyzed using metallic W as a standard and measuring the W Lα resolved with a LiF crystal with a detection limit of 74 ppm. For analyzing Fe, we used a Fe_2O_3 standard, measuring Fe Kα resolved with a LiF crystal with a detection limit of 25 ppm. We used a diopside standard to analyze Ca Kα resolved with a PET crystal with a detection limit of 13 ppm. For analyzing Mg, we used a periclase standard, measuring Mg Kα resolved with a TAP crystal with a detection limit of 9 ppm.

Fig. 28. Electron Microprobe (EMP) with five spectrometers at the CIC-UGR.

Laser-ablation inductively coupled plasma analyses (LA-ICP-MS)

Trace element analyses in zircon grains of high-temperature experiments were done using a Perking Elmer NexION 350X ICP-MS coupled to a New Wave Research NR 213 laser ablation system (Fig. 29). The analyses were performed on the same mounts used for scanning electron microscope and electron microprobe using the NIST-610 glass as an external standard, which was measured every six analyses. Spots to be analyzed were pre-ablated for 15 seconds with a laser fluency of 2.5 Jcm^{-2}, and then ablated for 60 seconds with a laser fluency of 7.5 Jcm^{-2}. Before each measurement, a blank, measured under the same conditions but with zero laser energy. LA-ICPMS software (available from F. Bea upon reasonable request) written in the STATA™ programming language is used for data reduction.

Each analysis consists of 60 mass scans. The counts obtained for the selected elements P, Ti, La, Y, Hf, Pb, U, and Th for each mass scan are projected against the scan number to identify peaks that may indicate small inclusions within the ablated zircon crater. The entire analysis is eliminated if these peaks are observed. This was the case for more than 100 analyses of sample REG20, which shows a huge number of inclusions and cracks that do not allow for clean zircon analyses. Reducing the beam diameter does not help as the laser pit is always 60 microns or more deep.

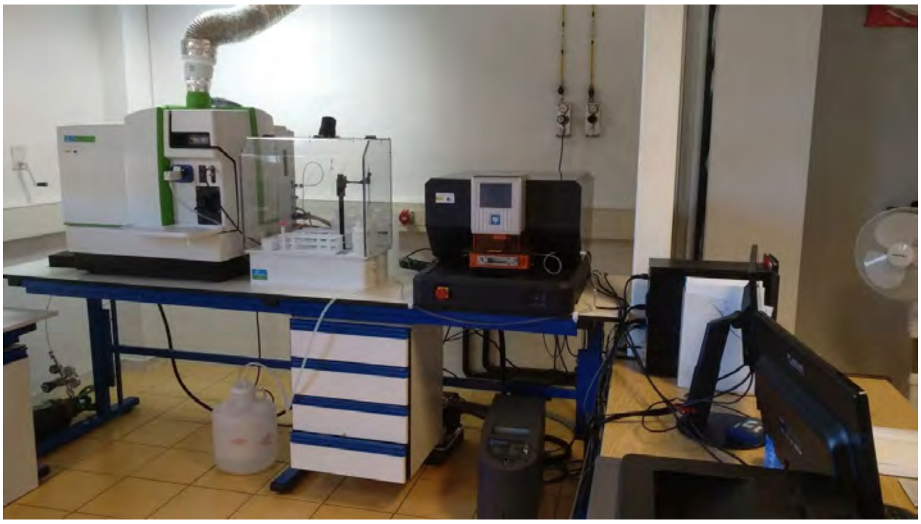

Fig. 29. Laser Ablation Inductively Coupled Plasma-Mass Spectrometry (LA-ICP-MS) with New Wave Research NR 213 laser ablation system at the CIC-UGR.

II.1.3.4 Isotope analyses: Sensitive High-Resolution Ion Microprobe (SHRIMP)

Geochron analysis:

U-Th-Pb analyses in zircon grains of high-temperature experiments were done using the IBERSIMS SHRIMP IIe/mc ion microprobe (Fig. 30). The SHRIMP U-Th-Pb analytical method followed the described by Williams & Claesson (1987). To produce a spot diameter of approximately 18 microns on the zircon surface, a Kohler aperture of 120 microns is set in the SHRIMP primary ion optics. Uranium concentration is calibrated using the reference zircon SL13 with a uranium concentration of 238 ppm. The TEMORA-II reference zircon (417 Ma; Black et al., 2004) is used to calibrate the U/Pb ratios and is measured every four analyses. If necessary, the common Pb is corrected from the ^{204}Pb/^{206}Pb measurements, using the model of terrestrial Pb evolution of Cumming & Richards (1975). If necessary, the U-Pb ages are also corrected for excess ^{230}Th. At the standard age the point-to-point errors (95 % C.I.) are ± 0.23% for ^{206}Pb/^{238}U and ± 0.46% for ^{207}Pb/^{206}Pb. The SHRIMPTOOLS software (downloadable from www.ugr.es/~fbea) is used for data reduction using the STATA™ programming language. Errors on averages are reported at 95 % confidence level (≈2 s). Errors for individual analyses are reported at one sigma.

Oxygen isotopes analysis:

Once analyzed for U-Th-Pb, the mounts were cleaned, re-polished to eliminate the pits and coated with a 30 nm thick gold layer for oxygen isotope analyses. The analyses were done in the same position as the U-Th-Pb-spots. Kohler aperture of 120 microns is set in the SHRIMP primary ion optics. The Cs gun is set to yield a ~8 nA Cs^+ beam. The e-gun to neutralize Cs ions on non-conductive materials is set to an intensity of ~1 µA. Before starting the measurements, the points to be analyzed are burned for 3 minutes, during which time the secondary beam and the direction of the electron gun were fully optimized to maximize the ^{16}O signal. The data collection time is 200 seconds per spot, as each scan lasts 10 seconds and 2 sets of 10 scans are made.

The electron-induced secondary ion emission (EISIE) background was recorded for 10 s before and after each set and subtracted from the ^{18}O and ^{16}O counts. TEMORA-II zircon is used again as a standard with measurements every four analyses and 91500 zircon is used as cross-check with measurements every 20 analyses.The reproducibility of the standards is $\partial^{18}O = 8.17 \pm 0.34$ (2s) for the TEMORA and $\partial^{18}O = 9.98 \pm$

0.26 (2s) for the 91500 zircon. Data reduction was made with the POXY program developed by P. Lanc and P. Holden at the Australian National University.

Fig. 30. Sensitive High-Resolution Ion Microprobe (SHRIMP) at the CIC-UGR.

II.1.3.5 Analysis of solutions

Inductively Coupled Plasma Optical Emission Spectroscopy (ICP-OES)

The major elements of the solutions were analyzed by Inductively coupled plasma emission spectrometer (ICP-OES) PERKIN-ELMER OPTIMA 8300 with automatic sampler PERKIN-ELMER S10 (Fig. 31) using Yttrium (40 ppm) as internal standard. The instrumental conditions were: radio-frequency power of 1400 W, plasma gas flow rate for Argon was 9 l/min, plasma gas flow rate for air was 0.8 l/min, plasma gas flow rate for Nitrogen was 0.65 l/min. The standards used are mono-elemental dissolutions made by PERKIN-ELMER and the emission wavelength for the quantification of each element was 396.153 nm (Al), 317.933 nm (Ca), 238.204 nm (Fe), 766.490 nm (K), 285.213 nm (Mg), 251.611 nm (Si) and 589.592 nm (Na).

Fig. 31. Inductively Coupled Plasma Optical Emission Spectroscopy (ICP-OES) with automatic sampler PERKIN-ELMER S10, at the CIC-UGR.

Solution-Nebulization Inductively Coupled Plasma Mass Spectroscopy (SN-ICP-MS)

Trace elements and REE analyses (Fig. 32) in dissolutions resulting from hydrothermal experiments were analyzed using a quadrupolar mass spectrometer NexION 300D (Perkin Elmer) equipped with a nebulization system for sample introduction and a cell reaction to eliminate complex ions interferences. The hydrous solutions resulting from the experiments were carried to 10 ml volume using 4% HNO_3. Additionally, the leachate samples from the experiments with sodium fluoride were evaporated to dry to remove the excess fluorine and subsequently dissolved in 100 ml of 4 % HNO_3. The resulting dissolutions were further diluted ten times with a dissolution containing 5 ppm Rh, which was used as an internal standard.

The external standards used were solutions of the international geostandards UBN, DRN, WSE, PMN, and GA with concentrations made as close as possible to the samples to be analyzed (Fig. 32).

The measurements were performed in standard mode using Argon for plasma formation and sample nebulization. The instrumental conditions were: radiofrequency power of 1600 W, plasma gas flow rate of 18.00 l/min, an auxiliary gas flow rate of 1.20 l/min, nebulization gas flow rate of 1.01 l/min, a collision-cell gas flow rate of 2.6/2.5/6.0 l/min, Input voltage in KED mode of -3.00 V, Output voltage in KED mode of -32.00 V, concentric nebulizer, cyclonic spray in the nebulization chamber, Peak jump as scan mode, number of scans per reading of 50, number of readings of 2, number of replicates of 3, a dwell time of 25 s and a retarding potential quadrupole of 0.25.

The precision obtained is between ±2 and ±5 % for analyte concentrations of 50 ppm and 5 ppm, respectively.

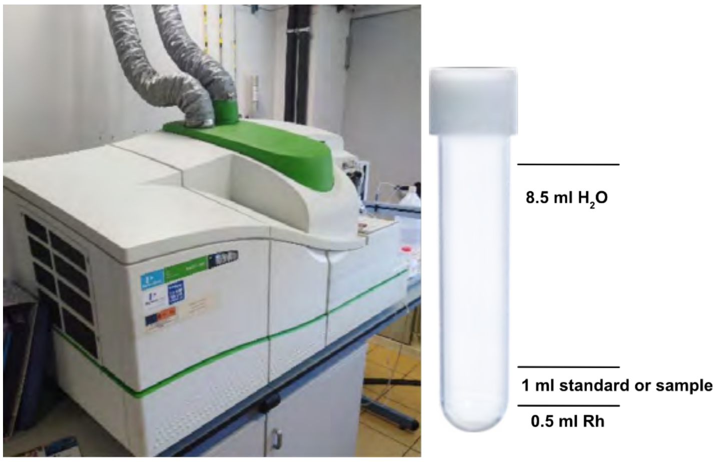

Fig. 32. Mass spectrometer with plasma torch ionization source and cuadrupole ion filter NexION 300D and example of sample or standard preparation, at the CIC-UGR.

II.2 Results of the high temperature experiments: annealing

Annealing experiments, described in **section II.1.2.1**, were done on zircon grains from samples SAB50, SAB51 and REG20; see **section II.1.1** for details.

II.2.1 Experimental products

The main textural characteristics and mineral and glass inclusions for zircon grains after heat treatment are summarized in Table 9. Trace elements of the host zircon grains are reported in Tables 10, 11, and 12, and the major-element compositions of glasses and selected mineral phases are listed in Tables 13, 14, 15 and 3, respectively.

Annealed zircon grains present extensive melting and recrystallization in the darkest CL zones, especially if they are metamict. This effect causes some zircon grains to exhibit an onion-like structure with alternating unaltered and highly recrystallized zones that may even be partially melted (Fig. 33).

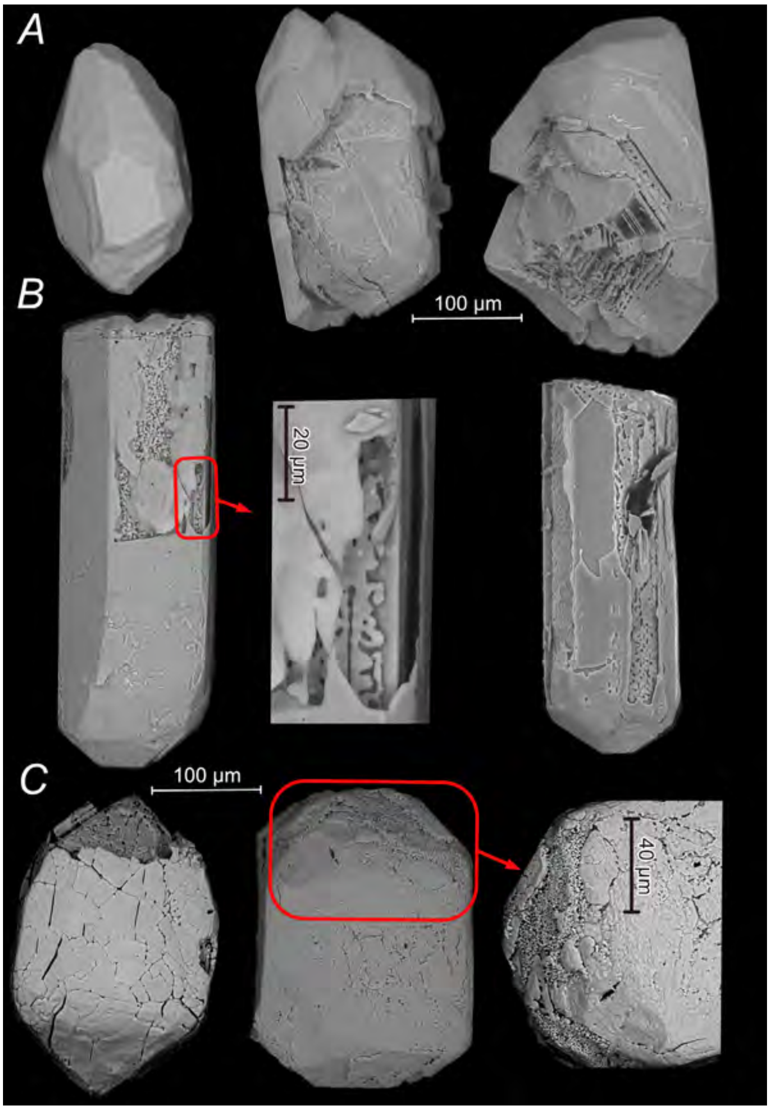

Fig. 33. BSE images of annealed zircons from orthogneiss SAB50 (A), tonalite SAB51 (B), and syenite REG20 (C). Annealed zircons have acquired an onion-like structure with alternating little altered and heavily recrystallized, even partially melted zones.

The annealed zircon grains from sample SAB50 orthogneiss host inclusions of glass, baddeleyite, fluorite, fluor-apatite, monazite, scheelite and srilankite, of which the last two we never found in the untreated grains (Table 9; Figs. 34 and S1 from Supplementary Material). Glass inclusions are the most abundant; they appear preferentially placed at the core-rim interface either as continuous and relatively voluminous elongated zones that indicate considerable melt migration to these interfaces or, as micropore alignments (Figs. 34A and S1A). Glass inclusions also appear as isolated 10-20 µm tear drop-shaped globules or replacing dark cathodoluminescent zones. Some of them are partially filled with fluorite, euhedral baddeleyite or both (Figs. 34A, B, D and S1B). The compositions of the glasses (see next **section II.2.1.1**) range from high-K or Ca-rich silicic glasses in the teardrop-shaped globules to low-K rhyolitic, mostly placed at the core-rim interfaces.

A remarkable fact about this sample (SAB50) and the sample SAB51 is the presence of Ca-Fe-Mg tungstates inclusions (Figs. 34A, 35C, E, and S1C), which are inclusions that have never been found in untreated zircon grains, despite considerable search with SEM.

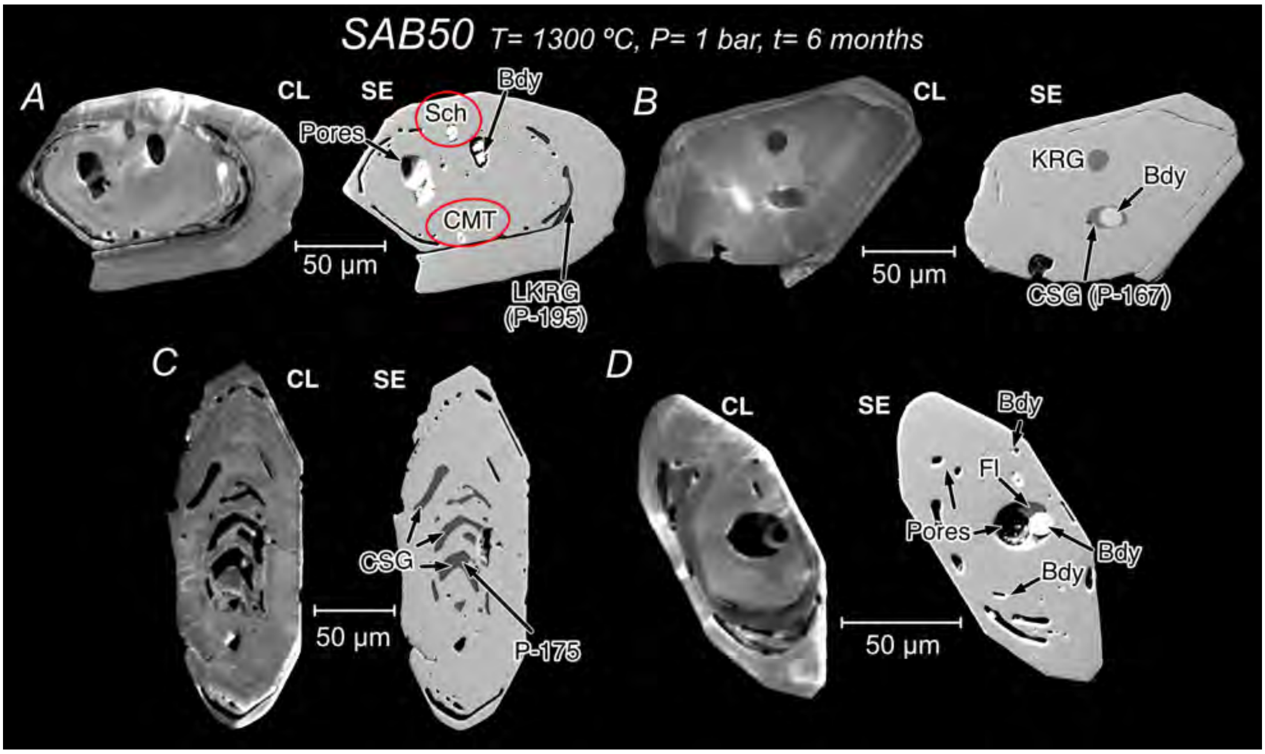

Fig. 34. CL and SE images of annealed zircon grains from orthogneiss SAB50. (A) Zircon hosting monomineralic inclusions of Ca−Mg tungstates, scheelite (red ovals), and baddeleyite and low-K rhyolite glass inclusions lying along the core−rim interface. (B) Zircon with oscillatory zoning and a shell rimming a core that hosts a tear drop-shaped potassic rhyolite glass inclusion and a multi-phase inclusion of euhedral baddeleyite + calcic silicate glass (see analysis in Table 13). (C) Zircon with abundant inclusions of calcic silicate glass (see analysis in Table 13) parallel to the compositional zoning of the core. (D) Zircon with oscillatory zoning and a shell rimming a core that hosts a tear drop-shaped multi-phase inclusion of fluorite + euhedral baddeleyite with a micropore. Also note the occurrence of baddeleyite inclusions in elongated micropores with rounded tips opened mostly along the core−rim interface. Mineral abbreviations after Whitney & Evans (2010). Other abbreviations: CSG = calcic silicate glass; FSG = fluorosilicate glass; KRG = potassic rhyolite glass; LKRG = low-K rhyolite glass; SH = SHRIMP analysis spot; and CMT = Ca−Mg tungstate.

The annealed zircon grains from sample SAB51 tonalite host inclusions of glass, baddeleyite, fluorite, scheelite and Ca-Mg tungstates (Fig. 35; Table 9). The slightly metamict dark cathodoluminescent bands of untreated zircon grains become highly luminescent because of zircon recrystallization (Figs. 35 and S2 from Supplementary Material), forming minute zircon grains and open spaces that either are filled with low-K rhyolitic glass (Figs. 35B, F and S2D-G) or remain empty (Figs. 35A and S2C). The glass can form massive patches, especially if there are polymineralic inclusions (Fig. 35B, F) or narrow and elongated veins (Fig. S2E, G). The glass is surrounded by zircon in blob-like shapes that suggest contact between two highly viscous fluids (Figs. 35F and S2D-G), melt and viscous zircon, and proves that the glass was derived from the melt that was generated during the heat treatment. Very tiny baddeleyite grains (less than 1 μm long) are included in the zircon blobs (Fig. 35F).

Besides, there are 20−30 μm rounded to elongated teardrop-shaped inclusions of fluoro-silicate glass and potassic rhyolite glass, locally accompanied by gas bubbles, and of fluoro-silicate glass + euhedral baddeleyite + fluorite (Fig. 35C, D, G, H).

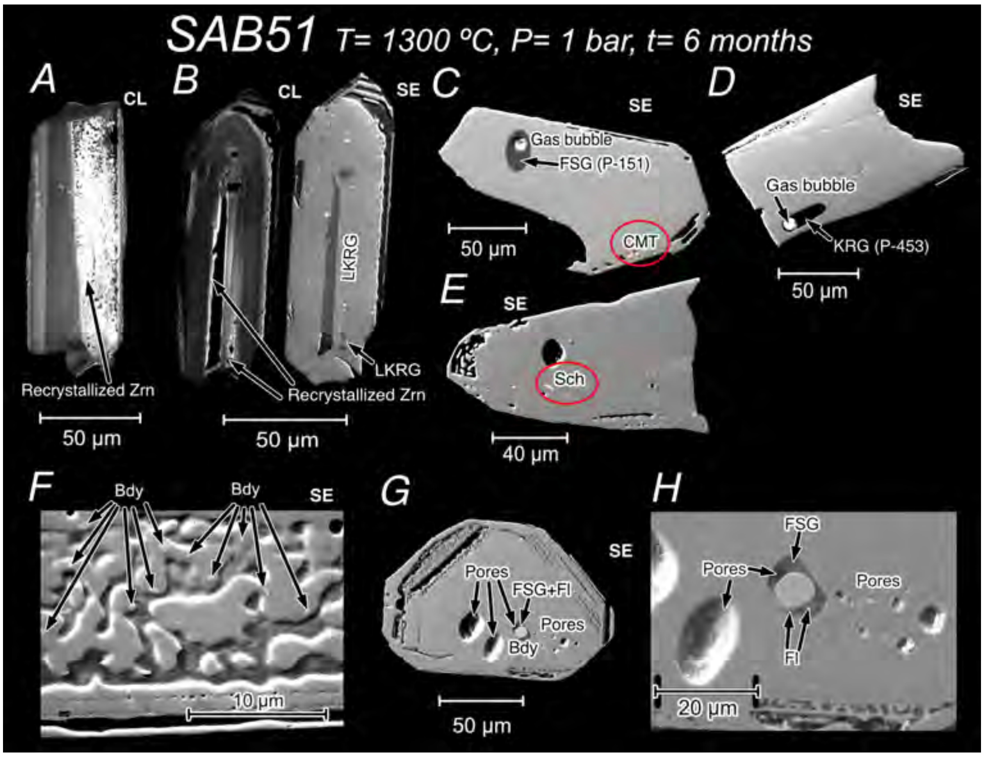

Fig. 35. CL and SE images of annealed zircons from tonalite SAB51. (A, B) Zircons showing that the bands parallel to prismatic and pyramidal faces become luminescent after heat treatment suggesting recrystallization. Note in (B) a large inclusion of low-K rhyolitic glass filling the micropores of the bands. (C) Zircon hosting a tear drop-shaped fluorosilicate glass inclusion (see analysis in Table 14) with a gas bubble. Note the presence of very tiny inclusions of bright Ca−Mg tungstates (red oval). (D) Zircon hosting an elongated tear drop-shaped potassic rhyolite glass inclusion (see analysis in Table 14) with a gas bubble. (E) Zircon hosting a scheelite inclusion (red oval). (F) Zircon with very tiny baddeleyite grains included in zircon in contact with an empty space which possibly contained glass. (G) Zircon hosting micropores and a multi-phase inclusion of fluorosilicate glass + fluorite + euhedral baddeleyite with a micropore. (H) Detail of the multi-phase inclusion shown in G. Mineral abbreviations after Whitney & Evans (2010). Other abbreviations: CMT = Ca−Mg tungstate; FSG = fluorosilicate glass; KRG = potassic rhyolite glass; and LKRG = low-K rhyolite glass.

The annealed zircon grains from sample REG20 syenite show significant changes compared to untreated zircon grains. Many of them fractured during recovery due to the increase in previous fractures. The porous metamict zones from the core, the bends parallel to oscillatory zoning, and the microcracks became luminescent. Mineral inclusions consist of glass and relatively coarse (up to ten μm long) anhedral baddeleyite (Fig. 36A-C; Table 9). The glass is calcic- and silica-rich with abundant gas micro-bubbles. The Th-REE accessory phases frequent in untreated zircon disappear after heat treatment. As suggested by the significant Th concentrations shown by the glasses (Table 15), these phases likely were dissolved into the calcic-silicate glass.

It is worth mentioning that the treated REG20 grains show no, or very little, common-lead, as seen later in section **II.2.1.4**: Common-Pb leaching.

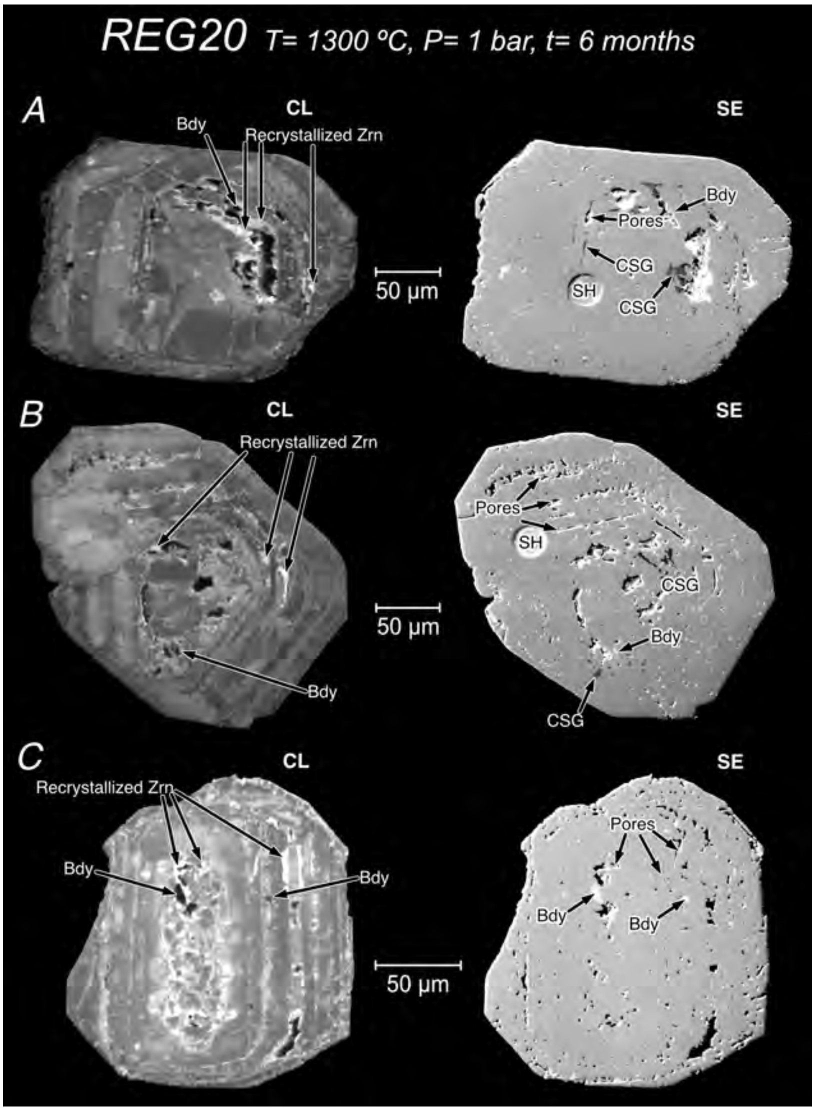

Fig. 36. CL and SE images of annealed zircon grains from syenite REG20. (A−C) Zircons showing that the porous metamict domains become luminescent due to recrystallization and are filled by calcic silicate glass with abundant gas micro-bubbles. Also note the occurrence of anhedral baddeleyite in recrystallized domains and the absence of Th-REE accessory phases that were most probably dissolved into the calcic silicate glass (see text for discussion); microcracks also turn luminescent after heat treatment. Mineral abbreviations after Whitney & Evans (2010). Other abbreviations: CSG = calcic silicate glass and SH = SHRIMP analysis spot.

Table 9. Summary of mineral assemblages and textures in annealed zircon grains

Run conditions: 1300 °C and six months				
Run	**Starting material**	**Grain number**	**Mineral and glass inclusions**	**Main textural features**
E2	SAB50	260	LKRG (10)	(1) Preferentially placed at the core-rim interface as continuous elongated zones or as micropore alignments; (2) replacing dark cathodoluminescent zones of the cores or as isolated tear-drop shapes bubbles, some of them partially filled with euhedral baddeleyite, fluorite or both
			FSG^1 (2)	
			FSG^2 (5)	
			KRG (9)	
			CSG (3)	
			Bdy (31)	Euhedral shapes accompanied glass inclusions
			Bdy + Fl (1)	
			F-Ap (13)	Anhedral shapes
			Mnz (3)	
			Fl (2)	
			Sch and CMT (26)	
			Sri (1)	
E1	SAB51	268	LKRG (9)	Massive or filling aligned micropores patches
			FSG^1 (4)	Elongated drop-like glass inclusions locally accompanied by gas bubbles or by euhedral baddeleyite + fluorite
			KRG (8)	
			Bdy (30)	Euhedral shapes accompanied glass inclusions
			Bdy + Fl (2)	
			Sch and CMT (24)	Anhedral shapes
E3	REG20	92	CSG (27)	Anhedral shapes with abundant gas micro-bubbles
			Bdy (20)	Anhedral shapes

Mineral abbreviations after Whitney & Evans (2010). Other abbreviations: CSG= Calcic silicate glass; FSG^1 = high-silica fluorosilicate glass; FSG^2 = low-silica fluorosilicate glass; KRG= potassic rhyolite glass; LKRG = low-potassium rhyolite glass; CMT= Ca-Mg tungstate; Sri = srilankite. Number of grains with the reported inclusions indicated in parentheses.

Table 10. LA-ICP-MS analyses of trace elements in annealed SAB50 zircon grains (data in ppm).

Sample	**SAB50, Orthogneiss**												
Type	**Annealed**												
Point	**31**	**32**	**33**	**34**	**36**	**46**	**21**	**22**	**28**	**75**	**76**	**82**	**84**
Texture[a]	**C**	**C**	**C**	**C**	**C**	**C**	**C**	**C**	**C**	**R**	**R**	**R**	**R**
P	1197	297	202	1409	847	299	853	387	1618	1593	1296	1161	1666
Ti	19.8	8.72	14.5	36.5	66.9	48.5	132	52.1	45.4	25.7	12.2	14.1	38
Y	2833	971	867	3894	2290	2136	2155	1031	3076	2138	3261	2963	3810
La	0.03	0.17	0.36	0.04	2.34	0.32	1	0.16	0.07	0.16	0.04	0.27	1.26
Ce	0.58	19.6	25.8	1.59	35.6	14.9	27.4	11.5	8.58	3.53	0.36	1.58	3.93
Pr	0.03	0.46	0.12	0.03	0.70	0.63	1.45	0.21	0.46	0.32	0.26	0.27	0.84
Nd	0.76	2.95	2.56	2.81	1.00	6.12	5.66	2.98	3.62	3.7	4.63	5.37	8.01
Sm	1.96	4.80	5.52	7.15	9.05	14.9	6.08	2.93	2.15	3.97	3.59	5.96	7.76
Eu	0.25	0.55	2.16	0.46	1.66	0.25	1.25	0.25	0.62	0.77	0.62	1.18	1.99
Gd	26.5	31.6	18.0	29.3	34.8	75.0	42.1	29.7	22.3	16.8	36.9	39	29.7
Tb	15.8	5.46	5.83	18.2	16.5	21.6	16.5	10.5	12.9	12.4	17.2	17.6	17.2
Dy	216	92.8	71.2	325	204	238	186	99.7	263	183	268	219	230
Ho	97.4	32.7	25.9	130	79.3	88.2	71.1	34.9	93.9	68.4	112	97.9	97.3
Er	474	156	137	636	374	375	373	178	543	407	548	534	667
Tm	113	33.7	32.2	136	90.2	68.3	81.6	33.7	121	92.2	121	120	134
Yb	981	262	231	1197	754	505	706	288	1153	818	1052	1149	1253
Lu	190	60.9	47.4	241	160	106	143	61.9	211	167	213	214	272
Hf	10348	8345	8537	9373	8387	7684	7938	7306	9760	10046	9832	9966	9021
Pb	20.8	13.3	18.0	13.1	14.3	11.8	21.7	13.9	22.3	19	18	14.9	18.6
Th	35.1	105	101	25.7	71.2	81.0	139	43.9	25.5	20.7	30.4	20.7	19.4
U	232	121	136	197	109	106	163	102	243	193	221	194	210
Sc	na	na	na	na	na	na	na	na	na	na	na	na	na
Nb	na	na	na	na	na	na	na	na	na	na	na	na	na
Ta	na	na	na	na	na	na	na	na	na	na	na	na	na

[a] R = rim; C = core; na = not analyzed.

Table 11. LA-ICP-MS analyses of trace elements in annealed SAB51 zircon grains (data in ppm).

Sample	**SAB51, Tonalite**												
Type	**Annealed**												
Point	**63**	**64**	**66**	**67**	**51**	**52**	**48**	**53**	**54**	**55**	**4**	**10**	**15**
Texture[a]	**DB**	**DB**	**DB**	**DB**	**DB**	**DB**	**DB**	**DB**	**DB**	**DB**	**LB**	**LB**	**LB**
P	3194	132	1380	156	572	1084	223	346	325	241	203	310	130
Ti	30.4	17.9	46.1	28.8	41.0	100	6.94	34.7	11.7	41	29.4	21.5	32.2
Y	1899	1017	1734	1335	846	1205	1064	906	1307	978	1793	718	524
La	2.44	0.91	1.8	0.59	1.33	1.88	0.44	1.61	0.83	1.16	0.4	0.28	0.08
Ce	11.1	5.17	13.2	5.99	7.66	14.4	7.31	6.38	5.71	3.47	6.82	3.9	4.37
Pr	2.20	0.62	1.24	0.65	1.49	1.23	0.58	1.02	0.93	0.13	0.4	0.2	0.58
Nd	10.9	10.6	20.1	6.99	5.94	6.96	3.89	6.01	18.2	4.42	13.2	3.81	6.24
Sm	12.0	2.17	22.7	12.6	5.23	7.88	16.7	6.38	16.1	9.18	27.9	11.8	3.55
Eu	2.51	1.14	3.53	1.49	2.05	2.90	1	0.42	3.83	0.59	3.34	2.67	0.62
Gd	72.5	42.8	51.5	62.4	34.7	26.0	42.7	42	60.6	40.9	78.5	34.9	7.79
Tb	16.8	12.4	18.2	15.9	6.86	9.70	13.8	11.5	18	12.1	17.6	12.9	6.23
Dy	191	111	174	171	54.66	115	108	101	139	107	231	79	46.2
Ho	69.3	36.9	63.5	49.2	33.9	40.3	39.9	29.8	45	33.8	61.8	29.4	20.9
Er	316	155	249	176	161	196	161	134	204	139	246	113	80.5
Tm	64.6	32.2	49.2	38.7	29.0	42.0	29.9	23.9	39.3	28.7	52.6	18.1	13.2
Yb	538	232	429	301	297	348	243	173	305	236	384	158	134
Lu	98.8	43.6	83.2	54.4	58.8	77.5	54.8	46.9	45.4	49.5	72.1	24.7	27.4
Hf	9032	8101	9448	8289	9349	8440	9913	7809	7142	8807	8262	7554	8702
Pb	23.3	15.1	23.5	24.4	10.3	24.3	19.4	11.4	14.5	21.6	33.5	8.4	10.8
Th	379	201	382	299	96	213	227	186	244	202	430	121	101
U	519	291	509	383	278	450	334	235	306	340	519	194	191
Sc	na	na	na	na	na	na	na	na	na	na	na	na	na
Nb	na	na	na	na	na	na	na	na	na	na	na	na	na
Ta	na	na	na	na	na	na	na	na	na	na	na	na	na

[a] LB = light band; DB = dark band; R = rim; C = core; bdl = below detection limit; na = not analyzed.

Table 12. EMP analyses of Mg, Ca, Fe and W in annealed zircon grains (data in ppm)

Sample	**SAB50, orthogneiss**											**SAB51, tonalite**										
Type	**Annealed**											**Annealed**										
Point	**1**	**2**	**3**	**4**	**5**	**6**	**7**	**8**	**12**	**13**	**14**	**1**	**2**	**3**	**4**	**5**	**6**	**7**	**8**	**12**	**13**	**14**
Texture[a]	R	C	R	C	R	C	R	C	C	C	R	H DB	RB	H DB	H LB	H DB	H LB	RB	H LB	H DB	H LB	H LB
Mg	31	36	33	34	38	41	41	83	214	39	37	92	95	62	55	148	23	442	40	41	36	37
Ca	-	-	-	18	-	-	-	62	316	-	-	138	184	37	36	349	-	2526	-	-	-	-
Fe	-	-	-	-	-	-	-	-	-	-	-	-	-	-	-	-	-	39	-	-	-	-
W	590	195	601	124	369	200	200	188	220	267	476	392	326	271	145	347	255	554	138	218	193	194

[a] H = host; LB = light band; DB = dark band; MB = metamict band; RB= recrystallized band; R = rim; C = core.

II.2.1.1 Composition of glass inclusions

Four compositional types of glasses can be distinguished in zircon grains after heat treatment (Fig. 37; Tables 13, 14 and 15): (1) fluoro-silicate, (2) low-K rhyolite, (3) potassic rhyolite, and (4) calcic- andesite to dacite. The first three glasses appear in SAB50 and SAB51. The last glass occurs in SAB50 and REG20.

Fluor-silicate glasses can be divided into two types, one with high-silica rhyolite composition (silica between 75-78 wt %) having 14-15 wt % Al_2O_3, < 1.6 wt % CaO, 1.2-2.2 wt % Na_2O, 3.4-4.4 wt % K_2O, and fluorine ranging from 1.2-1.7 wt % in sample SAB50 to ca. 5 wt % in sample SAB51 and the other which only appears in SAB50, with low silica (24-33 wt %), variable Al_2O_3 (0-15 wt %) and MgO (3.6-14 wt %), high CaO(31-43 wt %) and fluorine (17-32 wt %).

The potassic rhyolite glasses (> 4.1 wt % K_2O) show a composition similar to that of the fluorine-bearing high-silica rhyolite, with 75-78 wt % SiO_2, 12-16 wt % Al_2O_3, 0.53-3.1 wt % CaO, and 0.99-2.5 wt % Na_2O.

The low-K rhyolite glasses (<1.9 wt % K_2O) have more variable silica (range: 75−87 wt %), similar alumina (range: 11−16 wt %), <2.1 wt % CaO, and 0.28−1.9 wt % Na_2O.

The calcic- andesite to dacite glasses (up to 23 wt % CaO) contain 54−68 wt % SiO_2, variable alumina (range: 6−25 wt %), low Na_2O (<1.2 wt %), and negligible K_2O. Of these glasses, those found in the zircon grains of REG20 show variable enrichment in ThO_2 (range: 3.0-11 wt %) and contain up to 2.3 wt % Ce_2O_3, 1.2 wt % Nd_2O_3, and 3.5 wt % Y_2O_3.

It can be seen in Fig. 37 how the composition of the potassic rhyolite glasses in zircon grains SAB50 and SAB51 are slightly more enriched in silica and K_2O and depleted in alumina than their corresponding host rocks. This effect is consistent with the interest that the glass inclusions represent evolved residual melts entrapped in zircon during its growth. However, the composition of the other glass types can hardly be related to the host-rock composition by simple magma fractionation processes. Therefore, they represent the products of either mineral inclusion melting or the interaction of zircon with the silica sealant.

Table 13. Selected EDX analyses of glass inclusions (weight per cent)

Sample	**SAB50, Orthogneiss**														
Grain	**1**	**2**	**3**	**4**	**5**	**6**	**7**		**8**		**9**	**10**	**11**		**12**
Type[a]	**FSG**[1]	**FSG**[2]	**FSG**[2]	**KRG**	**KRG**	**KRG**	**LKRG**		**KRG**	**CSG**	**LKRG**	**LKRG**	**LKRG**		**CSG**
Point	**15**	**127**	**131**	**185**	**191**	**275**	**212**	**215**	**166**	**167**	**5**	**189**	**195**	**193**	**175**
SiO_2	76.7	33.4	24.1	77.1	78.1	76.8	82.5	83.2	80.7	57.4	84.4	74.5	82	82	63.7
TiO_2	-	1.06	-	-	0.33	-	-	-	-	-	-	0.28	0.5	-	-
Al_2O_3	15.4	14.6	-	13.2	13.5	14.2	14.5	14.7	11.6	24.4	12.3	15.8	13	13	24.7
FeO	-	-	-	1.24	-	0.38	-	0.36	-	-	-	-	-	-	-
MgO	0.54	3.89	14.4	-	-	0.72	-	-	-	-	0.35	4.93	-	-	2.09
CaO	0.67	30.9	43.3	0.63	0.53	0.77	0.31	0.24	0.66	17.2	1.72	2.08	1.1	1.2	8.37
Na_2O	1.36	-	-	2.48	1.69	2.45	1.48	0.28	0.99	1.08	0.95	0.73	1.9	1.7	1.23
K_2O	3.46	-	-	5.32	5.79	4.67	1.24	1.18	6.07	-	0.23	0.25	1.9	1.9	-
P_2O_5	-	1.44	-	-	-	-	-	-	-	-	-	-	-	-	-
Y_2O_3	-	2.25	-	-	-	-	-	-	-	-	-	-	-	-	-
Ce_2O_3	-	0.95	-	-	-	-	-	-	-	-	-	-	-	-	-
Nd_2O_3	-	0.73	-	-	-	-	-	-	-	-	-	-	-	-	-
F	1.69	18.7	31.7	-	-	-	-	-	-	-	-	-	-	-	-
Cl	1.15	-	-	-	-	-	-	-	-	-	-	-	-	-	-
Total	101	108	113	100	100	100	100	100	100	100	100	100	100	100	100
-O≡F	0.71	7.89	13.3												
-O≡Cl	0.26														

[a] CSG: Calcic silicate glass; FSG[1] = high-silica fluorosilicate glass; FSG[2] = low-silica fluorosilicate glass; KRG= potassic rhyolite glass; LKRG = low-potassium rhyolite glass.

Table 14. Selected EDX analyses of glass inclusions in SAB51 zircon grains (weight per cent)

Sample	SAB51, Tonalite									
Grain	**1**		**2**	**3**		**4**	**5**	**6**	**7**	**8**
Type[a]	**FSG^1**	**KRG**	**KRG**	**KRG**		**FSG^1**	**LKRG**	**LKRG**	**LKRG**	**LKRG**
Point	**435**	**440**	**448**	**456**	**453**	**151**	**120**	**55**	**148**	**49**
SiO_2	76,8	77	73,9	76	76	75	79,1	83,1	80,6	87,1
TiO_2	-	-	-	0,23	-	-	-	-	-	-
Al_2O_3	14,2	14	16,3	14,9	15	13,9	16,7	13,6	15,5	10,8
FeO	-	-	-	-	-	-	-	-	-	-
MgO	-	-	-	-	-	-	0,69	0,41	0,57	-
CaO	2,96	2,88	2,2	2,05	2,1	1,57	1,91	1,41	1,7	0,94
Na_2O	1,94	1,89	1,56	1,86	1,9	2,25	1,41	1,29	1,47	0,95
K_2O	4,12	4,24	5,44	4,95	4,9	4,37	0,18	0,19	0,19	0,16
P_2O_5	-	-	-	-	-	-	-	-	-	-
Y_2O_3	-	-	-	-	-	-	-	-	-	-
Ce_2O_3	-	-	-	-	-	-	-	-	-	-
ThO_2	-	-	-	-	-	-	-	-	-	-
F	-	-	-	-	-	5,02	-	-	-	-
Cl	-	-	0,62	-	-	-	-	-	-	-
Total	100	100	100	100	100	102	100	100	100	100
-O≡F						2,12				

[a] FSG^1 = high-silica fluorosilicate glass; KRG= potassic rhyolite glass; LKRG = low-potassium rhyolite glass.

Table 15. Selected EDX analyses of glass inclusions (weight per cent)

Sample	REG20, Syenite				
Grain	**1**	**2**	**3**		
Type[a]	**CSG**	**CSG**	**CSG**		
Point	**179**	**293**	**184**	**187**	**186**
SiO_2	65.5	54.1	64.6	66.9	67.8
TiO_2	0.38	-	0.78	0.78	0.72
Al_2O_3	7.05	5.93	7.03	6.3	6.82
FeO	-	-	-	-	-
MgO	2.83	2.25	2.4	2.05	2.34
CaO	21.3	23.3	20.4	17.6	19.2
Na_2O	-	-	-	0.14	-
K_2O	-	-	-	-	-
P_2O_5	-	1.42	-	-	-
Y_2O_3	-	-	-	2.58	-
Ce_2O_3	-	2.32	0.58	-	-
ThO_2	2.98	10.6	4.28	3.68	3.16
F	-	-	-	-	-
Cl	-	-	-	-	-
Total	100	100	100	100	100
-O≡F					

[a] CSG: Calcic silicate glass.

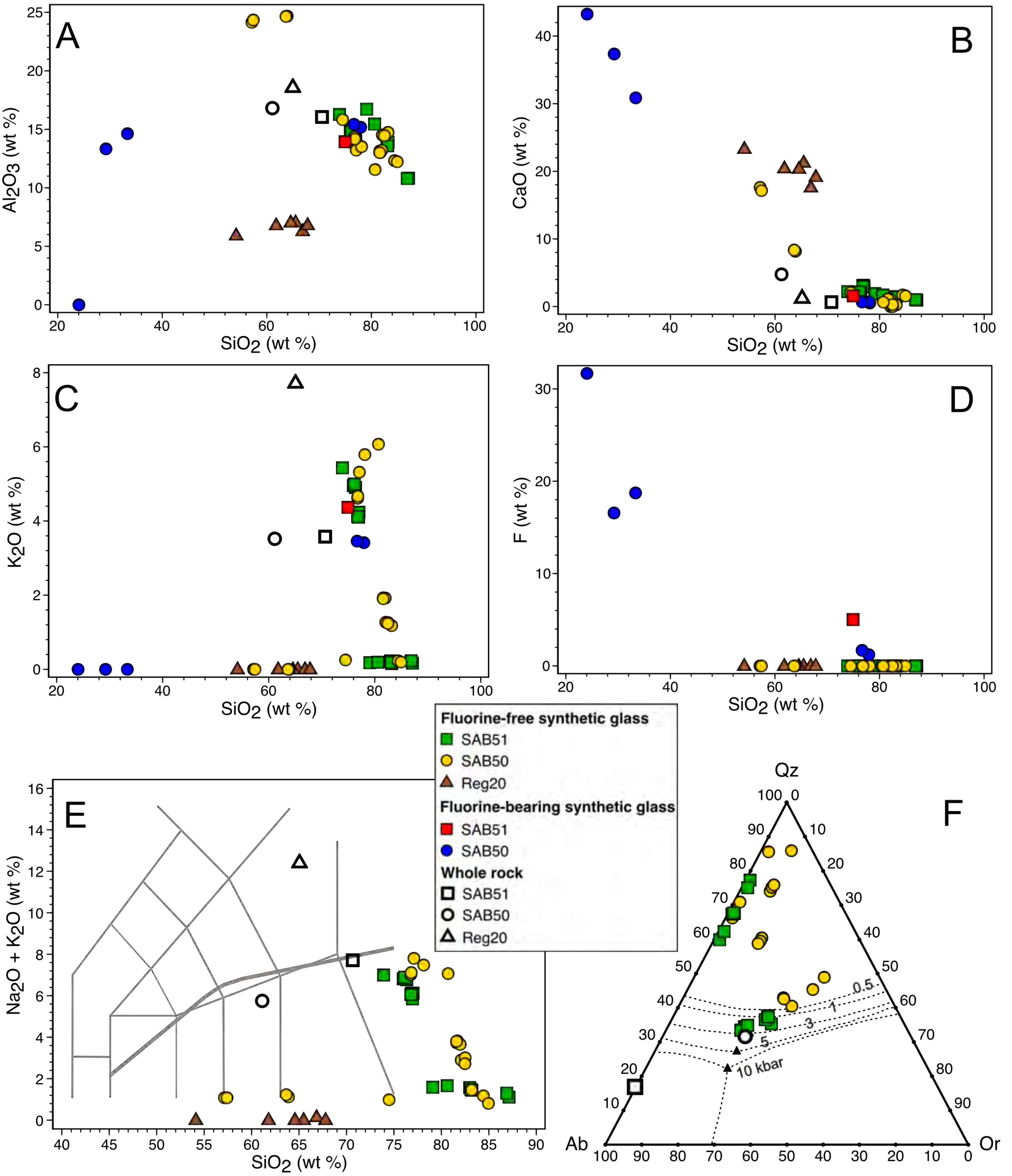

Fig. 37. Composition of glass inclusions of the annealed zircon grains from orthogneiss SAB50, tonalite SAB51, and syenite REG20. (A) Al_2O_3 vs silica. (B) CaO vs silica. (C) K_2O vs silica. (D) Fluorine vs silica. (E) Total alkalis vs silica (TAS) diagram. (F) Phase equilibrium diagram of the Qz-Ab-Or ternary projected from anorthite following the procedure of Blundy & Cashman (2001); cotectic lines drawn from experimental data by Tuttle & Bowen (1958), Luth et al. (1964), and Ebadi & Johannes (1991).

II.2.1.2 Composition of recrystallized zircons

The trace-element and Ti concentrations in zircon grains SAB50 and SAB51 were determined by LA-ICP-MS without any problem, given the large areas free of inclusions. However, this is not the case for zircon grains of REG20, in which no clean LA-ICP-MS analysis could be obtained.

A comparison between untreated and annealed zircon grains from samples SAB50 and SAB51 (Fig. 38) reveals that the annealed ones are noticeably impoverishment in LREE except for Ce, which remains constant or increases slightly. This effect causes an increase in Ce anomalies in both samples (Fig. 38). However, in some zircon grains, annealed and untreated, these anomalies are less intense or absent due to a higher La content. In annealed SAB50 zircon, the cores and rims show more similar W concentrations (core: av. 219 ppm, range: 124−347 ppm; rim: av. 424 ppm, range: 200−601 ppm) than untreated ones (Fig. 39; Table 12).

In annealed SAB51 zircon grains, there are little differences in W concentrations between light and dark bands, with average values of ca. 267 ppm (range: 193-347 ppm) and ca. 217 ppm (range: 138-392 ppm), respectively. However, in recrystallized domains, the W concentrations are higher (av. 440 ppm; 326-554 ppm; Fig. 39, Table 12).

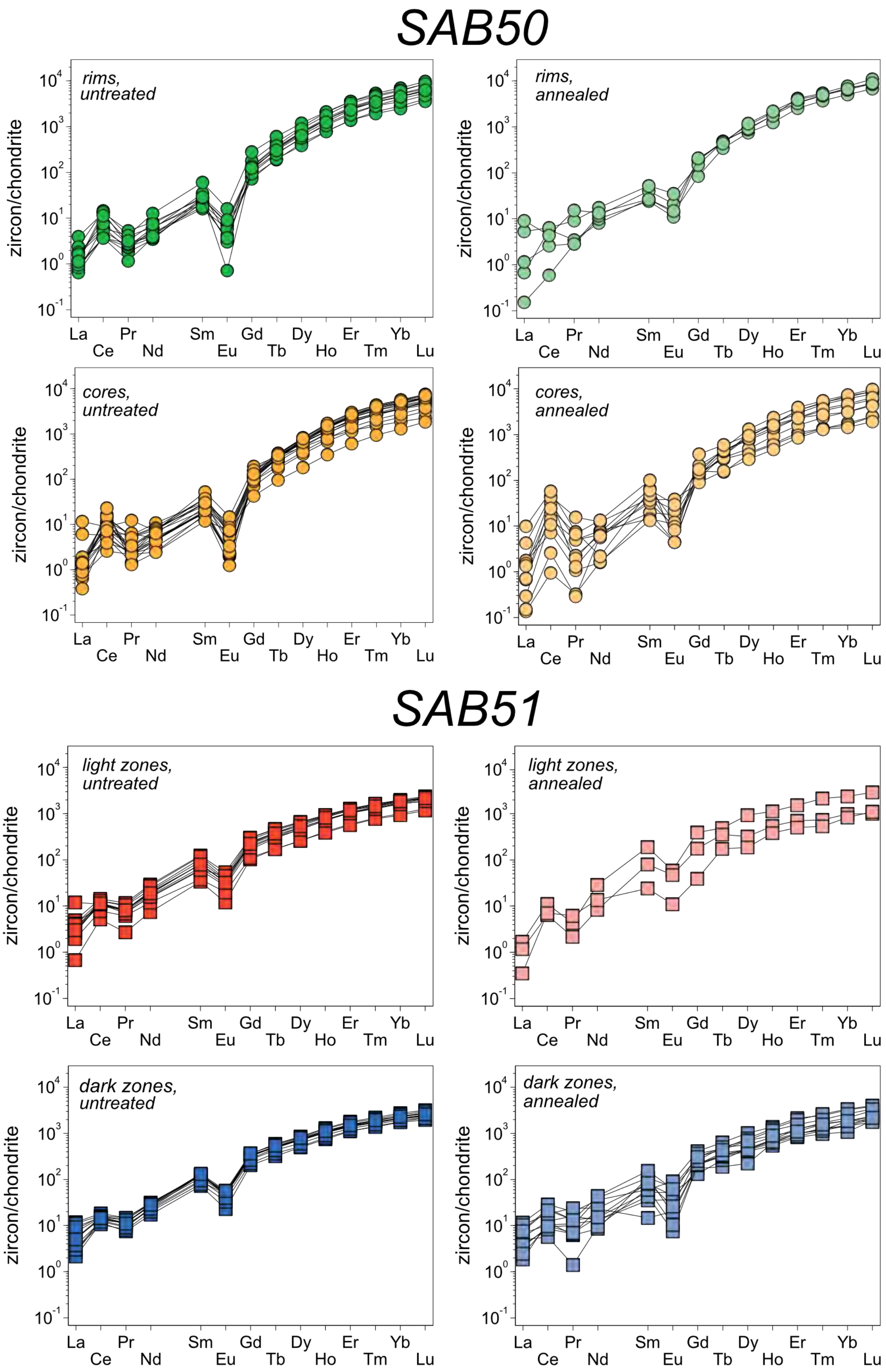

Fig. 38. Chondrite-normalized REE patterns from untreated and annealed zircon grains from orthogneiss SAB50 and tonalite SAB51. SAB50: the REE compositions of the rims and cores are clearly close to each other. SAB51: the darker bands are richer in HREE than the lighter ones.

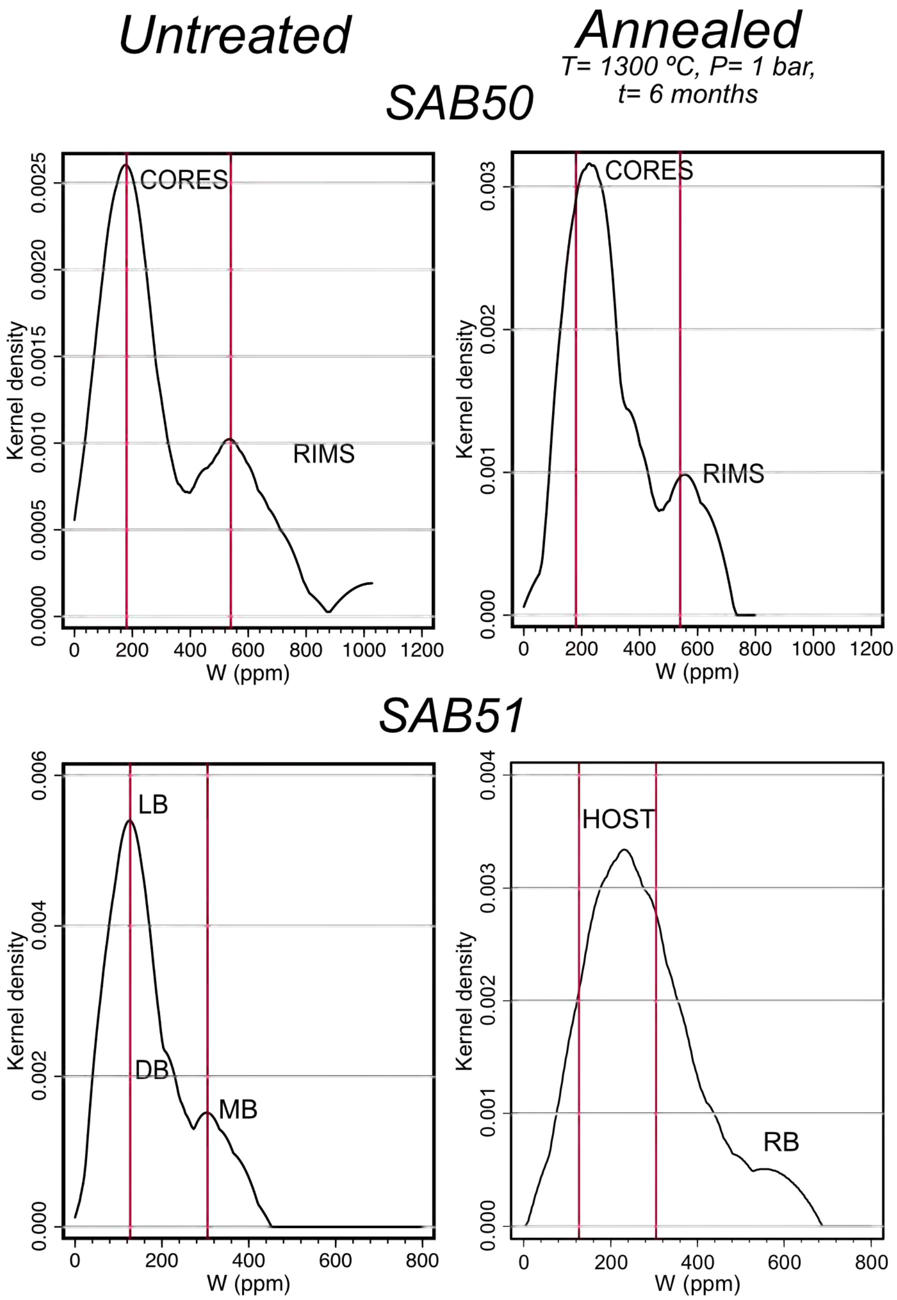

Fig. 39. Tungsten distribution of untreated and annealed zircon grains in the orthogneiss SAB50 and tonalite SAB51. Untreated SAB50 zircons have a clear difference in W between cores and rims (177 and 570 ppm, respectively), remaining practically unchanged in the annealed ones (cores: 225 ppm, rims: 555 ppm). Note that the untreated SAB51 zircons show two peaks, for light and dark bands (104 and 164 ppm, respectively) and a peak for metamict bands (305 ppm), whereas annealed ones show no difference between light and dark bands, thus indicating homogenization, but there are still differences between host and recrystallized bands. Abbreviations: LB = light bands, DB = dark bands, MB = metamict bands, and RB = recrystallized bands.

In the annealed zircon grains, the concentration of Ti increases slightly, and the distribution of Ti-in-zircon temperatures (Bea et al., 2007; Watson et al., 2006) widens in all cases; the SAB50 cores and the SAB51 increase to peak values around 800-900 ºC, but the SAB50 rims decrease slightly, peaking at ca. 800 ºC, that is, lower than the cores, thus reversing the situation observed in the untreated zircon grains (Fig. 40).

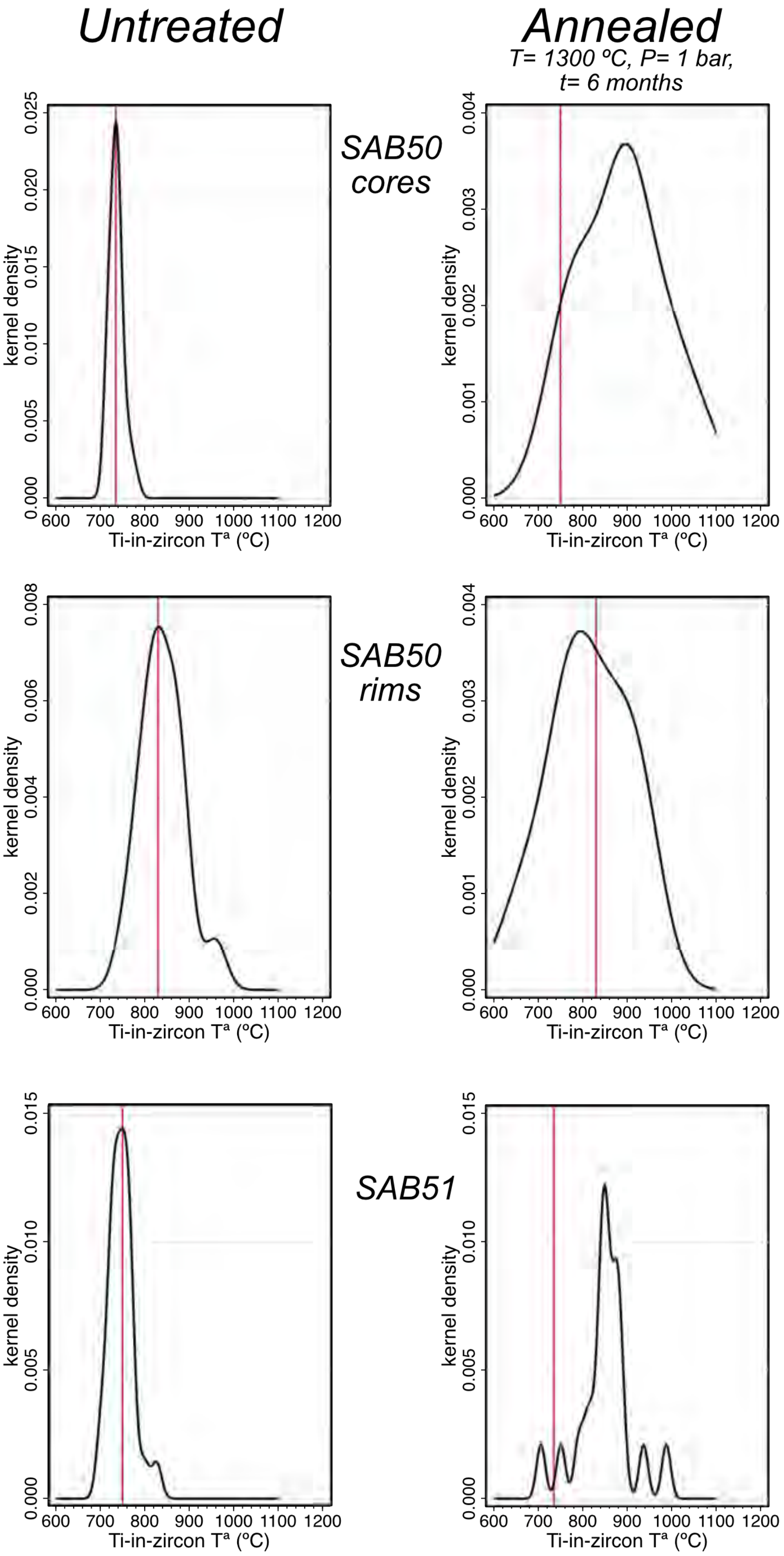

Fig. 40. Distribution of Ti-in-zircon temperatures calculated with the expression of Watson & Harrison (2005) for untreated and annealed zircon grains from samples SAB50 and SAB51. Note that Ediacaran cores of untreated SAB50 and untreated SAB51 peak similar (about 740 and 750 °C, respectively), whereas Cambrian−Ordovician rims of untreated SAB50 peak at 830 °C. When annealed, the Ti-in-zircon temperatures for SAB50 cores and SAB51 increase to peak values around 800−900 °C, but Ti-in-zircon temperatures for SAB50 rims decrease slightly, peaking at 800 °C.

II.2.1.3 Oxygen isotopes

Oxygen isotopes also vary between untreated and annealed zircon grains. Fig. 41 shows the distribution of ∂^{18}O in the untreated and high-temperature experiments zircon grains of samples SAB50 and SAB51 (see data in Table ST1 in the Supplementary material). The dashed purple lines represent the range of ∂^{18}O values of embedding cristobalite, and the green lines are the modal value of ∂^{18}O from the untreated zircon grains. In untreated zircon grains from SAB50, there are two populations, one from the Ediacaran inherited cores at six of ∂^{18}O and one from the Cambro-Ordovician rims at nine ∂^{18}O (as mentioned in **"Starting material" section**, Fig. 17). In untreated zircon grains from SAB51, there is a single clear population at 6.8 of ∂^{18}O (as mentioned in the **"Starting materials" section**, Fig. 20).

Fig. 41 shows the ∂^{18}O distribution from untreated zircons to zircons heated at 1300 °C for 1, 3 and 6 months from left to right for both samples. The heating of the zircon grains of the SAB50 produces in 1 and 3 months a continuous shift of ∂^{18}O towards higher values, starting to produce a homogenization between core and rim, which after 6 months is perfectly observed. In addition, after 6 months, it can be observed how the ∂^{18}O slightly shifts towards lower values, starting to homogenize with the embedding cristobalite (Fig. 41). The heating of the zircon grains of the SAB51 produces a homogenization of ∂^{18}O values of zircon grains and embedding cristobalite with time, increasing the range of ∂^{18}O values towards lower values (embedding cristobalite values) (Fig. 41).

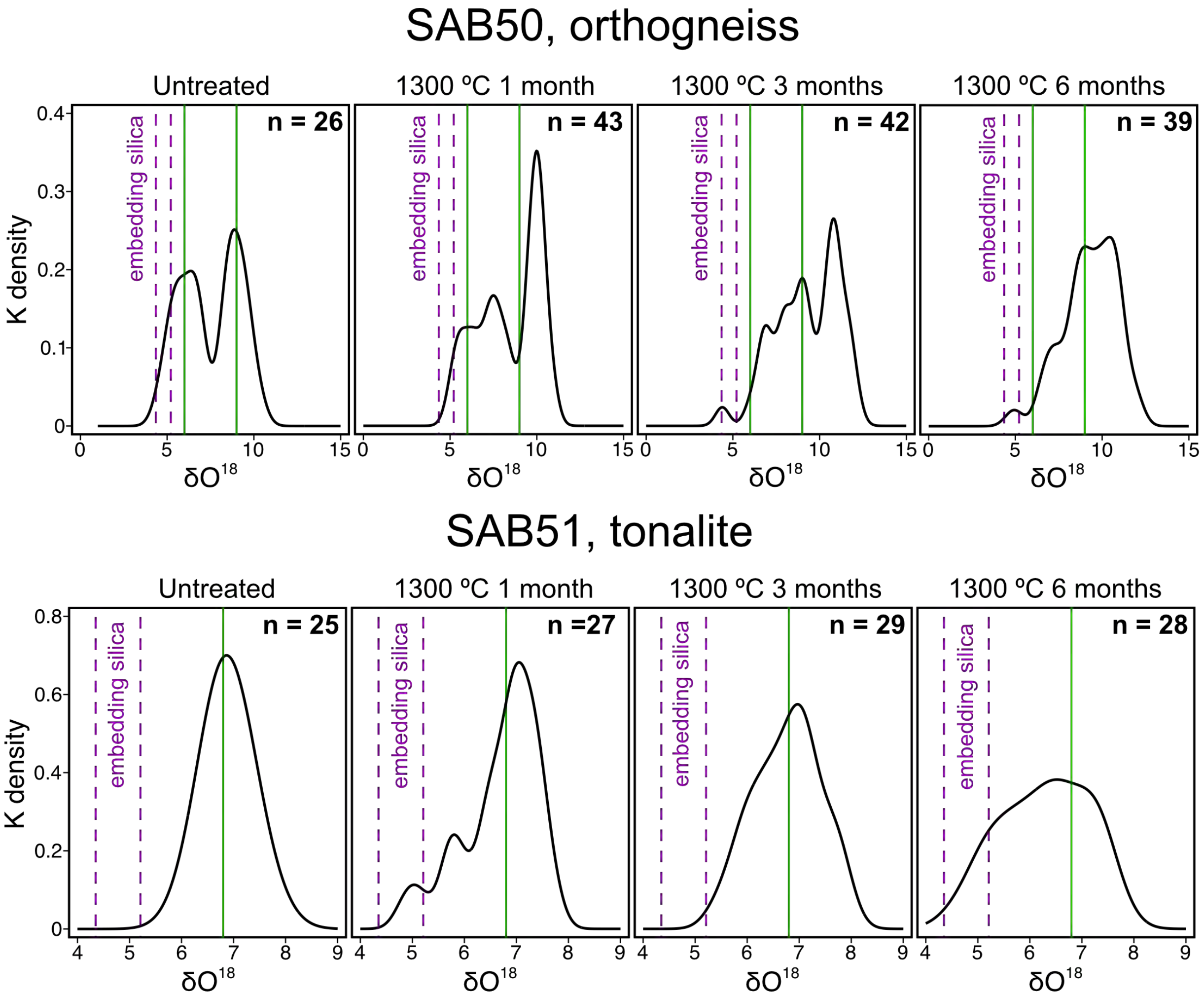

Fig. 41. ∂^{18}O distributions of untreated and high-temperature experiments zircon grains from samples SAB50 and SAB51. Note the homogenization of both samples with embedding silica and between cores and rims in sample SAB50.

II.2.1.4 Common Pb Leaching

The U-Pb SHRIMP results for zircons SAB50 and SAB51, which contain negligible common Pb, are generally concordant with little or no loss of radiogenic Pb. Bea et al. (2018b) performed heating experiments that revealed that zircons not in contact with the melt do not lose radiogenic Pb but homogenize their concentration within the zircon, perturbing the ^{206}Pb/^{238}U and ^{207}Pb/^{235}U ratios, and causing discordances only if the zircon was chemically heterogeneous.

On the other hand, the situation is significantly different for REG20 zircons. The intense metamictization, the high abundance of common Pb and the radiogenic Pb loss in this sample completely prevent U-Pb SHRIMP dating. However, the geological position of REG20 syenite in the outer rim of the funnel-shaped Awsard intrusion suggests that their age must be close to that of the nepheline and kalsilite syenites of the body's interior. The zircon grains from the nepheline and kalsilite syenites give a U-Pb SHRIMP ages of 2459 ± 11 Ma (MSWD = 2.9) and 2458 ± 8 Ma (MSWD = 1.2), respectively (Bea et al., 2013, 2014).

Fig. 42A shows the SHRIMP U-Pb data we obtained for this sample for common Pb-uncorrected. The points define a cloud from which no reasonable age can be obtained. Using the common Pb evolution scheme of Cumming & Richards (1975), we obtain an upper intercept of the 204-corrected ages at 2376 ± 88 Ma (MSWD = 63.6) (Fig. 42B), which is unacceptable as a crystallization age. In contrast, and very surprisingly, it can be seen in Fig. 42C that the annealed zircon grains give a well-fitted common lead-uncorrected discordia with the upper intercept at 2473 ± 12 Ma (MSWD = 19.5). With the 204-correction, the result is improved up to 2458 ± 10 Ma (MSWD = 12.6) (Fig. 42D), which is identical to the ages given above for nepheline and kalsilite syenite zircons and is within the errors of the uncorrected discordia. In addition, the lower intercept decreases from ca. 250 Ma in the untreated zircons to about 60-90 Ma in the annealed ones, indicating that there is also a loss of radiogenic lead.

The massive common Pb loss leading to well-fitted discordances, according to Bea & Montero (2013), occurs at temperatures above 1100 °C but not below, even when the zircons undergo extensive recrystallization. This fact suggests that common Pb dissolves in the melt migrating through the crystal. Therefore, if the melt does not form, the common Pb would remain similar to the untreated zircons despite the zircon annealing.

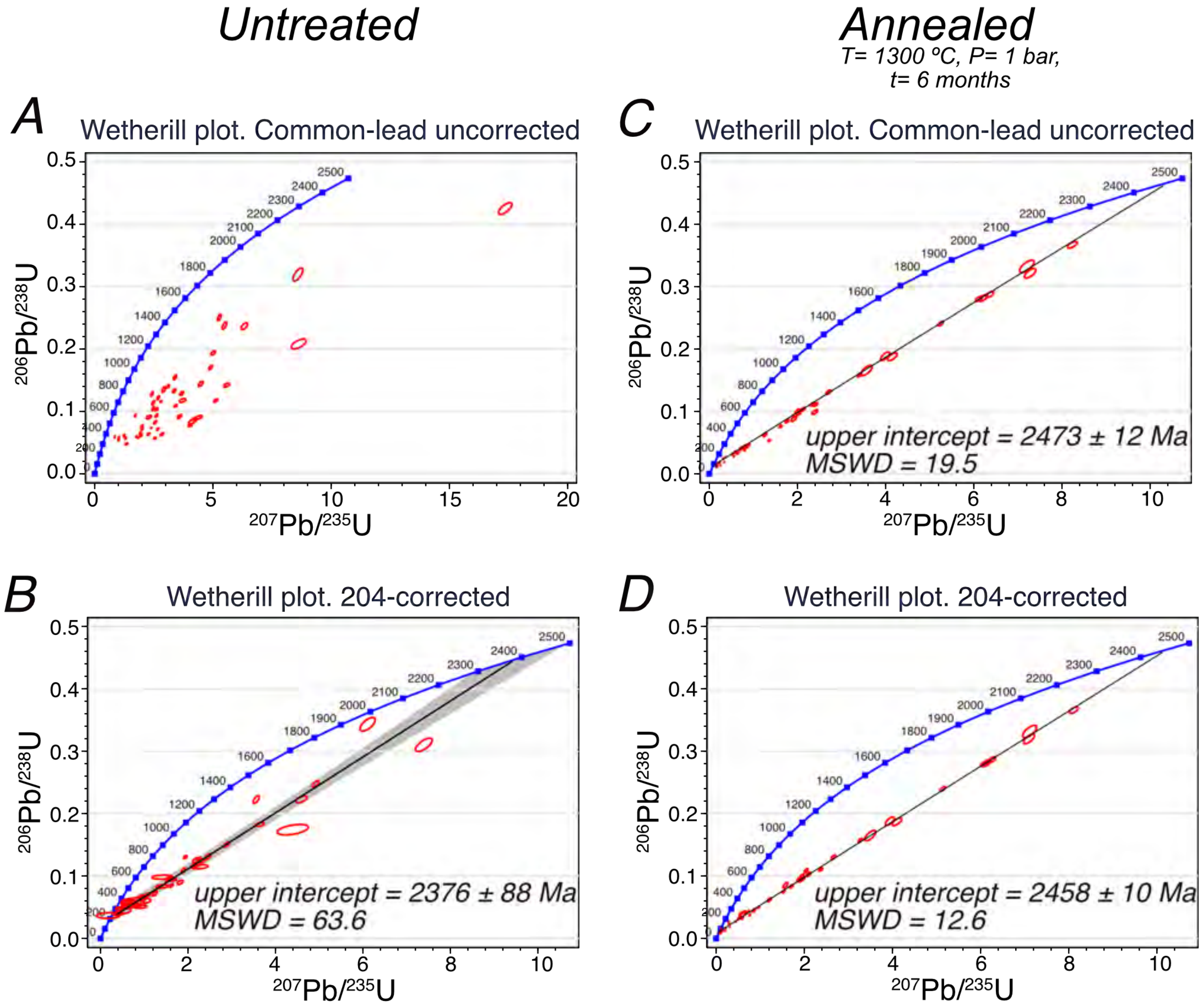

Fig. 42. Wetherill plot of SHRIMP data obtained from untreated and annealed zircon grains of syenite REG20. (A) Wetherill plot with common lead uncorrected for untreated REG20 zircons. Note that the points define a cloud from which no sensible age can obtained. (B) Wetherill plot with the 204-correction for untreated REG20 zircons. Note that there is an upper intercept of 204-corrected ages at 2376 ± 88 Ma. (C) Wetherill plot with common lead uncorrected for annealed REG20 zircons. Note that the annealed zircons yielded a well-fitted common lead uncorrected discordia with an upper intercept at 2473 ± 12 Ma. (D) Wetherill plot with the 204-correction for annealed REG20 zircon. Note that the 204- corrected ages improve to 2458 ± 10 Ma (see ***section II.2.2.4*** *for discussion). Data reported in Tables ST2 and ST3 from the Supplementary Material.*

II.2.2 Discussion

II.2.2.1 Inferences on the crystallization of zircon from the Variscan, Cambrian−Ordovician, and Ediacaran magmatism.

A valuable method for determining zircon-saturated melt compositions is to analyze the glass inclusions in zircon (Thomas et al., 2003). In the SAB50 and SAB51 untreated zircon grains, the tear-drop shapes of quartz + K-feldspar-bearing inclusions suggest that they were initially granite-melt inclusions.

During annealing, the inclusions gave rise to the potassic rhyolite glass (Tables 13, and 14), whose compositions lie along the quartz-feldspar cotectic valley of the Qz-Ab-Or ternary (Fig. 37). This fact suggests that the zircon grains from both samples grew from granite residua at low pressure, which is consistent with their geological mode of occurrence.

Furthermore, the appearance in the untreated zircon grains of both samples of gas bubbles plus fluoride and silicate minerals suggests the presence of a fluorine-rich fluid phase during zircon growth. This fact implies a high fluorine activity in the late magmatic fluids occurring during Ediacaran and Variscan times.

High W concentrations in zircon, such as those seen in zircons SAB50 and SAB51, have not been reported in the literature. This peculiarity in the zircons of these samples is probably related to the abundant tungsten deposits found in Western Spain, particularly in the Sanabria Zone, where these samples were collected (Arribas, 1980; Gil Agero & Moro Benito, 1991).

II.2.2.2 Contrasting Behavior of Ti and W in Zircon with Increasing Temperature.

Given the redox conditions prevailing in the earth's crust, titanium occurs mainly as a tetravalent ion. Therefore, Ti^{4+} (ionic radius: 0.42 Å) may be incorporated into the zircon lattice either as $^{IV}Ti^{4+}$ within silica tetrahedra, substituting for $^{IV}Si^{4+}$ (ionic radius: 0.26 Å), the dominant mechanism (Watson et al., 2006), or as $^{VIII}Ti^{4+}$ (ionic radius: 0.74 Å) within ZrO_8 triangular dodecahedra, replacing $^{VIII}Zr^{4+}$ (ionic radius: 0.84 Å). In both cases, a compensating ion is not required as the substitution is homovalent; however, the large differences in ionic radius make substitution difficult. Hence, the concentration of Ti in zircon is always low and increases with temperature, resulting in a useful thermometer (Watson et al., 2006; Watson & Harrison, 2005). Increasing Ti concentrations after the experiments on zircon grains SAB50 and SAB51 indicates that some titanium has been incorporated into the zircon lattice during heating. It is proposed that the sources of titanium were tiny Ti-rich inclusions such as rutile, which are abundant in untreated grains.

Given the redox conditions prevailing in the earth's crust, tungsten occurs mainly as a hexavalent ion, W^{6+} (ionic radius: 0.42 Å in fourfold coordination). It can only be incorporated into the zircon lattice by replacing $^{IV}Si^{4+}$ and requiring the coupled incorporation of a divalent cation, such as Ca^{2+}, Mg^{2+}, or Fe^{2+}, for compensating charges. The compensating ion necessarily replaces $^{VIII}Zr^{4+}$ within the ZrO_8 triangular dodecahedra. However, this substitution disturbs the zircon structure due to the large differences in ionic charge and radius between $^{VIII}Zr^{4+}$ and any potential compensating ion.

After heating, the overall abundance of tungsten increases with respect to the untreated equivalents, as in the case of titanium, and as shown by the concentration values above the detection limit of the tungsten analysis of the annealed zircon grains (Fig. 39 and Table 12). These relationships can be explained similarly to titanium, i.e., by the dissolution of minute W-mineral impurities, which are mostly concentrated in the CL dark and more metamict areas. However, the W in the zircon structure has a more limited solubility (mostly of the order of hundred ppm), so zircon rejects part of the W and the coupled divalent cations (Ca, Mg and Fe) to form new tungstate inclusions, mostly scheelite, as observed in the annealed SAB50 and SAB51 zircon grains (Figs. 34A, S1C, and 35C and E).

Low-ppm level analytical chemistry of tungsten is required for ore deposit prospecting, which is complex due to the lack of sensitivity of most techniques, the isobaric interferences by Er oxides in ICP-MS, and the W contamination produced by most grinding systems.

In contrast, using an electron microprobe to identify minimum W concentrations or an SEM with EDAX for identifying scheelite inclusions is quick and straightforward. Therefore, it is suggested that W analyses directly on zircons in thin sections or zircon annealing and searching for scheelite and other tungstate inclusions are tools that offer considerable potential for searching for W deposits.

II.2.2.3 Permeability Creation by Zircon Annealing: Evidence for an Open-System Behavior.

Due to transport pathways present in metamict domains, such as a network of microcracks and micropores, natural zircon can be permeable (Geisler et al., 2007). The permeability of zircon can be increased by recrystallization of metamict zircon by annealing, which occurs rapidly at temperatures above 900 °C (e.g., Bea et al., 2018b; Ewing et al., 2003), because nanopore formation occurs due to a significant volume reduction of the domains that are recovered (Geisler et al., 2004, 2007; Schmidt et al., 2006). Therefore, the migration of low-K rhyolite melts in the porous bands parallel to the pyramidal or prismatic faces of SAB51 zircon grains can be explained by this micropore network.

Sample SAB50 presents an interesting case, previously observed by Bea et al. (2018b) (Fig. 34), which is the accumulation of melt at the boundaries between the core and the rim of zircon crystals. Zaraisky & Balashov (1994) and references therein realized that the volume increase resulting from the thermal expansion of a given rock is larger than the sum of the volume increase of its constituent minerals because of the creation of additional intergranular pore space rocks upon heating. The reason is that thermal expansion is a tensorial property, and the rock minerals are variously orientated. This same effect seems to occur in zircon grains with a core and a rim with different crystallographic orientations. Therefore, this anisotropic thermal expansion opens up pore spaces at the core-rim interface that can act as an attractor for the mobile melt being concomitantly filled by molten inclusions, whose migration through the crystal can be either through micropores and microcracks or through the crystal lattice itself as described by Schiano et al. (2006).

II.2.2.4 Oxygen isotopes diffusion.

Diffusion of Oxygen in zircon under dry conditions is extremely retentive of their oxygen isotopic signatures if the temperature keeps lower than 900 ºC (Watson & Cherniak, 1997). Our experiments under dry conditions simulate zircon xenocrysts with high $\partial^{18}O$ surrounded by a mineral with a low $\partial^{18}O$ (embedding cristobalite) at mantle temperatures during one, 3 and 6 months (Fig. 41). The SAB50 sample with two distinct $\partial^{18}O$ populations (core and rim) after heating and, over time, homogenizes with each other and with the embedding cristobalite. The sample SAB51, after heating and over time, also homogenizes with the embedding cristobalite. These results show that high $\partial^{18}O$ zircons surrounded by a low $\partial^{18}O$ mineral tend to homogenize with this mineral. This effect suggests that zircon xenocrysts found in mantle rocks cannot inhabit them for long at mantle temperatures (Montero et al., 2020).

II.2.2.5 Leaching of Impurities by the Migrating Melt.

In the metamict domains, mineral and trace element impurities are mainly concentrated, and these domains are prone to melt and develop high porosity during annealing. This is the case for REG20 zircons (Fig. 36), which formed abundant micro-veins of calcic andesite to dacite melts. The melt migration through the recrystallizing crystal permitted the effective dissolution of U, Th, and REE accessory phases, which disappear from the annealed crystals and cause a high abundance of these chemical components in the calcic andesite to dacite glasses that fill the micropores and cracks.

This process is particularly interesting in this sample because it favors zircon dating by leaching common Pb (see Fig. 42). Several authors have shown it (Kusiak et al., 2015; Whitehouse et al., 2017; Kusiak et al., 2019; Lyon et al., 2019) that lead in old and metamict zircons tends to form metallic lead nanospheres or lead oxides.

Metallic lead and oxides are highly soluble in silicate melts, where Pb^{2+} behaves like a network modifier if its concentration is below the level of a few per cent (Ben Kacem et al., 2017). Given that the recrystallized zircon domains lost almost all their common Pb. It is therefore suggested that the common Pb mainly resided in the nanospheres or other readily soluble phases in the melt. However, radiogenic Pb is mainly retained in the zircon lattice; only very little of it moves into the melt, as indicated by the lower intercept age of the discordia lines of the annealed zircons compared to that of the untreated zircons (Fig. 42). This observation provides a way to date highly metamict zircons, which would otherwise be impossible given the combination of radiogenic Pb loss and common Pb gain.

This observation also fits in with the work of Mattinson (2005), who showed that combining annealing and multi-step HF leaching of zircon concentrates markedly decreases the discordance caused by common lead and lead loss in TIMS analyses. The glassy inclusions that acted as Pb sinks and the microcrystalline SiO_2 (+baddeleyite) resulting from annealing easily dissolve in HF, and the baddeleyite, once deprived of surrounding silica, “falls” apart from the well-recrystallized areas of zircon grains.

It was not expected that the common lead, not structurally bound to the zircon lattice, would be so easily removed by the drilling of the molten inclusions, leaving only radiogenic Pb in the structurally rebuilt parts of the zircon. However, this could explain why high-temperature zircons, whether metamorphic (Kooijman et al. 2011; Halpin et al. 2012; Bea et al., 2020) or xenocrysts scavenged in hot mafic magmas (Bortnikov et al., 2008; Skolotnev et al., 2010; Torró et al., 2018), rarely contain common lead and are concordant or well-matched discordia lines. This suggests that the described leaching mechanism could frequently occur in overheated zircons.

II.2.2.6 Opening Pathways for the Interaction of External Fluids with Zircon.

During annealing, several transport pathways are generated that can connect the surface of the zircon to its interior, allowing the entry of external mobile phases. In the annealed SAB50 and SAB51 zircon grains, there is textural and compositional evidence indicating that the formation of abundant low-K high-Si rhyolite melts required a significant contribution from the external silica sealant. The untreated zircons contain many feldspars but very few quartz inclusions. Nonetheless, the glass compositions of annealed zircons show high normative quartz, and the compositions lie in the primary phase field of silica minerals in the Qz-Ab-Or ternary, far from the quartz-feldspar cotectic valleys (Fig. 37F). This effect implies that the melts were saturated in a silica mineral. As there is a shortage of quartz inclusions, the only silica-saturated phase can be the external silica sealant. Finally, since rhyolite glass appears in textural sites that had no felsic silicate minerals in the untreated grains, such as the core-rim interfaces in SAB50 and the metamict porous bands with only a few trace element impurities in SAB51, it suggests transport on a single grain scale, which is what is required for the entry of an external mobile phase.

For the generation of the calcic andesite to dacite melt in the annealed REG20 zircon grains, the contribution of the external silica sealant could also be significant, given its high porosity (Figs. 21 and 36), although its composition differs significantly from that of the melts saturated in a silica mineral.

This open system behavior involves the ingress of silica vapor and the outflow of a mobile phase from the zircon interior. This is understandable, given the observation of dendrites composed of tiny zircon crystals at the boundaries between zircon and cristobalite (Fig. 43). Since there is no evidence of zircon evaporation at the temperatures of the experiments, the appearance of tiny but euhedral zircon crystals suggests that they could have been generated in the presence of a melt released from the zircon interior.

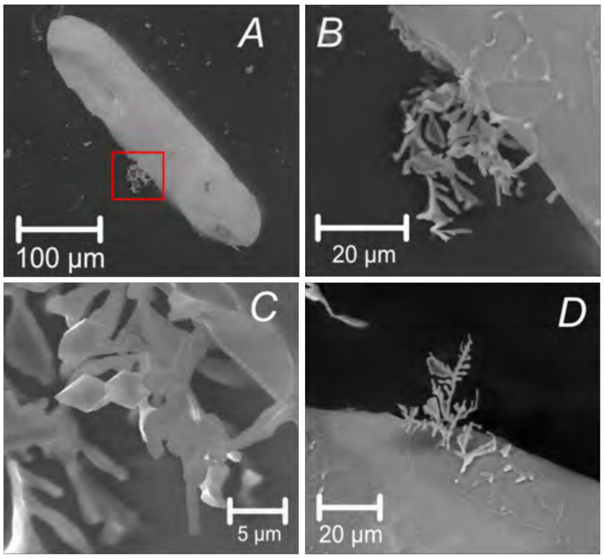

Fig. 43. SE images of annealed zircon grains from tonalite SAB51 (A−C) and orthogneiss SAB50 (D). Note the formation of dendrites composed of tiny but euhedral zircon crystals at the zircon− cristobalite boundaries.

II.2.2.7 Zircon−baddeleyite stability relationships.

The breakdown of unaltered pure zircon to $SiO_2 + ZrO_2$ occurs at a temperature close to 1675 °C (1676 ± 7, Butterman, 1967; 1674 ± 7, Kamaev et al., 2005; and 1673 ± 10 °C, Kaiser et al., 2008). However, the presence of impurities and metamictization cause the appearance of baddeleyite at temperatures below 1600 °C (e.g., 1380−1480 °C, Kober, 1986; 1477 °C, Mursic et al., 1992; 1285 °C, Pavlik et al., 2001; 1400 °C, Pena & de Aza, 1984, Wang et al., 2006, Kaiser et al., 2008, and Váczi et al., 2009). Notably, baddeleyite has also been reported at even lower temperatures by recrystallization of highly metamict zircon (900 °C, McLaren et al., 1994; 927 °C, Capitani et al., 2000; 852 °C, Zhang et al., 2000; 800−950 °C, Nasdala et al., 2002; and 600−900 °C, Lewerentz et al., 2019).

In the annealing experiments carried out in this thesis with zircon grains SAB50, SAB51 and REG20, baddeleyite is formed by two main mechanisms: (1) incongruent dissolution of zircon into molten mineral inclusions of appropriate composition and (2) recrystallization of metamict domains assisted by silica migration from the reaction site.

The first mechanism produced the formation of the relatively coarser baddeleyite hosted in zircons SAB50 and SAB51, i.e. it was produced by the incongruent dissolution of zircon. The textural relationships show mineral inclusions can melt, reacting with the host zircon to produce baddeleyite. Most of them are enriched in fluorine, but calcic silicates can also give rise to the appearance of baddeleyite. Therefore, the compositional relationships suggest that zircon + baddeleyite can coexist with a large variety of melts ranging from ultrabasic fluoro-silicate to fluorine-free andesite and dacite. Interestingly, the only compositional feature shared by all these melts is a high CaO content (>8 wt %). Hydrothermal experiments by Lewerentz et al. (2019) have shown baddeleyite formation after zircon when the molar amount of CaO in the fluid is close to or greater than that for silica. In the baddeleyite + zircon-saturated melts, the molar CaO/SiO_2 ratio is very variable, ranging from 0.14 to 1.9, but it is always significantly higher than in baddeleyite-undersaturated melts (around 0.04). These data suggest that a high CaO abundance in the melt may favor baddeleyite saturation, although the compositional requirements are not as strict as in fluids.

Tiny baddeleyite crystals in the pore bands of SAB51 zircons and anhedral baddeleyite in the pore domains of highly metamorphic REG20 zircons suggest that the second mechanism generated it. The larger grain size and higher abundance of baddeleyite in the latter resulted from more extensive metamictization. In both cases, baddeleyite grains are surrounded by cathodoluminescent zircon produced by recrystallization of the metamict domains. It has been proposed that amorphous zircon recrystallizes via de-mixing of the metamict zircon into more stable oxides (e.g., (Carrez et al., 2003; Monaghan et al., 2005); see Váczi et al. (2009) for further discussion). This implies the transient growth of a silicate mineral and baddeleyite and the subsequent elimination of the silica excess to preserve baddeleyite. The transport of excess silica to the outside is facilitated by the previous high porosity of the metamict domains and the secondary porosity created during zircon recrystallization, as indicated in subsection **II.2.2.6**.

II.2.3 Conclusions

The thermal treatment of natural zircon grains from three different samples shows, on the one hand, several phenomena that can find practical applications, and, on the other hand, the behavior of zircons during thermal shock related to magma hybridization and rock assimilation can be understood, despite the high-temperature conditions. Annealed zircon grains experience recrystallization of metamict domains, formation of nanopores and microcracking, propagated by thermos-elastic stress accumulated at the interface between domains with different lattice orientations, and melting of polymineralic inclusions. The enhanced porosity permits melt migration through the crystal, leaching out impurities. However, since the permeability of the zircon grain is increased by creating these open spaces, dry conditions should be maintained during cooling to prevent the entry of polluting fluids.

Highly metamorphic zircons with high losses of common and radiogenic Pb, such as REG20, are impossible to date with SHRIMP. Due to the leaching after annealing at 1300 °C, these zircons lose almost all common Pb but little radiogenic Pb, producing significant well-fitted discordias with a significant upper intercept age. The requisite for losing almost all common Pb is melt formation. It is suggested that this is a way of dating "undateable" zircons and that common Pb dwells in metallic or Pb oxide nanospheres while radiogenic Pb remains attached to the zircon lattice.

Annealed zircons containing minute inclusions of rutile or other Ti-bearing minerals increased their Ti concentrations in the lattice (SAB51 and SAB50 zircons). Zircons from a region with abundant W deposits (Arribas, 1980; Gil Agero & Moro Benito, 1991) have high W concentrations. Upon annealing, minute W-mineral impurities also dissolved in the zircon lattice, causing an overall increase in W concentration in the zircon. Furthermore, since the solubility of W in zircon is limited, a fraction of the released W is consumed in forming W-rich minerals such as scheelite.

Although further studies are required to understand oxygen diffusion in zircon inclusions quantitatively, the experimental data unequivocally suggest that zircon xenocryst with high $\partial^{18}O$ found in mantle rocks cannot inhabit them for a long time at mantle temperatures without homogenization with surrounded minerals.

During annealing, baddeleyite is formed at temperatures considerably lower than the thermal decomposition temperature of pure zircons. Two main mechanisms for their formation have been identified: (1) incongruent dissolution of zircon into molten mineral inclusions with a high CaO/SiO_2 ratio and (2) recrystallization of metamict domains assisted by silica migration from the reaction site.

II.3 Results of hydrothermal experiments

For the hydrothermal experiments, SAB50 zircon grains have been used in the Teflon bomb experiments and the autoclave experiments. Zircon grains of sample SAB51 and granite powder GREB-354 were only used for the Teflon bomb experiments. For more details on starting materials, see section **II.1.1**.

In both types of hydrothermal experiments, ultrapure H_2O, 2M NaCl, 2M $CaCl_2$ and 1M NaF have been used. The solutions were prepared with the corresponding amounts of ultrapure H_2O and salts to achieve the desired.

II.3.1 Teflon bomb experiments

Teflon bomb experiments were carried out at a temperature of 170 ºC, with the saturated water pressure (swp) at approximately this temperature, i.e. 10 bar, and 43 days. A total of 12 experiments have been carried out. For more detail about the procedure and types of experiments, see section **II.1.2.2** and Table 8.

II.3.1.1 Experimental products

In Teflon bombs, more than 95 % of zircon grains were recovered. The main characteristic of these zircon grains in both samples after the experiments is that they are highly fractured.

Zircon grains of sample SAB50 consist of transparent or slightly pinkish or brownish prisms, mostly euhedral and short, terminated by long pyramids (Fig. 44). During the experiments, the fluids infiltrated to the inner parts of the grain through the core-rim interface of partially broken zircons and the radial microcracks (see Figs. 12A and 45A), causing preferential dissolution of zircon at the core-rim interfaces, leading to an increase of permeability (Fig. 46A and Fig. 47A and B for comparison with untreated zircon). Note tiny aggregates of calcium hydroxide (probably portlandite) on the zircon faces (Fig. 46), probably produced by quenching.

SAB50 zircon grains present scarce rounded mineral inclusions of K-feldspar, plagioclase and quartz. Most of these inclusions are located in the Ediacaran cores or at the core-rim interface (Fig. 48). The CL images (Figs. 45A and 48) of the zircon grains from sample SAB50 present luminescent cores and dark rims. No recrystallization is observed in these images.

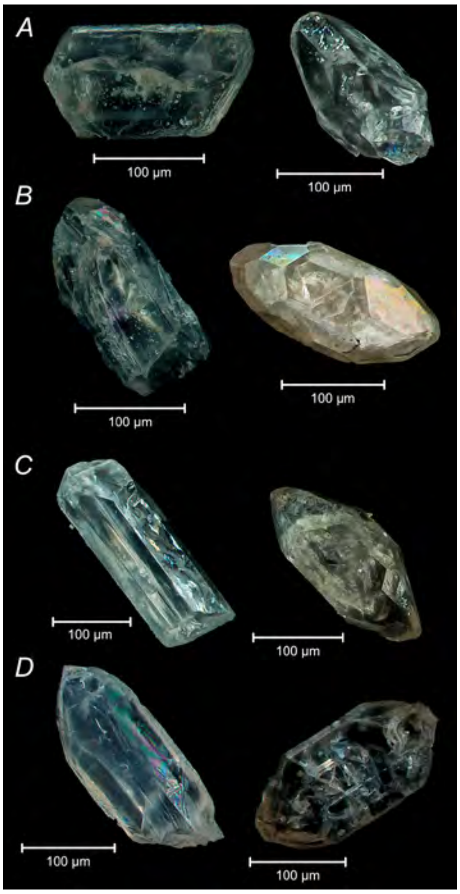

Fig. 44. Macro-photographs of hydrothermal low-T leaching experiments zircon grains from orthogneiss SAB50, and tonalite SAB51. A) ultrapure H_2O leaching experiments, SAB51 and SAB50. B) 2M NaCl leaching experiments, SAB51 and SAB50. C) 2M $CaCl_2$ leaching experiments, SAB51 and SAB50. D) 1M NaF leaching experiments, SAB51 and SAB50. Images obtained by optical microscopy using a focus stacking technique and non-polarized visible light (see ***Section II.1.3****. for details).*

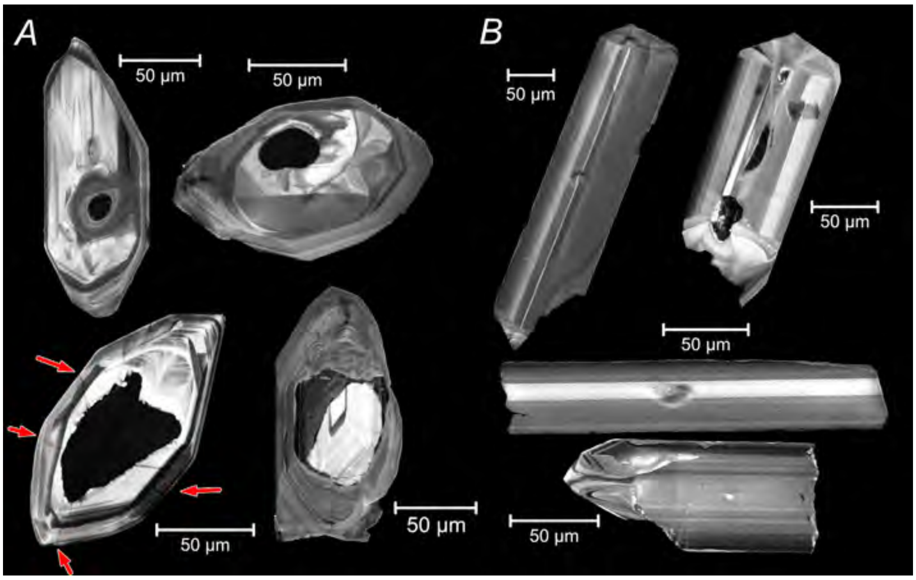

Fig. 45. CL images of hydrothermal low-T leaching experiments from zircons of orthogneiss SAB50 (A), and Tonalite SAB51 (B). A: Euhedral grains with inherited core and concentric zoning, showing, some of them, radial microcracks (red arrows). B: zircon grains with pronounced and luminescent bands of variable cathodoluminescence.

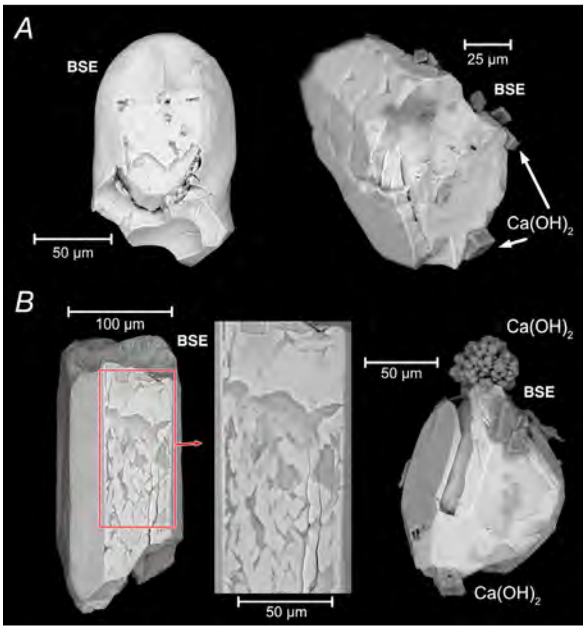

Fig. 46. BSE images of hydrothermal low-T leaching experiments from zircons of orthogneiss SAB50 (A), and Tonalite SAB51 (B). A) Zircon grain exposing its core with a microcrack parallel to the core-rim interface produced by dissolution; Fractured anhedral zircon grain. Note tiny aggregates of calcium hydroxides on the zircon faces. B) Porous band emerging on the surface of the zircon grain with channels produced preferential dissolution of the finer particles by the infiltrating fluids; Zircon grain with partially broken faces due to partial dissolution of the grain interior. Note very tiny aggregates of calcium hydroxides on the zircon faces.

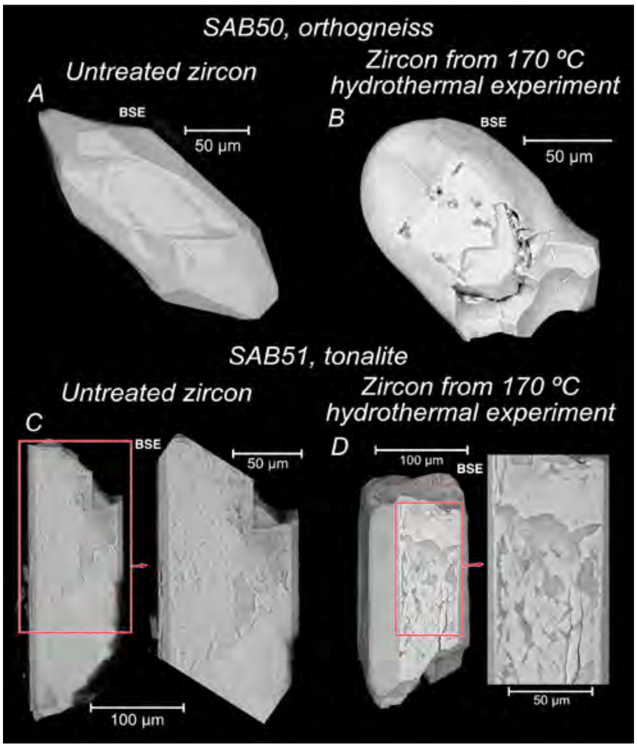

Fig. 47. BSE images of untreated and hydrothermal low-T leaching experiments zircon grains for sample SAB50 and SAB51. A) Subhedral short stubby prism untreated zircon terminated by long pyramids with a partially broken face exposing the inner core. B) Zircon grain exposing its core with a microcrack parallel to the core-rim interface produced by dissolution for low-T hydrothermal experiment. C) Split untreated zircon grain with microporous bands exposed at a fracture surface perpendicular to the prismatic faces. D) Porous band emerging on the surface of the zircon grain with channels produced preferential dissolution of the finer particles by the infiltrating fluids for low-T hydrothermal experiment.

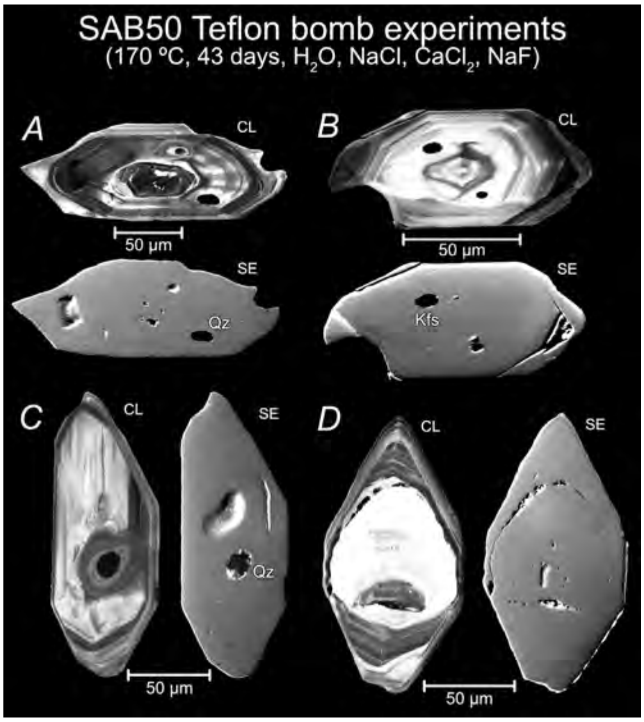

Fig. 48. SE and CL images of low-T leaching experiments from zircons of orthogneiss SAB50. A) Euhedral zircon grain from experiment with H_2O *(run Z-3) with a quartz inclusion, oscillatory zoning and an euhedral inherited core overgrown by a rim. B) Euhedral zircon grain from experiment with NaCl (run Z-5) with a k-feldspar inclusion, oscillatory zoning and an euhedral inherited core overgrown by a rim. C) Euhedral zircon grain from experiment with* $CaCl_2$ *(run Z-7) with a quartz inclusion, oscillatory zoning and an euhedral inherited core overgrown by a rim. D) Zircon grain from experiment with NaF (run Z-9) with oscillatory zoning and an euhedral inherited core overgrown by a rim.*

Zircon grains of sample SAB51 are euhedral, transparent and colorless. Most grains form long, narrow prisms ending in short pyramids (Fig. 44). During the experiments, fluids infiltrated the porous bands exposed at the surface of the zircon grains (either broken grains or unshelled faces). The fluids preferentially dissolved the smaller particles of porous bands (see Fig. 12B with untreated grains) that presented a higher surface/volume ratio, thus creating channels that increased zircon permeability (Figs. 46B and 47C and D). The microporous bands less affected by interaction with the fluid remain non-cathodoluminescent after the experiment (Figs. 45B and 49A-C), thus indicating no recrystallization of metamict zircon.

Only quartz inclusions and impurities of F, Al, Na, Ca, and Mg are found (Fig. 49C). These impurities are located in the slightly metamict and porous bands that are present in the starting materials section (section **II.1.1)**. Note the presence of tiny aggregates of calcium hydroxide (probably portlandite) on the grain surfaces (Fig. 46), probably produced by quenching. In 1M NaF leaching experiments (Fig. 49D), rare microporous luminescent zircon appears in very thin bands roughly parallel to fracture surfaces of broken grains that may be evidence for local zircon recrystallization (see further discussion in section **II.3.3.1**). In CL images (Fig. 45B), zircon grains show pronounced and luminescent bands of variable cathodoluminescence.

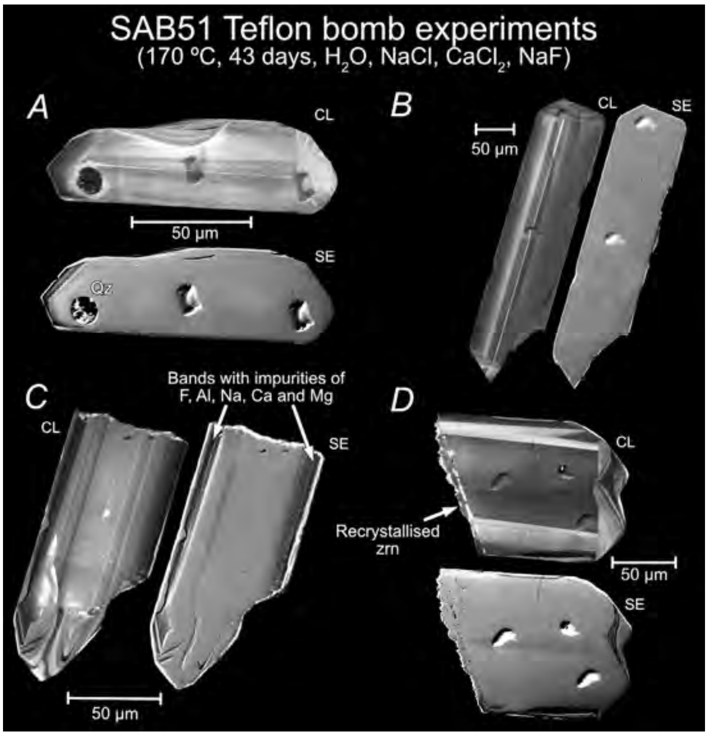

Fig. 49. SE and CL images of low-T leaching experiments from zircons of tonalite SAB51. A) Zircon grain from H_2O *leaching experiment (run Z-2) that appears zoned with alternating light-gray and dark-gray bands parallel to the longest axis. B) Zircon grain from NaCl leaching experiment (run Z-4), that appears zoned with alternating light-gray and dark-gray bands parallel to the longest axis. C) Zircon grain from* $CaCl_2$ *leaching experiment (run Z-6), that appears zoned with alternating light-gray and dark-gray bands parallel to the longest axis. These bands present impurities of F, Ca, Na and Mg. D) Zircon grain from NaF leaching experiment (run Z-8); very thin band roughly parallel to a fracture surface of a split grain with abundant micropores and luminescent zircon.*

Zircon is stable (no baddeleyite formation) for all experiments carried out in teflon bomb (Figs. 42-48).

II.3.1.2 Composition of fluids

The composition of leachate extracted from the experiments carried out in Teflon bombs and of the solution added to the experimental charges are summarized in Table ST4 (for experimental procedures and run conditions, see Table 8).

Double normalization to Zr and to the average of the LA-ICP-MS analyses of the untreated zircons ($(j/Zr)_N = (j/Zr)^{liq}/(j/Zr)^{Zrn}_{Un}$ where j is the abundance of a chemical element by weight and "Un" stands for untreated) were used to display the compositions of leachates in spiderdiagrams. This permits us to evaluate the fractionation between trace elements and Zr with respect to that of untreated zircon (Fig. 50).

In H_2O leachates from whole-rock powder, fractionation of the trace-elements with respect to Zr of the leachate decreases from Nb, La, Ce, Pr, and Nd ($(j/Zr)_N$ ratios > 10^4), to Th, U, Pb, and the rest of REE whose $(j/Zr)_N$ ratios decrease continuously from 10^4 to 40, whereas $(Hf/Zr)_N$ ratios in the leachates are similar to those in the untreated zircon. In H_2O leachates with added zircon, the fractionation of trace-elements with respect to Zr in the leachate shows a similar pattern, excepting in Eu that is more variable. This imply that the contribution of zircon grains to the leachates is significantly smaller than this of the rock powder. It is remarkable to note that, in both type of experiments, the fractionation of Y and Th with respect to Zr are higher than those of Yb and Lu, and U, respectively.

In 2M NaCl leachates, the fractionation of Pb with respect to Zr is very intense ($(Pb/Zr)_N$ ratios of ca. 10^7), whereas this for U is higher than Th. Fractionation of REE-Y, Nb and Hf with respect to Zr, excluding Eu, are similar to those from the H_2O leachates; however, this for Pr, Nd, Sm, Gd to Lu and Y is higher in zircon added than in whole-rock powder experiments, suggesting a significant contribution of zircon to the leachate.

In 2M $CaCl_2$ leachates, the fractionation patterns share many features with the previous experiments including a larger $(Y/Zr)_N$ with respect to HREE. REE fractionation with respect to Zr, including Eu, shows a systematic decrease with increasing atomic number with maximum values for $(La/Zr)_N$ ratios of ca. 10^9. The fractionation of all elements with respect to Zr, except Nb, Pb and Hf, in zircon added experiments is significantly higher than in whole-rock powder ones. Notably, fractionation of Hf with respect to Zr is 10 times higher than that of untreated zircon. As observed in H_2O leachates, the fractionation of Th with respect to Zr is higher than for U.

In 1M NaF leachates, the overall fractionation patterns are similar to those of H_2O leachates. However, there are clear differences between zircon added and whole-rock powder experiments, being detected in this latter a general decrease of double normalized trace-elements ratios that reach values of one for U and Y and even lower than one for the heaviest REE and Hf. This effect may be due to the precipitation of the aggregates of calcium hydroxide that may entrap a fraction of the trace-elements released from zircon.

II.3.1.3 Oxygen isotope in zircon

The $\partial^{18}O$ distribution for the H_2O, 2M NaCl, 2M $CaCl_2$ and 1M NaF leaching experiments with the sample SAB50 are represented in Fig. 51. They show the $\partial^{18}O$ modal values of the pristine zircons in green vertical lines and the $\partial^{18}O$ of the experiment itself in red vertical lines.

The $\partial^{18}O$ distribution in the untreated zircon grains of sample SAB50 presents two populations, one from the Ediacaran inherited cores at six of $\partial^{18}O$ and one from the Cambro-Ordovician rims at nine $\partial^{18}O$.

In the H_2O leaching experiment, the $\partial^{18}O$ distribution of untreated zircon grains slightly varies. The distribution of the cores becomes bimodal, and that of the rims shifts hardly to an $\partial^{18}O$ of 10.

In $CaCl_2$ and NaCl leaching experiments, the two populations (cores and rims) of untreated zircon grains shift considerably to the right, i.e. towards higher $\partial^{18}O$ values (Rims: 8.3 and 8.4, and cores:10.4 and 10.5 for $CaCl_2$ and NaCl, respectively). In addition, Figs. 50C and D show how these two distinct populations of cores and rims in the untreated zircon grains start to overlap in the $CaCl_2$ experiment and even more so in the NaCl experiment.

In the NaF leaching experiment, the $\partial^{18}O$ distribution is shifted even further to the right. The distribution of cores increases to an $\partial^{18}O$ of 9.3 and the distribution of rims to 11.3. The overlap between the two populations is even higher, but it is still possible to distinguish between cores and rims.

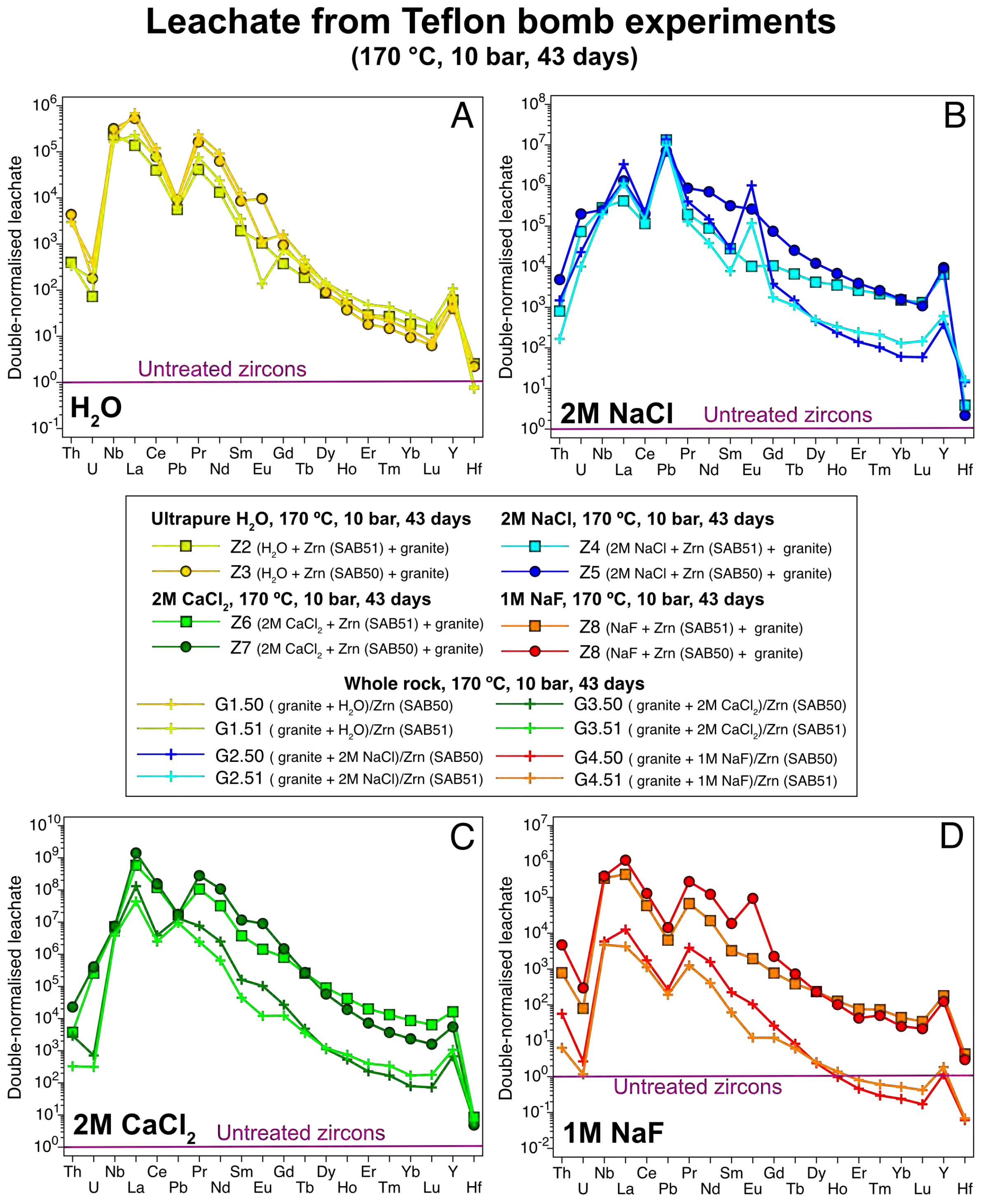

Fig. 50. Double-normalized leachate plots from the low-T leaching experiments from sample SAB50 orthogneiss, SAB51 tonalite and whole rock. A) ultrapure H_2O leaching experiments (gold and yellow-green circles, squares and pluses, whole-rock + SAB50, whole-rock + SAB51 and whole-rock, respectively). B) 2M NaCl leaching experiments (light-blue and dark-blue circles, squares and pluses, whole-rock + SAB50, whole-rock + SAB51 and whole-rock, respectively). C) 2M $CaCl_2$ leaching experiments (the light-green and dark-green circles, squares and pluses, whole-rock + SAB50, whole-rock + SAB51 and whole-rock, respectively). D) 1M NaF leaching experiments (the red and orange circles squares, and pluses, whole-rock + SAB50, whole-rock + SAB51 and whole-rock, respectively). See Table 8 for specific data of each experiment.

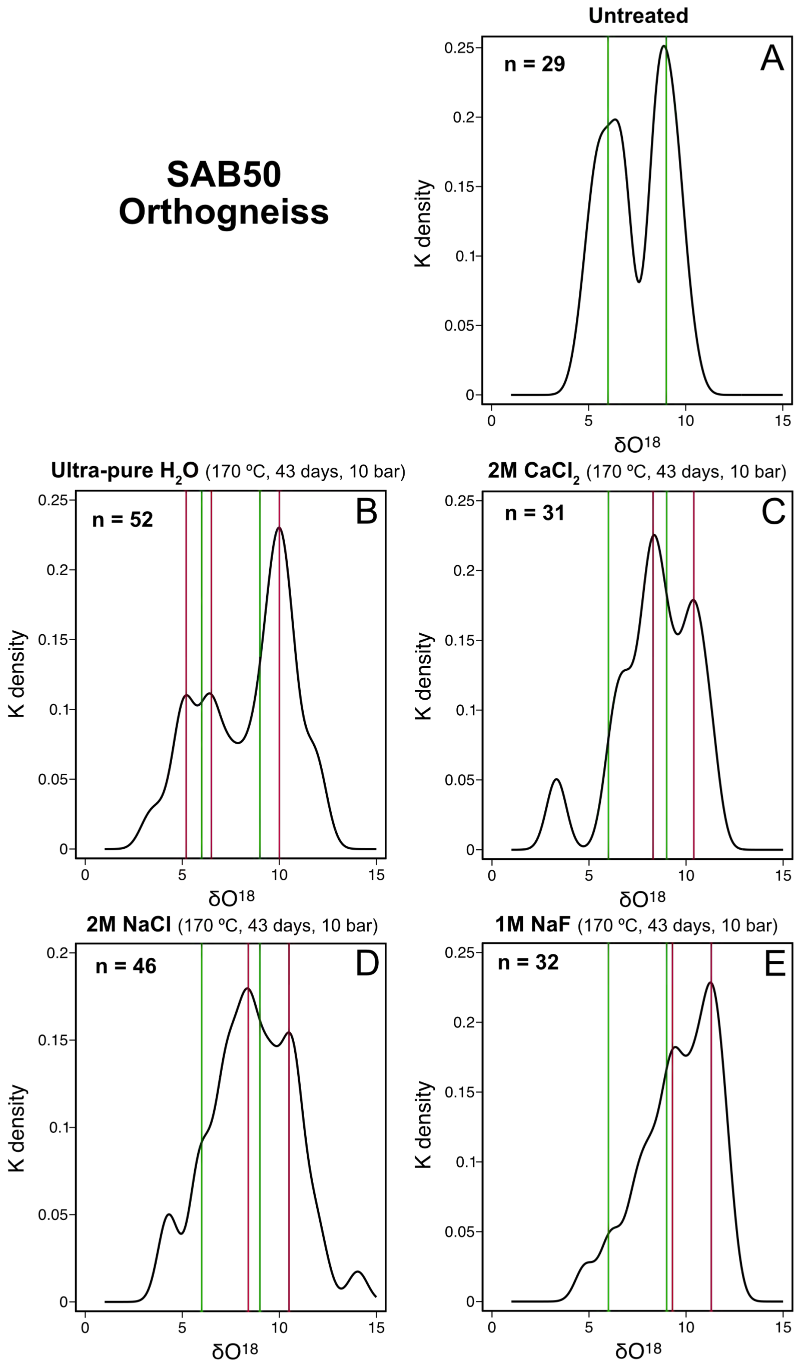

Fig. 51. ∂^{18}O distributions of untreated zircon grains and low-T leaching experiments from sample SAB50. A) Untreated zircon grains, B) H_2O leaching experiment, C) $CaCl_2$ leaching experiment, D) NaCl leaching experiment, and E) NaF leaching experiment. Vertical green lines represent modal values for untreated zircon grains. Vertical red lines represent modal values for experiments See Table ST5 for data.

The ∂^{18}O distribution for the H_2O, 2M NaCl, 2M $CaCl_2$ and 1M NaF leaching experiments with the sample SAB51 are represented in Fig. 52. They show the same vertical green lines with the modal values of the untreated zircon grains and the vertical red lines for the modal values of each experiment.

The ∂^{18}O distribution of untreated zircon grains from sample SAB51 presents a clear population of 6.8.

In the H_2O leaching experiment, the ∂^{18}O distribution has shifted slightly to the right with an ∂^{18}O value of 7.4.

In the $CaCl_2$ leaching experiment, the $\partial^{18}O$ distribution is practically unchanged concerning untreated zircon grains. The modal value of $\partial^{18}O$ is 6.5.

In the NaCl leaching experiment, the $\partial^{18}O$ distribution shifts considerably to the right reaching an $\partial^{18}O$ value of 8.7.

In the NaF leaching experiment, the $\partial^{18}O$ distribution shifts to the right up to an $\partial^{18}O$ value of 8.

The $\partial^{18}O$ data for both experimental samples and untreated zircon grains are given in table ST5.

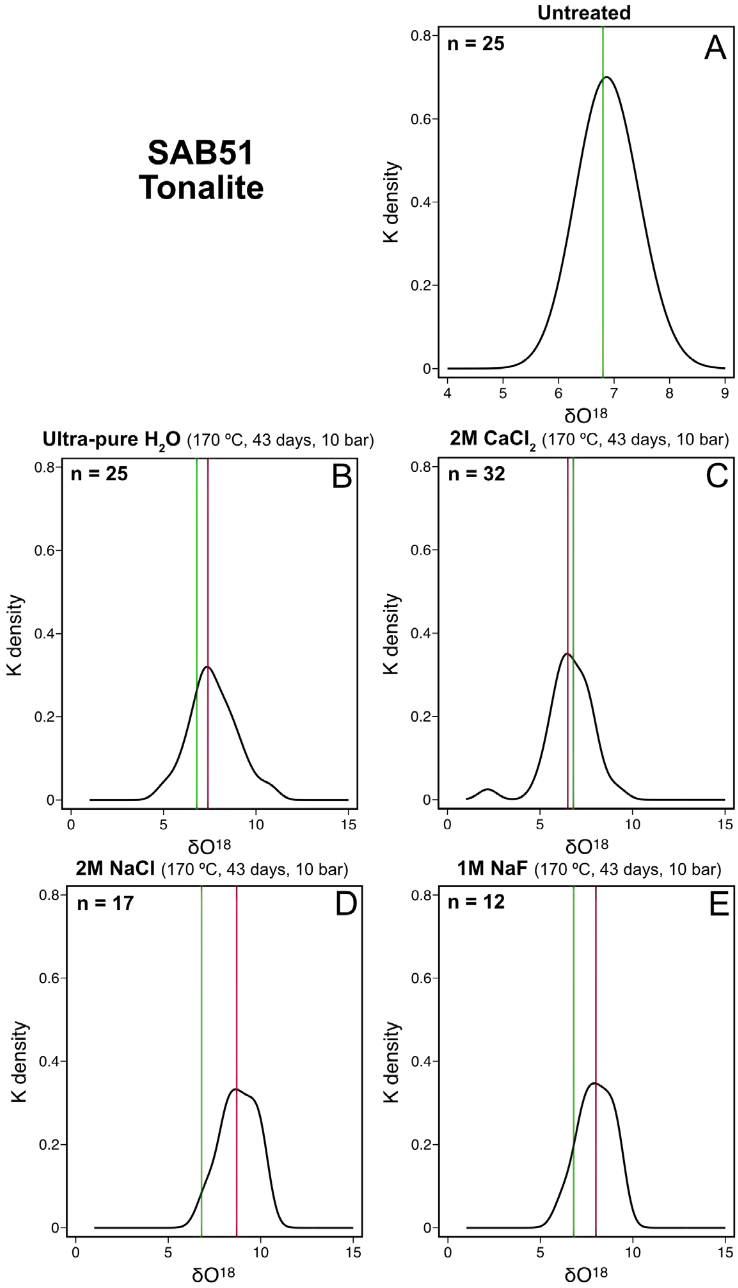

Fig. 52. $\partial^{18}O$ distributions of untreated zircon grains and low-T leaching experiments from sample SAB51. A) Untreated zircon grains, B) H_2O leaching experiment, C) $CaCl_2$ leaching experiment, D) NaCl leaching experiment, and E) NaF leaching experiment. Vertical green lines represent modal values for untreated zircon grains. Vertical red lines represent modal values for experiments. See table ST5 for data.

II.3.2 Autoclave experiments

Autoclave hydrothermal experiments were carried out in zircon SAB50 under silica-saturated and undersaturated conditions and employing ultrapure H_2O and 2M NaCl, 2M $CaCl_2$ and 1M NaF solutions to determine its stability relationships and to characterize the traces-elements released from this (see section **II.1.2.3** and Table 8, for experimental procedures and run conditions).

II.3.2.1 Experimental products

Fluid infiltration into the interior of zircon grains was enhanced by radial microcracks and the core-rim interface of partially broken zircons that caused preferential dissolution and zircon replacement by dissolution-precipitation mechanism.

II.3.2.1.1 Silica saturated experiments

In the silica-saturated H_2O leaching experiment (run HT-30), 94 % of zircon grains were recovered after the experiment. Quartz appears as thin films and dendritic aggregates onto the surface of zircon grains and infilling microveins, which may suggest quartz precipitation upon quenching (Figs. 53 and 54B).

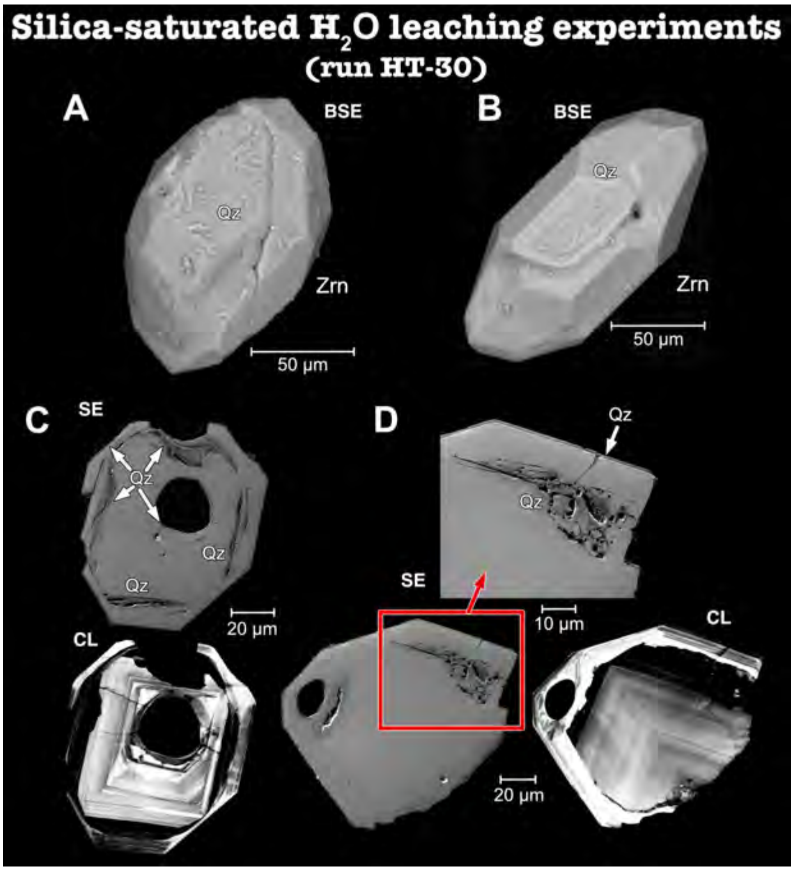

Fig. 53. BSE, SE and CL images of products from high-T silica-saturated H_2O leaching experiments. A and B) zircon grains with a thin film and dendritic aggregates of quartz onto the surface. C and D) SE and CL images of zircon grains with a thin film and infilling micro veins of quartz. Mineral abbreviations after Whitney & Evans (2010).

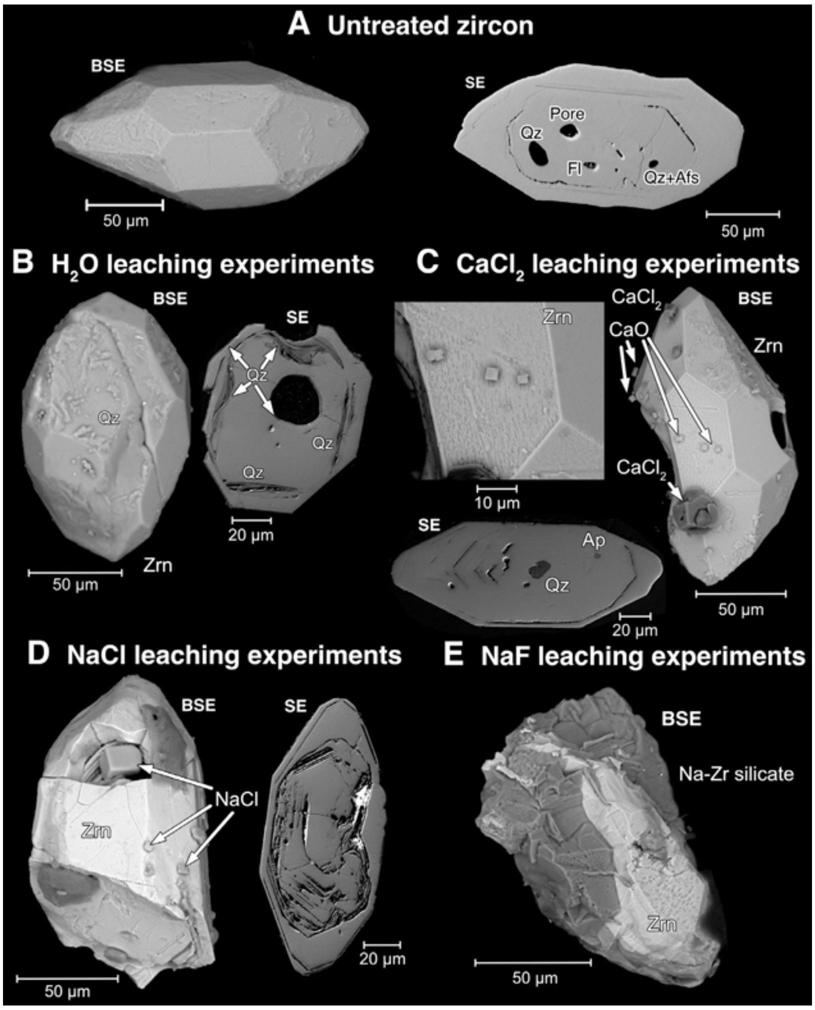

Fig. 54. BSE and SE images of untreated and hydrothermal high-T silica-saturated experiments zircon grains. A) Untreated euhedral short stubby prism zircon grain terminated by long pyramids with smooth and slightly rough faces. Euhedral zircon grain hosting monomineralic inclusions of quartz and fluorite and a tear drop-shaped polymineralic inclusion of quartz + alkali feldspar. B) H_2O leaching experiments: euhedral zircon grain with a thin film and dendritic aggregates of quartz onto the surface; zircon grain with a thin film and infilling micro veins of quartz C) $CaCl_2$ leaching experiments: zircon grain partially dissolved with a very fine zircon network deposited onto the face. There are calcium chloride and Calcium oxide euhedral grains onto the zircon surface; Euhedral zircon grain with mineral inclusions of apatite and quartz. D) NaCl leaching experiments: subhedral zircon grain with dissolution channels along the radial microcracks and the core-rim interface. There are sodium chloride euhedral grains onto the zircon surface; euhedral zircon grain where it can be observed dissolution channels along the core-rim interface. E) NaF leaching experiments: anhedral zircon grain partially replaced by a sodium zirconium silicate that is locally porous. Mineral abbreviations after Whitney & Evans (2010).

In the silica-saturated $CaCl_2$ leaching experiment (run HT-15), 90 % of zircon grains were recovered after the experiment. A very fine zircon network is deposited onto the face of the zircon grains (Figs. 54C and 55A and B), thus removing the rough surface that characterizes untreated zircon grains (see Fig. 54A). Occasionally irregular films of zircon are deposited onto this network. These textural relationships suggest the congruent dissolution of zircon in a silica-saturated fluid and the reprecipitation of a new generation of zircon. Acicular grains of Cl-Ca silicates are also developed (Fig. 55D and E).

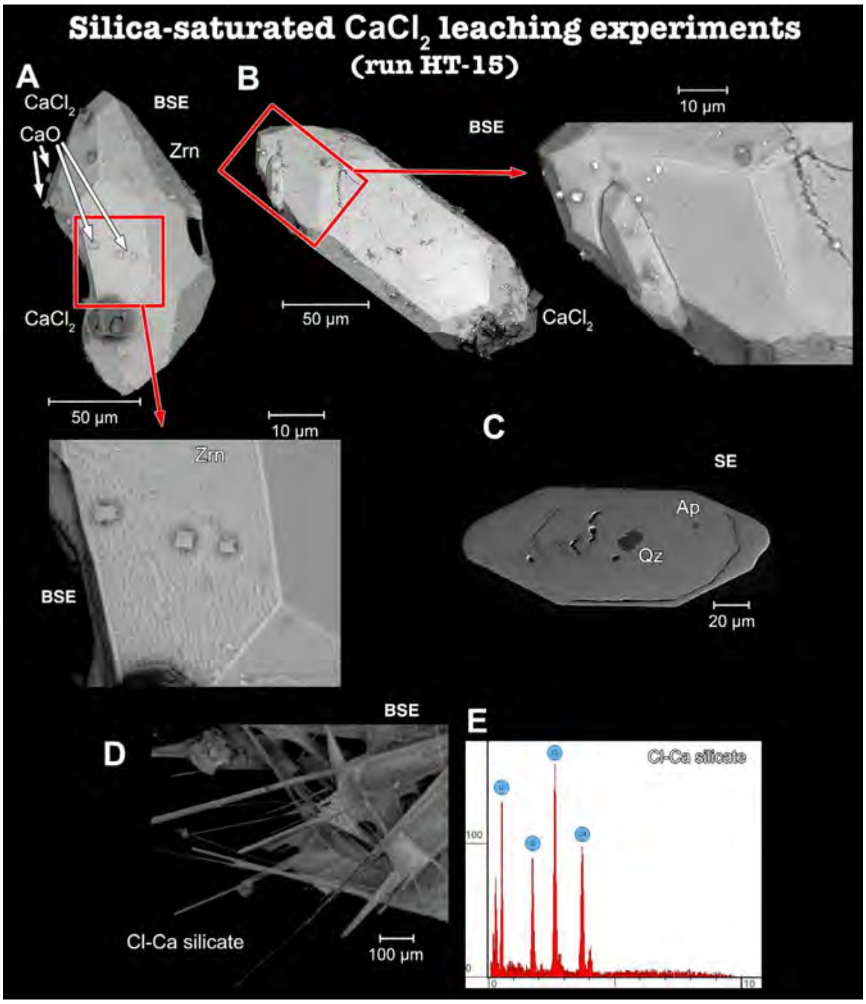

Fig. 55. BSE and SE images of products from high-T silica-saturated $CaCl_2$ leaching experiments. A) Zircon grain partially dissolved with a very fine zircon network deposited onto the face. There are calcium chloride and Calcium oxide euhedral grains onto the zircon surface. B) Euhedral zircon grain with a very fine network deposited onto the faces. C) Euhedral zircon grain with mineral inclusions of apatite and quartz. D) Acicular grains of Ca-Cl silicates. E) Spectrum of the Cl-Ca silicate. Mineral abbreviations after Whitney & Evans (2010).

In the silica-saturated NaCl leaching experiment (run HT-22), 44 % of zircon grains were recovered after the experiment. The low efficiency of zircon recovery suggests that zircon dissolution was significant, with dissolution channels observed along the radial microcracks and the core-rim interface of broken grains, thus giving evidence for congruent zircon dissolution (Figs. 56A-C, and 54D). Rare cathodoluminescent porous zircon bands crosscut the oscillatory zoning at the core-rim interface of zircon grains (Fig. 56B) may be evidence for zircon reprecipitation. It was also observed the precipitation of quench halite and rare thin films of quench quartz onto zircon faces (Fig. 56A-B).

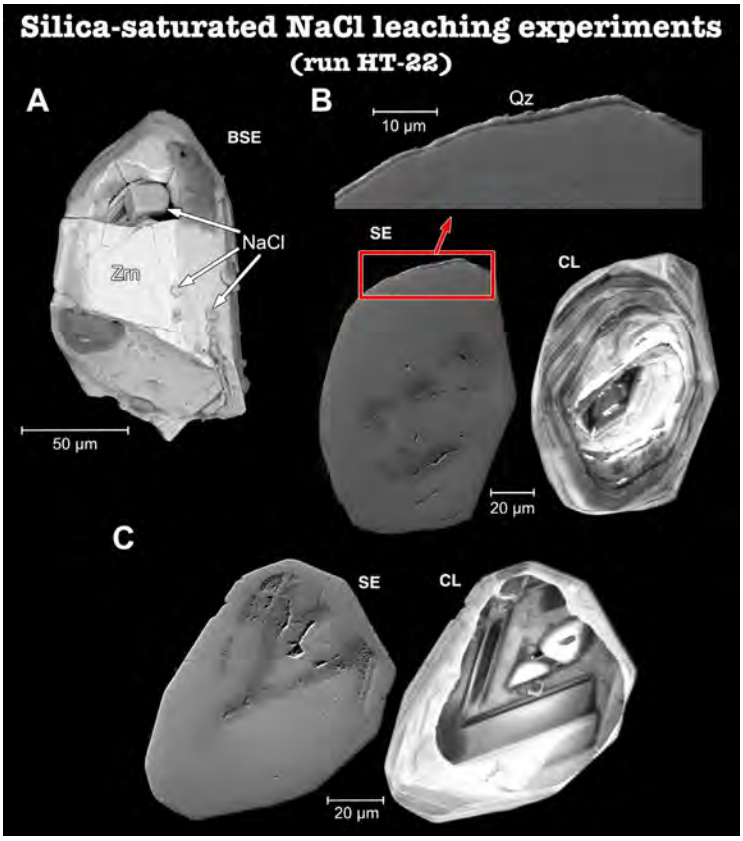

Fig. 56. BSE, SE and CL images of products from high-T silica-saturated NaCl leaching experiments. A) Subhedral zircon grain with preferential dissolution along concentric shells. There are sodium chloride euhedral grains onto the zircon surface. B) Euhedral zircon grain with a thin film of quartz onto zircon surfaces. In CL image, a cathodoluminescent porous zircon bands at the core-rim interface crosscutting the oscillatory zoning of the rim. C) Euhedral zircon grain with oscillatory zoning and an Ediacaran euhedral inherited core overgrown by a Cambro−Ordovician rim. Mineral abbreviations after Whitney & Evans (2010).

In silica-saturated NaF leaching experiments (run HT-24), only 31 % of zircon grains were recovered, suggesting significant dissolution. All recovered zircon grains are anhedral, appearing replaced partially by a locally porous Na-Zr-silicate (Fig. 57A, C and D). This mineral phase also appears to fill zircon microcracks (Fig. 57C) and as fibrous aggregates that were probably dispersed in the solution (Fig. 57B).

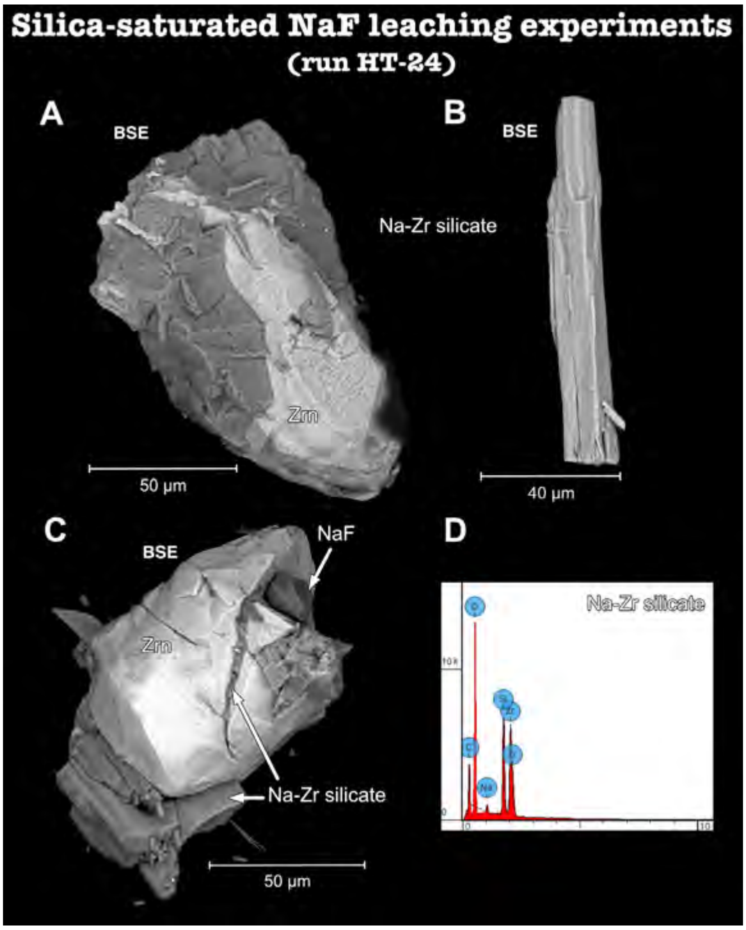

Fig. 57. BSE images of products from high-T silica-saturated NaF leaching experiments. A) Anhedral zircon grain partially replaced by a sodium zirconium silicate that is locally porous (most probably vlasovite). B) Isolated sodium zirconium silicate fibrous aggregate. C) Anhedral zircon grain partially replaced by a, locally porous, sodium zirconium silicate. This mineral phase also appears filling zircon microcracks. D) Spectrum of sodium zirconium silicate.

II.3.2.1.1 Silica undersaturated experiments

In the silica-undersaturated H_2O leaching experiment (run HT-31), 73 % of grains were recovered. The zircon grains appear pseudomorphically replaced by very tiny aggregates of microporous baddeleyite that appear along rims and microcracks (Fig. 58); they also contain fluorine-free euhedral apatite (Fig. 58B-C), thus evidencing its dissolution and re-precipitation. However, no zirconium silicates were observed, implying that the silica released from zircon was dissolved in the fluid. The baddeleyite aggregates are usually equidimensional, appearing as more coarse prismatic grains perpendicular to the surfaces of microcracks and pores (Fig. 58D to G). The presence of micropores in the baddeleyite aggregates suggests that the replacement of zircon by baddeleyite took place by coupled dissolution-precipitation mechanisms, as discussed in section **II.3.3.1**.

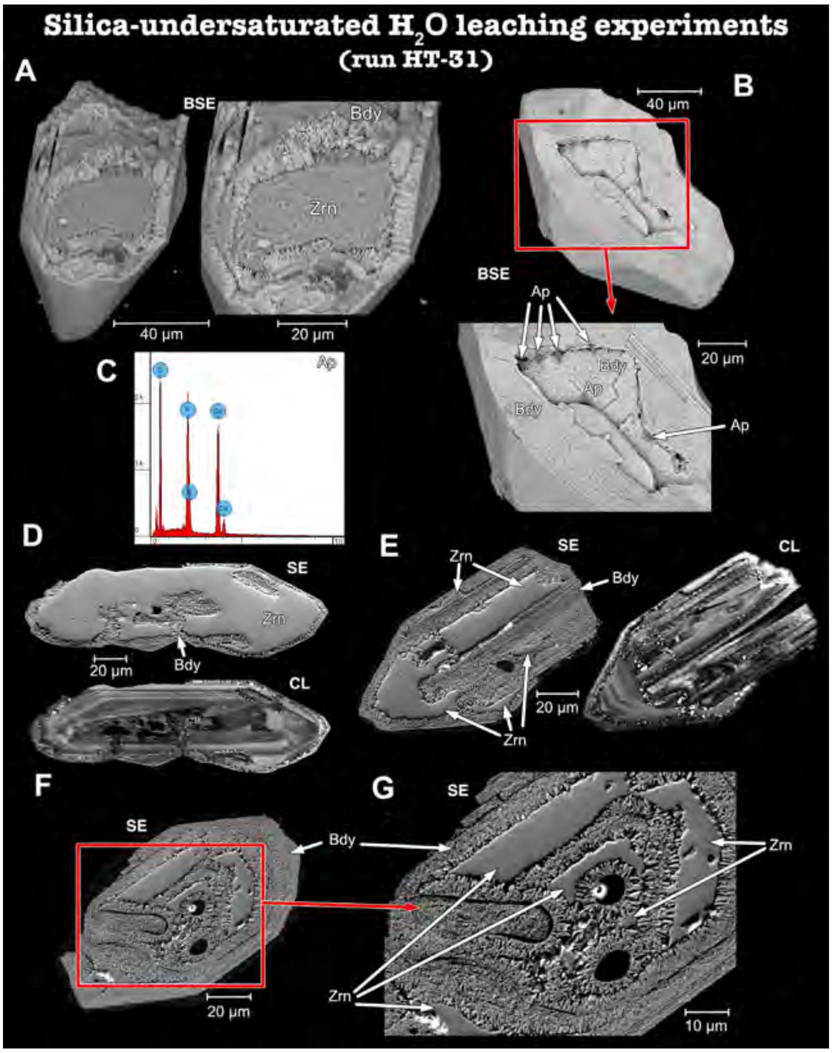

Fig. 58. BSE, SE and CL images of products from high-T silica-undersaturated H_2O leaching experiments. A) Partially broken zircon grain pseudomorphically replaced by tiny aggregates of microporous baddeleyite. B) Subhedral zircon grain pseudomorphically replaced by tiny microporous baddeleyite with Cl-apatite onto the surface. C) Spectrum of apatite from B. D, E and F) Euhedral zircon grain pseudomorphycally replaced by baddeleyite that appear along rim and microcracks. G) Detail image of the zircon grain F showing baddeleyite appears as more coarse prismatic grains perpendicular to the surfaces of the microcracks and pores. Mineral abbreviations after Whitney & Evans (2010).

In silica-undersaturated $CaCl_2$ leaching experiments, 81 and 71 % of zircon grains were recovered in runs HT-19 (3 days) and HT-14 (8 days), respectively. No significant mineral and textural differences were observed in the two runs. Zircon grains are pseudomorphically replaced by microporous baddeleyite aggregates showing textures very similar to those developed in the H_2O leaching experiments (Figs. 59 and 58). They also contain euhedral prismatic and botryoidal aggregates Cl-apatite evidencing its partial dissolution and re-precipitation (Fig. 58A, B, G and H) as happens in the H_2O, silica-undersaturated leaching experiments (run HT-31). Its composition contrasts with the absence of chlorine in apatite enclosed in the baddeleyite aggregates that are, most probably, relicts. Acicular Cl-Ca silicate that appears on the surface of baddeleyite pseudomorph after zircon and of $CaCl_2$ grains (Fig. 59A-D) are interpreted as quench mineral phases.

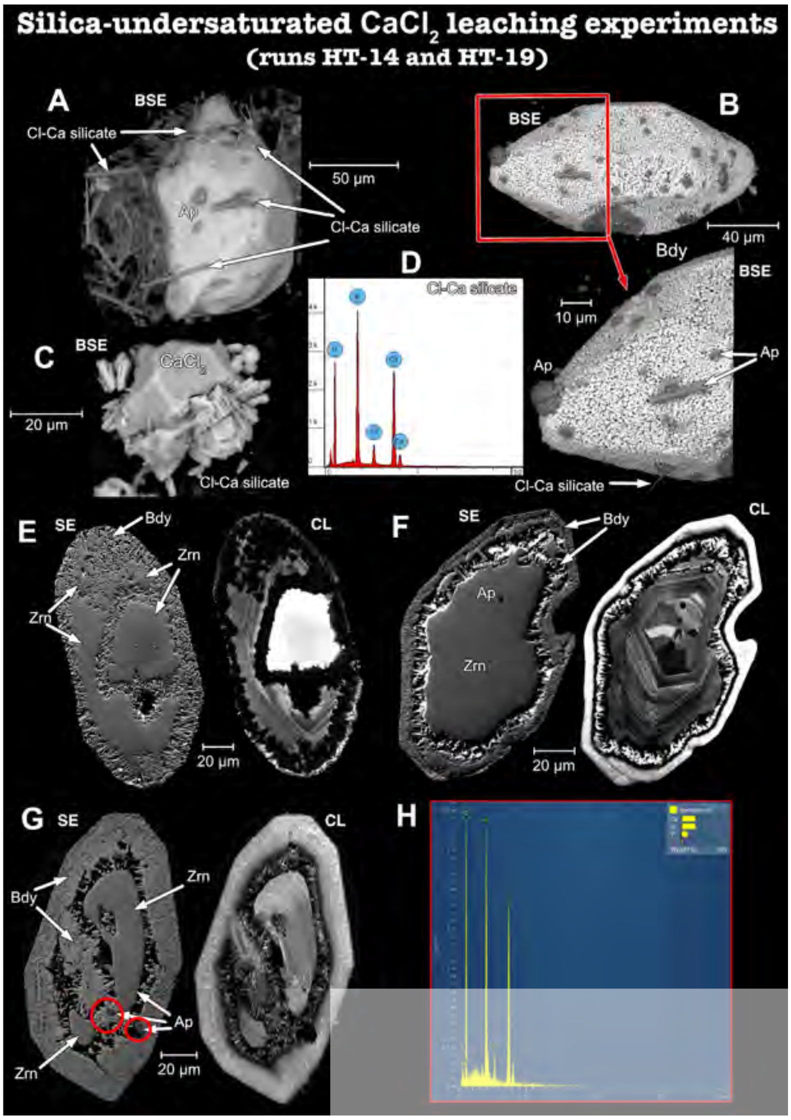

Fig. 59. BSE, SE and CL images of products from high-T silica-undersaturated CaCl$_2$ leaching experiments. A) Anhedral zircon grain from experiment HT-14 (run of 8 days) pseudomorphically replaced by microporous baddeleyite aggregates. It contains Cl-apatite and an acicular Cl-Ca silicate onto the surface of baddeleyite pseudomorph. B) Euhedral zircon grain from experiment HT-19 (run of 3 days) pseudomorphically replaced by microporous baddeleyite aggregates. It contains Cl-apatite and an acicular Cl-Ca silicate onto the surface of baddeleyite pseudomorph. C) Isolated amorphous and acicular grain of Cl-Ca silicate. D) Spectrum of Cl-Ca silicate. E and F) Euhedral to Subhedral zircon grains pseudomorphically replaced by baddeleyite along rims and microcracks from experiment HT-14. G) Euhedral zircon grain pseudomorphically replaced by baddeleyite along rim and microcracks from experiment HT-19. H) Spectrum of Cl-apatite from G. Mineral abbreviations after Whitney & Evans (2010).

In the silica-undersaturated NaCl leaching experiment (run HT-20), only 33 % of zircon grains were recovered. An aggregate of microporous baddeleyite totally replaces the zircon (Fig. 60A, B and D). This phase can also appear in aggregates forming euhedral prisms evidencing direct precipitation from the fluid (Fig. 60C).

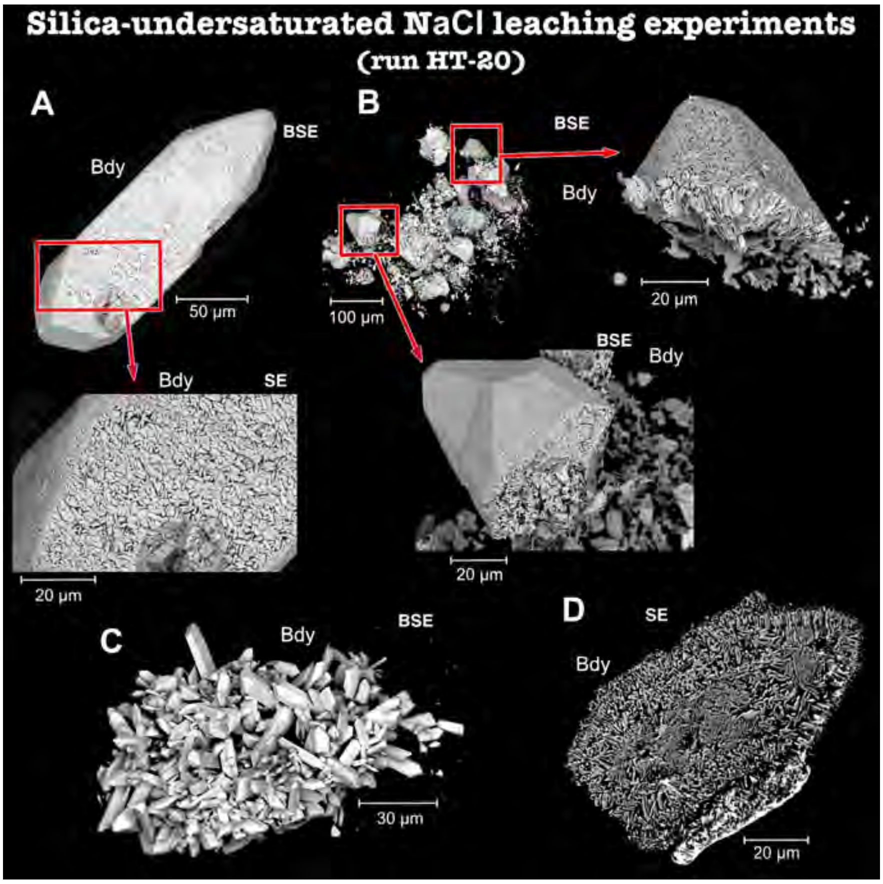

Fig. 60. BSE and SE images of products from high-T silica-undersaturated NaCl leaching experiments. A) Euhedral zircon grain replaced by an aggregate of microporous baddeleyite. B) Baddeleyite fragments pseudomorphically replacement zircon that evidence no zircon relict. C) Aggregate euhedral prisms of baddeleyite. D) Subhedral zircon grain totally replaced by an aggregate of microporous baddeleyite. Mineral abbreviations after Whitney & Evans (2010).

No relicts of zircon grains were recovered in silica-undersaturated NaF leaching experiments (runs HT-17 and HT-21). Only aggregates of euhedral prisms of baddeleyite (Fig. 61A), similar to those present in run HT-20, were observed. Rare quartz, probably produced during quenching, was also observed (Fig. 61B).

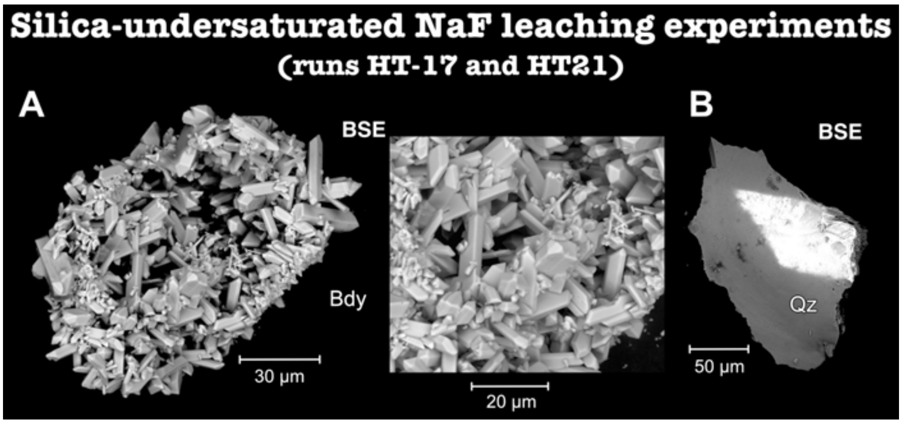

Fig. 61. BSE images of products from high-T silica-undersaturated NaF leaching experiments. A) Aggregates euhedral prisms of baddeleyite. B) Quartz grain. Mineral abbreviations after Whitney & Evans (2010).

II.3.2.2 Composition of fluids

The compositions of leachates extracted from the experiments carried out in the autoclave and of the solutions added to the experimental charges are summarized in Table ST4 (for experimental procedures and run conditions, see Table 8).

Double normalization to Zr and the average of the LA-ICP-MS analyses of the untreated zircons, $(j/Zr)_N$, was also used for displaying the compositions of leachates in spiderdiagrams (Fig. 62).

The overall patterns of leachate compositions from the both silica saturated and undersaturated, pure-water leaching experiments (runs HT-30 and HT-31) are very similar (Fig. 62A). They have a maximum for Nb and La ($(Nb/Zr)_N$ and $(La/Zr)_N$: > 10^6), a trough in Ce and Pb ($(Ce/Zr)_N$ and $(Pb/Zr)_N$: 1-4 10^5) and a continuous decrease from Pr ($(Pr/Zr)_N$: 10^6) to Hf ($(Hf/Zr)_N$: 3 in run HT-31; Hf is below detection limit in run HT-30), excepting two positive anomalies at Eu ($(Eu/Zr)_N$: 2-3 10^5) and Y ($(Y/Zr)_N$: 200-400). U and Th (only run HT-30) show a moderate fractionation ($(U/Zr)_N$ and $(Th/Zr)_N$: 400-1000) that is higher in Th.

The patterns of leachate compositions from both silica saturated and undersaturated, NaCl and $CaCl_2$ leaching experiments (runs HT-14, HT-15 and HT-19, HT-20 and HT-22) are very similar to those from the H_2O leaching experiments except for a strong positive Pb anomaly in the silica undersaturated $CaCl_2$ leaching experiments (runs HT-14 and HT-19) that is less pronounced in the silicate saturated $CaCl_2$ leaching one (run HT-15). Notably, there is a marked Th/U fractionation in this latter.

The leachate extracted from the silica-undersaturated H_2O experiment with zircon replacement by baddeleyite (run HT-31) shows a slightly higher fractionation of REE and Y with respect to Zr than this from the silica-saturated one (run HT-30), thus increasing by a factor of 1.8-4. The U/Zr ratio shows the opposite behavior being higher in the HT-30 run by a factor of 2.5.

By contrast, the fractionation of most LREE with respect to Zr in the leachate extracted from the silica-saturated NaCl experiment (run HT-22) is higher than in the silica-undersaturated one (run HT-20), increasing the La/Zr to Eu/Zr ratios by a factor of 2-9. Notably, the Nb/Zr ratio from this run is higher than in the baddeleyite-bearing HT-20 run by a factor of 35.

In the silica undersaturated $CaCl_2$ leaching experiments, the leachates from runs at 3 (run HT-19) and 8 (HT-14) days show relatively small differences in values for most elements, excepting Nb, La, Ce and Y that are higher in the run HT-19 by a factor ranging 2.5-6, and Th, Pb and Hf with higher values in the run HT-14 by a factor of 2.2-4. These differences may be attributed to a different extent of zircon-baddeleyite replacements and the amount of fluid added, which is higher in the HT-19 (Table 8). In the silica-saturated $CaCl_2$ leaching experiments (run HT-15), the leachate presents significantly lower values in Th/Zr, Pb/Zr, HREE/Zr and Y/Zr ratios and higher in U/Zr and Hf/Zr ratios.

The overall patterns of leachates from the NaF leaching experiments are similar to those from the other experiments. However, there is a significantly lower fractionation of the elements with respect to Zr, decreasing values by approximately one order of magnitude in the silica-undersaturated experiment (run HT-17) and by two orders of magnitude in the silica-saturated one (HT-24). The lower values detected in this latter could be the equilibration of fluid with Na-Zr-silicate instead of baddeleyite. However, in the former, it must be caused by a specific effect of the NaF solution, as it is saturated in baddeleyite as in the other silica-undersaturated runs.

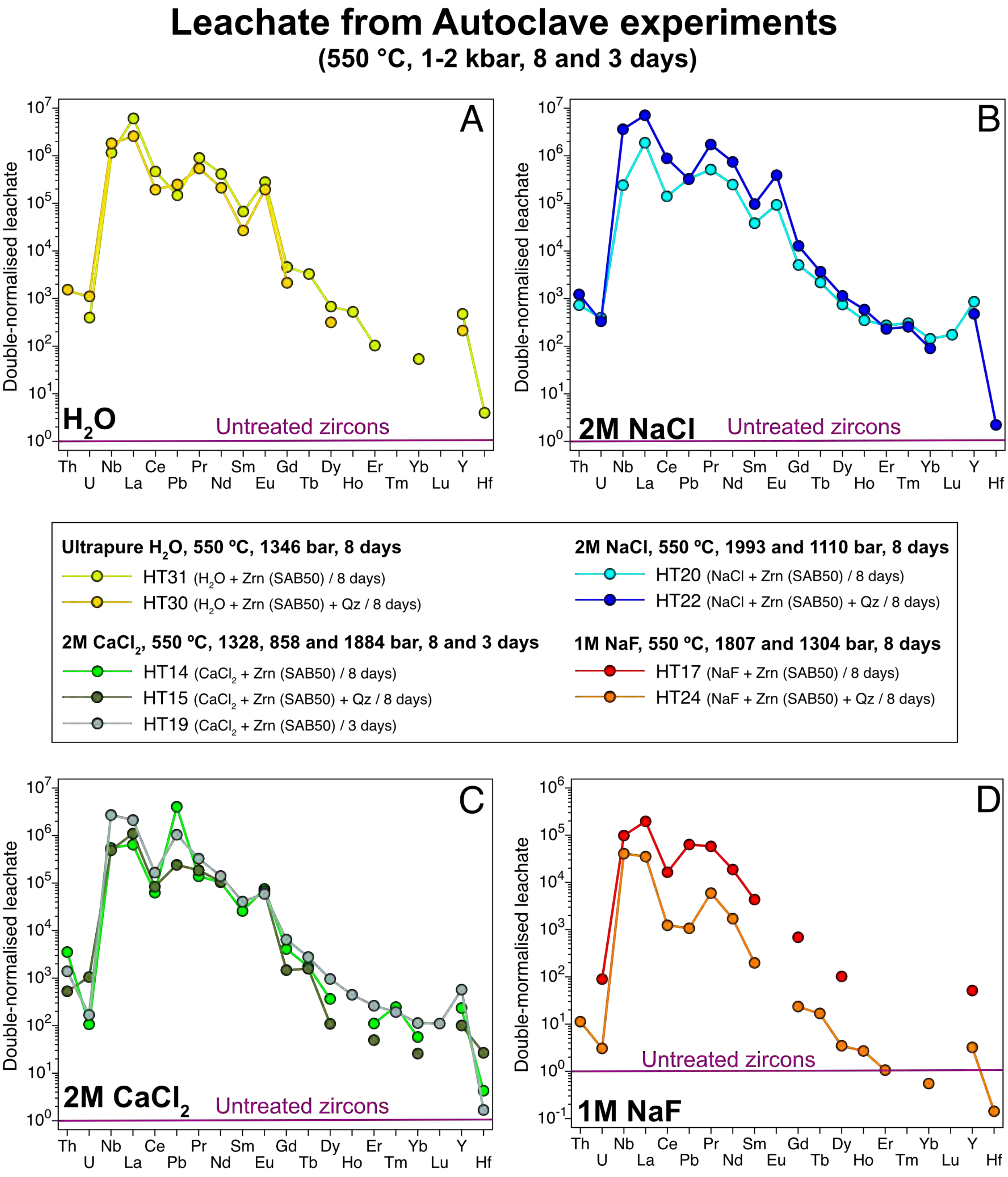

Fig. 62. Double-normalized leachate plots from the high-T leaching experiments from sample SAB50 orthogneiss. A) experiments carried out with ultrapure H_2O for SiO_2-saturated and SiO_2-undersaturated during 8 days. B) experiments carried out with 2M NaCl for SiO_2-saturated and SiO_2-undersaturated during 8 days. C) experiments carried out with 2M $CaCl_2$ for SiO_2-saturated and SiO_2-undersaturated during 8 and 3 days. D) experiments carried out with 1M NaF for SiO_2-saturated and SiO_2-undersaturated during 8 days. The yellow-green and gold circles are the experiments carried out with ultrapure H_2O (SiO_2-undersaturated and SiO_2-saturated respectively), the light-blue and dark-blue circles are the experiments carried out with NaCl (SiO_2-undersaturated and SiO_2-saturated respectively), the light-green and dark-green circles are experiments carried out with $CaCl_2$ during 8 days (SiO_2-undersaturated and SiO_2-saturated respectively), the grey circles are for the experiment of 3 days duration with $CaCl_2$ (SiO_2-undersaturated), and the red and orange circles are the experiments with NaF (SiO_2-undersaturated and SiO_2-saturated respectively).

II.3.3 Discussion of the hydrothermal experiments

II.3.3.1 Zircon-baddeleyite-Na-Zr-silicates phase relationships

The experimental results show that zircon can dissolve incongruently to baddeleyite and Na-Zr-silicates in the presence of aqueous and saline solutions giving rise to a large diversity of replacement textures.

In the low-T whole-rock powder, zircon added leaching experiments, the absence of baddeleyite and zirconium silicates shows that the zircon remained stable in the presence of the silica-saturated, H_2O and saline fluids. Geisler et al. (2002 and 2003b) have indicated that no recrystallization of metamict zircon occurs in hydrothermal experiments at T < 200 ºC. Accordingly, the micropores bands of SAB-51 zircon remain non-cathodoluminescent after the experiments (compare with high-T dry annealing experiments (Figs. 35A and B and ST2A-E and G), see also Morales et al. (2022), for a discussion). In contrast, the occurrence of local cathodoluminescent zircon suggests only very rare recrystallization in the NaF leaching experiment on sample SAB-51 (Fig. 49D). On the other hand, the permeability increase detected in radial microcracks and along the core-rim interfaces of SAB-50 zircons and in microporous bands of SAB-51 zircons (Fig. 47) instead suggests congruent zircon dissolution that caused releasing of the impurities residing in its crystalline structure into the fluids.

Zircon dissolved congruently in the high-T, silica-saturated leaching experiments with H_2O, $CaCl_2$ and NaCl fluids. In addition, zircon reprecipitated on the grain faces of zircon in the $CaCl_2$ leaching experiment (Fig 55) and along the core-rim interface of zircon grains from the NaCl leaching experiment (Fig 56). In the experiments with NaF, however, zircon dissolved incongruently, forming Na-Zr-silicates. The absence of these mineral phases in the NaCl experiment suggests that the solution's fluoride anions favored the replacement. However, the replacement of zircon by Na-Zr-silicates has also been reported by Ayers et al. (2012) in both silica-saturated and undersaturated NaOH solutions, and by Rizvanova et al. (2000) in Na_2CO_3 solutions. Ph measurements of the solutions used in the leaching experiments performed in this work at room temperatures indicate that the NaF solutions are significantly more basic (Ph = 10) than NaCl (Ph = 8.4) and $CaCl_2$ (Ph = 7.86). Therefore, the presence of Na cations in a basic medium may be the critical factor for the incongruent dissolution of zircon to the Na-Zr-silicates.

Zircon dissolved incongruently to baddeleyite in all the high-T, silica-undersaturated leaching experiments. The replacement seems to be less intense in H_2O and $CaCl_2$ leaching experiments, where abundant zircon relicts occur, being, however, much more intense in NaCl and NaF leaching experiments where zircon replacement went to completion. The presence of micropores in the baddeleyite aggregates suggests that the incongruent dissolution of zircon occurred by a coupled dissolution-precipitation mechanisms (Putnis, 2002; Geisler et al., 2007; Putnis et al., 2009; Putnis & Austrheim, 2013). The importance of fluid infiltration along microcracks and pores in enhancing zircon replacement by baddeleyite is evidenced by the presence of zircon grains with very different degrees of transformation and by the growth of the relatively coarser grain of prismatic baddeleyite next to these channels (Figs. 58, 59 and 63A-B). The porosity creation during the zircon-to-baddeleyite transformation, which also speeded up the kinetics of this process, was caused by the silica releasing from the reaction site and by the smaller molar volume of baddeleyite (zircon: 42.92 cm^3/mol; baddeleyite: 20.98 cm^3/mol). Indeed, we did not detect significant mineral and textural differences in $CaCl_2$ leaching experiments with run durations of 3 and 8 days (Fig. 63) supporting very fast dissolution kinetics when grain permeability enables fluid circulation. The complete replacement of zircon by baddeleyite in the NaCl and NaF leaching experiments suggests that solutions with the monovalent Na cation are more reactive than those with the divalent Ca cation.

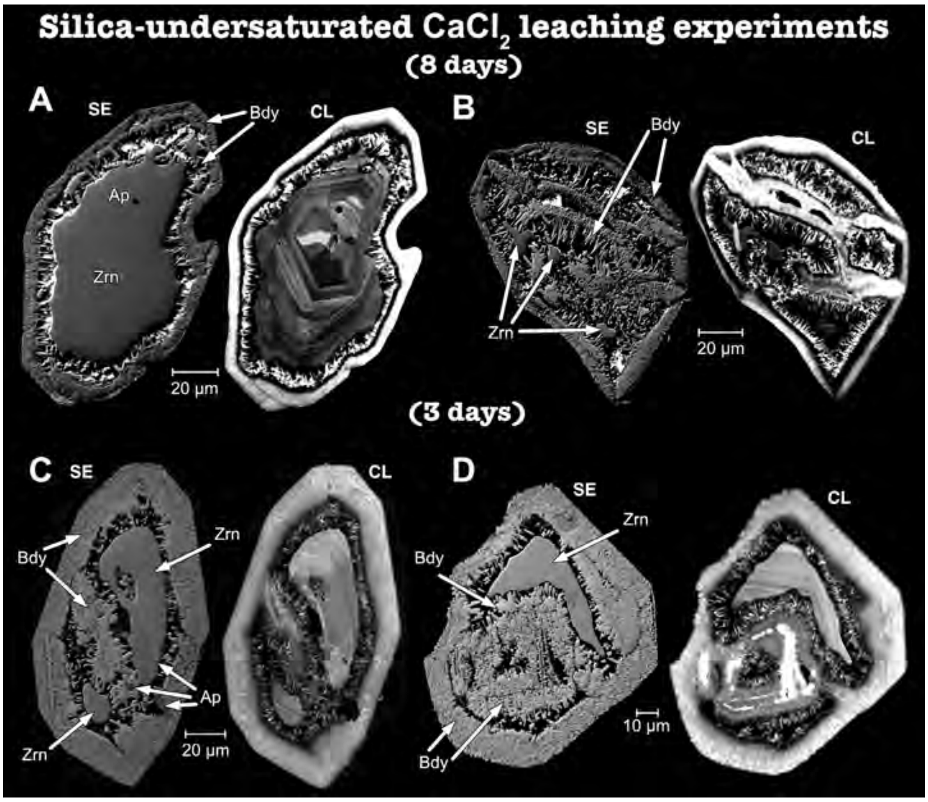

Fig. 63. SE and CL images of products from silica-undersaturated $CaCl_2$ leaching experiments. A) Euhedral zircon grain pseudomorphically replaced by baddeleyite along rim (run HT-14, 8 days); B) Subhedral zircon grains almost completely replaced by baddeleyite along rims and microcracks. (run HT-14, 8 days); C) Euhedral zircon grain pseudomorphically replaced by baddeleyite along rim and microcracks (run HT-19, 3 days); D) Euhedral zircon grain pseudomorphically replaced by baddeleyite along rim and microcracks from experiment HT-19. Mineral abbreviations after Whitney & Evans (2010).

The stability relationships between quartz (granite in low-T experiments, but assumed to be saturated in quartz), zircon, baddeleyite and aqueous and salt fluids (silica-saturated, NaF experiment excluded) are qualitatively displayed in the chemographies from Fig. 64. The phase-relations diagrams were constructed using constraints from experiments on silica solubility in H_2O fluids (Kennedy, 1950; Anderson & Burnham, 1965; Manning, 1994) and salt solutions (Shmulovich et al., 2006). The high fluid/zircon ratios used in the low-T whole-rock powder, zircon added leaching experiments (Fl/Zrn = 0.98, by weight), and in the high-T silica-saturated and silica-undersaturated ones (Fl/Zrn= 0.97 and 0.99, respectively) along with the presence of one or two zirconium phases in the experimental runs suggest a limited solubility of Zr in the fluids (Figs. 64A-B) that contrasts with the larger compositional field proposed for acid solutions by Kovalenko & Ryzhenko (2009) (see their Fig. 5). The extensive replacement zircon by baddeleyite in the high-T, silica-undersaturated 2 M $CaCl_2$ leaching experiment contrasts with the paucity of baddeleyite in the 3-4 M $CaCl_2$ leaching experiments by Lewerentz et al. (2019). The differences could be due to their experiments' lower fluid/zircon ratio (Fl/Zrn = 0.89).

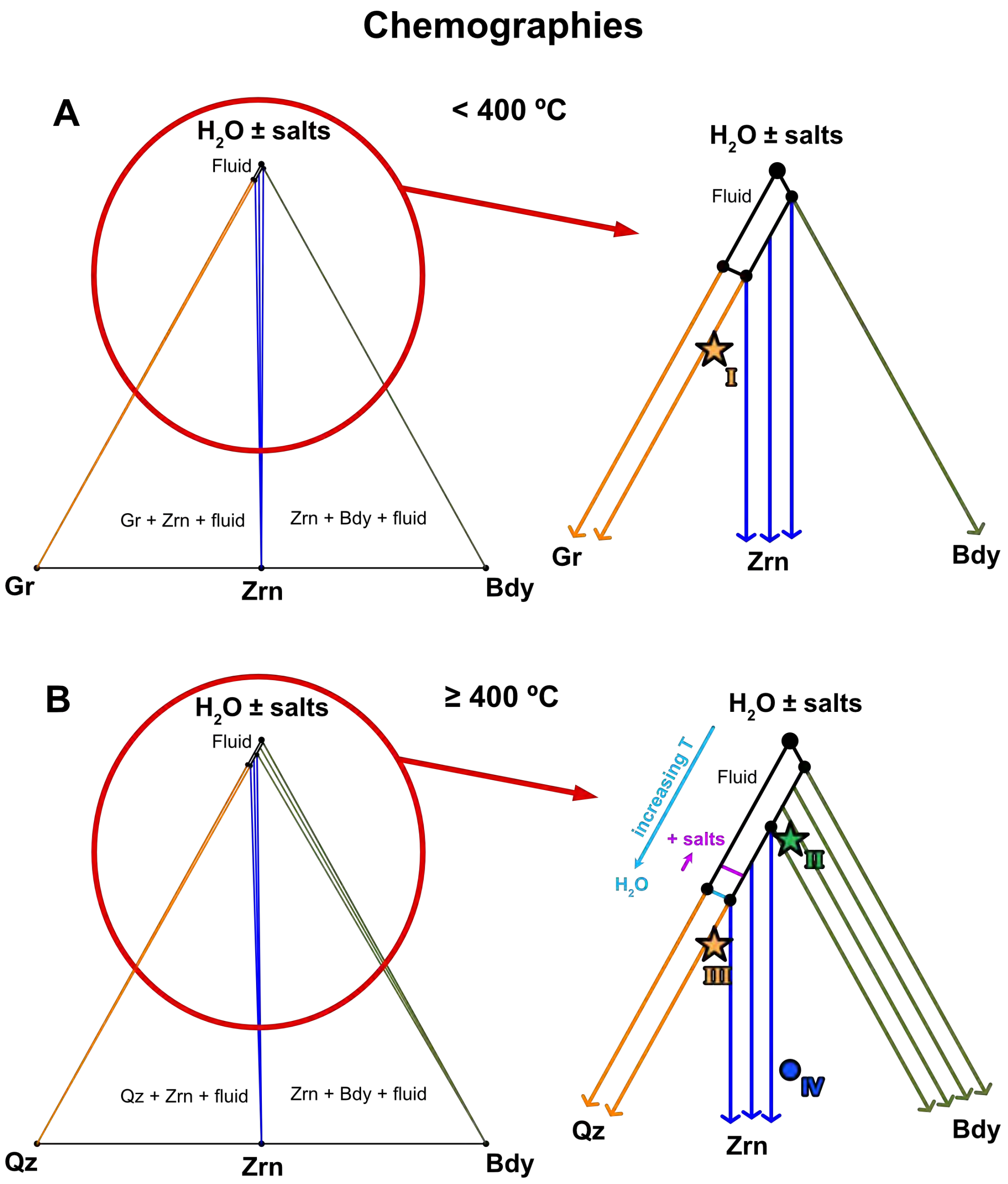

Fig. 64. Schematic zircon-baddeleyite-fluid phase relationships in hydrothermal systems. A) "Granite"-Baddeleyite-Fluid (H_2O+salts) system at $T<400$°C where zircon + fluid is stable in the granite composition of the leaching experiments performed in this work (star I; Fl/Zrn = 0.98, by weight). Baddeleyite-fluid relationships cannot be explored with the experiments performed at 170°C, but the paucity of baddeleyite in silica-undersaturated hydrothermal experiment performed by many authors (Sinha et al., 1992; Geisler et al., 2002, 2003a, 2003b; Rizvanova et al., 2000, 2007; Migdisov et al., 2011) suggest that the compositional region of the baddeleyite-fluid assemblage must be small. B) Quartz-Baddeleyite-Fluid (H_2O + salt) system at $T > 400$°C where it is qualitatively indicated the expected variations of the fluid region with increasing silica solubility with rising temperature in a H_2O fluids (light blue arrow and labels), as indicted by Kennedy (1950), Anderson & Burnham (1965) and Manning (1994), and decreasing silica solubility in salt solutions (purple arrows and labels), as shown by Shmulovich et al. (2006) (and the references therein). The compositional relationships have been drawn to account for the replacement of zircon by baddeleyite in the silica-undersaturated fluids, and for the stability of zircon in silica-saturated fluids (excluding the NaF experiment where zircon is replaced by Na-Zr-silicate) in the leaching experiments performed in this work (stars II and III with Fl/Zrn ratios of 0.99 and 0.97, respectively). The scarcity of baddeleyite in the 3-4 M $CaCl_2$ leaching experiments by Lewerentz et al. (2019) (circle IV) may be caused by the lower fluid/zircon ratio used in the experiment (Fl/Zrn = 0.89). Abbreviations: Bdy, baddeleyite, Gr, granite, Qz, quartz and Zrn, zircon. Stars I, II and III, bulk composition of the experiments performed in this work; dark blue circle IV, experiments by Lewerentz et al. (2019).

II.3.3.2 Leachates compositions

As far as the author knows, there are no direct analyses of trace elements in leachates extracted from zircon in hydrothermal experiments, except a work by Pidgeon et al. (1966) who determined U and Pb by isotopic dilution. Thus, trace-element exchanges between zircon and fluids have been inferred by comparing the compositions of relicts and reacted rims of zircon, determined by La-ICP-MS, SEM-EDS and EMP-WDS and SHRIMP (Sinha et al., 1992; Rizvanova et al., 2000; Geisler et al., 2001, 2002, 2003a; Rizvanova et al., 2007; Lewerentz et al., 2019).

The compositions of leachates extracted from the hydrothermal experiments at low-T conditions show a clear dependence on the nature of the solution added to the experimental charges, although leachates extracted from whole-rock + zircon NaF and from of H_2O experiments (both zircon added and whole-rock powder) present more similar compositions.

By contrast, the fact that the leachates from the high-T experiments have similar compositions shows that, in general, fractionation of the trace elements with respect to Zr is less sensitive to the nature of the solution and the mineral phase, replacing zircon. However, lower ratios for most elements in the leachates extracted from saturated NaF experiments suggest that the extensive replacement of zircon by Na-Zr-silicates could affect the fractionation of the trace elements with respect to Zr.

An unexpected result of this work is a decoupling of the geochemical behavior of Y and HREE in the leachates extracted from both high-T and low-T hydrothermal experiments where Y is significantly more fractionated into the fluid than HREE (compare Y/Yb ratios of 7-30 in low-T and 10-30 in high-T leachates with a value of 2-4 in untreated zircons; Figs. 65A and 66A)

Th and U present a more similar geochemical behavior in most hydrothermal experiments, with Th/U ratios similar to or slightly higher than the untreated zircons (Figs. 65B and 66B). However, a huge decrease is detected in the Th/U ratio of leachates extracted from low-T $CaCl_2$ (only zircon added) and NaCl (both whole-rock and zircon added) experiments caused by a strong partitioning of U into the fluid.

Compared with untreated zircons, Pb/U ratios of leachates are ca. 1-2 magnitude order higher in low-T experiments and 2-5 order of magnitude higher in high-T experiments, the former being more consistent with the data from (Pidgeon et al., 1966) (Figs.65C and 66C).

The leaching experiments show that Pb is markedly more partitioned into the fluid than U, as inferred by many authors from compositional differences between untreated and reaction rim zircons (Sinha et al., 1992; Geisler et al., 2001; Rizvanova et al., 2007; Lewerentz et al., 2019) and from fluid composition analyses (Pidgeon et al., 1966).

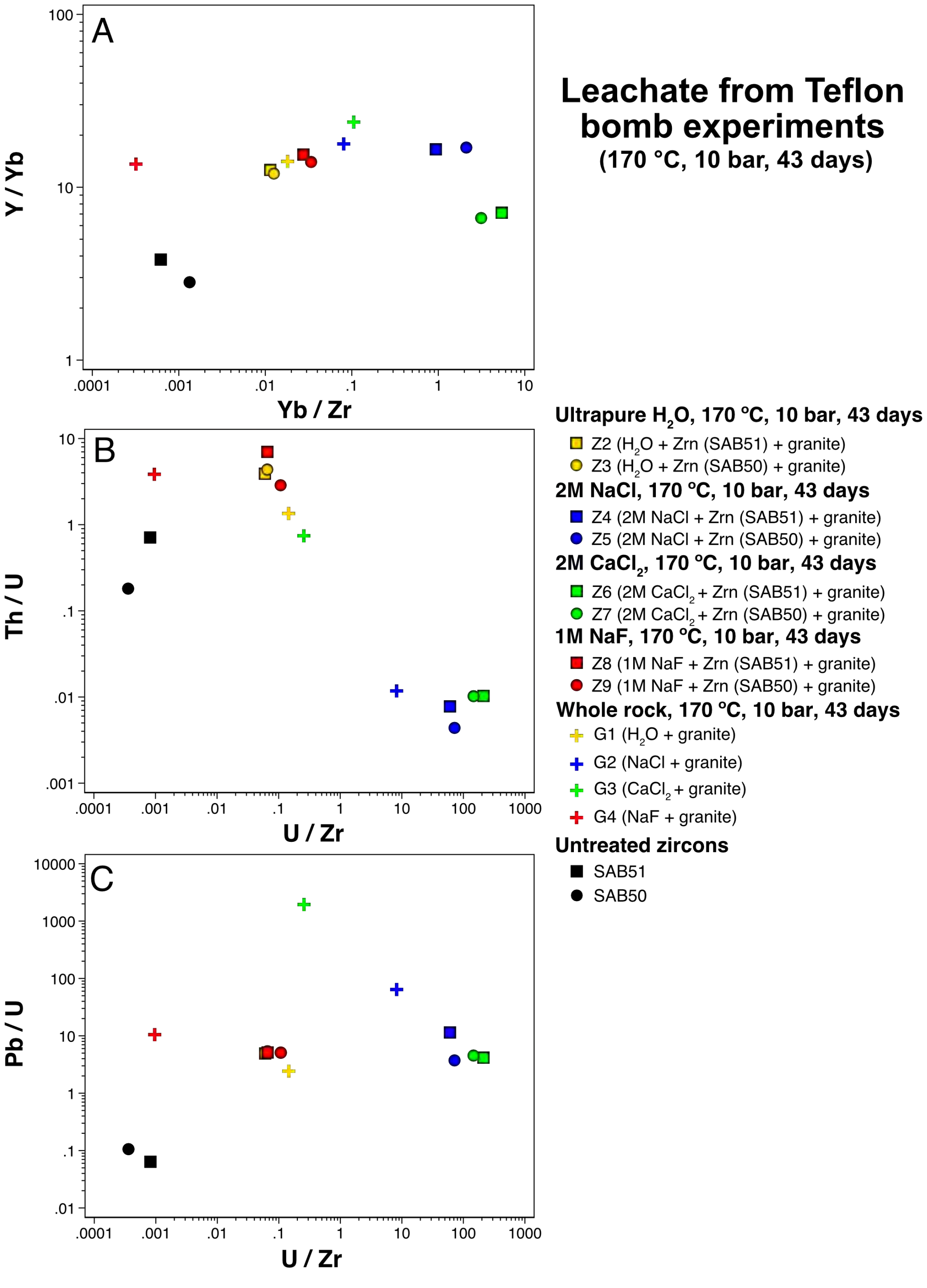

Fig. 65. Binary diagrams of the leachates from the low-T leaching experiments. A) Y/Yb vs. Yb/Zr. B) Th/U vs. U/Zr. C) Pb/U vs. U/Zr. Note that there is a geochemical decoupling of Y respect to HREE in which the former is significantly more fractionated into the fluid than the latter. Th/U ratio of leachates from $CaCl_2$ (zircon added) and NaCl (both whole-rock and zircon added) experiments present a huge decrease with respect to untreated zircons. A significant Pb fractionation with respect to U into the fluid occurred.

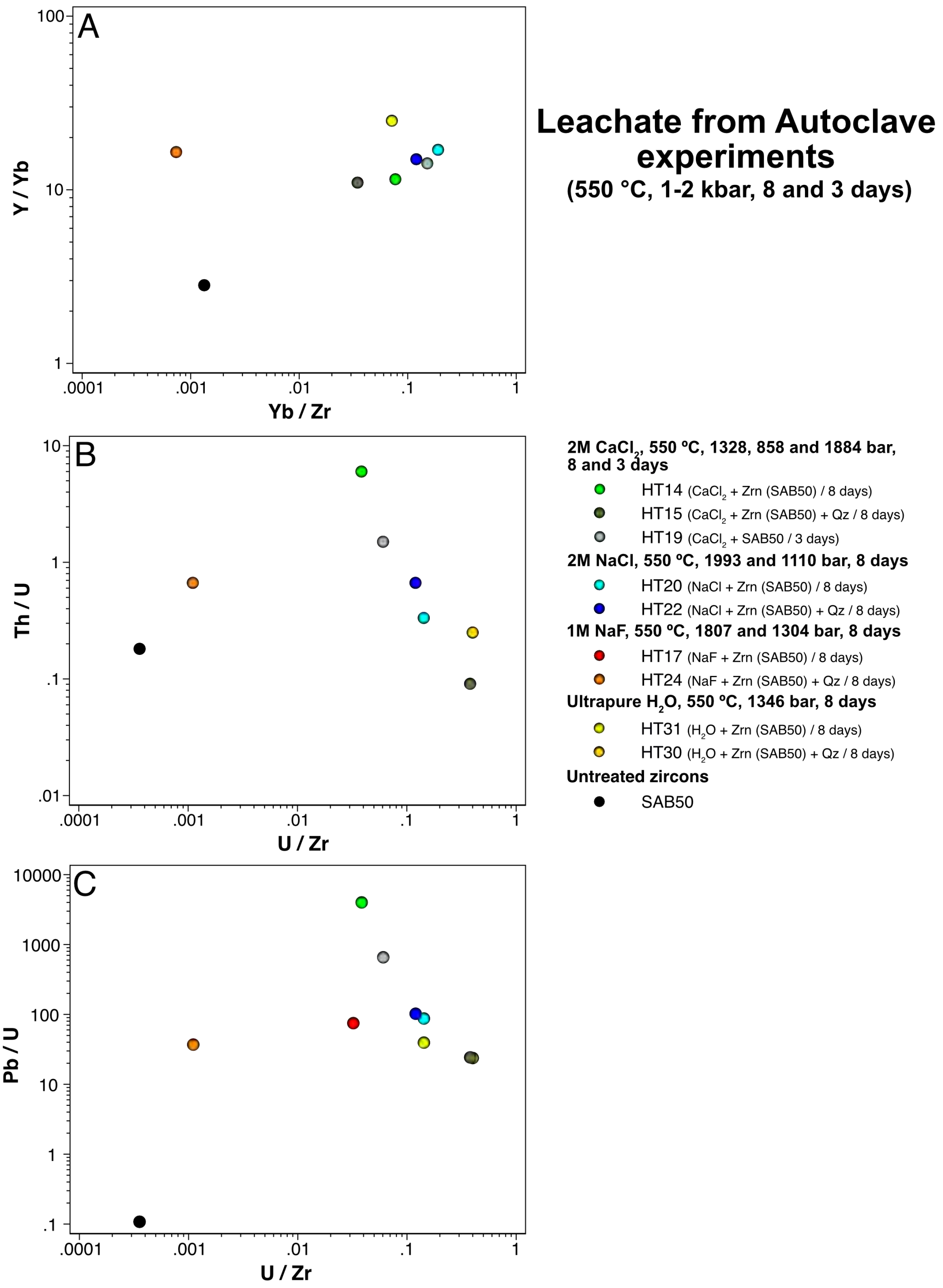

Fig. 66. Binary diagrams of the leachates from the high-T leaching experiments. A) Y/Yb vs. Yb/Zr. B) Th/U vs. U/Zr. C) Pb/U vs. U/Zr. Note that there is a geochemical decoupling of Y respect to HREE in which the former is significantly more fractionated into the fluid than the latter. Th and U present a similar geochemical behavior with Th/U ratios analogue or slightly higher than untreated zircons. There is a significant Pb fractionation with respect to U into the fluid.

II.3.4 Conclusions of the hydrothermal experiments

In low-T whole-rock powder plus zircon leaching experiments, zircon remained stable in silica-saturated H_2O and saline ($CaCl_2$, NaCl and NaF) fluids, as evidenced by the absence of baddeleyite and zirconium silicates. In general, metamict zircon did not recrystallize except in the sample SAB51 leached with NaF, where cathodoluminescence imaging show some recrystallization of the metamict bands. Permeability increasing along the radial microcracks and core-rim interfaces of SAB50 zircons and in the microporous bands of SAB51 zircons suggests congruent zircon dissolution.

In the high-T silica-saturated leaching experiments, congruent zircon dissolution also occurred in H_2O, $CaCl_2$ and NaCl experiments, while zircon reprecipitation took place at the grain faces and along the core-rim interface in $CaCl_2$ and NaCl experiments, respectively. In the NaF experiments, incongruent dissolution of zircon to Zr-Na silicates was observed.

In all high-T silica-unsaturated leaching experiments, zircon dissolved incongruently to baddeleyite. The replacement seems less intense in the H_2O and $CaCl_2$ leaching experiments, where relicts of zircon are found, but in the NaCl and NaF leaching experiments, it is more intense, with total zircon disappearance. The presence of microcracks and pores enhanced the transformation of zircon to baddeleyite. Silica release from the reaction site and volume reduction associated with the zircon-to-baddeleyite transformation increased the porosity, accelerating the reaction kinetics. The complete replacement of zircon by baddeleyite in the NaCl and NaF leaching experiments suggests that solutions with the monovalent Na cation are more reactive than those with the divalent Ca cation.

These results are relevant for the stability of zircon in hydrothermal environments subjected to a high fluid/rock ratio, indicating that not only saline but also water solutions can efficiently dissolve zircon in epithermal to pneumatolytic processes.

The compositions of leachates extracted from the hydrothermal experiments at low-T conditions show a clear dependence on the nature of the solution considered in the experimental charges, except for leachates from whole-rock + zircon NaF and H_2O experiments (both zircon added and whole-rock powder) where compositions are similar. However, a similar composition of the leachates from the high-T experiments evidences that fractionation of trace elements with respect to Zr is less sensitive to the nature of the solution and the mineral phase replacing the zircon, except in silica-saturated NaF experiment with the formation of Na-Zr silicate, where it is less extensive. Importantly, geochemical decoupling of Y with respect to HREE in all leachates extracted from the high- and low-T hydrothermal experiments is reported in this work for the first time, being Y significantly more partitioned into the fluid than HREE. The experiments show a negligible Th-U fractionation in most of the leachates from the hydrothermal experiments, with the exception of low-T $CaCl_2$ and NaCl leaching experiments in which U was strongly partitioning into the fluid. A significant fractionation of Pb with respect to U into the fluid occurred in all leaching experiments.

PART III. NUMERICAL MODELING

III.1 Zircon inheritance in granite rocks

III.2 Zircon crystallization from Zr-low mafic magmas

The next paragraphs discuss how we used numerical methods to study two aspects of zircon behavior that can hardly be reproduced in laboratory experiments. These are; (i) the survival of source zircons in granite magmas and (ii) the precipitation of zircon in low-Zr, zircon undersaturated mafic magmas, on the other hand.

III.1 Zircon inheritance in granite rocks

A variable fraction of zircon crystals entrained in magmas may survive the contact with the melt to remain as inherited grains in the resulting magmatic rocks. These older-than- host zircons appear as individual grains or old cores rimmed by newly formed magmatic zircon. Zircon inheritance is frequent in granitoids (e.g., Miller et al., 2003, and references therein) but also in mafic rocks, including MORB basalts and gabbros (e.g., Bea et al., 2020, and references therein), even in carbonatites (Montero et al., 2016). Because of the exponential increase of zircon solubility with temperature and melt basicity (Watson, 1979), zircons inherited by mafic rocks hardly come from the magmatic source but rather from scavenged xenoliths or mixed felsic magma, thus carrying information about the emplacement dynamics and the nature of the pierced crust (Bea et al., 2020). Zircons inherited by granite rocks, in contrast, mostly come from the magmatic source. Consequently, they can yield information about the materials that melted, their melting conditions, and melt extraction mechanisms.

After the pioneering experimental work of Watson (1979), several authors have studied the solubility of zircon in melts and applied it to determine the zircon saturation temperatures (T_{Zr}, Hanchar & Watson, 2003). Based on this parameter, calculated from whole-rock Zr contents, Miller et al. (2003) divided granite rocks into "hot" ones (T_{Zr} > 800 °C), with little or no inherited zircon, and "cold" ones (T_{Zr} < 800 °C) with abundant inherited zircon. However, the situation seems far more complicated, especially for "cold" granites. We have found that coeval and neighboring T_{Zr} < 750 °C S-type granites presumably derived from similar sources often have radically different zircon inheritance. Excellent examples come from Variscan batholiths of Central Iberia. Figure 67 shows two extreme cases of ca. 305 Ma two-mica plutons (SHRIMP data in Tables ST6 and ST7; chemical composition in Table ST8; see supplementary material), the Ledesma and the Pedrobernardo granites, both with SiO_2 around 72 wt%, ASI ≈ 1.25, and Zr ≈ 150 ppm, but markedly different modal proportions of zircons with inherited cores, about 97 and 5%, respectively. Ledesma is a small late- to post-tectonic sub-autochthonous pluton composed of two-mica granites. It is located in the Tormes Dome (40.0939° N; 5.9951° W), emplaced as an asymmetric diapir within the Cambrian-Ordovician Ollo de Sapo glandular gneisses from which it derived (López Plaza, 1980; Talavera et al., 2013). Pedrobernardo is also a small allochthonous pluton composed of two mica granites. It is located in the axial zone of the Avila Batholith (40.3069° N; 5.9951° W), forming a 1 km thick, vertically-differentiated sill emplaced within cordierite-biotite anatectic granodiorites (Bea et al., 1994a; Bea, 2010).

For a given thermal regime, the survival of zircon in contact with melt depends on three main factors: (i) the zircon solubility into the melt, (ii) the zircon dissolution kinetics, (iii) the volume of melt in contact with the zircon. The last factor is critical for controlling local zircon saturation when the melt phase dwells in small isolated pores (Bea et al., 2001; Cambeses & Chakraborty, 2018). However, this can hardly be a limiting factor in crustal melting, because the minimum fraction of viscous melt that may escape from a rigid framework is about 0.1–0.2 (see "Methods"). There- fore, how many source zircons can be inherited by crustal magmas depends on the melting temperature, zircon solubility, and the ratio between the zircon dissolution rate, on the one hand, and the melt generation and extraction rates, on the other hand. The first two factors are closely related to the source composition and melting temperature. The last two are related to the heat supply mechanism and the geodynamic regime.

For understanding the relationships between these parameters we built grids relating temperature with (i) the melt fraction and (ii) the Zr concentration required for zircon saturation in melts derived from different source compositions with variable water contents and pressures. Then, we addressed the relations between zircon solution kinetics and the melt production rate in geologically reasonable scenarios, discussing the effects of deformation-enhanced melt segregation. The calculations were performed with COMSOL™ - based programs provided by F. Bea.

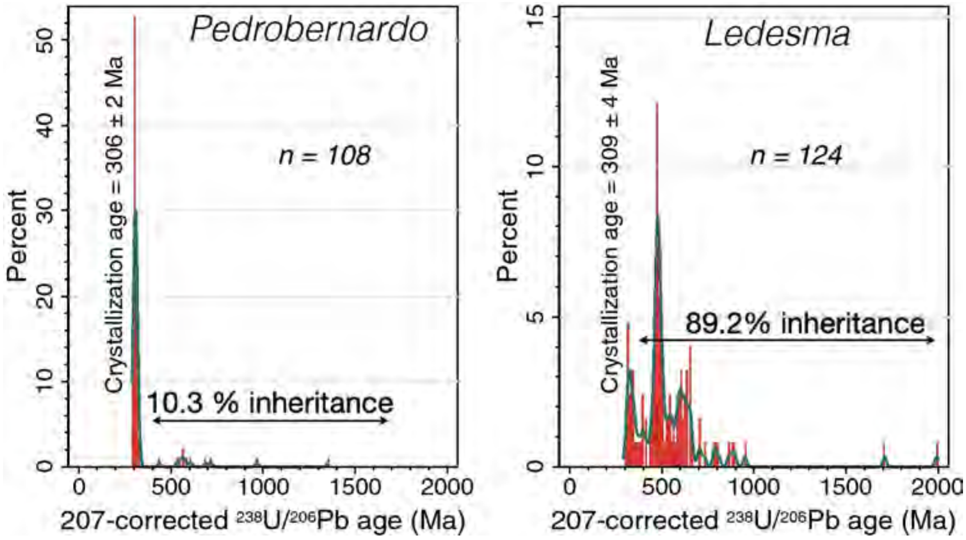

Fig. 67. SHRIMP U-Pb distributions in two extreme zircon inheritance cases in two-mica granites from Central Iberia with almost the same composition, zircon modal abundance and T_{Zr}. SHRIMP data are in Tables ST6 and ST7 of the Supplementary Material. The Pedrobernardo granite yielded very few spots (<10%) with SHRIMP U-Pb determinations older than the zircon crystallization age (306±2 Ma) that is slightly older than the Rb-Sr age (296±3 Ma, Bea, 2010). The Ledesma granite, in contrast, have very few U-Pb determinations representing its crystallization age, 309±4 Ma, also close to the Rb-Sr age (306±5 Ma; Table ST9 of the Supplementary Material). The Variscan zircon component in Ledesma granites is a very narrow rim that grew over an older core. The fraction of zircon with inherited cores is close to 97%, according to CL images. The fraction of older-than-crystallization analyses in Pedrobernardo granite (Table ST6) is superior to the fraction of zircons with inherited cores (<5%, according to CL images), because we over-represented them searching for the age of inheritance. The fraction of syn-magmatic ages in Ledesma (Table ST7) is also over-represented searching for the crystallization age.

III.1.1 Starting compositions and methods

The starting compositions used in the following calculations corresponded to three common crustal rocks (Table 16), one peraluminous greywacke, one metaluminous granodiorite, and one gabbrodiorite. We recalculated their anhydrous compositions to contain 2, 4, 6, 8 and 10 wt% of H_2O, and processed them with rhyolite- MELTS (Gualda et al., 2012) at pressures of 3, 6 and 9 kbar, and temperatures from 650 °C to the liquidus, recording the fraction of melt produced each 10 °C.

Then, we estimated the composition of the melts using Winther's method (1995), and the zircon solubility into the resulting melts with the Borisov & Aranovich (2019) zircon solubility model. Afterwards, we plotted the fraction of melt for different H_2O contents and zircon solubilities against the temperature in combined diagrams with two different vertical axes: left axis represents the fraction of melt; right axis represents the

Zr solubility in logarithmic scale (Fig. 68). Then, we divided the resulting diagram into three parts using two rheological thresholds (Vigneresse et al., 1996, but see Barboza, 1998). The Melt Escape Threshold (MET) occurs at 20–25% of melt volume, when the melt may move freely through an interconnected net of intergranular pores. The Rigid Percolation Threshold (RPT) occurs at 50–55% of melt volume when the mush reaches the critical melt fraction; i.e., it no longer behaves as a solid framework but as a dense suspension (Arzi, 1978; Molen & Paterson, 1979; Wickham, 1987). At this point, the mush's density is sufficiently low to create buoyancy so that the magma unroots, ascends and cools, thus preventing further dissolution of entrained zircons. Below the zircon saturation line, and in the absence of kinetic effects, zircon may only survive if it is shielded from the melt. This situation may occur if the zircon is fully included in a major and stable mineral or dwells within a restite or a xenolith (Bea & Montero, 2013).

Table 16. Composition of magmatic sources used in the numerical experiments.

Id	Peraluminous greywacke	Metaluminous tonalite	Gabbro-diorite
SiO_2	69.33	61.42	51.97
TiO_2	0.53	0.86	1
Al_2O_3	16.15	17.41	16.82
Fe_2O_3	0.44	0.94	2.77
FeO	2.93	4.82	8.21
MnO	0.05	0.14	0.2
MgO	1.2	2.44	4.15
CaO	1.92	4.35	9.77
Na_2O	3.07	4.38	3.52
K_2O	4.08	3.02	1.08
P_2O_5	0.31	0.22	0.5
sum	100.01	100	99.99
ASI	1.25	0.95	0.68
Fe/(Fe+Mg)	0.61	0.56	0.59

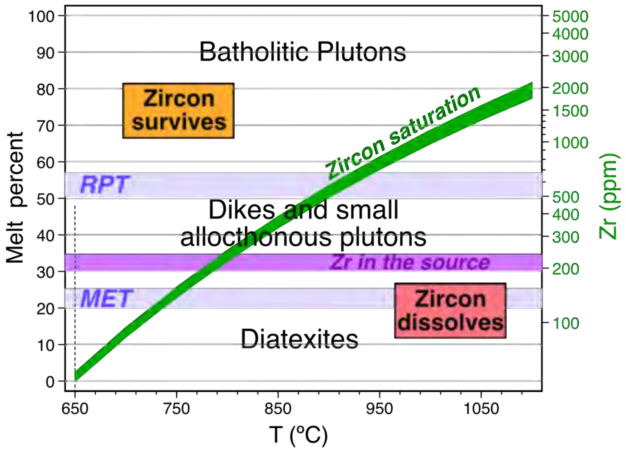

Fig. 68. Grid explanation. Below the MET (Melt Escape Threshold, Vigneresse et al., 1996), and in the absence of regional stress, crustal protoliths form diatexites and some aplopegmatitic dikes. Between the MET and the RPT (Rigid Percolation Threshold, Vigneresse et al., 1996) large granite dikes may form, and these eventually may coalesce to form granite plutons. Above the RPT, one surpassed the critical melt fraction, a mobile mushy magma may form; this may ascend through the crust to form batholitic-scale granites. The thickness of the zircon saturation line is caused by changes in the melt composition with temperature and water content. Above the zircon saturation line, the melt is unable to dissolve more zircon. Below it, the melt can dissolve zircon until reaching saturation. The purple horizontal band marks the range of Zr ppm in the source.

These experiments assume that source zircons and melt are in equilibrium when melt migrates away from the source, that is to say, no metastable zircons were entrained in the segregated source. To determine whether this assumption is valid, we calculated the melt production rate in three granite-forming geological scenarios: (i) a highly radioactive thickened crust, (ii) a typical crust that undergoes a sudden increase of subcrustal heat flux, (iii) a regular crust underplated by a high-T mafic magma. Then, we compared these results with the kinetics of zircon solution within the melt. The melt production rate was calculated using the COMSOL^{TM} 2D models of Bea (2012) and the zircon solution kinetics with Watson's model (1996).

III.1.2 Results

III.1.2.1 Peraluminous greywacke

The Zr concentration in the magmatic sources is one of the primary parameters controlling whether all their zircon dissolves at given conditions. In most crustal protoliths, Zr commonly ranges from 150 to 270 ppm. For example, the average concentration of Zr in 110 samples of fertile greywackes and orthogneisses from Central Iberia analyzed in our laboratories is 215 ppm, with a 95% confidence interval between 193 and 237 ppm. Melting these sources produces peraluminous magmas with compositions similar to two mica granites, which require about 770–820 °C for the total dissolution of the source's zircon (Fig. 69). At these temperatures, the proportion of water in the source needed to overcome the Rigid Percolation Threshold is ca. 2 wt% at 3 kbar and ca. 3–3.5 wt% at 6–9 kbar. Therefore, in the absence of kinetic effect caused by fast unrooting, emplacement and cooling, peraluminous granites formed at ≥ 800 °C are likely to have very low or no zircon inheritance, as signaled by Miller et al. (2003).

The zircon solubility in melts derived from similar sources mostly depends on the temperature, but the melt fraction also depends on the water content (Fig. 69). Whereas lowering the temperature reduces much the solubility of zircon, the fraction of melt may remain above the Rigid Percolation Threshold if the water concentration increases concomitantly. This effect suggests that magmas derived from water-rich sources have much more chance of inheriting source zircons than magmas generated from water-poor sources but similar zircon contents.

At 750 °C, for example, the melt becomes zircon-saturated with 150 ppm Zr (i.e., 50–70 ppm less than in the source of our example), and the proportion of water required to overcome the Rigid Percolation Threshold is 3, 5, and 6% at 3, 6, and 9 kbar (Fig. 69). With just 2% water in the source, the melt amounts to 45, 30, and < 20% for the same pressures. Accordingly, at a 750 °C and 3–6 kbar, the peraluminous greywacke may generate enough mobile magma to form granite plutons with moderate zircon inheritance of around 20–25% if the water present was ≈ 2–3 wt%, which is perfectly reachable by dehydration melting (e.g., Clemens, 1984).

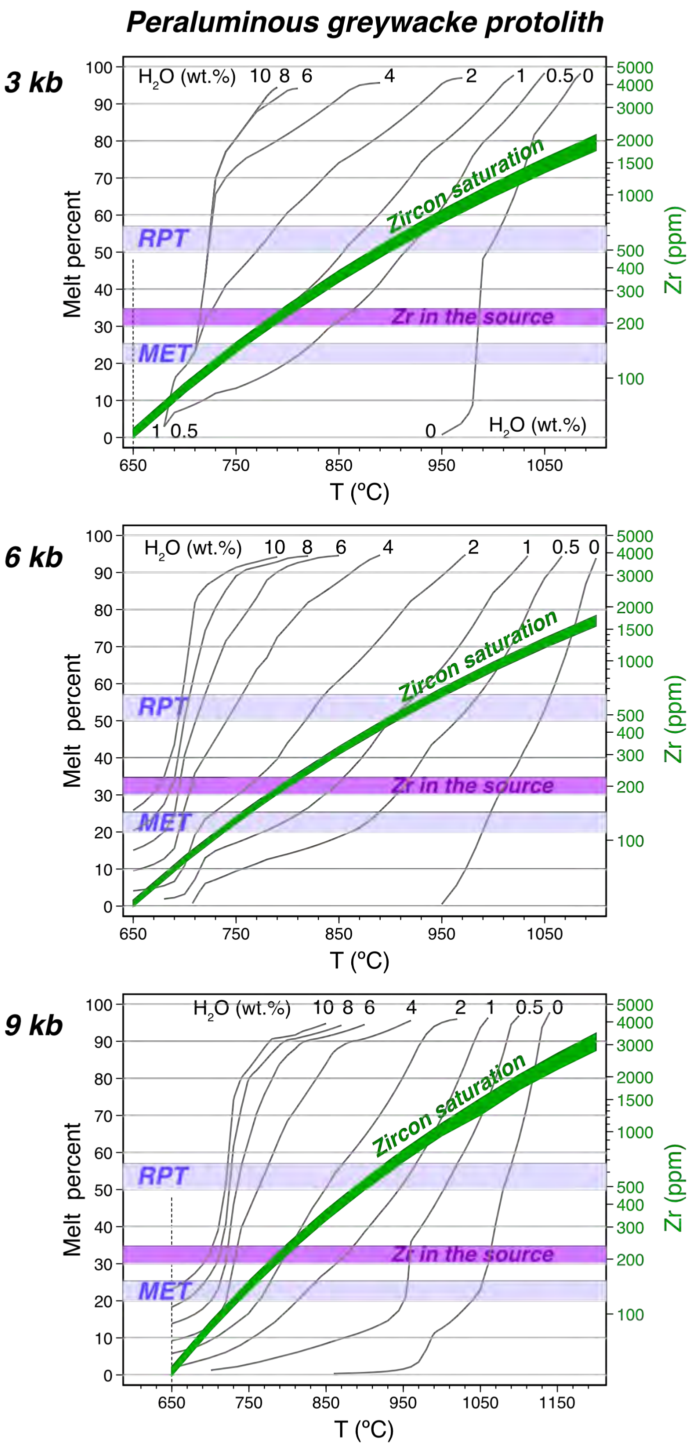

Fig. 69. Grid for the peraluminous greywacke. Note that for temperatures >770-790 ºC, no source zircon will survive if it touches the melt. At these temperatures, the formation of batholitic granites, i. e., melt fraction above the RPT, requires 2, 3 and ca. 4 wt% H_2O for 3, 6 and 9 kbar, respectively. Note also that the temperature must not be >700-710 ºC to produce granites with elevated zircon inheritance. At such low temperatures, the generation of granite batholiths is only possible if the source has a water content ≥8 wt% and the pressure is between 4 and 6 kbar, see Fig. 70.

On the other hand, the generation of granites with elevated zircon inheritance requires a melt phase saturated in zircon with barely 70–80 ppm Zr, implying melting temperatures of 700 °C or lower. At 700 °C, the amount of water required to overcome the Rigid Percolation Threshold is enormous, 8–10 wt%, and this only happens within a narrow window of pressure between 4.5 and 6 kbar (Fig. 70). With 4 wt% water content, the melt fraction increases above the Melt Escape Threshold between 4 and 6 kbar, but it does not reach the Rigid Percolation Threshold so that large granite bodies may hardly form. Therefore, it seems that extensive peraluminous granite magmatism with elevated zircon inheritance can only result from the melting of extremely water-rich mid-crustal sources at temperatures ≤ 700 °C.

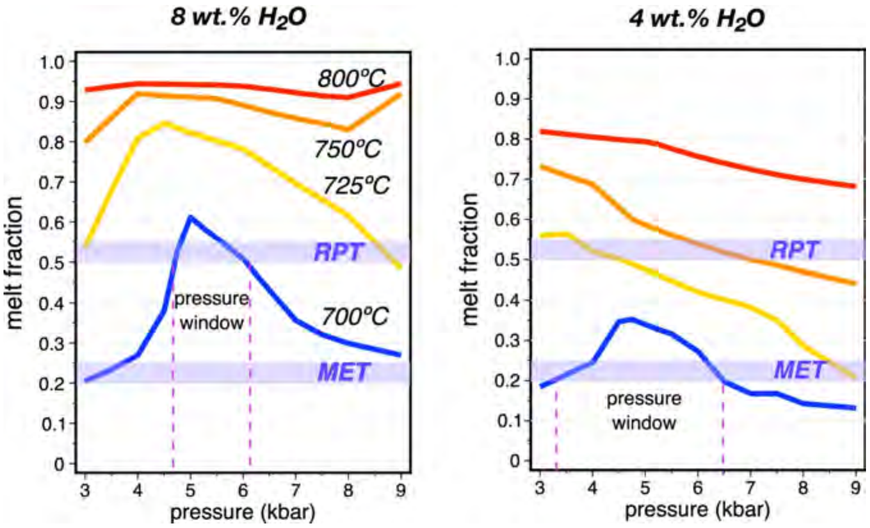

Fig. 70. Variation of the melt fraction (%) generated from the peraluminous greywacke as a function of the pressure for temperatures of 700, 750, and 800 ºC for source water contents of 8 and 4 wt%. At 700 ºC, i. e., producing elevated zircon inheritance, only magmas generated in a pressure window between 4.5 and 6 kbar can form batholitic granites if the source has approx. 8 wt% H_2O*, this involving external water fluxing. If the source has only 4 wt%* H_2O*, the pressure window enlarges from approx. 3-3.5 to 6.5 kbar, overcoming the MET but not reaching the RPT. These conditions only lead to dikes or small granite plutons with high zircon inheritance.*

III.1.2.2 Metaluminous granodiorite

At the same temperature and water content, the metaluminous granodiorite (Table 16) generates less melt than the peraluminous greywacke. The melts produced are slightly more mafic and need more Zr to become zircon-saturated at the same temperature.

Metaluminous sources also tend to contain less zircon that the peraluminous ones at equivalent silica content. The average of 189 metaluminous granodiorites and gneisses from all over the world analyzed in our labs is 168 ppm (95% confidence interval of 155–184 ppm Zr), corresponding to a Zr saturation temperature of about 740 °C (Fig. 71) which is significantly smaller than the saturation temperature of peraluminous greywacke considered in the previous section. In principle, therefore, zircon survival has fewer chances in metaluminous than in peraluminous sources. Figure 71 shows that at 3 kbar and 740 °C even the most water-rich sources generate very little melt, needing about 2 wt% H_2O at 880 °C, and 1 wt% H_2O at 970 °C to reach the Rigid Percolation Threshold.

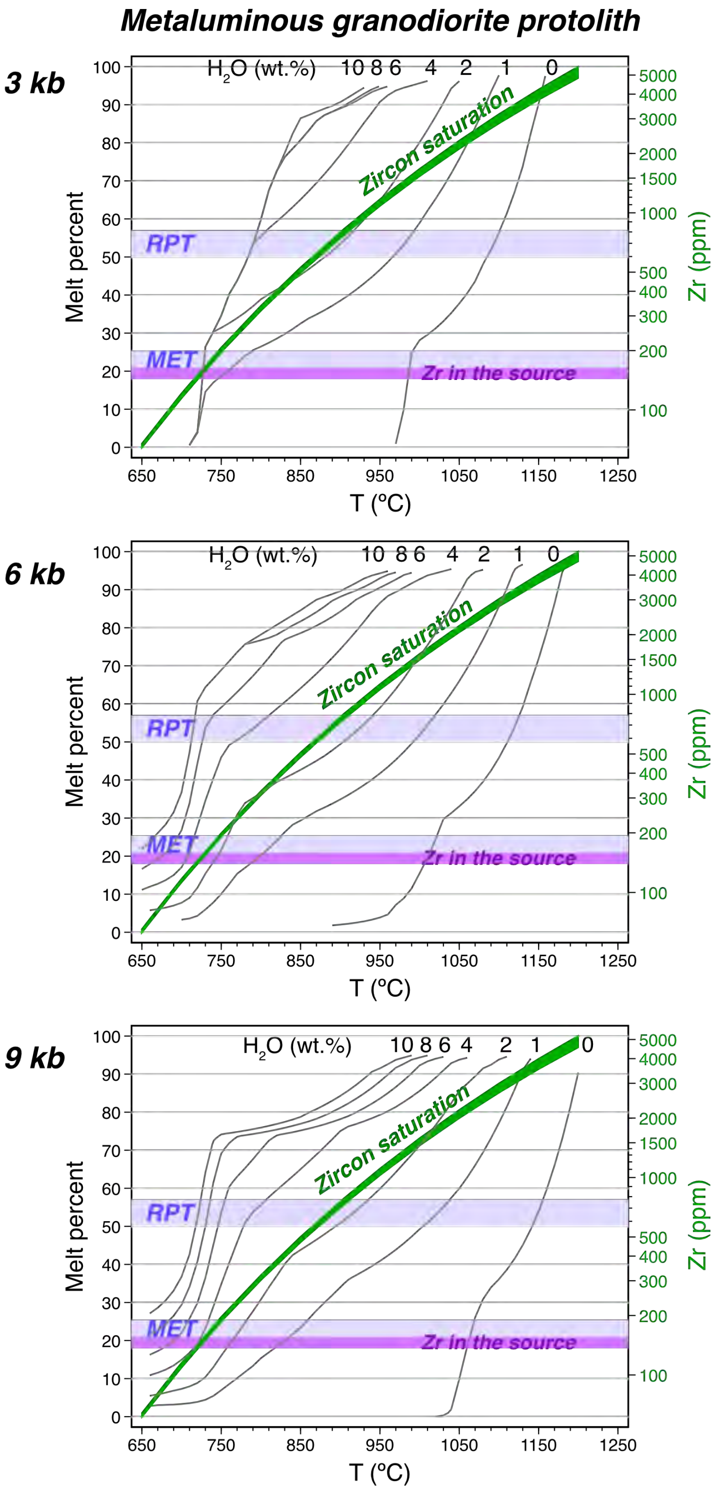

Fig. 71. Grid for the metaluminous granodiorite. Note that for temperatures >740-750 ºC, significantly smaller than the saturation temperature of peraluminous greywacke, no zircon for the source will survive if it touches the melt. At these temperatures, even the most water-rich sources generate very little melt, needing about 4 wt% H_2O at 880 ºC, and 2 wt% H_2O at 970 ºC to reach the RPT.

Figure 72 shows the melt-fraction lines as a function of pressure for different temperatures and 8 and 4 wt% water content. Melts with 8 wt% H_2O reach the Melt Escape Threshold at 4.5 kbar if T ≈ 700 °C, and the Rigid Percolation Threshold at P between 4 and 3 kbar if T > 725 °C. The so-generated melts will always be zircon-undersaturated, i.e., with little, if any, chances of preserving source zircons metastably suspended in them.

Figure 72 also shows that a source with 4 wt% H_2O and T < 800 °C cannot produce enough volume of zircon-saturated melt to overcome the Rigid Percolation Threshold. At T > 800 °C the melt will always be able to dissolve all source zircon. However, between 3.5 and 6 kbar and at 725 °C, it is possible to form a zircon-laden saturated melt in sufficient volume to overcome the Melt Escape Threshold (Fig. 72).

Considering the stability of biotite and amphibole, whether a metaluminous source at 725 °C can release about 4 wt% H_2O from the breakdown of their hydrous minerals is more than dubious. To get 8 wt% H_2O seems simply impossible without external fluxing, as discussed in "Implications of the model" (see also Collins et al., 2016). These results suggest that source zircons suspended in magmas derived from partial melting of metaluminous protoliths have little survival chances.

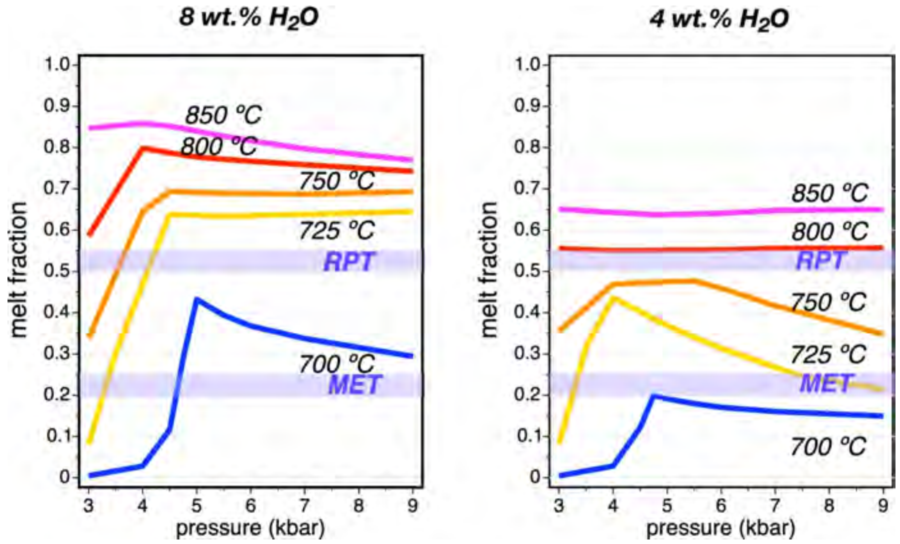

Fig. 72. Variation of the melt fraction generated from the metaluminous granodiorite source as a function of the pressure for temperatures of 700, 725, 750, 800 and 850 °C for source water contents of 8 and 4 wt%. With 8 wt% H_2O and variable pressure, always greater than 4.5 kbar, the source overcomes the MET at 700 °C, and the RPT at 725 °C, sufficiently low to reach zircon saturation. With 4 wt% H_2O the source cannot produce enough volume of melt saturated in zircon to overcome the RPT. However, between 3.5 and 6 kbar and at 725 °C, it is possible to form zircon-saturated magmas carrying a few suspended crystals in sufficient volume to overcome the MET.

III.1.2.3 Gabbro-diorite

The Zr concentration in mafic rocks is so variable that it is difficult to fix an accurate average. Here we assumed a range of 100–150 ppm Zr with an average of 125 ppm, which is the higher side. This concentration implies that the melts generated from the gabbro-diorite source (Table 16) become zircon-saturated at ≈ 710 °C or less. However, such temperatures cannot produce significant magma volumes, even if the sources contain an excess of water (Fig. 73).

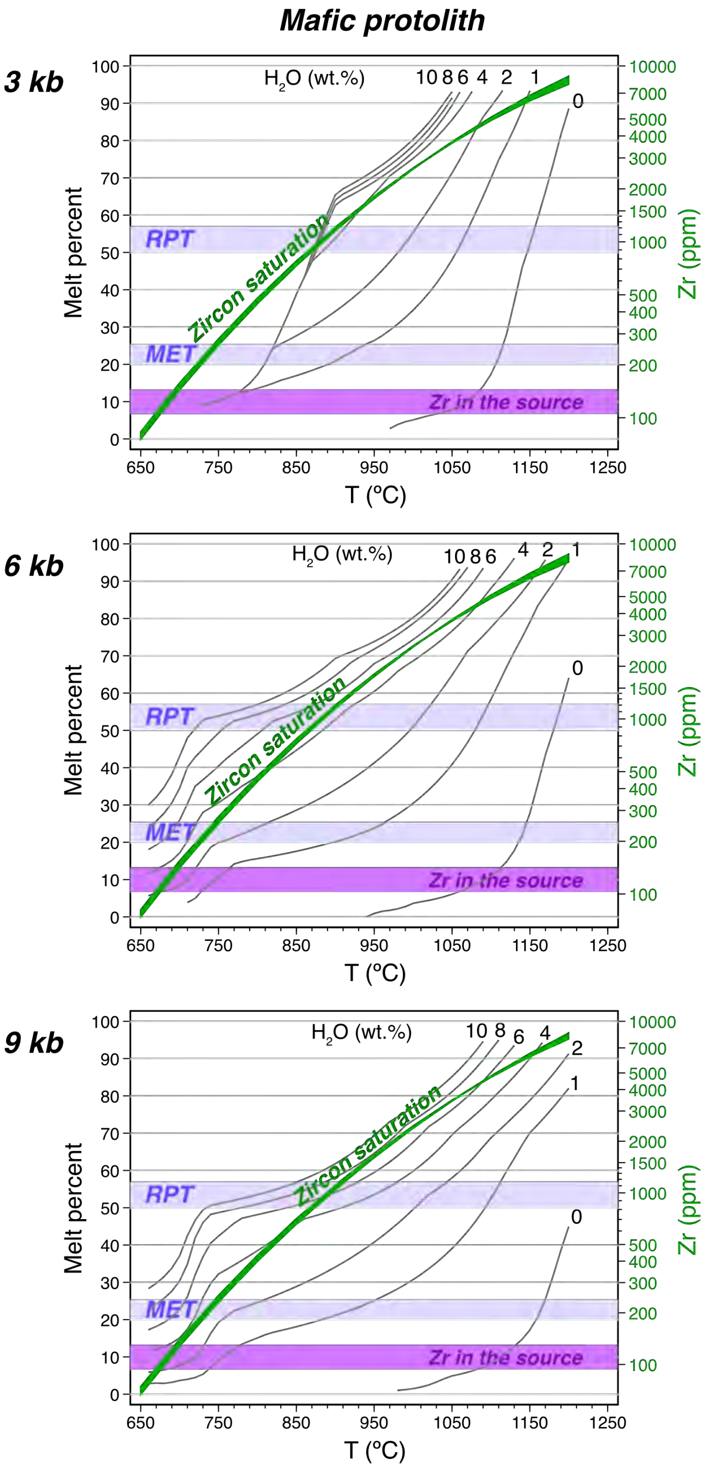

Fig. 73. Grid for the gabbrodiorite. Melts derived from it reach zircon saturation at approx. 710 ºC or less. Accordingly, if this rock melts, even being water-fluxed from outside, source zircons hardly can survive.

The minimum temperatures required for melts generated from the gabbro-diorite source to reach the Melt Escape Threshold range from 840 °C at 3 kbar with about 10 wt% of water, to 740 °C at > 6 kbar with about 3.5 wt%. These figures increase to > 870 °C at ≥ 6 kbar and 10 wt% H_2O, and > 850 °C and 4 wt% H_2O for reaching the Rigid Percolation threshold. Therefore, the chances for source zircons to survive in magmas derived from partial melting of mafic rocks are minimal.

III.1.3 Discussion

III.1.3.1 Zircon solubility and melt production

The quality of a numerical model relies on how well-founded its assumptions are and the accuracy and robustness of the calculations. The results presented here depend on (i) rhyolite-MELTS (Gualda et al., 2012) for estimating the melt fraction, (ii) Winther's method (1995) for determining the melt compositions, and (iii) the zircon solubility equation of Borisov & Aranovich (2019).

The last equation, checked against other independently built experimental models (Boehnke et al., 2013), agrees well for intermediate and felsic rocks and seems the most accurate for mafic rocks. We have also tested the Winther's method (1995), based on empirical equations built of 1608 experimental results from the literature, against other experimental data with excellent results. Perhaps our models' weakest point is the accuracy of the fraction of melt calculated with rhyolite-MELTS, especially at low temperatures. Nevertheless, the figures obtained here fit well with field observations and experimental data (e.g., Johannes & Holtz, 1990). Accordingly, we believe that the conclusions based on the models described in the previous section approximate the situation in nature reasonably well and can thus be useful for understanding zircon inheritance despite the naivety of the melt-extraction model. This aspect is discussed in the next section.

III.1.3.2 Equilibrium or non-equilibrium: the influence of heat supply and melt segregation mechanisms

Clarifying whether the zircon dissolution in anatectic melts is governed by kinetics or by the phase equilibrium relation is important to consider that the models presented are realistic. Clemens (2003) suggested that equilibrium experiments such as those of Watson & Harrison (1983) have little relation to petrogenesis and raised questions about the time it takes for a zircon grain from the source to dissolve in a granitic melt. Given that the segregated melt migrating upwards would not further increase its temperature, the problem reduces to comparing melt production and zircon dissolution rates before segregation, that is to say, whether zircon grains entrained by the escaping melt are in equilibrium with it or represent metastable phases amenable to further dissolution.

Suppose zircon dissolution is faster than melt production. If so, zircon and newly produced melt will swiftly reach equilibrium, and no metastable crystals will be entrained in the melt upon segregation, just zircons that cannot dissolve anymore, because the melt is already zircon-saturated. On the contrary, suppose the melt generates at a faster pace than zircon dissolves. In this case, source zircons will be metastable within the melt; if this cools slowly, zircons will dissolve until saturating the remaining melt. If, on the contrary, the melt cools swiftly, the metastable zircons can survive as inherited crystals, thus invalidating the conclusions of the models presented in "Results".

The way melt escapes from the magmatic source still is a matter of discussion (see Etheridge et al. (2020), and references therein). In the absence of regional stress, the melt will segregate mainly by gravitational compaction (Bagdassarov et al., 1996) and porous flow (Jackson et al., 2003) accumulating upwards until its fraction is sufficient to disrupt the solid framework. Then, the partially molten rock behavior changes from a solid to a high viscose fluid. This point is called Critical Melt Fraction (Arzi, 1978; Molen & Paterson, 1979; Wickham, 1987; see also Weinberg, 2006), roughly equivalent to the Rigid Percolation Threshold of Vigneresse et al. (1996). Suppose the melt is not drained from the source and accumulates in a given volume. The density of the melt- rich rock will be lower than the surrounding melt-poor rocks. This situation leads to a Rayleigh–Taylor-instability and may cause the ascend of the magma through the crust as a diapir, if the temperature of the wall rocks is sufficiently high (Marsh, 1982; Mahon et al., 1988; Weinberg, 1997).

Clemens and Stevens (2016, and references therein) argued against the diapir model and denied the accumulation of large volumes of melt in the source region, proposing rapid, semi-continuous, and disequilibrium withdrawal of small magma batches instead, even in the absence of regional deformation. Etheridge et al. (2020) support this hypothesis, concluding that regions undergoing vapor-absent melting are unable to retain their melt except at the lowest melt-production rates.

These ideas may be controversial, but what is indisputable is that melt segregation and extraction can be significantly enhanced if the partially molten rock undergoes deformation (e.g., Bea et al., 2005), especially if the source consists of layers with different fertility (e.g., Johannes, 1988; Johannes et al., 1995). In large anatectic complexes, where rocks are plastic, ductile deformation can create lower fluid pressure sinks that draw fluid towards shear zones facilitating the melt escape (Etheridge et al., 2020).

To our effects, the particular mechanism of melt extraction is irrelevant. The critical questions are (i) the minimum fraction at which melt can escape and (ii) whether melt and source zircons reached equilibrium when the former escapes from the source. If not, the segregated melt will be Zr-undersaturated and may entrain metastable zircons. In this case, if the upwards migrating zircon-laden melt cools fast enough, these zircons may survive and so invalidate our models.

The first question is not easy to answer. Tectonically-enhanced melt escape likely occurs at a fraction smaller than the Melt Escape Threshold. However, numerical and physical experiments (Pilotti, 2000; Kaasschieter & Frijns, 2003; Rabinowicz & Vigneresse, 2004; van den Ende et al., 2018) indicate conclusively that no fluid can be extracted from a porous media below a given fraction, which for highly viscous fluids hardly can be less than 0.2–0.1. Although the majority of these experiments were not done for magmatic systems, we think their results are a good starting point for our purposes.

The second question depends on how the source melting rate compares with the zircon dissolution rate. If the former is higher than the latter, the still zircon-undersaturated extracted melt may entrain metastable zircons. If, on the contrary, the melting rate is slower than the zircon dissolution rate, the melt will be zircon-saturated before extraction, and entrained zircons will stay as such in the resulting magmas independently of their emplacement and cooling histories.

Figure 74 shows that the melting rate of a fertile layer with an elevated heat production (3.5 μW m^{-3}) located at a depth of 35 km is such that it requires about 3 and 5 million years after the beginning of melting to reach 0.1 and 0.2 melt fractions, respectively (Fig. 74a). Accordingly, the melt will not entrain metastable zircons even if the extraction occurs when the melt fraction is as low as 0.1.

Figure 74b shows the situation for a layer located at 35 km depth in a crust that, whatever the mechanism, begins to experience an anomalously high subcrustal heat flux of 100 mW m^{-3}. The melting rate is faster than before, but the zircon and melt still reach equilibrium before the melt fraction increases to 0.1; again, therefore, the tectonically extracted melt will not entrain metastable zircons.

Figure 74c shows what happens when a sizable mafic sill with T = 1300 °C emplaces beneath the crust and heats the overlying crustal materials. In this case, the melt production is so fast that it may be extracted before reaching zircon saturation and, therefore, capable of carrying many metastable zircons in suspension. The future of these zircons depends on the cooling gradient of the extracted melt. If the gradient is slower than 0.002 °C $year^{-1}$, the suspended metastable zircons will not survive. With faster gradients, metastable zircons can dissolve partially but not totally, remaining as inherited phases in the consolidated magmatic rock.

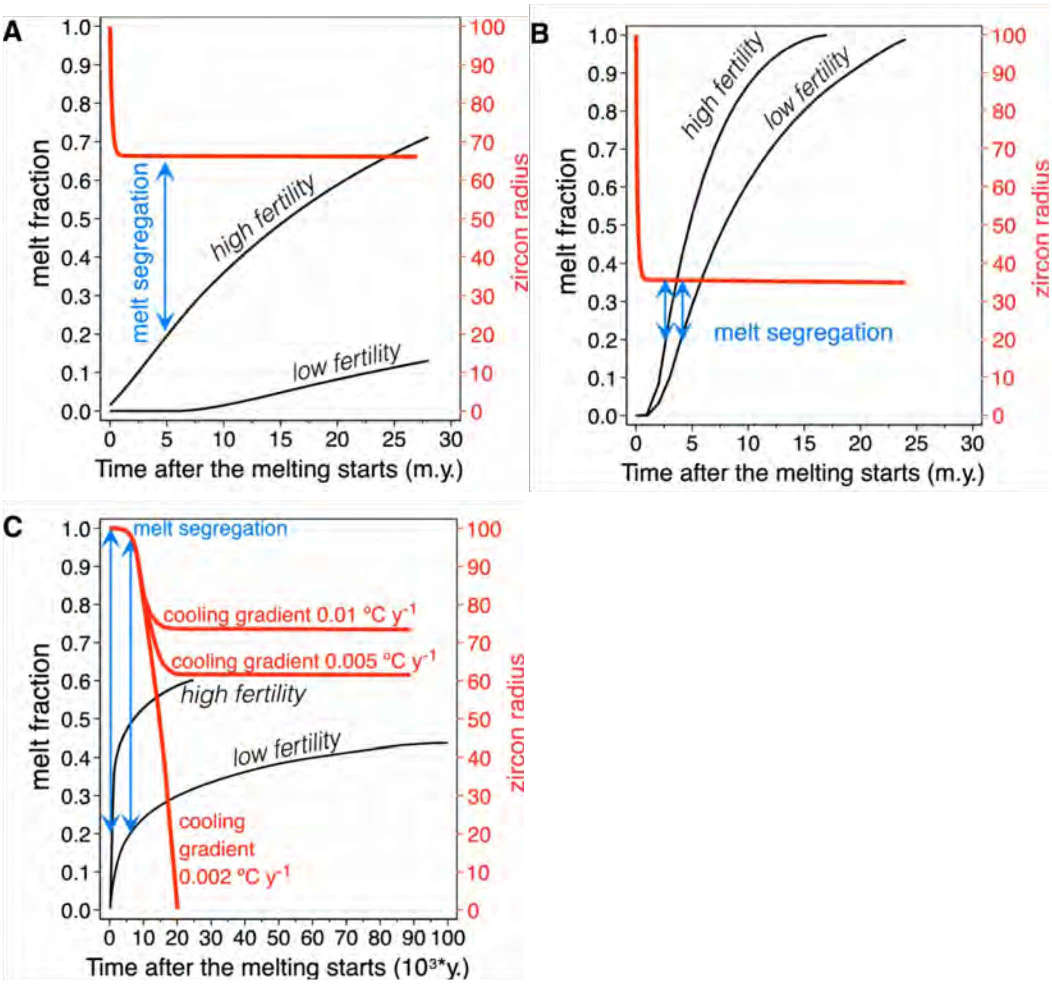

Figura 74. Melt production and zircon solubility in the resulting melts as functions of time. The melt fraction was calculated using 2D COMSOL thermal models (Bea, 2012). We equaled it to the average production within a square (1 km side) located at the crust base in models B and C and 35 km depth in model A (thickened crust). Zircon solubility is represented as the radius variation of a spherical zircon (initial radius of 100 μm) suspended within a felsic melt with temperature evolving from the beginning of melting until the melt fraction reaches 0.2. We considered this value close to the minimum at which significant melt volumes can be tectonically extracted from the source; remarkably, the same conclusions hold if extraction happens when the melt fraction is just 0.1. A) Evolution of a stacked continental crust with a layer located at 35 km depth with a very high heat production of 3.5 μWm^{-3}. The heat generation rate is so slow that the zircon dissolution rate exceeds the melt generation rate. The radius of entrained zircons decreases swiftly during the initial stages of melting, but it stabilizes long before the melt segregation occurs. B) Evolution of a normal 35 km thick crust that suddenly receives an extraordinarily high subcrustal heat flux of 100 mWm^{-2}. As before, melt segregation occurs when zircons are in equilibrium with the melt. C) Evolution of a normal 35 km thick crust underplated by a 5 km thick mafic sill with temperature of 1300 ºC. In this case, heat is supplied so quickly that the melt fraction in the source reaches 0.2 before zircon and melt can attain equilibrium. Melt extracted when its fraction in the source reaches 0.2 will contain numerous metastable entrained zircons, the fate of which depends on the melt cooling gradient after extraction. If this is 0.002 ºC year^{-1} or slower, metastable zircons in the resulting rock. The last situation will happen if the melt is swiftly displaced to upper crustal levels.

Therefore, we suggest that deformation-enhanced melt extraction has no significant effects on zircon inheritance except at top of underplated (or intraplated) hot mafic magmas (Bea et al., 2007). In all other crustal melting scenarios, the limiting factor is the enormous specific heat of melting of silicates (qm ≈ 400,000 J kg^{-1}). Because of this value, to generate melts fast enough to prevent equilibrium with zircon requires a much faster heat flux than it can conceivably be supplied by radiogenic heat generation or asthenospheric upwelling. Only underplating, in which most of the heat transferred to the crust is the latent heat of crystallization released by the mafic magma, fulfills this requirement.

III.1.3.3 Implications of the model

A fertile peraluminous source with about 200–230 ppm Zr, such as the one considered here, can produce a volume of zircon-free magmas enough to overcome the Rigid Percolation Threshold if the temperature is 770–820 °C, and its water content is about 2–3 wt% (depending on the pressure). These are "dry" magmas compared with the experimentally determined H_2O vs. temperature correlation for granitic magmas shown by Clemens & Watkins (2001; Fig. 2 of these authors, based on data compiled by Scaillet et al., 1998).

The same source with about 8 wt% H_2O can melt copiously at about 700 °C overcoming the Rigid Percolation Threshold, but only within a pressure window between 4.5 and 6 kbar (Fig. 70). The result will be a "wet" magma laden with partially dissolved source zircons.

These observations account for the situation of the two granites shown in Fig. 67. Pedrobernardo, with low inheritance, likely formed at about 750 °C (close to its average T_{Zr}) and 2–3 wt% water is "dry". Ledesma, with very high zircon inheritance, likely formed at about 700 °C and 8 wt% water is "wet". Remarkably, in the two cases, the crustal melting occurred around 4–5 kb to 5 kb (Pereira, 1998; Escuder Viruete, J. et al., 1994) i.e., within the window of maximum melt production mentioned before.

The inheritance of source zircons in magmas derived from metaluminous felsic to intermediate sources is not that straightforward. First, because they usually contain less Zr that the peraluminous sources and a part of it dwells in titanite, amphibole, and clinopyroxene (Bea et al., 2006b). These minerals release Zr to the melt quicker than zircon does, thus contributing to reaching saturation faster. Second, melts tend to be less silicic and require more Zr to attain saturation at the same temperature than melts derived from peraluminous sources. Magmas with moderate zircon inheritance cannot overcome 725 °C, and high inheritance magmas cannot overcome 700 °C (Fig. 69). At 725 °C, the amount of water required to surpass the Rigid Percolation Threshold is ≥ 8 wt%, and the pressure must be > 4.5 kbar (Fig. 72). With 4 wt% water and 725 °C, the system can only overcome the Melt Escape Threshold at pressure ≥ 3.5 kbar, but at 700 °C, the melt cannot escape from the source (Fig. 72).

The situation for mafic sources is even worse, because in general, they contain less Zr and zircon (some Zr is in other minerals), and the melts generated from them have higher zircon solubility (Fig. 73). Solely an extraordinary combination of very low melting temperature and an unusual excess of water at pressures > 5 kbar might result in magmas laden with some source zircons.

III.1.3.4 The sources of water

The results described in section **III.1.2** indicate that sources with very high water content, higher than what their hydrated minerals can provide by decomposition, can produce magmas with a high fraction of inherited zircon, so there must be a contribution of water from outside. The question is, therefore, the origin of this extra water.

We believe that most of this extra water must come from the non-fertile meta-sedimentary rocks at the bottom of the crustal section undergoing anatexis (see Collins et al., 2016). Metapelitic and metapsammitic rocks can provide water via dehydration of phyllosilicates, because they are involved in metamorphic reactions at relatively low temperatures. Grant (1985), for example, showed that the reactions quartz + muscovite = K-feldspar ± aluminosilicate + H_2O; and quartz + aluminosilicate + biotite = K-feldspar + garnet + H_2O intersect at about 6 kbar and 720 °C, producing considerable water. If these reactions occur in a fertile rock, that is to say, containing Na-rich plagioclase, the water released will be used to generate melt. If, on the other hand, the rock is unfertile, with very little or no plagioclase as is the case of many metapelites, the released H_2O would migrate upwards until finding a fertile level that will melt to produce water-rich magmas if the temperature is appropriate. The so-generated water-rich magmas will have little ascensional capability but given that they occur in large anatectic complexes, they still can move upwards developing diapir-like structures as long as the wall rocks are at nearly the same temperature than the magmas.

Extra water for crustal melting might also be exsolved from crystallizing underplated or intraplated mafic magmas, even from subducted materials in supra-subduction zones. However, the temperatures involved in these contexts probably exceed the required for zircon saturation. Therefore, it is uncertain whether the resulting magmas may contain abundant zircon inherited from their sources.

III.1.3.5 Does inherited zircon reflect the fraction of restite in granites?

This is a not trivial question that has many implications on the origin of granite rocks. We agree with Clemens (2003) that the answer is no, although for somewhat different reasons. This author suggested that one reason is the highly refractory behavior of zircon during partial melting, which is true, but it is still more important that it neither reacts to form other phases nor decomposes until T > 1400 °C (Kaiser et al., 2008). Sillimanite is as refractory as zircon but quickly reacts with a hydrated granitic melt to form muscovite. Clemens (2003) also suggested that most zircon in the sources is included in other minerals, especially biotite (see also Bea, 1996a), which “when decomposes liberates many zircons that because of their small size, can be carried away as the melt rapidly segregates and ascends” (sic.). However, the fact is that refractory minerals formed by the decomposition of biotite, such as garnet, retain most of the zircon inclusions originally contained in the biotite (Bea et al., 2018a, Fig. 5).

The key point for understanding why the abundance of inherited zircon does not have to reflect the restite fraction is that, for the same source composition and temperature, the melt fraction depends on the amount of available H_2O, whereas zircon inheritance mainly depends on temperature. Accordingly, magmas with the same melt fraction, hence with similar restite loading, may have very different zircon inheritance. Additionally, the discharge of restitic major minerals is easier than the discharge of inherited zircon grains merely because of the smaller size of the latter. Neither gravity, not filter pressing would be able to separate crystals with a maximum dimension of 100–200 μm, generally much less, from a liquid with viscosity > 10^5 Pa s even if the crystal-melt difference in specific gravity is around 1.5.

These small zircon crystals suspended in the melt can be transported as long as they do not dissolve. The magma can interact with wall rocks, get contaminated, or experience other processes affecting its isotopic and chemical composition, and still keeping zircons inherited from the source, which would be the only reliable witnesses of the source’s nature.

III.1.3.6 The locus of “wet” high-inheritance granites

Granites with high zircon inheritance (≥ 95% of grains with inherited cores) are reasonably frequent in Central Iberia. They share many characteristics: they are very peraluminous with a varietal mineralogy consisting of two micas ± cordierite and rarely show garnet. So far, six high-inheritance “wet” plutons have been identified by Bea et al. (2021), but the catalogue is far from complete due to the extensive fieldwork and SHRIMP needed for conclude it. These plutons always occur within anatectic or thermal dome complexes, being autochthonous to sub-autochthonous plutons with short magmatic history. Plutons occur where non-fertile metapelites are closely related to highly fertile gneisses, which, according to spatial relationships and zircon ages, were the source of the high-inheritance granites. On the other hand, the large amount of water needed to form these "wet" high-inheritance granites comes from the dehydration of the metapelites. Remarkably, large anatectic areas such as the Peña Negra complex of Central Iberia, which is mostly composed of fertile greywackes and sparse non-fertile metapelites (Bea et al., 1994b; Pereira, 1998), have no or very few high-inheritance granites.

III.1.4 Conclusions

Older-than-host zircons inherited from the source are characteristic of granite rocks, where they may appear in large concentrations depending on the water present in the granite magmas.

The interplay between zircon saturation in the melt phase and magma mobility determines whether or not an igneous rock can inherit zircons from their source. The most likely parameter to cause large variations of zircon inheritance in otherwise similar granites is the water content, because it has very little influence on the zircon saturation but increases the melt fraction vastly.

In most cases, the kinetics of zircon dissolution is notably faster than the rate of generation of anatectic melts, because the production rate of these is limited by the enormous specific heat of melting of silicates ($q_m \approx 400{,}000$ J kg−1). To generate melts fast enough to prevent equilibrium with zircon requires a much more intense heat flux to the magmatic source than it can be supplied by radiogenic heat generation or asthenospheric upwelling. Only underplating by hot mafic magmas, in which most of the heat transferred to the crust comes from the mafic magma latent heat of crystallization, meet this requirement. The consequence of the zircon dis- solution kinetic outpacing the melt generation rate is that fast melt extraction usually has little influence on zircon inheritance. Only melts generated atop of underplated or intraplated mafic sills may entrain abundant metastable zircons, which, depending on the cooling rate of the extracted melts, may dissolve entirely or survive as inherited xenocrysts. In this case, the conclusions of our models would not apply. In the rest, zircon would always be in equilibrium with the anatectic melt so that the abundance of inherited zircon will reflect the abundance of water in the source.

Our results foresee that zircon survival during anatexis is more probable if the source consists of fertile peraluminous metasedimentary rocks instead of metaluminous felsic to mafic rocks. Extensive zircon inheritance is characteristic of S-type water-rich granite magmas generated within a pressure window of 4.5–6 kbar. In contrast, moderate or no inheritance is characteristic of water-poor granite magmas, because these require higher temperatures to produce the same fraction of melt. The occurrence of other Zr-bearing phases such as garnet and xenotime in peraluminous protoliths and amphibole, clinopyroxene, and titanite in metaluminous protoliths, hardly affects zircon solubility unless their modal abundances are very high.

The Miller et al. (2003) classification in "hot" and "cold" granites according to their zircon inheritance and T_{Zr} may be further refined by splitting the "cold" granites ($T_{Zr} < 800$ °C) into two categories, "dry" with little inheritance and "wet" with a very high zircon inheritance.

Wet granites, mostly S-type, require a water-fluxed source. We propose that the extra water comes from dehydration reactions of the unfertile metasedimentary rocks beneath the crustal section undergoing anatexis. In Central Iberia these wet granites with exceptionally high zircon inheritance occur in anatectic areas, where unfertile metapelites are closely spatially related to highly fertile gneisses. It seems, therefore, that whereas the gneisses provided the material for melting, the metapelites dehydration provided the vast amount of water required to form low T (i.e., with little capability for dissolving zircon) voluminous melts.

III.2 Zircon crystallization from Zr-low mafic magmas

III.2.1 The problem

Early experimental studies on lunar basalts revealed that zircon could not form until 99.96-99.92% of the liquid had already crystallized (Hess et al., 1980; Dickinson & Hess, 1982), an idea confirmed by later experiments on terrestrial low-silica melts (e.g., Borisov & Aranovich, 2019; Shao et al., 2019) (Fig. 9). Nonetheless, and against what is foreseen by the experimental data, syn-magmatic zircon crystals abound in many mafic and ultramafic rocks (e.g. Claeson (1999); Williams & Hergt (2000); Bea et al. (2006a); Grimes et al. (2011); Yang et al. (2018); etc.), even as inclusions in early-formed major minerals (Fig. 10), thus indicating that zircon can precipitate before the bulk mafic melt became zircon-saturated. A remarkable case is the occurrence of zircon in the troctolites and gabbros from the Mid-Atlantic Core Complexes (Bortnikov et al., 2005, 2008; Grimes et al., 2009; Silantyev et al., 2010; Skolotnev et al., 2010), where most zircon-bearing rocks are early-stage cumulates formed from zircon-undersaturated incompatible-element depleted MORB magmas. Additionally, and to further increase the incongruence with bulk-rock composition, these zircons have abundant inclusions rich in incompatible elements (see Supplementary Material).

The notable coincidence of the experimental models signaling the elevated solubility of zircon in mafic magmas indicates that this is a genuine feature unaffected by factors other than the melt composition and temperature. Therefore, to explain why zircon precipitates from zircon-undersaturated magmas, we must consider other factors different from increasing the Zr bulk concentration in the melt because of volume reduction as the crystallization progresses. To this end, we did a 2D finite element study of how the Zr^{4+} ions rejected by growing major minerals diffuse into the melt, using COMSOL™ - based programs provided by F. Bea. The study was based on Smith et al. (1955) mathematical analysis of solute redistribution during solidification. It was constrained to simulate the evolution of inter-cumulus melt in the Mid-Atlantic zircon-bearing gabbroic cumulates because these contain abundant syn-magmatic zircon. Our results reveal that the formation of transient locally-saturated zones at the crystals-melt interfaces during confined crystallization can explain the discrepancy between experiments and observations.

III.2.2. Zircon in Mid-Atlantic cumulates: inclusions and Ti-in-zircon temperatures

The gabbros from the Mid-Atlantic Ridge (MAR) represent adcumulates and mesocumulates from abyssal tholeiite magma at various stages of advancing fractionation. Miyashiro & Shido (1980) classified them into three groups: early stage, middle stage, and later stage, which sharply differ in Fe_{tot}/Mg and incompatible elements, these increasing from the early- to late-stage gabbros. The occurrence of both inherited and syn-magmatic zircon in Mid-Atlantic gabbros is well known and poses many exciting problems (Pilot et al., 1998; Bortnikov et al., 2005, 2008; Grimes et al., 2009; Silantyev et al., 2010; Skolotnev et al., 2010; Bortnikov et al., 2019, 2022). Bea et al. (2020) discussed the survival of inherited zircons; hence it will not be further debated here. In this paper, we focussed on syn-magmatic zircons trying to understand how they precipitated from MORB magmas. To this end, we studied zircon grains found in eleven samples —chiefly early-stage gabbros formed of olivine, labradorite-bytownite, and scarce clinopyroxene, with neither Ti-minerals nor amphibole— collected in seven MAR localities from N 0º to about N 30º (Bortnikov et al., 2019). The collection contained about 116 grains, 89 syn-magmatic according to their SHRIMP U-Pb ages and Oxygen isotope compositions (Table ST10, see Bea et al. (2020), for discussion).

III.2.2.1 Inclusions

Syn-magmatic zircons contain many cavities and inclusions. Cavities seemingly were filled with fluids; in most cases, they appear within an outer anhedral aureole surrounding a large cavity-free euhedral core (see Figs. 13 and 14 in Aranovich et al., 2017), a feature that, to our knowledge, seems exclusive to oceanic zircons. The inclusions (Figs. S3 to S14) are polymineralic or monomineralic, drop-like to irregular, occasionally infilling veinlets and corrosion channels. Drop-like polymineralic inclusions composed of quartz + albite to oligoclase + alkali feldspar ± amphibole ± biotite ± apatite in different combinations probably represent recrystallized melt inclusions. Bimineralic or monomineralic inclusions likely consisted of solid phases already existing when zircon precipitated. These inclusions show a notable mineralogical variety (see Figs. S3 to S14) that suggests a wide range of zircon crystallization temperatures: clinopyroxene, Ca-rich plagioclase, and baddeleyite inclusions suggest high-T melts, whereas Cs-rich micas, Th minerals, and xenotime inclusions point to highly-evolved, low-T, incompatible element enriched magmas and fluids, which is most remarkable considering the scarcity of these elements in the bulk rock. It is also worth noting that we found just one inclusion of a Ti-rich mineral (rutile); this indicates low titanium activity ($a\text{TiO}_2$) in the melts zircon crystallized from, an observation relevant to interpreting the Ti-in-zircon thermometer results described below.

III.2.2.2 Ti-in-zircon temperatures

The Ti-in-zircon thermometer (Watson & Harrison, 2005; Watson et al., 2006) yielded temperatures from 667 ºC to 923 ºC, with a peak at 780 ºC (Fig. 75A). These values likely underestimate the crystallization temperatures because the thermometer, to be accurate, requires the SiO_2 and TiO_2 activities in the melt to be one. That said, the question is to determine whether the underestimation is similar for all grains so that the amplitude of Ti-in-zircon distribution is similar to the range of zircon crystallization temperatures, which is relevant to understanding how zircons formed.

At elevated temperatures, the low silica activity can compensate, at least partially, the effects of low $a\text{TiO}_2$ (Ferry & Watson, 2006; Harrison et al., 2007). The increase of $a\text{SiO}_2$ with differentiation will change the extension of the compensation and thus cause unrealistic variations of the Ti-in-zircon temperature. However, these potential variations will cease once the MORB magmas are saturated in silica, likely occurring at about 1020 ºC according to rhyolite-MELTS calculations. Above this temperature, the MORB crystallinity is barely enough to produce the confined crystallization required for local saturation (see below) so that no zircons will form. Below 1020 ºC, on the other hand, all residual melts had $a\text{TiO}_2 < 1$ and $a\text{SiO}_2 \approx 1$, so that the Ti partition into zircon would remain similarly affected in all cases, thus yielding a Ti-in-zircon output range unaffected by possible variations of these components activity. The idea that the Ti-in-zircon output range resembles that of the actual crystallization temperatures finds support from comparing the Ti-in-zircon output from zircon grains with high-T inclusions to those having low-T inclusions (Fig. 75A). The former averaged 786 ºC with a 95% confidence interval between 771 ºC and 801 ºC; the latter averaged 763 ºC with a 95% confidence interval of 751 ºC to 775 ºC. The difference between the means is significant with a probability > 97.95% and reinforces the idea that MORB zircons crystallized over a wide temperature interval, a question that does not fit with the "last drop" crystallization foreseen by the elevated zircon solubility.

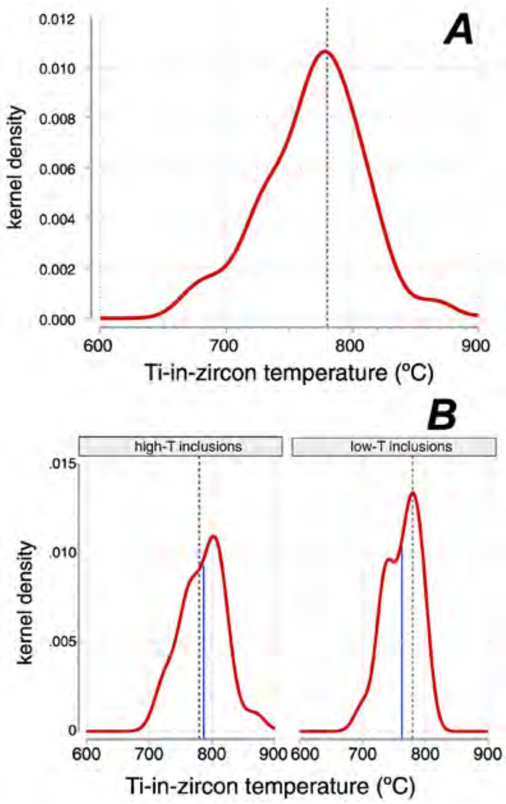

Fig. 75. A) Distribution of the Ti-in-zircon temperatures in the whole collection. Note the wide range characteristic of zircons crystallized from mafic rock (Fu et al., 2008). In this case, the thermometer underestimates the crystallization temperature because of the low Ti activity in the zircon-crystallizing magmas. B) Comparison of the Ti-in-zircon temperature in grains containing high-T and low-T inclusions. The dashed lines represent the mode of all analyses. The blue lines represent each group's average. See text for discussion.

III.2.3. The numerical model

III.2.3.1 Starting considerations

The immediate neighborhood of a growing crystal is a complex region undergoing marked thermal and diffusive effects. Adjacent to the crystal/melt interface, there is a volume affected by diffusion to and from the crystal as it grows called the diffusion boundary layer (see Henderson, 1982). Each chemical species in the melt has its diffusion boundary layer, the thickness of which depends on the diffusivity.

The dimensions of the diffusion boundary layer are markedly affected by the melt movements. If these occur, the relative displacement of melt and crystals will erode it, increasing the bulk diffusion towards the far-away melt of Zr and all other components rejected by the growing crystals. Considering the factors that affect magma dynamics, it seems evident that crystallization with no melt stirring may occur only in small isolated melt pockets formed in cumulated rocks, i.e. after the rock has reached the critical crystallinity, that is, the point at which the random close packing of solids is reached which is close to 70-75% solidification (Vigneresse et al., 1996). This kind of crystallization, called "in confinement", has not been yet studied for silicate melts, but experience with other crystallization systems revealed that it profoundly affects crystal nucleation and growth (Meldrum & O'Shaughnessy, 2020). For our purposes here, it suffices to consider that confined crystallization permits the broadest and most stable diffusion boundary layer in front of a growing crystal-melt interface. Therefore, we modeled the evolution of the melt in an occluding pore with walls formed on Zr-free minerals.

III.2.3.2 Mafic magma composition

We worked with the MORB composition reported by Allan et al. (1989) and used by Ghiorso (1997) as an example for running the software rhyolite-MELTS (Gualda et al., 2012; Ghiorso & Gualda, 2015). For Zr, we assumed a concentration of 2.86 mol m^{-3} (≈100 ppm), i.e., slightly less than the N-MORB average of Hofmann (1988). With rMELTS, we calculated the isobaric crystallization of the MORB magma at 0.5 kbar, subsequently using the composition of liquids for calculating the melt viscosity (rMELTS), Zr^{4+} diffusivity, and zircon solubility (Borisov & Aranovich, 2019) in each liquid.

III.2.3.3 Zr diffusivity.

We assumed that all zirconium present in the melt was Zr^{4+}, which diffuses slowly (e.g. Holycross & Watson, 2016). To account for the changes in the melt composition, instead of calculating the diffusion coefficient with an Arrhenius equation such as the provided by the above-mentioned authors, we used the Eyring (1936) diffusion coefficients, $D_{Zr} = kT/\eta\boldsymbol{\lambda}$, where k is the Boltzmann constant, T is the temperature (K), η is the dynamic viscosity as calculated by rMELTS, and $\boldsymbol{\lambda}$ is the jumping distance for the diffusional species. We calculated this last value for 1100 ºC using $D_{Zr} = 8.9732 * 10^{-13}$ m^2s^{-1} from the Zr^{4+} self-diffusion coefficient for an haplobasaltic melt at 1100 ºC determined by LaTourrette et al. (1996), and found a value of 0.33 nanometers, very close to the assumed by Zhang & Xu (2016) for rhyolitic melts.

III.2.3.4 The finite elements model

To study the diffusion kinetics of Zr rejected by growing minerals, and based on Smith et al. (1955) mathematical analysis of solute redistribution during solidification, we used 2D finite element models with moving mesh (see Supplementary animation). For this purpose, we employed COMSOL™, a commercial finite element software that links a given geometry with multiple partial differential equations. To avoid singularities and convergence problems that might stop the calculations, we started using the most straightforward 2D geometry, i.e., a 1000*1500 µm rectangular pore filled with melt (Fig. 76). The two lengthiest horizontal sides are considered thermally insulated. The right vertical side is the phase-change interface that displaces to the left as the system cools. Cooling is caused by heat loss on the opposite side (Fig. 76). The heat flow through this wall was adjusted to cause a growth rate of $1.6* 10^{-8}$ ms^{-1}, implying a low undercooling of $\Delta T < 5$ ºC (Kirkpatrick, 1981). The model simulated cooling during 1000 minutes displacing the phase change interface 980 µm to the left and duly reducing the melt volume to one third. The fully functional COMSOL 5.6 model and a video of the evolving model are given in the supplementary material. Additional models with two moving interfaces do not change the results.

First, we calculated the changes in the melt composition assuming that no Zr was incorporated into the growing crystal, for example, olivine, orthopyroxene, or plagioclase (Bea et al., 2006b); accordingly, the Zr mass in the melt keeps constant, increasing its concentration simply because of the volume reduction. Second, we assumed that the growing crystal incorporates some Zr, such as clinopyroxene, amphibole, or garnet, and studied the effects of different partition coefficients on the evolution of the melt composition.

III.2.4. Results

The evolution of the Zr diffusion field in front of Zr-free growing minerals is shown in Figure 77. It reveals how the diffusion field contracts perpendicularly to the growing face displacement and the Zr concentration near the interface increases as the crystal grows, reaching zircon saturation once the melt volume is reduced to about half and the temperature decreases to about 1020 ºC, i.e., likely marking the onset of zircon crystallization. From this point onwards, zircon may precipitate uninterruptedly until the last melt drop, causing the wide range of Ti-in-zircon temperatures shown in Figure 75.

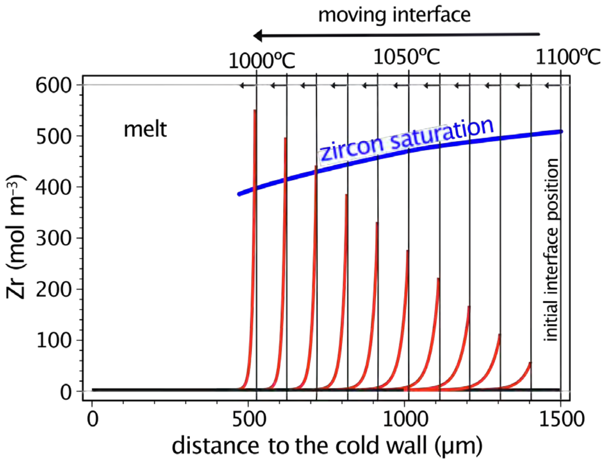

Fig. 77. Evolution of the Zr concentration (red lines) near the crystal-melt interface (light black lines) as it moves, closing the pore. The linear dimension of the pore is initially 1500 μm, when temperature is 1100 ºC, decreasing to 520 μm at 1000 ºC. Note the Zr concentration near the interface increase to saturation at 1020 ºC approximately and how the diffusion field contracts.

We built another model with two opposite sloped interfaces growing one toward the other to understand the situation in the junction (Supplementary animation 2). Although the finite element model does not converge once the two interfaces contact, it is still possible to visualize how the zone where Zr concentration reaches saturation is maximum in the apex, suggesting that oblique grain junctions of closing melt pores should favor zircon crystallization.

However, the creation of local zircon-saturated zones would be delayed, even totally prevented if the growing minerals can uptake some Zr, such is the case of clinopyroxene, amphibole, or garnet (Bea et al., 2006a and 2006b). Figure 78 shows the Zr concentration near the interface of minerals with different mineral/melt Zr partition coefficients. The calculations reveal that saturation can only be reached if the Kd_{Zr} <= 0.2.

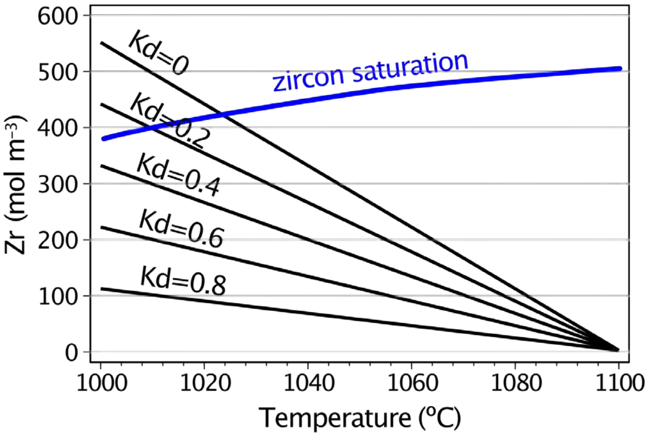

Fig. 78. Evolution of the Zr concentration at the moving interface of minerals with different Zr mineral/melt partition coefficient (Kd_{Zr}) as the temperature decreases. The concentration increases until zircon saturation only if Kd_{Zr} < 0.2, approximately. The amphibole crystallization and, to some extent, clinopyroxene will thus inhibit the recrystallization, explaining why zircon in Mid-Atlantic rocks is more abundant in troctolite and olivine gabbros than any other rock.

III.2.5. Discussion and conclusions

The COMSOL model presented here is an extreme simplification. Nonetheless, we believe that it adequately reflects how zircon crystallizes from mafic rocks, since it is based on internally consistent melting properties, conserves the mass of Zr in melting, and is consistent with many observations in nature.

The local Zr enrichment at the growing interfaces of major minerals can only occur after the magma reaches a crystallinity such that the residual melt remains confined in pores; otherwise, the relative displacement of melt and crystals caused by magma movements —inescapable at low crystallinities— would erode the Zr-rich melt created in the diffusion boundary layers. This phenomenon explains why the occurrence of Mid-Atlantic syn-magmatic zircons is restricted chiefly to cumulate rocks.

Local saturation near growing minerals interfaces seems to be the only way for explaining the formation of zircon much before the bulk mafic magma filling the pores becomes zircon-saturated. Our calculations for the average MORB composition foresee that zircon crystallization starts around 1020ºC and may continue until the last drop of fluid. Along this path, the whole melt may become zircon-saturated if its composition changes to water-rich and acidic (Borisov & Aranovich, 2019). The increasing water content and the switching from water-absent to water-present conditions is likely the cause for the development of anhedral and cavity-rich rims around euhedral cavity-free cores described by Aranovich et al. (2017).

The wide range of crystallization temperatures foreseen by the model may explain (i) the mineralogical variety of zircon inclusions, (ii) the range of Ti-in-zircon temperatures characteristically found in mafic rocks (Valley et al., 2006) and (iii) the fractionation of Zr isotopes as proposed by Chen et al. (2020). The enrichment in rejected ions near the interface will also occur for other incompatible elements, thus producing abundant inclusions of minerals rich in these elements such as Cs-rich felspars and micas, Th minerals, and Y-REE phosphates.

On the other hand, the crystallization of major minerals able to partition Zr will hinder, even totally prevent, the process. The model foresees that growing minerals with Zr mineral/melt partition coefficient (Kd_{Zr}) > 0.2 will not cause zircon-saturated diffusion boundary layers, which implies that mafic systems precipitating clinopyroxene and, especially, amphibole will never reach zircon saturation if they are not initially meaningfully richer in zircon than the MORB example considered here. This effect may explain why only the early-stage cumulates among the Mid-Atlantic rocks contain zircon primocrysts, whereas these lack in the more evolved second- and late-stage cumulates.

Therefore, we conclude that the answer to the question posed in this paper title is: yes, zircon crystallization in low-Zr mafic magmas is perfectly possible under confined crystallization.

PART IV. CONCLUSIONS

CONCLUSIONES

This final chapter summarizes the most important experimental results on the stability of zircon and its geochemical behavior, both at high temperatures and in the presence of aqueous and saline fluids. It also summarizes the main predictions of the numerical models about the importance of water in the magma on zircon inheritance in granite magmas and the mechanisms for zircon crystallization from low-Zr zircon-undersaturated magmas.

IV.1 Conclusions

Experimental studies

IV.1.1 High-temperatures experiments

Zircon annealing caused recrystallization of metamict domains, melting of polymineralic inclusions, formation of nanopores and microcracking, propagated by thermo-elastic stress accumulated at the interface between domains with different lattice orientations that enhanced permeability, allowing melt migration through the crystal and leaching out impurities.

The zircon-to-baddeleyite transformation took place during annealing at temperatures significantly lower than this for the thermal decomposition of pure zircon by two different mechanisms: (i) incongruent zircon dissolution in molten mineral inclusions with a high CaO/SiO_2 ratio, and (ii) recrystallization of metamict domains mediated by silica releasing from the reaction site.

Highly metamict zircon grains, impossible to date with the SHRIMP due to their high common Pb and radiogenic Pb loss, were successfully dated after annealing at 1300 ºC because all their common Pb but little radiogenic Pb were lost. It is concluded that the most important requirement for losing almost all common Pb is the generation of a melt, thus providing a method for dating “undateable” zircons. The different behavior of common and radiogenic Pb is attributed to the occurrence of the former as metallic or Pb oxide nanospheres and the latter as ions in the zircon lattice.

Ti concentration increased in the lattice of annealed zircon grains with minute inclusions of rutile or other Ti-bearing minerals. Tungsten can achieve high abundances in zircons from regions with W deposits. An overall increase in the W concentration of zircon occurred upon annealing because of the dissolution of minute W impurities into the zircon lattice. However, given the limited solubility of W in zircon, a fraction of the released W was consumed in forming W-rich minerals.

The oxygen isotope composition of annealed zircon grains included in mineral silicates drifts quickly to that of their host. Therefore, it is concluded that crustal-derived zircon xenocrysts with high $\partial^{18}O$ found in mantle rocks could not have resided within them at mantle temperatures for a long time.

IV.1.2 Hydrothermal experiments

Congruent zircon dissolution takes place in the presence of H_2O and saline fluids at 170ºC leading to an increase of zircon permeability along microcracks, both radial and along the core-rim interface of zircon with inherited cores, and microporous bands that were present in the untreated zircon.

At 550ºC, zircon also dissolves congruently in silica-saturated, H_2O, $CaCl_2$ and NaCl fluids but incongruently to yield Na-Zr silicates in silica-saturated NaF fluids. In high-T, silica-undersaturated fluids, even H_2O, zircon is transformed to baddeleyite by coupled dissolution-precipitation mechanisms enhanced by microcracks and pores and permeability creation associated with silica releasing from the reaction site and to the lower molar volume of baddeleyite. Solutions with the monovalent Na cation are more reactive than those with the divalent Ca cation as evidenced by the total zircon-to-baddeleyite transformation in NaCl and NaF fluids.

A remarkable decoupling of Y with respect to HREE is present in leachates extracted from both high- and low-T hydrothermal experiments, Yttrium being significantly more partitioned into the fluid than HREE. Pb is also partitioned into the leachates with respect to U in all experiments, whereas a significant Th-U fractionation is only present in $CaCl_2$ and NaCl fluids at low-T conditions, with Th being more partitioned into the fluid.

These results are relevant for the stability and geochemical behavior of zircon in hydrothermal environments, concluding that saline and H_2O fluids can efficiently dissolve zircon in epithermal to pneumatolytic processes at high fluid/zircon ratios.

Numerical modeling

IV.1.3 Zircon inheritance

The capacity of granitic magmas to inherit zircons from their source is a consequence of the interplay between zircon saturation in the melt and magma mobility. The numerical models suggest that the water content of magmas is the key parameter for controlling the abundance of inherited zircon that can be present in granitic rocks because its influence on melt fraction is important but negligible on zircon saturation.

In most cases, the zircon dissolution rate is notably faster than the anatectic melt generation rate because this latter is limited by the huge specific heat of silicate melting. A much more intense heat flux than the one supplied by radioactive decay or asthenospheric upwelling is necessary to generate melts fast enough to prevent equilibrium with zircon. This requirement is met only by hot mafic magma underplating, where most of the heat released to the crust comes from its latent heat of crystallization.

The calculations predict that zircon survival during anatexis is more likely if fertile peraluminous metasedimentary rocks rather than metaluminous felsic to mafic ones dominate the source. Zircon inheritance is extensive in S-type water-rich granite magmas generated at 4.5–6 kbar. In contrast, water-poor granite magmas are characterized by moderate or no inheritance because they need higher temperatures to produce a similar melt fraction. Zircon solubility is hardly affected by the appearance of other Zr-bearing phases, such as garnet and xenotime in peraluminous compositions and amphibole, clinopyroxene, and titanite in metaluminous ones if their modal abundance is not very high.

The classification of Miller et al. (2003) into “cold” and “hot” granites, according to their T_{Zr} and zircon inheritance, can be refined by dividing “cold” granites, with $T_{Zr} < 800$ °C, into two categories: “dry”, with low zircon inheritance and “wet”, with high zircon inheritance.

Wet, mostly S-type, granites are derived from a water-fluxed source. The extra water input comes from dehydration reactions of the unfertile metasedimentary rocks located below the anatectic crustal region.

IV.1.4 Zircon crystallization from Zr-low mafic magmas

The proposed COMSOL model allows us to explain satisfactorily the mechanism by which zircon can crystallize from mafic magmas because it is based on internally consistent melting properties, conserves Zr mass during melting and is consistent with many observations in nature.

Local Zr enrichment at growing interfaces of major minerals can only occur once magma reaches a crystallinity high enough to confine residual melts into pores; otherwise, relative melt and crystal displacement caused by magma circulation would erode the Zr-rich melt created in the diffusion boundary layers. This process explains the appearance of Mid-Atlantic syn-magmatic zircons being limited chiefly to cumulate rocks.

Local saturation next to growing mineral interfaces seems to be the only possible mechanism for explaining the appearance of zircon much before the achievement of zircon saturation by the bulk mafic magma that fills the pores. The calculations for the average MORB composition predict that zircon crystallization begins at 1020 ºC and may continue until the last melt drop. The bulk melt may reach zircon saturation along this path if it evolves towards water-rich, acidic compositions (Borisov & Aranovich, 2019). The change from water absent to water present conditions provides a likely explanation for the generation of anhedral cavity-rich zircon rimming euhedral cavity-free cores as described by Aranovich et al. (2017).

The large crystallization temperature ranges predicted by the numerical model may explain (i) the diversity of mineral inclusions hosted in zircon, (ii) the range of Ti-in-zircon temperatures typically estimated in mafic rocks (Valley et al., 2006) and (iii) the Zr isotope fractionation (Chen et al., 2020). Generation of inclusions of Cs-rich felspars and micas, Th minerals, and Y-REE phosphates would also be caused by an enrichment near the interface in other incompatible, rejected elements.

On the other hand, the proposed mechanism will be hampered, or even totally inhibited, by the crystallization of major minerals that can partition Zr. Thus, the model predicts that the growth of minerals with Zr mineral/melt partition coefficient (Kd_{Zr}) > 0.2, such as clinopyroxene and, especially, amphibole, will not produce a zircon-saturated diffusion boundary layer. This implies that the crystallization of these minerals in mafic systems will never reach zircon saturation unless they are much richer in Zr than the MORB considered in the model. These relationships explain the appearance of zircon primocrysts only in the earliest cumulates from the Mid-Atlantic rocks.

Este capítulo final resume los resultados experimentales más importantes sobre la estabilidad del zircón y su comportamiento geoquímico, tanto a altas temperaturas como en presencia de fluidos acuosos y salinos. También se resumen las principales predicciones de los modelos numéricos sobre la importancia del agua en el magma en la herencia del zircón en los magmas de granito y los mecanismos de cristalización del zircón a partir de magmas insaturados de zircón de bajo Zr.

IV.2 Conclusiones

Estudios experimental

IV.2.1 Experimentos de alta temperatura

El recocido del zircón provocó la recristalización de los dominios metamícticos, la fusión de las inclusiones poliminerales, la formación de nanoporos y la microfracturación, propagada por la tensión termoelástica acumulada en la interfaz entre los dominios con diferentes orientaciones de la red, que aumentó la permeabilidad, permitiendo la migración del fundido a través del cristal y la lixiviación de las impurezas.

La transformación de zircón a baddeleyita tuvo lugar durante el recocido a temperaturas significativamente inferiores a las de la descomposición térmica del zircón puro por dos mecanismos diferentes: (i) disolución incongruente del zircón en inclusiones minerales fundidas con una elevada relación CaO/SiO_2, y (ii) recristalización de dominios metamícticos mediada por la liberación de sílice del lugar de reacción.

Los granos de zircón altamente metamícticos, imposibles de datar con la SHRIMP debido a alto Pb común y pérdida de Pb radiogénico, fueron datados con éxito tras el recocido a 1300 ºC porque se perdió todo su Pb común pero poco Pb radiogénico. Se concluye que el requisito más importante para perder casi todo el Pb común es la generación de un fundido, proporcionando así un método para datar circones “no datables”. El diferente comportamiento del Pb común y radiogénico se atribuye a la aparición del primero como nanoesferas metálicas o de óxido de Pb y del segundo como iones en la red del zircón.

La concentración de Ti aumentó en la red de granos de zircón recocido con inclusiones diminutas de rutilo u otros minerales portadores de Ti. El wolframio puede alcanzar altas abundancias en los circones de regiones con depósitos de W. Se produjo un aumento general de la concentración de W en el zircón tras el recocido debido a la disolución de diminutas impurezas de W en la red del zircón. Sin embargo, dada la limitada solubilidad del W en el zircón, una fracción del W liberado se consumió en la formación de minerales ricos en W.

La composición isotópica de oxígeno de los granos de zircón recocidos incluidos en silicatos minerales se desplaza rápidamente hacia la de su huésped. Por lo tanto, se concluye que los xenocristales de zircón derivados de la corteza con alto $\partial 18O$ encontrados en las rocas del manto no podrían haber residido en ellas a temperaturas del manto durante mucho tiempo.

IV.2.2 Experimentos hidrotermales

La disolución congruente del zircón tiene lugar en presencia de fluidos con H_2O y salinos a 170ºC, dando lugar a un aumento de la permeabilidad del zircón a lo largo de las microfisuras, tanto radiales como a lo largo de la interfaz núcleo-borde del zircón con núcleos heredados, y las bandas microporosas que estaban presentes en el zircón no tratado.

A 550ºC, el zircón también se disuelve de forma congruente en fluidos saturados en sílice, H_2O, $CaCl_2$ y NaCl, pero de forma incongruente para dar lugar a silicatos de Na-Zr en fluidos de NaF saturados en sílice. En fluidos subsaturados en sílice de alta temperatura, incluso con H_2O, el zircón se transforma en baddeleyita por mecanismos acoplados de disolución-precipitación potenciados por microfisuras y poros y por la creación de permeabilidad asociada a la liberación de sílice del lugar de reacción y al menor volumen molar de la baddeleyita. Las soluciones con el catión monovalente Na son más reactivas que las que tienen el catión divalente Ca, como lo demuestra la transformación total de zircón en baddeleyita en los fluidos con NaCl y NaF.

En los lixiviados extraídos de experimentos hidrotermales tanto de alta como de baja temperatura se observa un notable desacoplamiento del Y con respecto a HREE, estando el Y significativamente más particionado en el fluido que las HREE. El Pb también se particiona en los lixiviados con respecto al U en todos los experimentos, mientras que un fraccionamiento significativo del Th-U sólo está presente en los fluidos con $CaCl_2$ y NaCl en condiciones de baja T, estando el Th más particionado en el fluido.

Estos resultados son relevantes para la estabilidad y el comportamiento geoquímico del zircón en ambientes hidrotermales, concluyendo que los fluidos salinos y de H_2O pueden disolver eficientemente el zircón en procesos epitermales a neumatolíticos a altas relaciones fluido/zircón.

Modelación numérica

IV.2.3 Herencia de zircón

La capacidad de los magmas graníticos para heredar circones de su fuente es una consecuencia de la interacción entre la saturación de zircón en el fundido y la movilidad del magma. Los modelos numéricos sugieren que el contenido de agua de los magmas es el parámetro clave para controlar la abundancia de zircón heredado que puede estar presente en las rocas graníticas, ya que su influencia en la fracción de fundido es importante pero insignificante en la saturación de zircón.

En la mayoría de los casos, la tasa de disolución del zircón es notablemente más rápida que la tasa de generación de fundido anatéctico porque esta última está limitada por el enorme calor específico de la fusión de los silicatos. Es necesario un flujo de calor mucho más intenso que el suministrado por la desintegración radiactiva o el afloramiento astenosférico para generar fundidos lo suficientemente rápido como para evitar el equilibrio con el zircón. Este requisito sólo lo cumple un magma máfico caliente underplating, donde la mayor parte del calor liberado a la corteza procede de su calor latente de cristalización.

Los cálculos predicen que la supervivencia del zircón durante la anatexis es más probable si las rocas metasedimentarias peraluminosas fértiles en lugar de las félsicas a máficas metaluminosas dominan la fuente. La herencia de zircón es extensa en los magmas graníticos ricos en agua de tipo S generados a 4,5-6 kbar. Por el contrario, los magmas graníticos pobres en agua se caracterizan por una herencia moderada o nula porque necesitan temperaturas más altas para producir una fracción de fundido similar. La solubilidad del zircón apenas se ve afectada por la aparición de otras fases portadoras de Zr, como el granate y la xenotima en las composiciones peraluminosas y el anfíbol, el clinopiroxeno y la titanita en las metaluminosas si su abundancia modal no es muy elevada.

La clasificación de Miller et al. (2003) en granitos “fríos” y “calientes”, según T_{Zr} y herencia de zircón, puede refinarse dividiendo los granitos “fríos”, con $T_{Zr} < 800$ °C, en dos categorías “secos”, con baja herencia de zircón y “húmedos”, con alta herencia de zircón.

Los granitos húmedos, en su mayoría de tipo S, proceden de una fuente con flujo de agua. El aporte extra de agua proviene de las reacciones de deshidratación de las rocas metasedimentarias no fértiles situadas bajo la región anatéctica de la corteza.

IV.2.4 Cristalización de zircón a partir de magmas máficos de bajo contenido en Zr.

El modelo COMSOL propuesto nos permite explicar satisfactoriamente el mecanismo por el cual el zircón puede cristalizar a partir de magmas máficos porque se basa en propiedades de fusión internamente consistentes, conserva la masa de Zr durante la fusión y es consistente con muchas observaciones en la naturaleza.

El enriquecimiento local de Zr en las interfaces de crecimiento de los principales minerales sólo puede ocurrir una vez que el magma alcanza una cristalinidad lo suficientemente alta como para confinar los fundidos residuales en los poros; de lo contrario, el desplazamiento relativo de la fusión y de los cristales causado por la circulación del magma erosionaría el fundido rico en Zr creado en las capas límite de difusión. Este proceso explica que la aparición de circones sinmagmáticos del Atlántico Medio se limite principalmente a las rocas acumuladas.

La saturación local junto a las interfases minerales en crecimiento parece ser el único mecanismo posible para explicar la aparición de zircón mucho antes de que se produzca la saturación de zircón por parte del magma máfico que rellena los poros. Los cálculos para la composición media del MORB predicen que la cristalización del zircón comienza a los 1020 ºC y puede continuar hasta la última gota de fundido. El fundido global puede alcanzar la saturación de zircón a lo largo de este camino si evoluciona hacia composiciones ácidas y ricas en agua (Borisov & Aranovich, 2019). El cambio de condiciones de ausencia de agua a presencia de agua proporciona una explicación probable para la generación de zircón anhedral rico en cavidades que bordea los núcleos euhedrales sin cavidades, tal y como describen Aranovich et al. (2017).

Los grandes rangos de temperatura de cristalización predichos por el modelo numérico pueden explicar (i) la diversidad de inclusiones minerales alojadas en el zircón, (ii) el rango de temperaturas de Ti-en-zircón típicamente estimadas en rocas máficas (Valley et al., 2006) y (iii) el fraccionamiento de isótopos de Zr (Chen et al., 2020). La generación de inclusiones de felspatos y micas ricas en Cs, minerales de Th y fosfatos de Y-REE también estaría causada por un enriquecimiento cerca de la interfase en otros elementos incompatibles y rechazados.

Por otro lado, el mecanismo propuesto se vería obstaculizado, o incluso totalmente inhibido, por la cristalización de minerales importantes que pueden particionar el Zr. Así, el modelo predice que el crecimiento de minerales con coeficiente de partición Zr mineral/fusión (Kd_{Zr}) > 0,2, como el clinopiroxeno y, especialmente, el anfíbol, no producirá una capa límite de difusión saturada de zircón. Esto implica que la cristalización de estos minerales en sistemas máficos nunca alcanzará la saturación de zircón a menos que sean mucho más ricos en Zr que el MORB considerado en el modelo. Estas relaciones explican la aparición de primocristales de zircón sólo en los primeros acumulados de las rocas del Atlántico Medio.

REFERENCES

References

Aja, S. U., Wood, S. A., & Williams-Jones, A. E. (1996). The Solubility of Some Alkali-Bearing Zr Minerals in Hydrothermal Solutions. *MRS Online Proceedings Library (OPL)*, *432*, 69-74.

Alderton, D. H. M., Pearce, J. A., & Potts, P. J. (1980). Rare earth element mobility during granite alteration: evidence from southwest England. *Earth and Planetary Science Letters*, *49*, 149-165.

Allan, J. F., Batiza, R., Perfit, M. R., Fornari, D. J., & Sack, R. O. (1989). Petrology of lavas from the Lamont seamount chain and adjacent East Pacific Rise, 10 N. *Journal of Petrology*, *30*(5), 1245-1298.

Amelin, Y. V., Lee, D.-C., & Halliday, A. N. (2000). Early-middle Archaean crustal evolution deduced from Lu-Hf and U-Pb isotopic studies of single zircon grains. *Geochimica et Cosmochimica Acta*, *64*(24), 4205-4225.

Anderson, G. M., & Burnham, C. W. (1965). The solubility of quartz in supercritical water. *American journal of Science*, *263*, 494-511.

Aranovich, L. Y., Bortnikov, N. S., Zinger, T. F., Borisovskiy, S. E., Matrenichev, V. A., Pertsev, A. N., Sharkov, E. V., & Skolotnev, S. G. (2017). Morphology and impurity elements of zircon in the oceanic lithosphere at the Mid-Atlantic ridge axial zone (6°–13° N): Evidence of specifics of magmatic crystallization and postmagmatic transformations. *Petrology*, *25*(4), 339-364.

Aranovich, L. Y., & Bortnikov, N. S. (2018). New Zr–Hf Geothermometer for Magmatic Zircons. *Petrology*, *26*(2), 115-120.

Arribas, A. (1980). Los yacimientos de tungsteno de la zona de Morille (provincia de Salamanca). *Boll. Geol. Min.*, *91*, 3-19.

Arzi, A. A. (1978). Critical phenomena in the rheology of partially melted rocks. *Tectonophysics*, *44*, 173-184.

Atencio, D., Andrade, M. B., Bastos Neto, A. C., & Pereira, V. P. (2017). Ralstonite renamed hydrokenoralstonite, coulsellite renamed fluornatrocoulsellite, and their incorporation into the pyrochlore supergroup. *Canadian Mineralogist*, *55*(1), 115-120.

Avigad, D., Kolodner, K., McWilliams, M., Persing, H., & Weissbrod, T. (2003). Origin of northern Gondwana Cambrian sandstone revealed by detrital zircon SHRIMP dating. *Geology*, *31*(3), 227-230.

Ayers, J. C., Zhang, L., Luo, Y., & Peters, T. J. (2012). Zircon solubility in alkaline aqueous fluids at upper crustal conditions. *Geochimica et Cosmochimica Acta*, *96*, 18-28.

Ayers, J. C., & Watson, E. B. (1991). Solubility of apatite, monazite, zircon and rutile in supercritical aqueous fluids with implications for subduction zone geochemistry. *Phil. Trans. R. Soc. London*, *335*, 365-375.

Bagdassarov, N. S., Dingwell, D. B., & Wilding, M. C. (1996). Rhyolite Magma Degassing - An Experimental-Study of Melt Vesiculation. *Bulletin of volcanology*, *57*(8), 587-601.

Barboza, S. A. B. G. W. (1998). Rheological transitions and the progress of melting of crustal rocks. *Earth*

Planet. Sci. Lett., *158*(1-2), 11.

Bea, F., Bortnikov, N., Cambeses, A., Chakraborty, S., Molina, J. F., Montero, P., Morales, I., Silantiev, S., & Zinger, T. (2022). Zircon crystallization in low-Zr mafic magmas : Possible or impossible. *Chemical Geology*, *602*(May), 6.

Bea, F. (1996a). Controls on the Trace Element Composition of Crustal Melts. *Transaction of the Royal Society of Edinburg: Earth Sciences*, *87*(133-41), 33-42.

Bea, F. (1996b). Residence of REE, Y, Th and U in granites and crustal protoliths; Implications for the chemistry of crustal melts. *Journal of Petrology*, *37*(3), 521-552.

Bea, F. (2010). Crystallization Dynamics of Granite Magma Chambers in the Absence of Regional Stress: Multiphysics Modeling with Natural Examples. *Journal of Petrology*, *51*, 1541-1569.

Bea, F. (2012). The sources of energy for crustal melting and the geochemistry of heat-producing elements. *Lithos*, *153*, 278-291.

Bea, F., Bortnikov, N., Montero, P., Zinger, T., Sharkov, E., Silantyev, S., Skolotnev, S., Trukhalev, A., & Molina-Palma, J. F. (2020). Zircon xenocryst evidence for crustal recycling at the Mid-Atlantic Ridge. *Lithos*, *354-355*, Article 105361, https://doi.org/10.1016/j.lithos.2019.105361.

Bea, F., Fershtater, G. B., Montero, P., Smirnov, V. N., & Molina, J. F. (2005). Deformation-driven differentiation of granitic magma: the Stepninsk pluton of the Uralides, Russia. *Lithos*, *81*, 209-233.

Bea, F., Fershtater, G. B., Montero, P., Whitehouse, M., Levin, V. Y., Scarrow, J. H., Austrheim, H., & Pushkariev, E. V. (2001). Recycling of continental crust into the mantle as revealed by Kytlym Dunite zircons, Urals Mts. Russia. *Terranova*, *13*, 407-412.

Bea, F., & Montero, P. (2013). Diffusion-induced disturbances of the U-Pb isotope system in pre-magmatic zircon and their influence on SIMS dating. A numerical study. *Chemical Geology*, *340-350*, 1-17.

Bea, F., Montero, P., González-Lodeiro, F., & Talavera, C. (2007). Zircon Inheritance Reveals Exceptionally Fast Crustal Magma Generation Processes in Central Iberia during the Cambro-Ordovician. *Journal of Petrology*, *48*(12), 2327-2339.

Bea, F., Montero, P., González-Lodeiro, F., Talavera, C., Molina, J. F., Scarrow, J. H., Whitehouse, M. J., & Zinger, T. F. (2006a). Zircon thermometry and U-Pb ion-microprobe dating of the gabbros and associated migmatites of the Variscan Toledo Anatectic Complex, Central Iberia. *Journal of the Geological Society, London*, *163*, 847-855.

Bea, F., Montero, P., Haissen, F., & El Archi, A. (2013). 2.46Ga kalsilite and nepheline syenites from the Awsard pluton, Reguibat Rise of the West African Craton, Morocco. Generation of extremely K-rich magmas at the Archean–Proterozoic transition. *Precambrian Research*, *224*, 242-254.

Bea, F., Montero, P., Haissen, F., Rjimati, E., Molina, J. F., & Scarrow, J. H. (2014). Kalsilite-bearing plutonic rocks: The deep-seated Archean Awsard massif of the Reguibat Rise, South Morocco, West African Craton. *Earth-Science Reviews*, *138*, 1-24.

Bea, F., Montero, P., Molina, J. F., Scarrow, J. H., Cambeses, A., & Moreno, J. A. (2018a). Lu-Hf ratios of crustal rocks and their bearing on zircon Hf isotope model ages: The effects of accessories. *Chemical Geology*, *484*, 179-190.

Bea, F., Montero, P., & Ortega, M. (2006b). A LA-ICPMS evaluation of Zr reservoirs in common crustal rocks: implications for Zr and Hf geochemistry, and zircon-forming processes. *Canadian Mineralogist*, *44*, 693-714.

Bea, F., Pereira, M. D., Corretgé, L. G., & Fershtater, G. B. (1994a). Differentiation of strongly peraluminous, perphoshorous granites. The Pedrobernardo pluton, central Spain. *Geochimica et Cosmochimica Acta*, *58*, 2609-2628.

Bea, F., Pereira, M. D., & Stroh, A. (1994b). Mineral/leucosome trace-element partitioning in a peraluminous migmatite (a laser ablation-ICP-MS study). *Chemical Geology*, *117*(1-4), 291-312.

Bea, F., Montero, P., & Molina Palma, J. F. (2018b). Experimental evidence for the preservation of U-Pb isotope ratios in mantle-recycled crustal zircon grains. *Scientific Reports*, *8*(1), 1-10.

Bea, F., Montero, P., & Molina, J. F. (1999). Mafic precursors, peraluminous granitoids, and late lamprophyres in the Avila batholith: A model for the generation of variscan batholiths in Iberia. *Journal of Geology*, *107*(4), 399-419.

Bea, F., Morales, I., Molina, J. F., Montero, P., & Cambeses, A. (2021). Zircon stability grids in crustal partial melts: implications for zircon inheritance. *Contributions to Mineralogy and Petrology*, *176*(3), 1-14.

Beard, W. C., Bradley, J. E., Butterman, W. C., & Foster, W. R. (1965). Research on phase equilibria approach to growth of doped single crystals of refractory compounds. *Aerospace Res.*, ARL 65-20.

Belousova, E. A., Griffin, W. L., O'Reilly, S. Y., & Fisher, N. I. (2002). Igneous zircon; trace element composition as an indicator of source rock type. *Contributions to Mineralogy and Petrology*, *143*, 602-622.

Belousova, E. A., Griffin, W. L., & Pearson, N. J. (1998). Trace element composition and cathodoluminescence properties of southern African kimberlitic zircons. *Mineralogical Magazine*, *62*(3), 355-366.

Ben Kacem, I., Gautron, L., Coillot, D., & Neuville, D. R. (2017). Structure and properties of lead silicate glasses and melts. *Chemical Geology*, *461*(March), 104-114.

Bernini, D., Audétat, A., Dolejš, D., & Keppler, H. (2013). Zircon solubility in aqueous fluids at high temperatures and pressures. *Geochimica et Cosmochimica Acta*, *119*, 178-187.

Black, L. P., Kamo, S. L., Allen, C. M., Davis, D. W., Aleinikoff, J. N., Valley, J. W., Mundil, R., Campbell, I. H., Korsch, R. J., Williams, I. S., & Foudoulis, C. (2004). Improved ^{206}Pb/^{238}U microprobe geochronology by the monitoring of a trace-element-related matrix effect; SHRIMP, ID-TIMS, ELA-ICP-MS and oxygen isotope documentation for a series of zircon standards. *Chemical Geology*, *205*(1-2), 115-140.

Blichert-Toft, J., & Albarede, F. (1997). The Lu-Hf isotope geochemistry of chondrites and the evolution of the mantle-crust system. *Earth Planet Sci Lett*, *148*(1-2), 243-258.

Blichert-Toft, J., & Albarède, F. (2008). Hafnium isotopes in Jack Hills zircons and the formation of the Hadean crust. *Earth and Planetary Science Letters*, *265*(3-4), 686-702.

Blundy, J., & Cashman, K. (2001). Ascent-driven crystallisation of dacite magmas at Mount St Helens, 1980-1986. *Contributions to Mineralogy and Petrology*, *140*(6), 631-650.

Boehnke, P., Watson, E. B., Trail, D., Harrison, T. M., & Schmitt, A. K. (2013). Zircon saturation re-revisited. *Chemical Geology*, *351*, 324-334.

Borisov, A., & Aranovich, L. (2019). Zircon solubility in silicate melts: New experiments and probability of zircon crystallization in deeply evolved basic melts. *Chemical Geology*, *510*, 103-112.

Borisova, A. Y., Bindeman, I. N., Toplis, M. J., Zagrtdenov, N. R., Guignard, J., Safonov, O. G., Bychkov, A. Y., Shcheka, S., Melnik, O. E., Marchelli, M., & Fehrenbach, J. (2020). Zircon survival in shallow asthenosphere and deep lithosphere. *American Mineralogist*, *105*(11), 1662-1671.

Bortnikov, N., Silant'ev, S. A., Bea F., Montero, Zinger, T., Skolotnev, S., & Sharkov, E. (2022). Multiple Melting of a Heterogeneous Mantle and Episodic Accretion of Oceanic Crust in a Spreading Zone: Zircon U-Pb Age and Hf-O Isotope Evidence from an Oceanic Core Complex of the Mid-Atlantic Ridge. *Petrology*, *30*, 1-24.

Bortnikov, N. S., Savel'eva, G. N., Matukov, D. I., Sergeev, S. A., Berezhnaya, N. G., Lepekhina, E. N., & Antonov, A. V. (2005). The zircon age of plagiogranites and gabbros based on SHRIMP data: Pleistocene intrusion in the MAR rift valley, 5°30.6′-5°32.4′N. *Doklady Earth Sciences*, *404*(7), 1054-1058.

Bortnikov, N. S., Sharkov, E. V., Bogatikov, O. A., Zinger, T. F., Lepekhina, E. N., Antonov, A. V., & Sergeev, S. A. (2008). Finds of young and ancient zircons in gabbroids of the Markov Deep, Mid-Atlantic Ridge, 5°54′–5°02.2′ N (Results of SHRIMP-II U-Pb Dating): Implication for deep geodynamics of modern oceans. *Dokl. Earth Sc.*, *421*(1), 859-866.

Bortnikov, N. S., Silantyev, S. A., Bea, F., Montero, P. A., Zinger, T. F., Skolotnev, S. G., & Sharkov, E. V. (2019). U-Pb Dating, Oxygen and Hafnium Isotope Ratios of Zircon from Rocks of Oceanic Core Complexes at the Mid-Atlantic Ridge: Evidence for the Interaction of Contemporary and Ancient Crusts in the Spreading Center of the Ocean Floor. *Doklady earth sciences*, *489*(2).

Butterman, W. C. (1965). Equilibrium phase relations among oxides in the systems GeO_2, GeO_2-B_2O_3,$HfO_2B_2O_2$, ZrO_2-SiO_2-$B_2)_3$ and ZrO_2SiO_2.

Butterman, W. C. (1967). Zircon Stability and ZrO_2-SiO_2 Phase Diagram. *Am. Mineral.*, *52*, 880.

Cambeses, A., & Chakraborty, S. (2018). Zircon preservation in mafic melts: a theoretical and experimental study. *Geological Society of America Abstracts with Programs.*, *Vol. 50, No. 6, 137-3; doi: 10.1130/abs/2018AM-320291*.

Capitani, G. C., Leroux, H., Doukhan, J. C., Ríos, S., Zhang, M., & Salje, E. K. H. (2000). A TEM investigation of natural metamict zircons: Structure and recovery of amorphous domains. *Physics and Chemistry of Minerals*, *27*(8), 545-556.

Carrez, P., Forterre, C., Braga, D., & Leroux, H. (2003). Phase separation in metamict zircon under electron irradiation. *Nuclear Instruments and Methods in Physics Research, Section B: Beam Interactions with Materials and Atoms*, *211*(4), 549-555.

Chen, X., Wang, W., Zhang, Z., Nie, N. X., & Dauphas, N. (2020). Evidence from Ab Initio and Transport Modeling for Diffusion-Driven Zirconium Isotopic Fractionation in Igneous Rocks. *ACS Earth and Space Chemistry*, *4*(9), 1572-1595.

Cherniak, D. J. (2010). Diffusion in Accessory Minerals: Zircon, Titanite, Apatite, Monazite and

Xenotime. *Reviews in Mineralogy & Geochemistry*, *72*, 827-869.

Cherniak, D. J., Hanchar, J. M., & Watson, E. B. (1997a). Diffusion of tetravalent cations in zircon. *Contributions to Mineralogy and Petrology 1997 127:4*, *127*(4), 383-390.

Cherniak, D. J., Hanchar, J. M., & Watson, E. B. (1997b). Rare-earth diffusion in zircon. *Chemical Geology*, *134*, 289-301.

Cherniak, D. J., & Watson, E. B. (2003). Diffusion in zircon. *Reviwes in Mineralogy*, *53*, 113-143.

Claeson, D. T. (1999). Geochronology of the Rymmen gabbro, southern Sweden; implications for primary versus inherited zircon in mafic rocks and rheomorphic dykes. *GFF*, *121:1*, 25-31.

Claoué-Long, J. C., King, R. W., & Kerrich, R. (1990). Archaean hydrothermal zircon in the Abitibi greenstone belt: constraints on the timing of gold mineralisation. *Earth and Planetary Science Letters*, *98*(1), 109-128.

Clemens, J., & Watkins, J. (2001). The fluid regime of high-temperature metamorphism during granitoid magma genesis. *Contributions to Mineralogy and Petrology*, *140*(5), 600-606.

Clemens, J. D. (1984). Water contents of silicic to intermediate magmas. *Lithos*, *17*, 272-287.

Clemens, J. D. (2003). S-type granitic magmas - petrogenetic issues, models and evidence. *Earth-Science Reviews*, *61*(1-2), 1-18.

Clemens, J. D., & Stevens, G. (2016). Melt segregation and magma interactions during crustal melting: Breaking out of the matrix. *Earth-Science Reviews*, *160*, 333-349.

Cocco, A., & Schromek, N. (1958). Stability of ZrSiO4 at high temperatures. *Ceramica*, *12*, 45-48.

Collins, W. J., Huang, H.-Q., & Jiang, X. (2016). Water-fluxed crustal melting produces Cordilleran batholiths. *Geology*, *44*(2), 143-146.

Compston, W., & Pidgeon, R. T. (1986). Jack Hills, evidence of more very old detrital zircons in Western Austraalia. *Nature*, *321*, 766-769.

Corfu, F., Hanchar, J. M., Hoskin, P. W. O., & Kinny, P. D. (2003). Atlas of zircon textures. In J. M. Hanchar & P. W. O. Hoskin (Eds.), *Zircon(Reviews in Mineralogy & Geochemistry, Vol. 53)* (pp. 468-500). Washington: Mineralogical Society of America & Geochemical Society.

Corfu, F., & Noble, S. R. (1992). Genesis of the southern Abitibi greenstone belt, Superior Province, Canada: evidence from zircon Hf isotope analyses using a single filament technique. *Geochimica et Cosmochimica Acta*, *56*(5), 2081-2097.

Cumming, G. L., & Richards, J. R. (1975). Ore lead isotope ratios in a continuously changing Earth. *Earth and Planetary Science Letters*, *28*, 155-171.

Curtis, C. E., & Sowman, H. G. (1953). Investigation of the Thermal Dissociation, Reassociation, and Synthesis of Zircon. *Journal of the American Ceramic Society*, *36*(6), 190-198.

Degeling, H., Eggins, S. M., & Ellis, D. J. (2001). Zr budgets for metamorphic reactions, and the formation of zircon from garnet breakdown. *Mineralogical Magazine*, *65*(6(433), 749-758.

Dhuime, B., Hawkesworth, C. J., Storey, C. D., & Cawood, P. A. (2011). From sediments to their source rocks: Hf and Nd isotopes in recent river sediments. *Geology*, *39*, 407-410.

Dickinson, J. E., & Hess, J. C. (1982). Zircon saturation in lunar basalts and granites. *Earth & Planetary Science Letters*, *57*, 336-344.

Diez Montes, A., Navidad, M., González Lodeiro, F., & Martínez Catalán, J. R. (2004). El Ollo de Sapo. In J. A. Vera (Ed.), *Geología de España* (pp. 69-72). Madrid: SGE-IGME.

Ebadi, A., & Johannes, W. (1991). Beginning of melting and composition of first melts in the system Qz-Ab-Or-H_2O-CO_2. *Contributions to Mineralogy and Petrology 1991 106:3*, *106*(3), 286-295.

Eiler, J. M., Graham, C., & Valley, J. W. (1997). SIMS analysis of oxygen isotopes: matrix effects in complex minerals and glasses. *Chemical Geology*, *138*(3-4), 221-244.

Escuder Viruete, J., Arenas, R., & Martínez Catalán, J. R. (1994). Tectonothermal evolution associated with variscan crustal extension in the Tormes gneissic dome (NW Salamanca, Iberian Massif, Spain). *Tectonophysics*, *238*, 117-138.

Etheridge, M. A., Daczko, N. R., Chapman, T., & Stuart, C. A. (2020). Mechanisms of melt extraction during lower crustal partial melting. *Journal of Metamorphic Geology*, 00:1-19. DOI: 10.1111/jmg.12561.

Ewing, R. C., Meldrum, A., Wang, L. M., Weber, W. J., & Corrales, L. R. (2003). Radiation effects in zircon. *Reviews in Mineralogy and Geochemistry*, *53*, 377-425.

Eyring, H. (1936). Viscosity, Plasticity, and Diffusion as examples of absolute Reaction rates. *The Journal of Chemical Physics*, *4*, 283.

Fedo, C. M., Sircombe, K. N., & Rainbird, R. H. (2003). Detrital Zircon Analysis of the Sedimentary Record. *Reviews in Mineralogy and Geochemistry*, *53*, 277-303.

Ferry, J. M., & Watson, E. B. (2006). New thermodynamic analysis and calibration of the Ti-in- zircon and Zr-in-rutile thermometers. *Geological Society of America Abstracts with Programs*, *38*, 243.

Flowers, R. M. (2000). Structural and geochronological investigation of the Archean basement along the projection of the Vredefort discontinuity, Vredefort impact structure, Kaapvaal Craton, South Africa.

Froude, D. O., Ireland, T. R., Kinny, P. D., Williams, I. S., Compston, W., Williams, I. R., & Myers, J. S. (1983). Ion microprobe identification of 4,100–4,200 Myr-old terrestrial zircons. *Nature*, *304*(5927), 616-618.

Fu, B., Page, F. Z., Cavosie, A. J., Fournelle, J., Kita, N. T., Lackey, J. S., Wilde, S. A., & Valley, J. W. (2008). Ti-in-zircon thermometry: applications and limitations. *Contributions to Mineralogy and Petrology*, *156*(2), 197-215.

Gehrels, G. E. (2012). Detrital zircon U-Pb geochronology: current methods and new opportunities. In C. Busby & A. Azor (Eds.), *Tectonics of Sedimentary Basins: Recent Advances* (pp. 47-62). Chichester, UK: Wiley-Blackwell.

Geisler, T., Pidgeon, R. T., Kurtz, R., van Bronswijk, W., & Schleicher, H. (2003a). Experimental hydrothermal alteration of partially metamict zircon. *American mineralogist*, *88*(10), 1496-1513.

Geisler, T., Pidgeon, R. T., van Bronswijk, W., & Kurtz, R. (2002). Transport of uranium, thorium, and lead in metamict zircon under low-temperature hydrothermal conditions. *Chemical geology*, *191*(1-3), 141-154.

Geisler, T., Seydoux-Guillaume, A. M., Wiedenbeck, M., Wirth, R., Berndt, J., Zhang, M., Mihailova, B., Putnis, A., Salje, E. K. H., & Schluter, J. (2004). Periodic precipitation pattern formation in hydrothermally treated metamict zircon. *AMERICAN MINERALOGIST*, *89*(8-9), 1341-1347.

Geisler, T., Zhang, M., & Salje, E. K. H. (2003b). Recrystallization of almost fully amorphous zircon under hydrothermal conditions: An infrared spectroscopic study. *Journal of nuclear materials*, *320*(3), 280-291.

Geisler, T., Schaltegger, U., & Tomaschek, F. (2007). Re-equilibration of zircon in aqueous fluids and melts. *Elements*, *3*(1), 43-50.

Geisler, T., Ulonska, M., Schleicher, H., Pidgeon, R. T., & van Bronswijk, W. (2001). Leaching and differential recrystallization of metamict zircon under experimental hydrothermal conditions. *Contrib Mineral Petrol*, *141*(1), 53-65.

Geller, R. F., & Lang, S. M. (1949). System SiO_2-ZrO_2. *Amer. Ceram. Soc.*, *32*, 157.

Gervasoni, F., Klemme, S., Rocha-Júnior, E. R. V., & Berndt, J. (2016). Zircon saturation in silicate melts: a new and improved model for aluminous and alkaline melts. *Contributions to Mineralogy and Petrology*, *171*(3).

Ghiorso, M. S., & Gualda, G. A. R. (2015). An H_2O-CO_2 mixed fluid saturation model compatible with rhyolite-MELTS. *Contributions to Mineralogy And Petrology*, *169, art 53*, https://doi.org/10.1007/s00410-015.

Ghiorso, M. S. (1997). Thermodynamic models of igneous processes. *Annual Review of Earth and Planetary Sciences*, *25*(1), 221-241.

Gieré, R. (1990). Hydrothermal mobility of Ti, Zr and REE: examples from the Bergell and Adamello contact aureoles (Italy). *Terra Nova*, *2*(1), 60-67.

Gil Agero, M., & Moro Benito, C. (1991). Geología y metalogenia de W (Sn,P) asociadas a los niveles calcasilicatados del Complejo Esquisto-grauváquico (C.ER.G) de Villalcampo (provincia de Zamora). *Studia Geológica Salmanticensis*, *XXVII*, 131-150.

Grant, J. A. (1985). Phase equilibria in partial melting of pelitic rocks. *Migmatites (J.R. Ashworth ed.), Blackie*, 86-144.

Griffin, W. L., Wang, X., Jackson, S. E., Pearson, N. J., O'Reilly, S. Y., Xu, X. S., & Zhou, X. M. (2002). Zircon chemistry and magma mixing, SE China: In-situ analysis of Hf isotopes, Tonglu and Pingtan igneous complexes. *Lithos*, *61*(3-4), 237-269.

Grimes, C. B., Wooden, J. L., Cheadle, M. J., & John, B. E. (2015). "Fingerprinting" tectono-magmatic provenance using trace elements in igneous zircon. *Contributions to Mineralogy and Petrology*, *170: 46 DOI 10.1007/s00410-015-1199-3*.

Grimes, C. B., John, B. E., Kelemen, P. B., Mazdab, F. K., Wooden, J. L., Cheadle, M. J., Hanghøj, K., & Schwartz, J. J. (2007). Trace element chemistry of zircons from oceanic crust: A method for distinguishing detrital zircon provenance. *Geology*, *35*(7), 643.

Grimes, C. B., John, B. E., Cheadle, M. J., Mazdab, F. K., Wooden, J. L., Swapp, S., & Schwartz, J. J. (2009). On the occurrence, trace element geochemistry, and crystallization history of zircon from in situ ocean lithosphere. *Contributions to Mineralogy and Petrology*, *158*(6), 757-783.

Grimes, C. B., Ushikubo, T., John, B. E., & Valley, J. W. (2011). Uniformly mantle-like δ18O in zircons from oceanic plagiogranites and gabbros. *Contributions to Mineralogy and Petrology*, *161*(1), 13-33.

Gualda, G.A.R., Ghiorso, M. S., Lemons, R. V., & Carley, T. L. (2012). Rhyolite-MELTS: A modified calibration of MELTS optimized for silica-rich, fluid-bearing magmatic systems. *Journal of Petrology*, *53*, 875-890.

Halpin, J. A., Daczko, N. R., Milan, L. A., & Clarke, G. L. (2012). Decoding near-concordant U–Pb zircon ages spanning several hundred million years: recrystallisation, metamictisation or diffusion. *Contrib Mineral Petrol*, *163*(1), 67-85.

Hanchar, J. M., & Miller, C. F. (1993). Zircon Zonation Patterns as Revealed by Cathodoluminescence and Backscattered Electron Images - Implications for Interpretation of Complex Crustal Histories. *Chemical Geology*, *110*(1-3), 1-13.

Hanchar, J. M., & Rudnick, R. L. (1995). Revealing hidden structures: The application of cathodoluminescence and back-scattered electron imaging to dating zircons from lower crustal xenoliths. *Lithos*, *36*(3-4), 289-303.

Hanchar, J. M., & Watson, E. B. (2003). Zircon saturation thermometry. In J. M. Hanchar & P. W. O. Hoskin (Eds.), *Zircon. Revs. in Mineralogy 53* (pp. 89-112). Min. Soc. Am. & Geochem. Soc.

Harrison, T. M., Watson, E. B., & Aikman, A. B. (2007). Temperature spectra of zircon crystallization in plutonic rocks. *Geology*, *35*(7), 635-638.

Henderson, P. (1982). *Inorganic Geochemistry*. Oxford: Pergamon Press.

Hess, J. C., Dickinson, J. E., & Rutherford, M. J. (1980). Solubility of zircon, whitlockite and apatite in lunar basalts and granites. *Lunar and Planetary Science*, *11*, 438-440.

Hofmann, A. W. (1988). Chemical differentiation of the Earth: the relationship between mantle, continental crust, and oceanic crust. *Earth and Planetary Science Letters*, *90*, 297-314.

Holycross, M. E., & Watson, E. B. (2016). Diffusive fractionation of trace elements in basaltic melt. *Contributions to Mineralogy and Petrology*, *171*(10), 171-180.

Hoskin, P. W. O. (1998). Minor and trace element analysis of natural zircon (ZrSiO4) by SIMS and laser ablation ICPMS : A consideration and comparison of two broadly competitive techniques. *Journal of trace and microprobe techniques*, *16*(3).

Hoskin, P. W. O., Kinny, P. D., & Wyborn, D. (1998). Chemistry of hydrothermal zircon: investigating timing and nature of water-rock interaction. *Water-Rock Interaction*, 545-548.

Hoskin, P. W. O., & Schaltegger, U. (2003). The composition of zircon and igneous and metamorphic petrogenesis. In *Zircon* (pp. 27-62).

Hoskin, P. W. O., & Black, L. P. (2000). Metamorphic zircon formation by solid-state recrystallization of protolith igneous zircon. *Journal of Metamorphic Geology*, *18*(4), 423-439.

Ickert, R., Hiess, J., Williams, I., Holden, P., Ireland, T., Lanc, P., Schram, N., Foster, J., & Clement, S. (2008). Determining high precision, in situ, oxygen isotope ratios with a SHRIMP II: Analyses of MPI-DING silicate-glass reference materials and zircon from contrasting granites. *Chemical Geology*, *257*(1-2), 114-128.

Iizuka, T., Yamaguchi, T., Itano, K., Hibiya, Y., & Suzuki, K. (2017). What Hf isotopes in zircon tell us about crust–mantle evolution. *Lithos*, *274-275*, 304-327.

Jackson, M. D., Cheadle, M. J., & Atherton, M. P. (2003). Quantitative modeling of granitic melt generation and segregation in the continental crust. *Journal of Geophysical Research-Solid Earth*, *108*(B7), 2332, doi:10.1029/2001JB001050.

Johannes, W. (1988). What controls partial melting in migmatites? *J. met. Geol.*, *6*, 451-465.

Johannes, W., & Holtz, F. (1990). Formation and composition of H_2O-undersaturated granitic melts. *Ashworth & Brom (eds.) High T metamorphism and crustal anatexis*, *Unwin Hyman*.

Johannes, W., Holtz, F., & Moller, P. (1995). REE distribution in some layered migmatites: Constraints on their petrogenesis. *Lithos*, *35*(3-4), 139-152.

Jonathan Patchett, P., Kouvo, O., Hedge, C. E., & Tatsumoto, M. (1982). Evolution of continental crust and mantle heterogeneity: evidence from Hf isotopes. *Contributions to Mineralogy and Petrology*, *78*(3), 279-297.

Kaasschieter, E. F., & Frijns, A. J. H. (2003). Squeezing a sponge: a three-dimensional solution in poroelasticity. *Computational Geosciences*, *7*(1), 49-59.

Kaiser, A., Lobert, M., & Telle, R. (2008). Thermal stability of zircon ($ZrSiO_4$). *Journal of the European Ceramic Society*, *28*(11), 2199-2211.

Kamaev, D. N., Archugov, S. A., & Mikhailov, G. G. (2005). Study and Thermodynamic Analysis of the ZrO_2-SiO_2 System. *Russian Journal of Applied Chemistry*, *78*(2), 200-203.

Kebede, T., Horie, K., Hidaka, H., & Terada, K. (2007). Zircon 'microvein' in peralkaline granitic gneiss, western Ethiopia: Origin, SHRIMP U–Pb geochronology and trace element investigations. *Chemical Geology*, *242*(1-2), 76-102.

Kemp, A. I. S., Hawkesworth, C. J., Foster, G. L., Paterson, B. A., Woodhead, J. D., Hergt, J. M., Gray, C. M., & Whitehouse, M. J. (2007). Magmatic and crustal differentiation history of granitic rocks from Hf-O isotopes in zircon. *SCIENCE*, *315*(5814), 980-983.

Kemp, A. I. S. (2018). Early earth geodynamics: cross examining the geological testimony. Philosophical Transactions of the Royal Society A: Mathematical, Physical and Engineering Sciences, 376(2132), 20180169.

Kempe, U., Gruner, T., Nasdala, L., & Wolf, D. (2000). Relevance of Cathodoluminescence for the Interpretation of U-Pb Zircon Ages, with an Example of an Application to a Study of Zircons from the Saxonian Granulite Complex, Germany. *Cathodoluminescence in Geosciences*, 415-455.

Kennedy, G. C. (1950). A portion of the system silica-water. *Economic Geology*, *45*, 629-653.

Kerrich, R., & King, R. (1993). Hydrothermal zircon and baddeleyite in Val-d'Or Archean mesothermal gold deposits: characteristics, compositions, and fluid-inclusion properties, with implications fortiming of primary gold mineralization. *Canadian Journal of Earth Sciences*, *30*(12), 2334-2351.

King, E. M., Tucker Barrie, C., & Valley, J. W. (1997). Hydrothermal alteration of oxygen isotope ratios in quartz phenocrysts, Kidd Creek mine, Ontario: Magmatic values are preserved in zircon. *Geology*, *25*(12), 1079-1082.

King, E. M., & Valley, J. W. (2001). The source, magmatic contamination, and alteration of the Idaho batholith. *Contributions to Mineralogy and Petrology*, *142*(1), 72-88.

Kinny, P. D., Williams, I. S., Froude, D. O., Ireland, T. R., & Compston, W. (1988). Early Archaean zircon ages from orthogneisses and anorthosites at Mount Narryer, Western Australia. *Precambrian Research*, *38*(4), 325-341.

Kirkpatrick, R. J. (1981). Kinetics of crystallization of igneous rocks. In A. C. Lasaga & R. J. Kirkpatrick (Eds.), *Kinetics of Geochemical Processes(8)* (pp. 321-396). Mineralogical Society of America.

Kober, B. (1986). Whole-grain evaporation for 207Pb/206Pb-age investigations on single zircons using a double filament thermal ionization source. *Contributions to Mineralogy and Petrology*, *93*, 482-490.

Kober, B. (1987). Single-zircon evaporation combined with Pb^{+} emitter-bedding for $^{207}\text{Pb}/^{206}\text{Pb}$ age investigations using thermal ion mass spectrometry and implications to zirconology. *Contributions to Mineralogy and Petrology*, *96*, 63-71.

Kogawa, M., Watson, E. B., Ewing, R. C., & Utsunomiya, S. (2012). Lead in zircon at the atomic scale. *American Mineralogist*, *97*(7), 1094-1102.

Konzett, J., Armstrong, R. A., Sweeney, R. J., & Compston, W. (1998). The Timing of Marid Metasomatism in the Kaapvaal Mantle - An Ion Probe Study of Zircons from Marid Xenoliths. *Earth and planetary science letters*, *160*(1-2), 133-145.

Kooijman, E., Upadhyay, D., Mezger, K., Raith, M. M., Berndt, J., & Srikantappa, C. (2011). Response of the U-Pb chronometer and trace elements in zircon to ultrahigh-temperature metamorphism: The Kadavur anorthosite complex, southern India. *Chemical Geology*, *290*(3-4), 177-188.

Kovalenko, N. I., & Ryzhenko, B. N. (2009). Comparative study of the solubility of zircon and baddeleyite. *Geochemistry International*, *47*(4), 405-413.

Kramers, J., Frei, R., Newville, M., Kober, B., & Villa, I. (2009). On the valency state of radiogenic lead in zircon and its consequences. *Chemical Geology*, *261*(1-2), 4-11.

Kresten, P., Fels, P., & Berggren, G. (1975). Kimberlitic zircons — A possible aid in prospecting for kimberlites. *Mineralium Deposita 1975 10:1*, *10*(1), 47-56.

Krogh, T. E. (1973). A low-contamination method for hydrothermal decomposition of zircon and extraction of U and Pb for isotopic age determinations. *Geochimica et Cosmochimica Acta*, *37*(3), 485-494.

Krogh, T. E. (1982a). Improved accuracy of U-Pb zircon ages by the creation of more concordant systems using an air abrasion technique. *Geochimica et Cosmochimica acta*, *46*(4), 637-649.

Krogh, T. E. (1982b). Improved accuracy of U-Pb zircon dating by selection of more concordant fractions using a high gradient magnetic separation technique. *Geochimica et Cosmochimica Acta*, *46*(4), 631-635.

Kusiak, M. A., Kovaleva, E., Wirth, R., Klötzli, U., Dunkley, D. J., Yi, K., & Lee, S. (2019). Lead oxide nanospheres in seismically deformed zircon grains. *Geochimica et Cosmochimica Acta*, *262*, 20-30.

Kusiak, M. A., Dunkley, D. J., Wirth, R., Whitehouse, M. J., Wilde, S. A., & Marquardt, K. (2015). Metallic lead nanospheres discovered in ancient zircons. *Proceedings of the National Academy of*

Sciences of the United States of America, *112*(16), 4958-4963.

Lackey, J. S., Hinke, H. J., & Valley, J. W. (2002). Tracking contamination in felsic magma chambers with delta O-18 of magmatic garnet and zircon.

LaTourrette, T., Wasserburg, G. J., & Fahey, A. J. (1996). Self diffusion of Mg, Ca, Ba, Nd, Yb, Ti, Zr, and U in haplobasaltic melt. *Geochimica et Cosmochimica Acta*, *60*, 1329-1340.

Lewerentz, A., Harlov, D. E., Scherstén, A., & Whitehouse, M. J. (2019). Baddeleyite formation in zircon by Ca-bearing fluids in silica-saturated systems in nature and experiment: resetting of the U–Pb geochronometer. *Contributions to Mineralogy and Petrology*, *174*(8), 64.

Li, J., Shen, B., Mao, D., Li, S., Zhou, H., & Cheng, Y. (1997). Mineralization Ages of the Jiapigou Gold Deposits, Jilin. *Acta Geologica Sinica - English Edition*, *71*(2), 180-188.

López Plaza, M. (1980). Comportamiento reológico, fuerza ascensional y deformación en el material granítico: Aplicación al plutón de Ledesma (Salamanca). *Bol. Geol. Min.*, *91*, 649-660.

Louvel, M., Sanchez-Valle, C., Malfait, W. J., Testemale, D., & Hazemann, J.-L. (2013). Zr complexation in high pressure fluids and silicate melts and implications for the mobilization of HFSE in subduction zones. *Geochimica et Cosmochimica Acta*, *104*, 281-299.

Luth, W. C., Jahns, R. H., & Tuttle, O. F. (1964). The granite system at pressures of 4 to 10 kilobars. *J. Geophys. Research*, *69*, 759-773.

Lyon, I. C., Kusiak, M. A., Wirth, R., Whitehouse, M. J., Dunkley, D. J., Wilde, S. A., Schaumlöffel, D., Malherbe, J., & Moore, K. L. (2019). Pb nanospheres in ancient zircon yield model ages for zircon formation and Pb mobilization. *Scientific Reports*, *9*(1), 1-9.

Mahon, K. I., Harrison, T. M., & Drew, D. A. (1988). Ascent of a granitoid diapir in a temperature varying medium. *Journal of Geophysical Research: Solid Earth*, *93*(B2), 1174-1188.

Manning, C. E. (1994). The solubility of quartz in H_2O in the lower crust and upper mantle. *Geochim Cosmochim Acta*, *58*, 4831-4839.

Marsh, B. D. (1982). On the mechanics of igneous diapirism, stoping, and zone melting. *American Journal of Science*, *282*(6), 808-855.

Mattinson, J. M. (2005). Zircon U-Pb chemical abrasion (”CA-TIMS”) method: Combined annealing and multi-step partial dissolution analysis for improved precision and accuracy of zircon ages. *Chemical Geology*, *220*(1-2), 47-66.

Maurice, O. D. (1949). Transport and deposition of the non-sulphide vein Minerals; [Part] 5, Zirconium minerals. *Economic Geology*, *44*(8), 721-731.

McGloin, M. V., Tomkins, A. G., Webb, G. P., Spiers, K., MacRae, C. M., Paterson, D., & Ryan, C. G. (2015). Release of uranium from highly radiogenic zircon through metamictization: The source of orogenic uranium ores. *Geology*, *44*(1), 15-18.

McLaren, A. C., Gerald, J. D. F., & Williams, I. S. (1994). The microstructure of zircon and its influence on the age determination from Pb/U isotopic ratios measured by ion microprobe. *Geochimica et Cosmochimica Acta*, *58*(2), 993-1005.

Meldrum, F. C., & O’Shaughnessy, C. (2020). Crystallization in Confinement. *Adv Mater*, *32*(31), e2001068.

Migdisov, A. A., Williams-Jones, A. E., & Wagner, T. (2009). An experimental study of the solubility and speciation of the Rare Earth Elements (III) in fluoride- and chloride-bearing aqueous solutions at temperatures up to 300°C. *Geochimica et Cosmochimica Acta*, *73*(23), 7087-7109.

Migdisov, A., Williams-Jones, A. E., van Hinsberg, V., & Salvi, S. (2011). An experimental study of the solubility of baddeleyite (ZrO_2) in fluoride-bearing solutions at elevated temperature. *Geochimica et Cosmochimica Acta*, *75*(23), 7426-7434.

Miller, C. F., McDowell, S. M., & Mapes, R. W. (2003). Hot and cold granites? Implications of zircon saturation temperatures and preservation of inheritance. *Geology*, *31*(6), 529-532.

Miyashiro, A., & Shido, F. (1980). Differentiation of gabbros in the Mid-Atlantic Ridge near 24 N. *Geochemical Journal*, *14*(4), 145-154.

Molen, I. V. D., & Paterson, M. S. (1979). Experimental Deformation of Partially-Melted Granite. *Contrib. Mineral. Petrol.*, *70*, 299-318.

Monaghan, S., Greer, J. C., & Elliott, S. D. (2005). Thermal decomposition mechanisms of hafnium and zirconium silicates at the atomic scale. *Journal of Applied Physics*, *97*(11).

Montero, M. P., Bea F., Molina Palma, J. F., Morales, I., & Cambeses, A. (2020). *Experimental evidence for oxygen isotopes diffusion in zircon*. Proceedings from Goldschmidt Conference.

Montero, P., Bea, F., González-Lodeiro, F., Talavera, C., & Whitehouse, M. (2007). Zircon crystallization age and protolith history of the metavolcanic rocks and metagranites of the Ollo de Sapo Domain in central Spain. Implications for the Neoproterozoic to Early-Paleozoic evolution of Iberia. *Geological Magazine*, *144*(6), 963-976.

Montero, P., Haissen, F., Mouttaqui, A., Molina, J. F., Errami, A., Sadki, O., Cambeses, A., & Bea, F. (2016). Contrasting SHRIMP U-Pb zircon ages of two carbonatite complexes from the peri-cratonic terranes pf the Reguibat Shield: Implications for the lateral extension of the West African Craton. *Gondwana Research*, *38*, 238-250.

Morales, I., Molina, J. F., Cambeses, A., Montero, P., & Bea, F. (2022). Experimental Annealing of Zircon: Influence of Inclusions on Stability, Intracrystalline Melt Migration, Common Lead Leaching, and Permeability to Fluids. *Earth and Space Chemistry*, d.o.i: https://doi.org/10.1021/acsearthspacechem.1c00212.

Mueller, P. A., Wooden, J. L., Mogk, D. W., Nutman, A. P., & Williams, I. S. (1996). Extended history of a 3.5 Ga trondhjemitic gneiss, Wyoming Province, USA: evidence from U-Pb systematics in zircon. *Precambrian Research*, *78*(1-3), 41-52.

Mursic, Z., Vogt, T., & Frey, F. (1992). High-temperature neutron powder diffraction study of $ZrSiO_4$ up to 1900 K. *Acta Crystallographica Section B Structural Science*, *48*(5), 584-590.

Mysen, B. (2015). An in situ experimental study of Zr^{4+} transport capacity of water-rich fluids in the temperature and pressure range of the deep crust and upper mantle. *Progress in Earth and Planetary Science*, *2*(1), 38.

Nasdala, L., Lengauer, C. L., Hanchar, J. M., Kronz, A., Wirth, R., Blanc, P., Kennedy, A. K., & Seydoux-Guillaume, A. M. (2002). Annealing radiation damage and the recovery of cathodoluminescence.

Chemical Geology, *191*(1-3), 121-140.

Patchett, P. J., Vervoort, J. D., Söderlund, U., & Salters, V. J. M. (2004). Lu–Hf and Sm–Nd isotopic systematics in chondrites and their constraints on the Lu–Hf properties of the Earth. *Earth and Planetary Science Letters*, *222*(1), 29-41.

Pavlik, R. S., Holland, H. J., & Payzant, E. A. (2001). Thermal Decomposition of Zircon Refractories. *Journal of the American Ceramic Society*, *84*(3-12), 2930-2936.

Peck, W. H., Valley, J. W., & Graham, C. M. (2003). Slow oxygen diffusion rates in igneous zircons from metamorphic rocks. *American Mineralogist*, *88*(7), 1003-1014.

Peck, W. H., Valley, J. W., Wilde, S. A., & Graham, C. M. (2001). Oxygen isotope ratios and rare earth elements in 3.3 to 4.4 Ga zircons: Ion microprobe evidence for high delta O-18 continental crust and oceans in the Early Archean. *Geochimica et cosmochimica acta*, *65*(22), 4215-4229.

Pena, P., & de Aza, S. (1984). The zircon thermal behaviour: effect of impurities. Part 1. *Journal of Material Science*, *19*, 135-142.

Pereira, M. D. (1998). P-T conditions of generation of the Pena Negra anatectic complex, central Spain. *Petrology*, *6*(6), 555-563.

Pidgeon, R. T., O'Neil, J. R., & Silver, L. T. (1966). Uranium and Lead Isotopic Stability in a Metamict Zircon under Experimental Hydrothermal Conditions. *Science*, *154*(3756), 1538-1540.

Pidgeon, R. T. (1992). Recrystallization of oscillatory zoned zircon - some geochronological and petrological implications. *Contributions to mineralogy and petrology*, *110*(4), 463-472.

Pidgeon, R. T., Nemchin, A. A., & Hitchen, G. J. (1998). Internal structures of zircons from Archaean granites from the Darling Range batholith: implications for zircon stability and the interpretation of zircon U-Pb ages. *Contributions to mineralogy and petrology*, *132*(3), 288-299.

Pilot, J., Werner, C. D., Haubrich, F., & Baumann, N. (1998). Palaeozoic and proterozoic zircons from the Mid-Atlantic ridge. *Nature*, *393*(6686), 676-679.

Pilotti, M. (2000). Reconstruction of Clastic Porous Media. *Transport in Porous Media*, *41*(3), 359-364.

Putnis, A. (2002). Mineral replacement reactions: from macroscopic observations to microscopic mechanisms. *Miner Mag*, *66*, 689-708.

Putnis, A., & Austrheim, H. (2013). Mechanisms of metasomatism and metamorphism on the local mineral scale: The role of dissolution-reprecipitation during mineral re-equilibration. In *Metasomatism and the chemical transformation of rock* (pp. 141-170). Springer.

Putnis, A., Oelkers, E. H., & Schott, J. (2009). Mineral replacement reactions. *Thermodynamics and kinetics of water-rock interaction*, *70*, 87-124.

Rabinowicz, M., & Vigneresse, J. L. (2004). Melt segregation under compaction and shear channeling: Application to granitic magma segregation in a continental crust. *Journal of Geophysical Research-Solid Earth*, *109*(B4), https://doi.org/10.1029/2002JB002372.

Ramezani, J., Dunning, G. R., & Wilson, M. R. (2000). Geologic Setting, Geochemistry of Alteration, and U-Pb Age of Hydrothermal Zircon from the Silurian Stog'er Tight Gold Prospect, Newfoundland Appalachians, Canada. *Exploration and Mining Geology*, *9*(3-4), 171-188.

Rasmussen, B. (2005). Zircon growth in very low grade metasedimentary rocks: Evidence for zirconium mobility at ~250°C. *Contributions to Mineralogy and Petrology*, *150*(2), 146-155.

Rizvanova, N. G., Gaidamako, I. M., Levchenkov, O. A., Bezmen, N. I., Makeev, A. F., & Levsky, L. K. (2007). Interaction of metamict zircon with fluids of various composition. *Geochemistry International*, *45*(5), 465-477.

Rizvanova, N. G., Levchenkov, O. A., Belous, A. E., Bezmen, N. I., Maslenikov, A. V., Komarov, A. N., Makeev, A. F., & Levskiy, L. K. (2000). Zircon reaction and stability of the U-Pb isotope system during interaction with carbonate fluid: experimental hydrothermal study. *Contributions to Mineralogy and Petrology*, *139*(1), 101-114.

Rojas-Agramonte, Y., Kroener, A., Demoux, A., Xia, X., Wang, W., Donskaya, T., Liu, D., & Sun, M. (2011). Detrital and xenocrystic zircon ages from Neoproterozoic to Palaeozoic arc terranes of Mongolia: Significance for the origin of crustal fragments in the Central Asian Orogenic Belt. *Gondwana Research*, *19*(3), 751-763.

Rubatto, D., & Hermann, J. (2007). Experimental zircon/melt and zircon/garnet trace element partitioning and implications for the geochronology of crustal rocks. *Chemical Geology*, *241*(1-2), 38-61.

Rubatto, D., & Gebauer, D. (2000). Use of Cathodoluminescence for U-Pb Zircon Dating by Ion Microprobe: Some Examples from the Western Alps. *Cathodoluminescence in Geosciences*, 373-400.

Rubatto, D., & Hermann, J. (2003). Zircon formation during fluid circulation in eclogites (Monviso, Western Alps): implications for Zr and Hf budget in subduction zones. *Geochimica et Cosmochimica Acta*, *67*(12), 2173-2187.

Rubin, J. N., Henry, C. D., & Price, J. G. (1989). Hydrothermal zircons and zircon overgrowths, Sierra Blanca Peaks, Texas. *American Mineralogist*, *74*((7-8), 865-869.

Rubin, J. N., Henry, C. D., & Price, J. G. (1993). The mobility of zirconium and other “immobile” elements during hydrothermal alteration. *Chemical Geology*, *110*(1-3), 29-47.

Sánchez-Rodríguez, L., & Gebauer, D. (2000). Mesozoic formation of pyroxenites and gabbros in the Ronda area (southern Spain), followed by Early Miocene subduction metamorphism and emplacement into the middle crust: U–Pb sensitive high-resolution ion microprobe dating of zircon. *Tectonophysics*, *316*(1), 19-44.

Savva, E. V., Belyatsky, B. V., & Antonov, A. V. (2009). *Carbonatite zircon - myth or reality: mineralogical-geochemical analysis*. Proceedings from Geochemistry of magmatic rocks 2009. School «Geochemistry of Alkaline rocks». http://alkaline09.narod.ru/abstracts/Savva_Belyatsky.htm.

Scaillet, B., Holtz, F., & Pichavant, M. (1998). Phase equilibrium constraints on the viscosity of silicic magmas – 1. Volcanic-plutonic association. *Journal of Geophysical Research Solid Earth*, *103*, 27257-27266.

Schaltegger, U. (2007). Hydrothermal zircon. *Elements*, *3*, 51-51.

Schaltegger, U., Fanning, C. M., Gunther, D., Maurin, J. C., Schulmann, K., & Gebauer, D. (1999). Growth, annealing and recrystallization of zircon and preservation of monazite in high-grade metamorphism: conventional and in-situ U-Pb isotope, cathodoluminescence and microchemical evidence. *Contrib Mineral Petrol*, *134*(2-3), 186-201.

Scharer, U., Corfu, F., & Demaiffe, D. (1997). U-Pb and Lu-HF Isotopes in Baddeleyite and Zircon Megacrysts from the Mbuji-Mayi Kimberlite - Constraints on the Subcontinental Mantle. *Chemical Geology*, *143*(1-2), 1-16.

Schiano, P., Provost, A., Clocchiatti, R., & Faure, F. (2006). Transcrystalline melt migration and Earth's mantle. *Science*, *314*(5801), 970-974.

Schmidt, C., Rickers, K., Wirth, R., Nasdala, L., & Hanchar, J. M. (2006). Low-temperature Zr mobility: An in situ synchrotron-radiation XRF study of the effect of radiation damage in zircon on the element release in H_2O + HCl ± SiO_2 fluids. *American Mineralogist*, *91*(8-9), 1211-1215.

Shao, T., Xia, Y., Ding, X., Cai, Y., & Song, M. (2019). Zircon saturation in terrestrial basaltic melts and its geological implications. *Solid Earth Sciences*, *4*(1), 27-42.

Shmulovich, K. I., Yardley, B. W. D., & Graham, C. M. (2006). Solubility of quartz in crustal fluids: experiments and general equations for salt solutions and H_2O-CO_2 mixtures at 400-800 ºC and 0.1-0.9 GPa. *Geofluids*, *6*, 154-167.

Silantyev, S. A., Aranovich, L. Y., & Bortnikov, N. S. (2010). Oceanic plagiogranites as a result of interaction between magmatic and hydrothermal systems in the slow-spreading mid-ocean ridges. *Petrology*, *18*(4), 369-383.

Silver, L. T., & Deutsch, S. (1963). Uranium-lead isotopic variations in zircons: a case study. *The Journal of Geology*, *71*(6), 721-758.

Sinha, A. K., Wayne, D. M., & Hewitt, D. A. (1992). The hydrothermal stability of zircon - preliminary experimental and isotopic studies. *Geochimica et Cosmochimica Acta*, *56*(9), 3551-3560.

Skolotnev, S. G., Bel'Tenev, V. E., & Lepekhina., E. N. (2010). Younger and older zircons from rocks of the oceanic lithosphere in the Central Atlantic and their geotectonic implications. *Geotectonics*, *44*, 462-492.

Smith, V. G., Tiller, W. A., & Rutter, J. W. (1955). A mathematical analysis of solute redistribution during solidification. *Canadian Journal of Physics*, *33*, 723-745.

Sommerauer, J. (1976). Die chemisch-physikalische Stabilität natürlicher Zirkone und ihr U-(Th)-Pb System.

Stevenson, R. K., & Patchet, P. J. (1990). Implications for the evolution of continental crust from Hf isotope systematics of Archean detrital zircons. *Geochim. Cosmochim. Acta*, *54*, 1683-1698.

Talavera, C., Montero, P., Bea, F., Gonzalez Lodeiro, F., & Whitehouse, M. (2013). U-Pb Zircon geochronology of the Cambro-Ordovician metagranites and metavolcanic rocks of central and NW Iberia. *International journal of earth sciences*, *102*(1), 1-23.

Talavera, C., Montero, P., Martinez Poyatos, D., & Williams, I. S. (2012). Ediacaran to Lower Ordovician age for rocks ascribed to the Schist–Graywacke Complex (Iberian Massif, Spain): Evidence from detrital zircon SHRIMP U–Pb geochronology. *Gondwana Research*, *22*, 928-942.

Taylor, R. P., Strong, D. F., & Fryer, B. J. (1981). Volatile control of contrasting trace element distributions in peralkaline granitic and volcanic rocks. *Contributions to Mineralogy and Petrology 1981 77:3*, *77*(3), 267-271.

Thirlwall, M. F., & Walder, A. J. (1995). In situ hafnium isotope ratio analysis of zircon by inductively coupled plasma multiple collector mass spectrometry. *Chem Geol*, *122*(1-4), 241-247.

Thomas, J. B., Bodnar, R. J., Shimizu, N., & Chesner, C. A. (2003). Melt Inclusions in Zircon. *Reviews in Mineralogy and Geochemistry*, *53*(1), 63-87.

Torró, L., Proenza, J. A., Rojas-Agramonte, Y., Garcia-Casco, A., Yang, J.-H., & Yang, Y.-H. (2018). Recycling in the subduction factory: Archaean to Permian zircons in the oceanic Cretaceous Caribbean island-arc (Hispaniola). *Gondwana Research*, *54*, 23-37.

Tuttle, O. F., & Bowen, N. L. (1958). Origin of granite in the light of experimental studies in the system $NaAlSi_3O_8$–$KAlSi_3O_8$–SiO_2–H_2O. *Memoir of the Geological Society of America*, *74*(1), 1-145.

Váczi, T., Nasdala, L., Wirth, R., Mehofer, M., Libowitzky, E., & Häger, T. (2009). On the breakdown of zircon upon "dry" thermal annealing. *Miner Petrol*, *97*(1-2), 129-138.

Valley, J. W., Graham, C. M., Harte, B., Eiler, J. M., & Kinny, P. D. (1998a). Ion microprobe analysis of oxygen, carbon, and hydrogen isotope ratios. *Rev Econ Geol*, *7*, 73-98.

Valley, J. W. (2003). Oxygen isotopes in zircon. *Reviews in mineralogy and geochemistry*, *53*(1), 343-385.

Valley, J. W., Cavosie, A. J., Fu, B., Peck, W. H., & Wilde, S. A. (2006). Comment on "Heterpogeneous Hadean hafnium: Evidence of continental crust ar 4.4 to 4.5 Ga". *Science*, *312*, 1139a, doi: 10.1126/science.1125301.

Valley, J. W., Kynny, P. D., Schulze, D. J., & Spicuzza, M. J. (1998b). Zircon Megacrysts from Kimberlite: Oxygen isotope heterogeneity among mantle melts. *Contribution to Mineralogy and Petrology*, *133*, 1-11.

Valley, J. W., Chiarenzelli, J. R., & McLelland, J. M. (1994). Oxygen isotope geochemistry of zircon. *Earth and Planetary Science Letters*, *126*(4), 187-206.

Valley, J. W., Kitchen, N., Kohn, M. J., Niendorf, C. R., & Spicuzza, M. J. (1995). UWG-2, a garnet standard for oxygen isotope ratios: strategies for high precision and accuracy with laser heating. *Geochimica et Cosmochimica Acta*, *59*(24), 5223-5231.

van den Ende, M. P. A., Marketos, G., Niemeijer, A. R., & Spiers, C. J. (2018). Investigating Compaction by Intergranular Pressure Solution Using the Discrete Element Method. *J Geophys Res Solid Earth*, *123*(1), 107-124.

Vavra, G., Gebauer, D., Schmid, R., & Compston, W. (1996). Multiple zircon growth and recrystallization during polyphase Late Carboniferous to Triassic metamorphism in granulites of the Ivrea Zone (Southern Alps): An ion microprobe (SHRIMP) study. *Contrib Mineral Petrol*, *122*(4), 337-358.

Vervoort, J. D., & Patchett, P. J. (1996). Behavior of hafnium and neodymium isotopes in the crust: constraints from Precambrian crustally derived granites. *Geochimica et Cosmochimica Acta*, *60*(19), 3717-3733.

Vervoort, J. D., & Kemp, A. I. S. (2016). Clarifying the zircon Hf isotope record of crust–mantle evolution. *Chemical Geology*, *425*, 65-75.

Vigneresse, J. L., Barbey, P., & Cuney, M. (1996). Rheological transitions during partial melting and crystallization with application to felsic magma segregation and transfer. *Journal of Petrology*, *37*(6), 1579-1600.

Wang, W., Scarratt, K., Emmett, J. L., Breeding, C. M., & Douthit, T. R. (2006). The Effects of Heat Treatment on Zircon Inclusions in Madagascar Sapphires. *Gems and gemology*, *42*, 134-150.

Washburn, E. W., & Libman, E. E. (1920). Approximate determination of melting point diagram of system zirconia-silica. *Amer. Ceram. Soc.*, *3*, 634-640.

Watson, E. B. (1979). Zircon saturation in felsic liquids: Experimental results and applications to trace element geochemistry. *Contributions to Mineralogy and Petrology*, *70*(4), 407-419.

Watson, E. B., & Harrison, T. M. (2005). Zircon thermometer reveals minimum melting conditions on earliest Earth. *Science*, *308*, 841-844.

Watson, E. B., Wark, D., & Thomas, J. (2006). Crystallization thermometers for zircon and rutile. *Contributions to Mineralogy and Petrology*, *151*(4), 413-433.

Watson, E. B. (1996). Dissolution, growth and survival of zircons during crustal fusion: kinetic principals, geological models and implications for isotopic inheritance. *Earth and Environmental Science Transactions of The Royal Society of Edinburgh*, *87*(1-2), 43-56.

Watson, E. B., & Cherniak, D. J. (1997). Oxygen diffusion in zircon. *Earth and Planetary Science Letters*, *148*(3-4), 527-544.

Watson, E. B., Cherniak, D. J., Hanchar, J. M., Harrison, T. M., & Wark, D. A. (1997). The incorporation of Pb into zircon. *Chemical Geology*, *141*(1-2), 19-31.

Watson, E. B., & Harrison, T. M. (1983). Zircon saturation revisited: temperature and composition effects in a variety of crustal magma types. *Earth and Planetary Science Letters*, *64*, 295-304.

Wayne, D. M., & Sinha, A. K. (1988). Physical and chemical response of zircons to deformation. *Contributions to Mineralogy and Petrology 1988 98:1*, *98*(1), 109-121.

Weinberg, R. F. (1997). Diapir-driven crustal convection: Decompression melting, renewal of the magma source and the origin of nested plutons. *Tectonophysics*, *271*(3-4), 217-229.

Weinberg, R. F. (2006). Melt segregation structures in granitic plutons. *Geology*, *34*(4), 305-308.

Whitehouse, M. J., Kusiak, M. A., Wirth, R., & Ravindra Kumar, G. R. (2017). Metallic Pb nanospheres in ultra-high temperature metamorphosed zircon from southern India. *Mineralogy and Petrology*, *111*(4), 467-474.

Whitney, D. L., & Evans, B. W. (2010). Abbreviations for names of rock-forming minerals. *American Mineralogist*, *95*(1), 185-187.

Wickham, S. M. (1987). The segregation and emplacement of granitic magmas. *J. Geol. Society, London*, *144*, 281-297.

Wilde, S. A., Valley, J. W., Peck, W. H., & Graham, C. M. (2001). Evidence from detrital zircons for the existence of continental crust and oceans on the Earth 4.4 Gyr ago. *Nature*, *409*(6817), 175-178.

Wilke, M., Schmidt, C., Dubrail, J., Appel, K., Borchert, M., Kvashnina, K., & Manning, C. E. (2012). Zircon solubility and zirconium complexation in H_2O+Na_2O+SiO_2±Al_2O_3 fluids at high pressure and temperature. *Earth and Planetary Science Letters*, *349-350*, 15-25.

Williams, I. S., & Claesson, S. (1987). Isotopic evidence for the Precambrian provenance and Caledonian metamorphism of high grade paragneisses from the Seve Nappes, Scandinavian Caledonides - II. Ion microprobe zircon U-Th-Pb. *Contributions to Mineralogy and Petrology*, *97*(2), 205-217.

Williams, I. S., & Hergt, J. M. (2000). U-Pb dating of Tasmanian dolerites: a cautionary tale of SHRIMP analysis of high-U zircon. In J. D. Woodhead, J. M. Hergt, & W. P. Noble (Eds.), Beyond 2000: New Frontiers in Isotope Geoscience, Lorne, 2000; *Abstracts and Proceedings* (pp. 185-188).

Williams, I. S., Compston, W., Black, L. P., Ireland, T. R., & Foster, J. J. (1984). Unsupported radiogenic Pb in zircon: a cause of anomalously high Pb-Pb, U-Pb and Th-Pb ages. *Contributions to Mineralogy and Petrology*, *88*, 322-327.

Winther, K. T. (1995). A model for estimating the composition of partial melts. *Miner Petrol*, *53*(1-3), 189-195.

Woodhead, J., Hergt, J., Shelley, M., Eggins, S., & Kemp, R. (2004). Zircon Hf-isotope analysis with an excimer laser, depth profiling, ablation of complex geometries, and concomitant age estimation. *Chemical Geology*, *209*, 121-135.

Yang, D.-G., Sun, D.-Y., Gou, J., & Hou, X.-G. (2018). Petrogenesis and tectonic setting of Carboniferous hornblende gabbros of the northern Great Xing'an Range, NE China: Constraints from geochronology, geochemistry, mineral chemistry, and zircon Hf isotopes. *Geological Journal*, *53*, 2084-2098.

Yeats, C. J., Mcnaughton, N. J., & Groves, D. I. (1996). Shrimp U-Pb Geochronological Constraints on Archean Volcanic-Hosted Massive Sulfide and Lode Gold Mineralization at Mount-Gibson, Yilgarn-Craton, Western-Australia. *Economic geology and the bulletin of the society of economic geologists*, *91*(8), 1354-1371.

Zanetti, A., Giovanardi, T., Langone, A., Tiepolo, M., Wu, F.-Y., Dallai, L., & Mazzucchelli, M. (2016). Origin and age of zircon-bearing chromitite layers from the Finero phlogopite peridotite (Ivrea–Verbano Zone, Western Alps) and geodynamic consequences. *Lithos*, *262*, 58-74.

Zaraisky, G. P., & Balashov, V. N. (1994). Thermal decompaction of rocks. *Fluids in the Crust: Equilibrium and transport properties*, 253-284.

Zhang, M., Salje, E. K. H., Capitani, G. C., Leroux, H., Clark, A. M., Schlüter, J., & Ewing, R. C. (2000). Annealing of -decay damage in zircon: a Raman spectroscopic study. *Journal of physics: Condensed Matter*, *12: 13*.

Zhang, Y., & Xu, Z. (2016). Zircon saturation and Zr diffusion in rhyolitic melts, and zircon growth geospeedometer. *American Mineralogist*, *101*(6), 1252-1267.

Zhirnowa, N. (1934). Melting diagram of system ZrO_2-SiO_2. *Anorg. Allgem.Chem.*, *218*, 193-200.